ON THE GENERATION AND CHARACTERISATION OF NON-THERMAL PLASMA FOR PHYSICAL PROCESS CONDITIONING

Thesis submitted in accordance with the requirements of the University of Liverpool for the degree of Doctor in Philosophy

by

M'dimoir Quaw

April 2008

especially the electrons, must possess a certain level of energy. This requires the existence of relatively strong electric fields in the non-thermal plasma region. In the present work this is realised by the application of high voltage across the electrode gap or the use of specific electrode configurations.

The operation of plasma systems with relatively large discharge spaces is of paramount importance in some cases. A novel DBD based discharge system has been developed in Chapter Two for the generation of filamentary discharge in spaces with adjustable electrode contact area. This configuration produces a stable and durable discharge environment. In addition the contact area of the discharge electrodes can be easily adjusted. The typical contact gap is 5mm and the coaxial electrode length can be varied between 0mm and 111mm. It was found that there exists an applied transition voltage of 10kV above which the discharge switches from silent (dark) discharge to a noisy filamentary regime. This threshold value is independent of the available electrode area. The typical discharge current in the plasma is 9mA and an estimate shows that the electron density range in the filamentary plasma is in the order of $(10^{12}\text{-}10^{15})m^{-3}$ which is comparable with figures given in other publications.

Glow discharge electrolysis occurs when an electrode is suspended above the surface of a liquid. Typically this plasma exists in a large volume with specific features. Practical issues, such as discharge current bypassing the electrode supporting rods in a moist environment, have been carefully considered. The generated plasma is stable and highly luminous. Spectroscopic investigation has shown that the plasma environment is dominated by species originating from the liquid and its container. The detailed electrical characteristics have been discussed. It has been observed that when moist, strong exothermal reactions on solid surfaces (PTFE) were initiated by plasma under high voltages. This could have a

positive implication towards application for energy production in processes that cannot be initiated using conventional methods of activation such as heating. The migration of species in the liquid towards the non-thermal plasma is an interesting point that requires further investigation. It opens the possibility that chemical species that are required in the discharge process can be transported through the liquid in a controlled manner.

Contact Glow Discharge Electrolysis (CGDE) represents another type of electrical discharge in a liquid environment. Its rather small discharge region puts it into the micro-discharge category. In the present work an electrical discharge system with silicon as the active electrode was developed. An electrical discharge was formed on the tip of the silicon electrode. Unlike the discharges investigated in the previous two cases, sustaining CGDE in this case only required a voltage level in the range of a few hundred volts because of its small size. This type of discharge results in a bright region whose diameter is in the order of a fraction of a millimetre. Its stable operation implies that this type of discharge can be considered for use as an open light source in liquid with brightness similar to a powerful LED. Results of energy balance analysis show that the total rate of energy received by the electrolyte stays at a more or less constant value when the applied voltage increases substantially. The fact that the applied voltage does not significantly affect the plasma conductance supports the argument that this type of plasma is self-regulated in energy dissipation inside the electrolyte. The excessive energy dissipated in the discharge system, when voltage further increases from 170V, is contained by the gas produced in the electrolysis process which is heated by the discharge.

The present studies have provided an overall physical characterisation of the various discharge configurations in different environments for the generation of stable electrical discharges. Their electrical behaviour as well

as their optical characteristics was experimentally observed. This forms a platform upon which further investigation can be made and potential stated applications pursued.

ACKNOWLEDGMENTS

The author wishes to acknowledge his supervisor Dr. J.D. Yan for his patience over the years; his willingness to hear new ideas and guidance have been of great benefit. His influence in the research has been thought-provoking and beneficial. The author acknowledges Dr. J.W. Spencer. It was his challenge that induced the undertaking of this research. His enthusiasm and positive outlook gave hope when things were not always straightforward. Mr. J.E. Humphries has been of incalculable benefit to the research. Although designated to supervise the author and neighbouring workers safety, he does not discourage one from exploring new ideas and procedures. Ever willing and interested to share an engineering problem, in him was found a kindred spirit. Very special thanks to Miss. M. Burns, Mrs. J.M. Anson, Miss. N.R. Telfer, Dr. A.C. Pate, Mr. K. Malloy and Dr. K.J. Wong within the Department of Electrical Engineering and Electronics.

The author's gratitude is not limited to his own department as there were several individuals on-campus who assisted with the research. They are Dr. J.C. Jarvis (School of Biological Sciences), Dr. M.F. Thomas (Department of Physics), Mr. S.G. Apter (Department of Chemistry) and Prof. D.J. Schiffrin (Department of Chemistry).

Mr. R. Lewallen (EZNEC) and Dr. R. Brownsword (Engineering and Physical Science Research Council) are also warmly thanked for their input and assistance.

The author is grateful for the opportunity to follow a life-long passion of experimentation in electromagnetism. Much is owed to several individuals

for the steps culminating to this position. A thesis is a laconic document and in this spirit the author chooses a handful of family and friends to acknowledge who have directly assisted the research. The author thanks Dr. R. Abbas for reviewing the thesis despite her time constraints and would also like to thank his brother for his active support with the literature review, compilation and for supplying much-needed equipment. The author is eternally grateful to his mother for the supply of equipment, shelter, maintenance and support. Finally, the author is grateful to the Prime Mover; without whom nothing is possible and with whom the events outlined in this thesis were.

This thesis is dedicated by the author to those who thought warmly of him and wished him well. Chief amongst these are Mr. H.A. Abadoo-Brew (Deceased), Ms. S.H. Abadoo-Brew, Mr. Q.Q. Quayson, Mr. D.B. Maloney, Mr. A.Y. Maama, Mr. J. Borbin, Mr. I. Mensah (Deceased), Mr. P Harvey, Mrs. J. Cannon and Mrs. S. Young. Thank you all.

TABLE OF CONTENTS

PREFACE

All units of measurement in this thesis are expressed in terms of S.I (Système international d'unités) unless otherwise stated. Relative quantities or "Rel." as the word may be abbreviated for aesthetics are by their very nature dimensionless. In the graphs they represent the ratio between any data point and a carefully chosen reference value (usually the point of greatest magnitude of that data set).

Although the units represented in this thesis are S.I., they may be preceded by prefixes indicating their order of magnitude. For example "nm" represents nanometre where the usual meanings of the prefixes are maintained. This system will be followed in the strictest sense in this thesis (unless otherwise stated) with any derived quantities defined prior to their appearance or shortly following.

On tables, the mean values of quantities are displayed with their uncertainties expressed as a percentage. The rules of obtaining these uncertainties are standard and will be demonstrated in Appendix II. In all cases, the uncertainties are additive (in quadrature) so only the most significant values were computed for simplicity although the exclusion of insignificant uncertainties was justified. The percentage uncertainty was quoted to a relevant number of significant figures. The tabulated and other precise results are quoted with their uncertainties. Results rendered in some analytical discussions are quoted without uncertainty as they are merely estimates (usually involving the work of others in conjunction with the present work). Many graphs are left free of uncertainty bars (if insignificant i.e., far shorter than the distance between the points) for the purpose of easy viewing. Most results were not assessed graphically (line

of best fit etc) and so uncertainty bars on them would be unnecessary. The graphs represent trends in data and were plotted from the spreadsheets therefore the spreadsheets could determine the results from direct calculation. It was counter productive to reproduce the volumes of raw data obtained from experiment in this document. To do so would be to mire the report in matters of data handling which were done automatically in Excel. The processing steps shall rather be mentioned and related to the equations that appear in the following chapters.

Most of the figures (graphs, illustrations, tables, photographs and diagrams) were produced by the author of this thesis from the present work. Images that are featured and readily available on the web (Reproduced so often that their primary source is obscured) are presented in this thesis with the most recent source indicated in the caption. Images from other publications with no adjoining journal references (conference papers etc) have their sources cited in the caption to acknowledge the authors of the corresponding literature. The citations do not appear in the reference section of this thesis (as they were not published in a journal).

Finally, the author's background is in physics must be conveyed. The symbols and fundamental approach used throughout the thesis may reveal this to some readers. Apparatus was often constructed by the author or reconfigured from existing experimental rigs. The finalised experiments whose results are reported in detail a fraction of the experimental work done to obtain the most suitable, stable, safe, environmentally friendly and economically viable configurations and substances. These stringent conditions are the criteria for the initial thrust of the work; research into alternative energy sources. This field has not been pursued in this manner or for this purpose in the recent history of the department but was initiated by work done by G. Petkos, W.D. Yuan, J. Humphries, J. Spencer, G.R.

Jones, and W. Hall on long-lived luminous particulate formation following arcing in high-voltage interrupters. The present done was often from scratch and very rewarding. The trials and errors have been catalogued here as well as the polished results and their implications.

Chapter 1

INTRODUCTION

1.1 Plasma and Non-thermal Plasma

The Universe mainly consists of plasma. Condensed or solid phase matter consists of atoms and molecules held in a crystal lattice or at fixed positions. Fluids in the liquid phase consist of atoms and molecules which have similar spacing to solids but are held in no particular position. Gases (also classified as fluids) have their atoms and molecules widely spaced from each other and are free to move at any orientation with respect to one another. Broadly speaking plasma is similar to a gas with the exception that its atoms and molecules no longer posses a full orbital (compliment) of electrons as the latter are free to move through space. The dissociation of electrons from their parent atoms or molecules makes plasmas electrically conductive and leaves the parent atoms or molecules (now ions) with a net positive charge. The change of matter from solid to plasma is accompanied by an increase in its energy content. This is normally realised by supplying energy to the matter via different possible methods; electrically, thermally or aerodynamically.

A gas becomes plasma when heated to such a degree that the thermal motions of the atoms cause ionisation (The removal of one or more electrons from an atom or molecule). More commonly (in laboratory conditions) in the presence of high electric fields, existing free electrons (stripped from their parent atom by cosmic or background radiation) are accelerated to high kinetic energies and collide with another atom or molecule. This may release a secondary electron by ionisation and the two

free electrons may go on to produce four when accelerated by the electric field. This effect cascades and an avalanche of electrons results: Ionisation equilibrium is realised. This occurs when the recombination of electron-ion pairs is equal to their creation (Ionisation rate becomes equal to recombination rate). An ionised gas can only be called a plasma when its characteristic length is much larger than the Debye length which reflect the extent of charge separation due to thermal movement of charged particles.

Thermal plasmas have very high energy content and its maintenance therefore requires very high power input when energy is escaping from the plasma region such as through thermal conduction or radiation. The maintenance of thermal plasma also requires that the energy exchange rates between different energy-levels through various types of collisions are much higher than the rate at which the energy is lost. Any mechanism that leads to stronger energy loss from the plasma can render the plasma into a non-equilibrium state. In electrical discharges, this can occur when the electron number density is low and electrons cannot transfer their high kinetic energies to the heavy particles thus resulting in a large difference between electron and heavy particle kinetic energies. Under such circumstances, the plasma formed is usually non-thermal.

It is worth noting that the definition and use of the concept of temperature has certain requirements. Strictly speaking, only when the distribution of energy of a collection of particles follows the Boltzmann distribution is the use of the word "temperature" valid. In non-equilibrium situations, the Boltzmann distribution may still be found in different degrees of freedom (energy partition), such as translation, excitation, vibration, rotation, etc. In this case, each degree of freedom can be quantified by a corresponding temperature.

1.2 Generation of Non-thermal Plasmas and their Applications

In a dielectric medium such as air and in the presence of ambient free charged particles (usually electrons caused by cosmic ray ionisation or background radiation) an electric field can accelerate such particles to kinetic energies high enough to cause ionisation in neutral atoms and molecules. In other words, fast electrons can dislodge other electrons from neutral atoms causing them to be free and the atoms to become electrically charged (positive). In nature these electrical fields are a consequence of unbalanced, exposed charges in space or due to time-varying magnetic fields. For example, a sheet of charge would generate a field **E** near its surface described by the following equations.

$$|\mathbf{E}| = \frac{\sigma}{2\varepsilon}$$

Equation 1.1

E is the electric field, σ is the surface charge density and ε is the permittivity of the medium (all units in this thesis are S.I. unless otherwise stated).

$$\sigma = \frac{dq}{dA}$$

Equation 1.2

Here q is charge and A is area. Since charge cannot be created or destroyed, a neutral system must undergo charge separation in order to produce a local electric field. Separating charges requires energy and the energy per charge is the potential difference. The electric field depends upon the potential difference across a region of space so from a practical point of view, the spatial separation of the terminals of a potential difference source determines the electric field between those terminals. For

parallel plate terminals, electrodes or dipole the electric field is given by the following equation.

$$\mathbf{E}(z) = \frac{V}{z}\hat{k}$$

Equation 1.3

Equation 1.3 holds true for the centre of a parallel plate dipole where V is the potential difference between the plates. The unit vector $\hat{k}$ indicates orientation of the field parallel to the z-axis in this case. To achieve electric breakdown in air a $3MVm^{-1}$ (or $3kVmm^{-1}$) electric field must be generated. With a perfectly smooth parallel plate configuration, the applied voltage would actually have to be 3kV or higher for every millimetre of plate separation (See figure 1.1).

It is known that the electric field experienced by the electron from its orbital around the proton at the nucleus of the hydrogen atom is approximately $144GVm^{-1}$; although it carries much less charge than the electrodes in this thesis, they generate a higher electric field due to their smaller separation. Using a pin-electrode is the closest way of recreating the point-charge previously mentioned for the hydrogen atom.

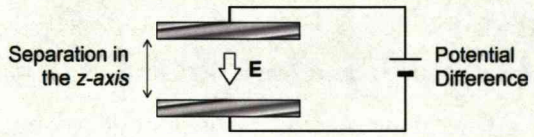

Figure 1.1 is a simple parallel plate configuration powered by direct current voltage source.

Illustrated in figure 1.2 are two conducting spheres that are equally yet oppositely charged. Although in reality, with the two spheres attached to a

cell the difference in electrode areas would probably cause the charges on both spheres to be slightly unequal. A surface with a small radius of curvature can behave as a point-charge and produce high electric fields. These local fields can be generated at low applied voltages (See figure 1.3). The electric field of a spherical distribution of charge is proportional to the inverse square of the distance from it. The radius of curvature of figure 1.3 is analogous to the spherical radius of figure 1.2 (sphere "a").

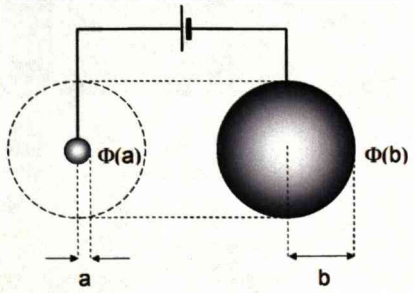

Figure 1.2 indicates that sphere *a* has a higher charge density and greater electric field near its surface than sphere *b*. ϕ is used here for potential instead of V for potential difference between two points.

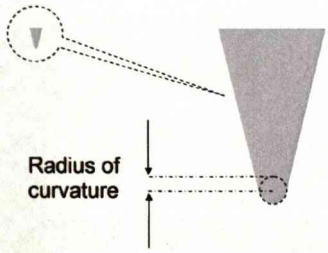

Figure 1.3 is a close-up of the pin-electrode and its similarity to the point-charge.

These basic concepts of electrode curvature (sharpness of a pin-electrode) and electrode separation describe how an electrical discharge is generated using any pair of electrodes. Every method of plasma generation discussed in detail in this thesis uses these basic premises.

1.2.1 Dielectric Barrier Discharge (DBD)

The dielectric barrier discharge (DBD) is the electrical discharge formed between one or more insulated electrodes under application of high-voltage. As the electrodes become charged by the voltage source they polarise the dielectrics that cover them.

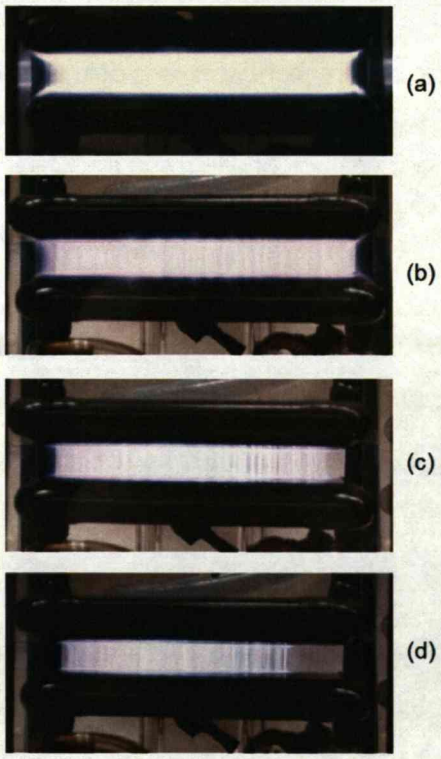

Figure 1.4 shows the appearance of the Mod I parallel plate One Atmosphere Uniform Glow Discharge Plasma™ (OAUGDP). The reactor operates under 1 atmosphere of helium at 4.5kV RMS and a gap spacing d = 25 mm at frequencies of (a) 30kHz; (b) 40kHz; (c) 60 kHz; and (d) 80kHz. Images courtesy of Roth et al.[1]

An induced surface charge exists on the dielectric(s) that generates an electric field in the inter-electrode gap. If the field is high enough, the medium in the gap undergoes electrical breakdown and a conductive current is established there (plasma). Kirchoff's law is not violated; a displacement current is established due to the changing electric fields (AC) within the dielectric. The rate of change of surface charges across the dielectric surfaces is also classed as and is equal in magnitude to the flow

of charge through the gap at any instant in time. The dimensional equivalence between the current-density and the rate of change of the electric field is shown by two terms on the right hand side of Maxwell's relation in equations 1.4

$$\nabla \times \mathbf{H} = \mathbf{J} + \dot{\mathbf{D}} = \frac{di}{d\mathbf{A}} + \varepsilon_0 \varepsilon_r \frac{d\mathbf{E}}{dt}$$

Equation 1.4

The graph of figure 1.5 maps the path on voltage-current axes of plasma in a low-pressure discharge tube. Although it is not identical to the situation reported for atmospheric pressures, it behaves as a good benchmark in a controlled, reduced pressure environment. For details on the technology that utilises plasma at these different regimes see work done by Roth et al.[1]

The curves from A to F represent the non-luminous regime. The initial non-luminous discharges produced a crackling sound and the smell of ozone gas in an oxygen-containing atmosphere. When the voltage is increased further, the luminous discharge was observed. At reduced pressures, a glow discharge is observed. This plasma appears as the luminous region between the two electrodes (at low pressures, dark and luminous bands can be observed in the glow discharge). Its volume is defined by some fraction of the electrode area and separation. When the voltage is increased, the discharge area simply increases until it covers that of the electrode; this is the normal glow discharge regime and its current-density does not noticeably vary. If the voltage is increased further, the discharge has no option but to increase its current-density. When the voltage required for the electrode area to be completely covered is surpassed, the abnormal glow discharge regime begins. If the voltage is increased further the vector cross-product of the current-density and its

associated magnetic field imposes a force that squeezes the discharge into thin filaments that are most commonly observed in nature and under atmospheric pressure (like lightning): This is the arc regime. Like most atmospheric pressure plasma, the DBD appeared filamentary and thin (~0.1mm diameter[1]).

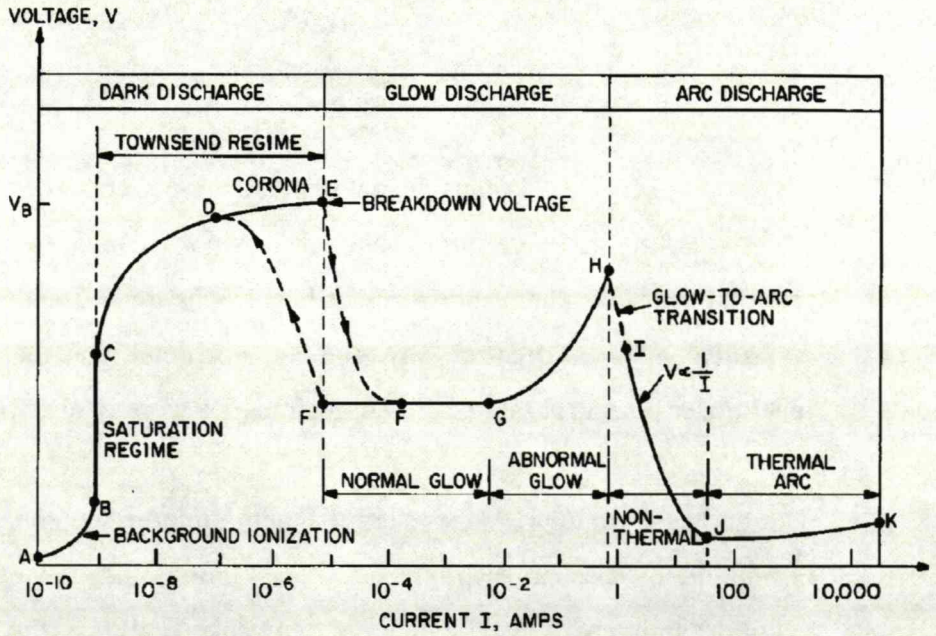

Figure 1.5 illustrates regimes of the classical DC electrical discharge. This image was featured in the literature[1] as well as several other online sources.

In order for a dielectric barrier discharge to appear uniform and non-filamentary, high frequencies must be applied (~20 kHz). The application of high-frequencies prevents the slower and heavier ions bombarding the dielectric surface and creating hotspots. These regions vaporise the dielectric material and are ionised. Their emergence from these spots contributes to the formation of thin filaments. In other words, the filaments are rooted to the dielectric via the spots. The high frequencies permit electrons to leave the dielectric surface (like a static discharge) without the bulk of the material being disturbed. The ions oscillate in the region

between the (virtual) electrodes of opposing polarities. Electrons move through the gap exciting and ionising the neutral species that it encounters. This explains the luminous component of the discharge and the conductivity of the medium between (virtual) electrodes.

The applications of DBD are diverse but tend to be used for surface treatment, sterilisation and implantation (see later text for references). An interesting physical process that the DBD is used to condition is the electrodynamic manipulation of fluid flow over its surfaces[2,3]. This approach is not unique as there is another example of a similar effect. Here the motion of ions by application of the electric field is used to manipulate or influence the motion of neutrals by momentum transfer. This phenomenon is electrokinetic and one such case is known as the Biefield-Brown effect (derivation of thrust by asymmetric high-voltage capacitors). The DBD can be used to alter conditions in the boundary layer of the electrodes and therefore influence its drag (the aerodynamic force that opposes thrust) coefficient, in a flow-stream.

The chemical aspects of the DBD are dealt with by several authors however in this thesis they were only observed but not analysed. The physical process conditioning was of importance so the gas, electrode geometry, configuration and materials[4-13] were considered. Glass was commonly used as the dielectric and the electrodes were metallic. The charge accumulated and discharged was also crucial in determining the behaviour of single filaments as well the energy content[14,15]. These factors were important for our purposes.

A more common use of the DBD in an oxygen-rich environment is for the production of ozone[16-18]. This gas is often dissolved in water and acts as a disinfectant. It has been used in many water purification applications. The

advantage of it is that it consists only of oxygen atoms and is safer to humans when it decomposes than in its initial state (ozone).

A homogeneous atmospheric pressure dielectric barrier discharge can also be used to chemically treat dielectric surfaces. This usually involves deposition[19,24]. If for example titanium tetrachloride (the coating material) is mixed with the gas of the discharge medium which may be oxygen/nitrogen, then thin titania films can form on a glass substrate. Typically ~10kV are applied with low current densities ~10Am^{-2}. The DBD has been utilised for its ability to sterilise surfaces[25-33] due to the production of free radicals. Free radical formation is something that will be discussed further in the glow discharge electrolysis section. The radicals and chemically active species denature bacteria and degrade toxic chemicals such as dyes. As a result DBD is used for advanced oxidation technology.

1.2.2 Glow Discharge Electrolysis (GDE)

An electrode was immersed in liquid water and another suspended above the water surface. When high-voltages were applied a relatively large volume plasma column was generated. This was done under atmospheric conditions in the present work. DBD experiments with setups mentioned in the previous sections produced only thin (~0.1mm diameter) filamentary plasmas at low frequencies. The dielectric barrier was removed and the electrical discharge was generated for some period of time (a few minutes) at higher power levels. Gases such as ozone and nitrogen dioxide were being formed. When water was used as a virtual electrode instead of a solid dielectric these gases were no longer detectable and the plasma volume appears much larger than the thin filamentary plasmas at low frequencies.

In the literature[34,35] non-thermal plasmas are often used for their ability to produce high-energy electrons and chemically active species due to the

formation of free radicals by electron or ionic bombardment. Where thermal plasma may be used for its high heating power density[36] (as was observed in the present work), non-thermal plasmas have the ability to cause the substances in its volume to become chemically active and these new species then react with the intended substance to produce new substances or achieve expected effect[37]. Traditionally non-thermal plasmas have been widely used for their role in chemical reactions and usually at reduced pressure. GDE in the present work was found to be highly luminous[38-46] due de-excitation after electron and ion collisions with the water molecule. This brings into question whether GDE[47] at atmospheric pressure is thermal plasma or non-thermal plasma. The work done by others will be discussed here and this debate will be left for the appropriate chapters. The involved reactions concerning GDE[48-52] are very complex and the products and yields are not as trivial to predict as those that occur from the combustion of oxygen with carbon for example. GDE is primarily used to degrade aqueous compounds and purify water[53].

In the last two decades, the method for producing radicals within the gas emissions of automobiles, chemical industries and other waste generating systems has been as diverse as the method and means of generating plasma. Ultraviolet light, heterogeneous photocatalysis, electron beam treatment, supercritical water oxidation, various combinations of hydrogen peroxide, ozone, cavitation and sonolysis are all methods that dissociate molecules in a medium and the radicals formed then go on to react with or attack the intended species that is considered a contaminant in the medium. These are all forms of "non electrical" advanced oxidation processing (AOP) and will not be discussed further as they do not relate directly to the work in the main body of this thesis.

Electrical discharges were also used underwater and more commonly in recent years a hybrid of gas and underwater discharges. In the former case,

both electrodes were submerged underwater. The discharge resembles lightning due to its branched structure. The voltages and water purity were not high enough to work with plasma in this regime. Water only undergoes electrical breakdown when it is highly purified and requires extremely high voltages to initiate underwater discharges. These conditions are severe and were not considered applicable to the present research.

Gaseous discharges can be initiated with much lower electric fields generated at the high voltage electrodes (~1kVmm^{-1}) in comparison to the fields required in the aqueous phase systems since the gas acts as an insulator while the liquid is generally conductive. The intermolecular/atomic spacing in a dielectric gas permits the acceleration of electrons to attain high energies whereas the closely packed molecules in a liquid cause charged particles to collide before reaching high enough energies. The mechanism and temporal evolution of various reactive species by the gas phase discharges is better understood than for the liquid phase discharges judging by the available literature. The application of voltage in gases energises free electrons to eventually cause dissociation and ionisation via collision to form ions, metastables, atoms and free radicals.

In dry electrode plasmas, ozone production is prevalent whilst water-based plasmas produce hydroxyl radicals. These aqueous plasmas have water in the liquid phase acting as a virtual electrode or in the gas phase in place of air. However energy economy has encouraged the development of electrical discharges above the aqueous surface as opposed to within its bulk for the purpose of waste product degradation.

The use of the pin-planar electrode configuration with a conductive pin suspended above an electrolyte's (in electrical contact with a submerged counter electrode) surface has been used extensively over the years to

produce an effect known as glow discharge electrolysis or merely the formation of coronal discharges from a suspended electrode to the water surface (The two are virtually indistinguishable in configuration but the former requires more power and is far more luminous and of greater discharge volume). In these cases, the plasma exists between the pin and electrolyte surface (only) upon the application of high-voltage. The bombardment of electrons and ions upon the surface produces radicals within the liquid and plasma column. The discharge can change some of the properties of the liquid.

Ivannikov et al.[53] have hypothesised that the formation of H_2O_2 takes place primarily in the cathode spot region in a thin layer (~0.1 mm) at the plasma-water interface due to recombination reactions of the reactive species $OH^{\bullet}$, $H^{\bullet}$, $HO_2^{\bullet}$, $O^{\bullet}$ and $O_2^{\bullet}$. This process is highly dependent upon electrode-electrolyte separation which varies between a few millimetres to a few tens of millimetres under atmospheric pressure. It has been observed in the present work that the high electric fields tend to raise the electrolyte surface in a bulge pointing towards the electrode by as much as a few millimetres due to electro-kinetic effects (to be discussed later in this chapter). As a result there is an inherent uncertainty in this type of experiment.

The reactive species, including $OH^{\bullet}$ and $H^{\bullet}$, are produced by the collision of the ions generated in the plasma with aqueous phase water molecules. Experiments have been conducted initiating positive and negative polarity high-voltage DC discharges in air a few millimetres above the water surface. The effect of ionic and neutral reactive species is observed. It was found that the neutral species (Nitrogen) reaching the liquid phase are primarily responsible for the changes in the pH observed in the liquid (This effect was also observed in the present work and reported in chapter three).

The production rates of various reactive species under different discharge modes have been quantified for discharges over water surfaces, e.g. ozone and hydrogen peroxide produced by corona, spark, and arc discharges (Piskarev et al.[48]). Hydroxyl and nitrogen radicals, ozone and hydrogen peroxide for pulsed corona and nanosecond streamer discharges were explored by Aristova et al.[52] It has been found that the voltage polarity influences the distribution and production rates in all discharge modes. Negative polarity leads to higher hydroxyl radical production.

GDE is readily accessible to spectroscopic analysis (especially at low pressures). Plasma may emit light due to several processes. In the present work, sodium atomic spectral lines were observed along with the broadband spectrum of water. These types of discrete spectra arise when an atom or molecule has been excited (by the absorption of a photon of the correct energy or collision with another particle). The atom or molecule then de-excites by emission of a photon. The molecule is made of more than one atom and so forms electronic energy-levels distinct from those of its constituent atoms.

The potential-well (quasi-harmonic but closely resembling the Leonard-Jones potential) that exists due to the attraction between atoms bound in a molecule also enforces energy quantisation just as an atom (nucleus-electron system) bound systems do in the electronic energy-level case. These energy-levels represent vibration of the atomic nuclei with respect to one another and are able to absorb and emit photons by excitation or de-excitation respectively. Vibration energy-levels exist only in molecules and are typically separated by ~0.01eV (Infra-red radiation).

For molecules, each electronic state has several vibration substates. The molecule is an extended object and rotation is another way that it expresses its energy. This is quantised for molecules with an electric dipole moment

and photons may be absorbed or emitted by excitation and de-excitation respectively. Several rotational energy-levels exist for each vibration level. It should be noted that for the atom and molecule, excitation of any of these energy states is possible by collision with other particles as well as photonic absorption. The rotation energy-levels are typically separated by ~0.0001eV (Microwave radiation).

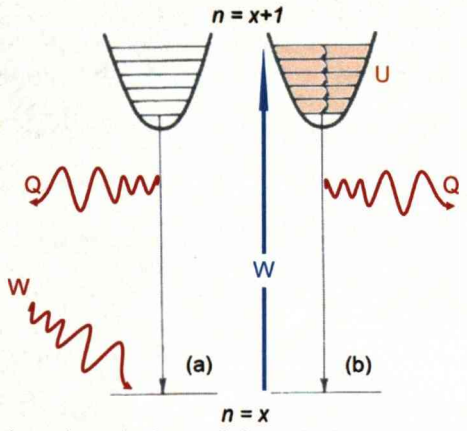

Figure 1.6 Diagram (a) photonic excitation and de-excitation. Diagram (b) collisional excitation and vibrational de-excitation followed by photonic de-excitation. n = x + 1 is the excited electronic state and n = x is one vibrational level of the electronic ground state. W, Q and U refer to the excitation work (photonic or collisional), emitted radiation and retained internal energy of the excited state respectively. Only two electronic levels are shown with several vibration levels. Rotation has not been illustrated here for clarity.

Figure 1.6 shows the complexity and fine-structure of an electronic molecular energy-level transition. Photons will be emitted between vibration states (of different rotational angular momentum). However the transition between adjacent (vibration or rotation) states cannot be observed by the spectroscope as their associated energy is in the infra-red or microwave region of the electromagnetic spectrum.

Returning to molecular vibration, we find that within each electronic level there are several vibration levels. The Leonard-Jones potential is harmonic at low energies (Observe the "U-shape" of the energy-levels of figure 1.6) and so has fundamentals (or rather overtones) associated with it. That is to say; the wavefunctions that describe the vibration state can exist as linear

combination of the fundamental wavefunction native to that state (In the same way one may generate standing waves of several frequencies on the same length of string). The shear number of these energy states that exist in a molecule can cause its spectrum to appear almost continuous or broadband especially when rotation spectra are superimposed.

True continuum spectra are produced by the free charged particles that exist in plasma. Recombination of electrons and ions will produce a range of photon energies limited only by the range in incident particle (mainly electron) energies prior to recombination. The energy state of the recombined atoms or molecules are well-defined and all other energy prior to recombination will be rejected as photons. The photon energy will be equal to the difference between the total initial kinetic energy and that of the final atomic or molecular state. Since electron kinetic energy is continuous, so too will be the photon energy spectrum.

Charged particles that do not recombine will scatter off one another. If this is inelastic then a photon will be emitted whose energy is equal to the change in total energy of the charged particles before and after the scattering. This is called Bremsstrahlung (breaking) radiation and the maximum photon energy in this spectrum will be equivalent to the maximum kinetic energy lost in charged particle scattering processes. Bremsstrahlung can occur between a charged and neutral particle but requires at least one charged particle to change its kinetic energy.

Plasma also absorbs certain (preferential) wavelengths of light due to its optical thickness and opacity. The spectroscope was only equipped to measure electromagnetic radiation at optical wavelengths so ascribing a blackbody fit or assigning a minimum wavelength to spectra was not totally convincing (especially for water spectra). Despite this, the assumed blackbody fit in the wavelength range available for observation in the

present work was made and compared with the nominal bremsstrahlung region of the spectral profile.

1.2.3 Contact Glow Discharge Electrolysis (CGDE)

Contact glow discharge electrolysis occurs when an electrode with a small surface area is immersed within a liquid electrolyte and partially sheathed in the gases produced by electrolysis. As the voltage increases, the current follows accordingly and by faraday's law the electrode becomes completely sheathed in electrolysed gas and steam produced by joule-heating. The current is highly restricted in this case and the gas undergoes electrical breakdown as the voltage is increased further. An electrical discharge is supported by the applied voltage in this minute gaseous sheath. Unlike GDE; CGDE has two electrodes immersed in the liquid and the gas forms and envelops the smallest one.

The high electric fields generated near the small wire-electrodes in CGDE produce electrical discharges. Non-faradic yields of H_2, O_2, and H_2O_2 are produced during anodic CGDE as researched by Sengupta et al.[54] amongst others. It has been proposed that the hydroxyl radicals are the primary reactive species formed in the liquid phase by CGDE based on the analysis of the by-products of benzoic acid degradation[55]. As well as the degradation of aqueous compounds[56], organic compounds and amino acids have been synthesised by other workers[57,58] researching CGDE. It has thus been suggested that electrical discharges may have assisted the process of biosynthesis from inorganic materials in primitive conditions in the prehistory of our planet[59]. It is interesting to note the similarity of the branched structure of lightning, underwater streamers, vegetation roots and nerve-fibres.

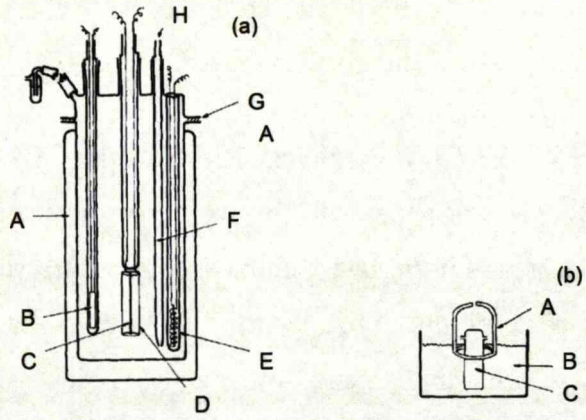

Figure 1.7(a) is a schematic diagram of the calorimeter used and (b) is a schematic diagram of the calorimeter and dome inside the thermostat. These drawings are rather antiquated and were kept in the original form to convey this. The labelling is as follows...(A) Dewar container; (B) platinum resistance thermometer; (C) working Pt electrode; (D) Pt gauze counter-electrode; (E) heater; (F) gas bubbler; (G) silicone rubber gasket and (H) argon inlet. Internal diameter = 4 cm; internal height (from bottom to the flange) = 18 cm. For figure 1.7(b) the labelling is as follows; (A) Thermostated dome, (B) thermostat, and (C) calorimeter.

Figure 1.7 illustrates the work done by Cunnane et al.[60] on electrochemical calorimetry of the normal electrolysis process in water. It should be noted that this represents conventional electrolysis and not contact glow discharge electrolysis. The cell of figure 1.8 was used by Miles[61]. This apparatus did not operate under CGDE conditions either. Normal electrolysis was the regime observed here for the cold fusion experiments. A light-water jacket was used here to regulate the heavy-water temperature. There was no vacuum flask used. Figure 1.9 is an illustration of the cell configuration adopted by Mizuno and Tanaka. They were two of the few authors that have presented work on CGDE calorimetery.

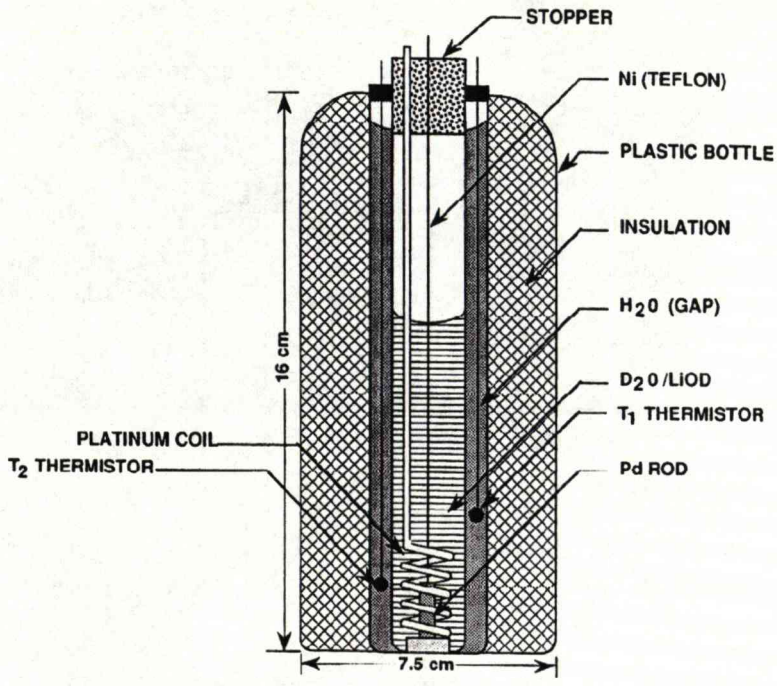

Figure 1.8 is another electro-calorimetric cell without the use of a Dewar flask. Note the co-axial electrode configuration. The inner electrode is a Pd (Palladium) rod, outer electrode a platinum coil. The illustration is courtesy of Miles[61].

The calorimetric setup used by Hansen et al. (see caption) is given in figure 1.10. As with most AOP's, CGDE is used to produce radicals to degrade waste, however Mizuno and Tanaka use this plasma to produce hydrogen from organic compounds. It is therefore a means of potential energy production however the required input power to extract the gas must be compared with power made available by using it as a fuel. Mizuno and Tanaka use a tungsten wire insulated by a shrinkable Teflon sleeve. Its exposed area is coaxial with a platinum meshed cylinder acting as a counter-electrode. The plasma envelops the tungsten wire and the evolved gas was collected and analysed. The attractiveness of this electrochemical cell was that it operated at 140V as opposed to the several kilovolts required for GDE.

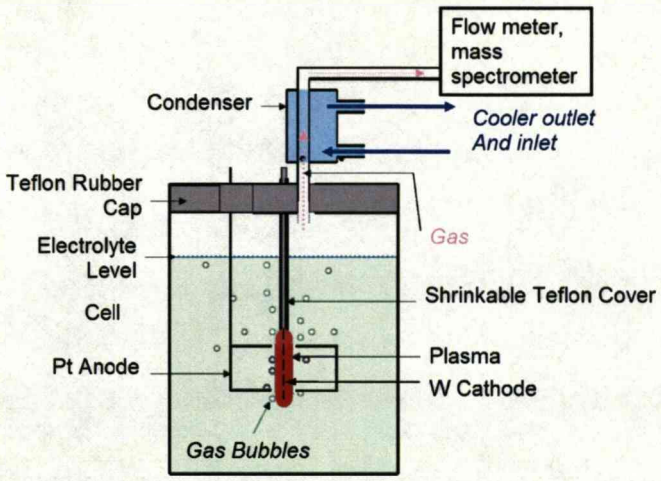

Figure 1.9 shows Mizuno and Tanaka's[a] CGDE electrolysis cell. The electrode configuration is co-axial in this cross-section. The outer coaxial electrode is the Pt anode. The cell rests within an incubator for thermostasis.

The amount of work done is vast however it appears that overall thermodynamic consideration of these discharges is often neglected except in topics related to cold fusion (as yet still unproven). No mention seems to be made in the literature to the plasma parameters of contact glow discharge phenomena perhaps due to its minute dimensions and optical inaccessibility (since it is submerged in an electrolyte).

[a] The illustration is courtesy of Mizuno T. and Tanaka Y. "Hydrogen Generation by Plasma Decomposition from Mixture of Organic Solution", AIAA 3rd International Energy Conversion Engineering Conference, San Francisco, California. 15 - 18 August. (2005)

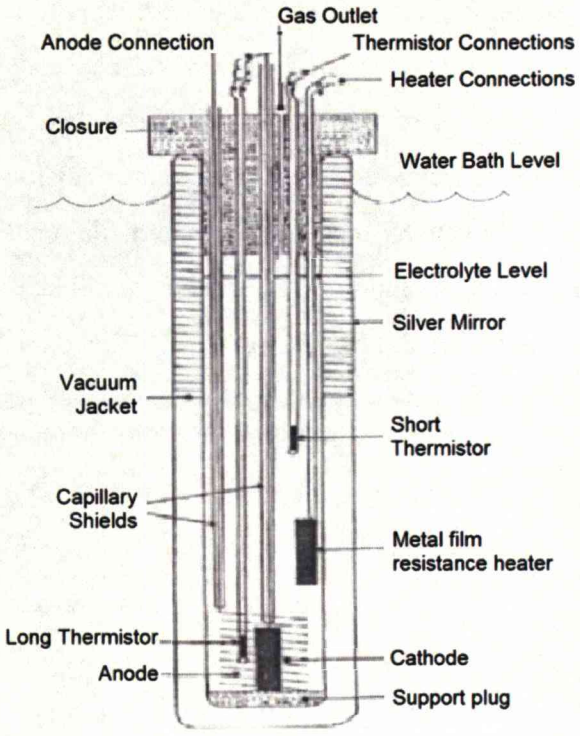

Figure 1.10 An electrochemical calorimetric cell encased by a Dewar-type vacuum flask and submerged in a water bath. Electrode configuration is co-axial yet again[a].

1.3 Overview of Current Work and Main Findings

1.3.1 Dielectric Barrier Discharge (DBD)

DBD were the first series of experiments. The initial aim was to devise a means of generating plasma with the minimum possible voltage under atmospheric pressure with high-stability. The electrode configuration was able to function repeatedly (minimum electrode wear), generate non-thermal plasma (done by using a dielectric sheath), resist arcing even at high-voltages, and was powerful enough to cause chemical changes to its surrounding medium (ozonation). The DBD provided the benchmark for other plasma generation in the present work.

[a] Image courtesy of Hansen W.N., Hansen, G.J. and Glenn D. "Analysis of Some Electrochemical Calorimetry Data". Tenth International Conference on Cold Fusion, Cambridge, MA (2003)

The dielectric barrier discharge experimental configuration finally arrived at was novel and robust. The co-axial electrodes were designed to have adjustable area. It was found that the voltage-current relations were not affected by electrode area. It was found that for dry electrodes, electrical discharges manifest themselves as thin filaments and their current at any given voltage is random. Despite their small size and low luminosity, each discharge had an average power of ~10W and an impedance of ~10kΩ.

From the literature; at higher applied frequencies the current-density, voltage, electron number density and radical concentration may be delicately controlled by manipulating voltage. From the current work, it is theoretically possible to increase electrode area without having to replace the electrodes. Thus high frequencies can be used to produce a uniform discharge and the increase in electrode area can forestall the transition of the glow discharge to the abnormal or arc regimes. This could be of great value for waste material degradation technologies and AOP research. The nominal electron number density was found to be ~$10^{12}m^{-3}$ to ~$10^{15}m^{-3}$ which is in agreement with the literature[15].

1.3.2 Glow Discharge Electrolysis (GDE)

The second series of experiments and the secondary experimental aim was to use the most suitable electrode configuration and composition to facilitate an exothermic plasma chemical reaction. As effective as the DBD experimental setup was at causing chemical change in the air-gap between the electrodes, it did not substantially involve the electrodes themselves chemically. Although it has been stated in the previous section that electrode wear should be avoided, the more molecules involved in reaction the better. A solid is denser than a gas in general and will provide more reagent per unit volume. Using a solid as fuel would require some sort of replenishing mechanism.

It was observed that the plasma column is only guaranteed to make contact with the electrodes that support it so the electrode material must be the reagent. Unfortunately electrode wear is an issue as previously mentioned and there was no guarantee that the ideal reagent would even conduct electricity (Although this is not necessarily a problem since the DBD utilised at least one dielectric virtual electrode). The solution to the problem was quite literally to use an aqueous solution. The liquid could indefinitely be replenished without complex mechanical interference. It would react with the plasma without being exhausted because another volume of liquid would replace the ablated quantity. As well as this, a variety of soluble solids and gases could be added to the solvent to sustain an exothermic reaction.

Extensive work with the dry electrodes at high power levels produced nitrogen dioxide as well as ozone. This was evidence of the occurrence of chemical reactions (but only in the air). Using water as one virtual electrode prevented the detection of these acrid and pungent gases and was therefore environmentally friendly. In the case of the aqueous solvent; chemical reaction and radicalisation did occur however the radicals produced were short-lived and always decomposed or recombined into water again and so were not detected. The existence of radicals within the plasma and its ability to radicalise molecules was a promising property for later experiments where it was hoped that the dissolved substances would be process conditioned for further chemical reaction.

The open nature of the GDE setup excluded the possibility of accurate calorimetry. The process was set up in both open and closed (Thermally insulated) systems. In both, water temperature was measured but gas temperature was only measured for the closed system. The gas temperature at horizontal displacements was a few hundred Kelvins (similar to room temperature) yet the gas at vertical displacements (Directly above) from

the discharge was over 1500K (Thermocouple limit). It should be noted that both displacements were relatively equidistant from the discharge.

Observation of the optical characteristics of GDE proved very instructive. It was observed that when contaminants were added to the electrolyte, the phenomena of florescence occurred prolonging the afterglow of the plasma at low voltages. This observation goes some way towards explaining the phenomena observed by Jones et al[a]. with circuit-breakers. This work was not published in a journal however it was the precursor to the present work and deserves citation. Metastables in the particulates (caused by PTFE ablation) may have formed in the plasma regime and remained non-luminous. The dielectric particulates may have possessed residual charges and through electrostatic attraction coalesced to form an ellipsoid. Collisions with the gases in the atmosphere would permit de-excitation to occur for the metastables. Observing GDE helped to better understand a possible explanation of the luminous matter formed in the circuit-breaker after current-zero.

In the present work and at the pressures the system operated under, the atomic spectral line of sodium was resorted to in order to understand the processes occurring in water. In most cases sodium's atomic spectrum was observed when aqueous sodium chloride electrolyte was used for GDE. The broadband spectrum of water[45-48] was observed in the absence of sodium chloride. The line spectrum of the sodium atoms carried in aqueous solution was also observed. Attempts to analyse plasma temperature from the broadening of sodium lines gave unphysical results. Instead, the electron temperature was deduced from the bremsstrahlung spectrum of

[a] "Particulates formation following arcing in high voltage interrupters". Proceedings of the XIII International Conference on Gas Discharges and their Applications. Glasgow UK, pp 226-229 September. (2000)

water plasma and this was considered the upper limit for ion and neutral temperatures.

The skew of the split doublet profile of the sodium "D lines" is indicative of quasi-static pressure broadening or Van der Waals broadening. The former comes about due to the high particle density that influences the energy-levels of any given atom in the medium. This in turn can affect the spectrum of emitted light. Van der Waals broadening occurs by the perturbation of an atom or molecule by the Van der Waals potential. Both quasi-static pressure broadening or Van der Waals broadening strongly indicate the highly dense conditions of the electrolyte-plasma interface as well as the aqueous environment for which Van der Waals forces are predominant (ligandation of the sodium ion). Under the high pressures of the system Doppler broadening was insignificant. Temperature estimates for the sodium atom due to Doppler broadening were unphysical. The Stark shift was found to produce lower temperatures for sodium atoms than were reasonable, so it was not included in this thesis.

It has been suggested in private communications with Schiffrin[60] but not in publication that the sodium species exist only as an aqueous spray near the electrolyte surface. The cessation of sodium spectra at large electrode separations was indicative of this. The author of this thesis also believes that increasing electrode separation required higher discharge-maintaining voltages and greater power. This would cause the excitation of other sodium and water energy-levels making the overall spectra appear white despite the possibility of the sodium species migrating across the entire length of the plasma column. The splitting of the sodium doublet can be attributed to the Stark effect. This effect (given the presence of high electric fields) seemed the most probable way to explain the enhanced splitting of a doublet whose two lines, originally separated by 0.6nm were observed to be split by 4.5nm.

Electro-kinetic[62-89] effects were observed by high-speed photography. The attraction of metal colloids[63,66] from the electrolyte surface to the suspended electrode was observed (due to high, localised non-uniform electric fields). This indicates the suspended metallic electrode was hot enough in places to be melted. It also supports the discovery of metallic emission spectra observed. The effect of a high electric field on steam[86-89] was observed in the absence of any form of luminous discharge. Its condensation indicted that water cluster formation is favoured despite the intense temperatures of the plasma (perhaps forming after every filamentary micro-discharge). The low-entropy of the water vapour would inherently be caused by low-energy electrolyte vaporisation (Work is done by electric fields to rotate, attract and hence condense steam).

Glow discharge electrolysis was investigated to assess the feasibility of introducing chemicals (dissolved in the electrolyte) into the plasma column. It was a success as sodium species were observed in the plasma column impinging on the water surface and suspended electrode.

Interestingly, the typical currents and discharge voltages associated with GDE are similar to those of DBD. The minimum energy required to heat and vaporise water was found (experimentally in the current work) to exceed the available electrical energy by a factor of three. It should be noted that the uncertainty in current magnitude was high and so with further statistical analysis the discrepancy may be resolved. With the results in hand however three possible explanations are rendered.

The first was that the presence of electrons, ions and high electric field incident upon the electrolyte surface encouraged the formation of water clusters. These are typically populated by tens of water molecules held together by an ion or electron and can exist in the gaseous phase. As a result, the molar enthalpy of vaporisation (the energy required to break one

mole of hydrogen bonds in the boiling process) can also be effectively reduced by factors of ten. In other words less bonds are broken to release water into the gaseous (mist) phase and less electrical energy is required. The problem with this conclusion was that the vapours were incandescent and were recorded to exceed 1500K. These temperatures are high enough to completely fragment the water clusters and transform them to steam. In this case, the standard vaporisation enthalpy applies.

The second is that the dynamic equilibrium maintained in water by the dissociation and recombination of the water molecule (self-ionisation) is affected or augmented by the high localised electric fields (The electric field was seen to distort the geometry of the water surface. This proves its presence and may have chemical effects). Any given water molecule naturally and spontaneously transfers its hydrogen atom to another water molecule forming $H_3O^+_{(aq)}$ (hydoxonium) and $OH^-_{(aq)}$ (hydroxide) in the absence of external fields. This occurs due to electric field oscillations of a colliding and oscillating molecular dipole. The electric field applied to the water surface as well as the ionic/electronic bombardment may enhance this process. The hydrated ions formerly mentioned are surrounded by adjacent water molecules in a ligand-cage much as the hydrated sodium and chloride ions are in aqueous sodium chloride. Since sodium species were carried into the plasma column it is possible that hydroxide and hydroxonium ions were also. The ionisation of water molecules contributes to its vaporisation in addition to the boiling (thermal) process due to bombardment and joule-heating.

The third possibility was that an exothermic chemical reaction was taking place that provided an alternative source of heat in addition to the electrical work. More detailed voltage-current analyses and calorimetry are required to justify this claim and this was sought with the contact glow discharge experiments. It was noticed that for GDE in an experimental rig open to the

atmosphere, the electrolytic pH decreased. This evidence may support the possibility of chemical reaction (atmospheric gas ions/neutrals bombard the electrolyte). The pH change effect was not observed for the closed experimental rig experiments. The same Nitrogen-Oxygen atmosphere was present however the acidic electrolyte may have become neutralised by reaction with its metal container. The open-rig container was ceramic.

1.3.3 Contact Glow Discharge Electrolysis (CGDE)

The investigation as to whether or not exothermic chemical reactions could be initiated by electrical discharges for readily available substances and produce relatively environmentally friendly by-products was concluded. Using ammonia (for its nitrogen and hydrogen content), sodium chloride (chiefly for its chlorine content) a silicon electrode (for its resilience to reaction and heat) and water (as a common solvent for the reagents) the following observations were made;

Calorimetry for aqueous ammonia solution was unresolved as the gas would be evolved and carry away heat. Using an approximation extrapolated from ammonia solution, liquid ammonia and saline solution it was observed that the ratio between observed heat evolution and electrical input work fluctuated below and above unity by an amount too small to be used as a fuel to generate electrical power. That is to say that with present conversion technologies, breakeven energy production would not be met and so the fuel mixture described above is not a viable power source.

If re-conversion to electrical energy is not an issue, then the kinetic energy may be utilised for other applications. At certain fuel mixtures, an explosive reaction was observed by the suspected (and intended) production of nitrogen trichloride which can be extremely potent for the purposes of spacecraft propulsion. This would be a chemically augmented electrothermal propulsion method.

The inability to produce heat energy in excess of electrical work may be attributed to the entropy of the electrical discharge and the energy cost of producing radicals that were not useful in implementing exothermic chemical reactions. Plasma phase chemical reactions are not as straightforward as those that occur within the other phases of matter.

A new appreciation of the minuteness of CGDE was found. Its voltage-current behaviour mimics the Child-Langmuir relation. Examination of the equation linking ion and electron temperatures to the Debye length suggest that the latter is similar to the dimensions of the contact glow discharge. As a result the contact glow discharge is unlikely to exhibit quasi-neutrality hence it is more correct to refer to it as an electrical discharge rather than plasma. The small dimensions give CGDE processes an unusually high energy density which can be used for micro-thrusters in electrical propulsion systems for spacecrafts[90-101]. Specifically, it may be well-suited for electro-thermal propulsion (see chapter 5).

What results from this series of experiments is actually an evolution in design, a new understanding and an attempt to quantify the parameters of the contact glow discharge.

1.4 Structure of Thesis

This thesis is organised into five chapters including the present chapter. The next three chapters describe the three major experiments done to generate, observe and utilise plasma and electrical discharges for energy production (DBD, GDE and CGDE respectively).

In each of these chapters there is a short introduction outlining the aims and purpose of the undertaking. The experimental setup and method are also outlined as these were developed by the author and show the direction, aim, advantages and limitations of the research. Results were displayed in

tables or graphs and reflect the raw data acquired as well as the conditions they were found in. Observations were made that support the analysis and general arguments presented here. Analysis takes the results to produce useful facts that help us towards our goals (namely energy production, physical process conditioning and novel or necessary understanding of the phenomena). The conclusion will round-off each chapter and assess the achievement of the goals set. The final chapter summarises the work in this thesis and reviews the work as a whole to make an overall conclusion. Suggestions to improve the present work are also given.

Chapter 2

DIELECTRIC BARRIER DISCHARGE (DBD)

2.1 Introduction

The aim of the current work was to generate stable non-thermal electrical discharge in a relatively large discharge space that could facilitate possible exothermic chemical reaction for the purpose of energy production. The non-thermal electrical discharge will act as a process conditioner to activate and sustain a particular process. Although much work exists with many stable DBD configurations[1-8], most were designed to run at a few kilovolts and with small (a few millimetres) electrode spacing. Their general applications were geared towards sterilisation and chemical decomposition. The requirement of maximising reagent volume and the possibility of having to raise the voltage significantly to produce required active species demands unique electrode design criteria that are not commonly encountered in the literature. Therefore, there is no established theory on the choice of stable discharges. Suitable electrode configurations and compositions can only be deduced by trial and error as a first step. There are two objectives in this chapter. Firstly using experiment a configuration for producing stable non-thermal electrical discharge will be derived. Secondly, the voltage-current characteristics of electrical discharge under atmospheric pressure conditions in relation to electrode geometry and discharge conditions will be analysed and explanations will be provided where necessary.

2.2 Design Considerations and Implementation

The choice of using air as the electrical discharge gas is based on the following considerations: Firstly, species in air are chemically stable and it is fairly easy to carry out experiments with the DBD system. Secondly, many energy production processes use the oxygen in air as a reactant. To achieve electrical breakdown in air to start a discharge, an electric field of at least $3MVm^{-1}$ or $3kVmm^{-1}$ must be present (These values are true for steady-state or low-frequency scenarios with smooth planar electrodes).

Special geometries however permit lower voltages per unit separation or greater separation per unit voltage to achieve breakdown. The use of a pin and plate electrodes for example result in breakdown of air at a fraction of the voltage that two parallel-plate electrodes would require. The curvature of the point of the pin concentrates charges on the surface that in turn enhances the electric field near the pointed edge. This principle was taken advantage of in many designs and a spark-plug was often adapted for use in experiment.

Figure 2.1 is a photograph of a worn pin-electrode (Sparkplug). The copper shaft is insulated by a hollow PTFE cylinder. The stainless steel flange allows fixture and support to experimental rigs. The pin has been eroded and is difficult to observe (right).

Taking the relevant safety precautions (See appendix 1), the apparatus was assembled as schematically displayed in figure 2.2. The fuse on the primary (5A) determines the maximum permitted RMS current on the secondary. Unless otherwise stated, this applies for the experiments described in the present chapter and Chapter Three.

The physical setup of the electrical discharge circuit is displayed in figure 2.3. The high-voltage cable and grounding cable lead to the electrodes (not shown) situated in the rig on the experimental surface. This was the generic setup for the high-voltage experiments.

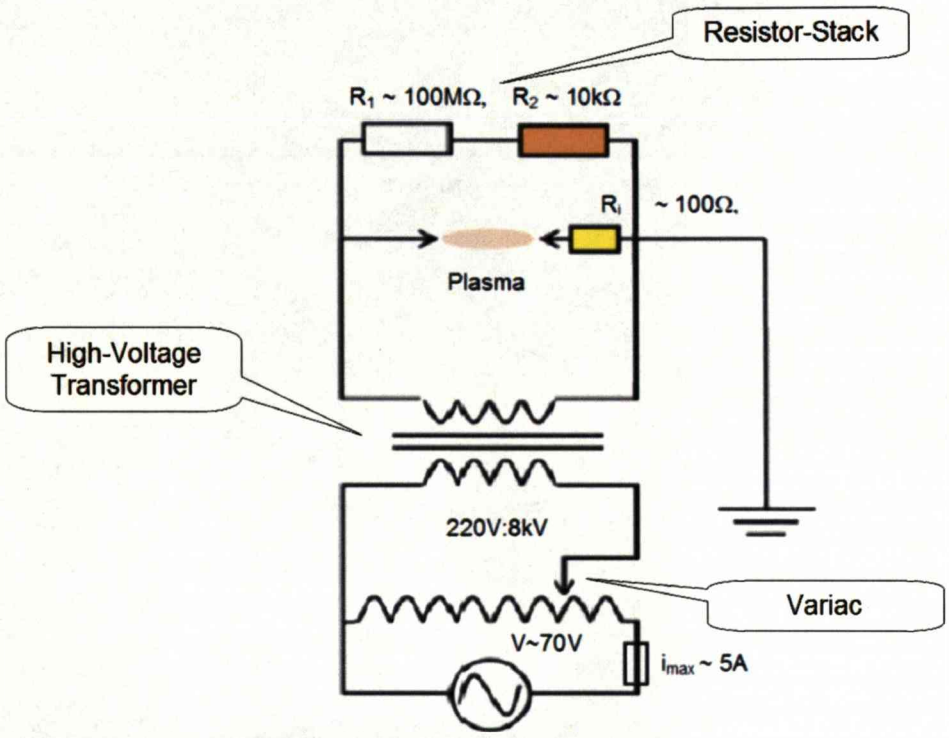

Figure 2.2 is a typical diagram for all of the high-voltage experiments. The electrical discharge potential difference was inferred from the measurement of the potential difference across R_2. The electrical discharge current was calculated from the potential difference across R_i (yellow resistor). R_1 and R_2 comprise the resistor stack and potential divider. See figure 2.3.

In some experiments the resistor stack was sometimes replaced by capacitors and the electrodes were frequently replaced to optimise the setup prior to experiment. At the low applied frequencies in the present work, using high-voltage capacitors with suitable capacitance was one way of safely dividing voltage for measurement and ensuring that most of the current passed through the electrical discharge. The disadvantage of using capacitors over resistors however was the inherent lack of accuracy when high-frequency voltage signals (spikes) are generated or induced. The

safety concern of residual charges being maintained by the capacitor after operation was another disadvantage.

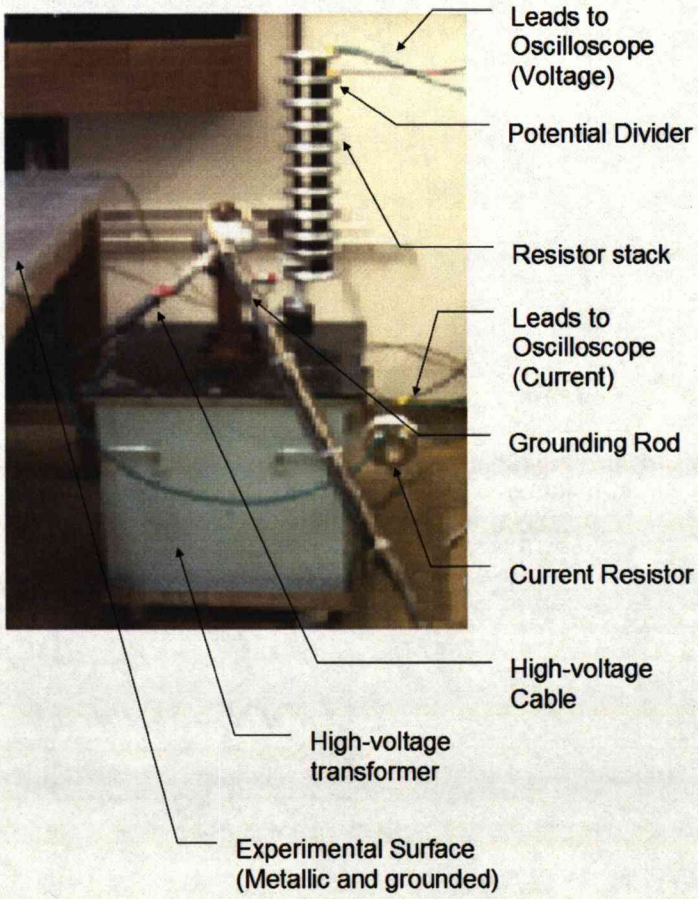

Figure 2.3 shows the common experimental setup for most high-voltage experiments. The components shown in this photograph are represented by figure 2.2. The green cable is the ground electrode connection. The grounding rod was a safety feature used to ensure there were no live components after experimentation or accumulated charges on capacitors (not dealt with here).

The Variac autotransformer in figure 2.2 was constructed at the University of Liverpool's Electrical Engineering Department. Its output voltage could be scaled up to 270V. Its input was 240V AC. The resistor stack was fashioned from several standard 1MΩ wire resistors connected in series and configured spatially to withstand high-voltages. The aluminium disks shown in figure 2.3 were used to section the resistive stack also allowed

external electrical connection. The high-voltage 80kVA transformer was manufactured by Ferranti and transformed 220V to a maximum of 80kV. An Agilent Technologies/Hewlett-Packard-54602B 150MHz Digital Storage Scope was used. Its sample-rate was 20 mega-samples per second. It has four Channels and can detect DC to 150MHz signals (Details courtesy of Instrumex GmbH).

A dielectric barrier is necessary between the two electrodes to prevent the electrical discharge from turning into a large-current thermal arc and to control the power density in the electrical discharge. AC voltage sources were used as this could be transformed up to a higher voltage to produce the discharges. Glass was used as the dielectric barrier material because of its excellent dielectric properties.

The experimental rig in figure 2.4 was modified and augmented by the electrodes of figure 2.5. In the latter, seventeen distinct tests are illustrated. All trial tests were conducted in air and under atmospheric pressure. Preliminary tests were carried out to evaluate which electrode configuration resisted thermal arcing at high-voltages with a typical operation time of thirty minutes. For a system to be of practical use, the operation time has to be long enough. The duration of 30 minutes is a good choice since it also allows visual observation of the stability of the whole system at high-voltage.

The diagrams displayed in figure 2.5 are simplified cross-sections of the active circuit components. The components are rotationally symmetric (vertical axis). The electrode plates and glass disks were circular or cylindrical. Tests (o) and (q) yield the most uniform and least filamentary discharges. They appeared diffuse and of large volume. Tests were operated at 50Hz and (o) and (q) were the only ones to generate such uniform and relatively silent discharges.

Although these discharges were ideal in that they were of large volume, the dielectric used to produce them was a thin polymer and with high current densities, could be destroyed (Polymers contain carbon and are typically more conductive than glass. The thinness of the polymer will also increase its conductivity. The above advantages that permit also eventually tend to allow high current-density when high-voltages are applied and power is available from the mains).

Figure 2.4 illustrates the platform for the preliminary tests. On it several electrode geometries (see figure 2.5) were tested for their durability and stability under the application of high-voltages. In all cases, the suspended electrode was live and the lower electrode was grounded. Apparatus was designed so that the sparkplug of figure 2.1 could slide into the PTFE block illustrated in figure 2.4. This feature allowed the discharge spacing to be adjusted between tests without having to radically alter the apparatus. This is a novel aspect of the design.

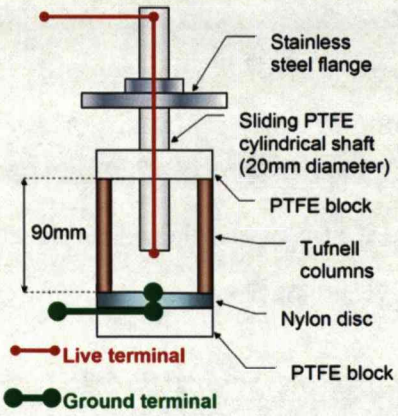

Figure 2.4 shows that a sparkplug was inserted into the elbow shaped rig and used extensively. The PTFE shaft could slide and the inter-electrode space could be varied. A glass disk was one of the many electrode augmentations that could be mounted on this versatile platform (See figure 2.5). The thin red lines and thick green lines are the live and ground cables respectively.

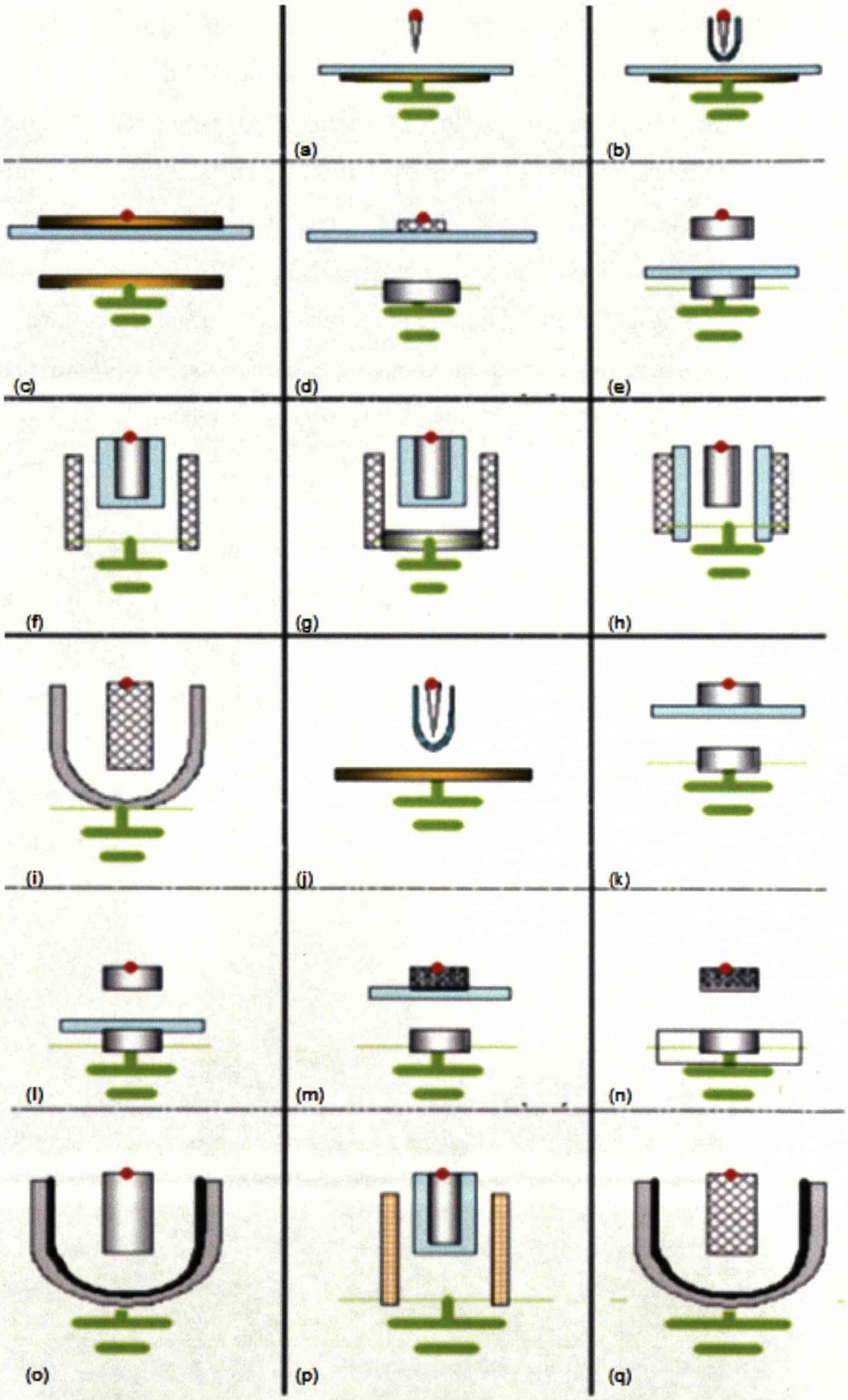

Figure 2.5 is a table of diagrams showing different designs for trial DBD experiments. Orange is copper. Matte grey is steel and shiny grey, aluminium. The meshes were of copper and steel. Glass is blue. The black thick regions of (o) and (q) are the thin polymer layer previously mentioned.

Experiment (f) was used as the benchmark for the detailed DBD experiments. This arrangement although producing filamentary discharges was most resistant to thermal arcing and produced the most luminous electrical discharge. The present work was primarily aimed at developing a robust set of electrodes which could withstand high-current and power densities when required. Because there may be situations that require a chemical process might require relatively severe conditions to activate. Experiments (a) to (q) are arranged in chronological order to display design evolution. The red points indicate the live terminals. The green symbol indicates the grounded points.

Figure 2.6 shows the parallel-planar electrode configuration. A weakness of this design is that it requires high-voltages to initiate electrical discharge. Once the discharge is established however, the electrodes are more resistant to wear because the discharge surface was planar and produces uniform field over its relatively large area. The dielectric area must be sufficiently large in order to prevent the discharge from forming into a thermal arc. Experience shows that there are often stability issues associated with this type of design.

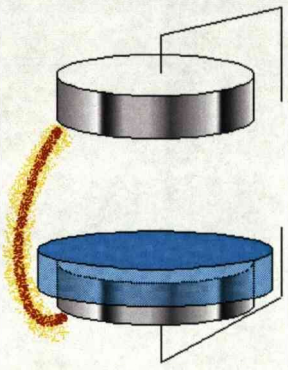

Figure 2.6 shows the red and yellow filament as the electrical discharge column. In this configuration it undermines the dielectric barrier at high-voltages or small barrier surface areas. The blue disk is the dielectric (glass) barrier.

A thermal arc is formed only when the dielectric barrier has been breached or compromised. There is another situation where the barrier is not large enough to completely prevent the discharge "arcing around" it (as shown in figure 2.6) however the increased path length is enough to raise the electrical discharge resistance to prevent thermal arcing. The result is a non-thermal arc. The current limitations of the high-voltage transformer and external circuit components also help to prevent thermal arc transition for a large enough electrode separation. It has been observed that over large electrode separations nitrogen dioxide would form in addition to the ozone usually accompanied by DBD.

Figure 2.7 shows the point-plate electrodes. The point is good for producing high electric fields so that electrical discharge may be initiated at relatively low applied voltages. The point electrode is highly susceptible to wear and once again the dielectric area is a critical factor in the prevention of thermal arc transition.

Figure 2.7 shows the pin-electrode suspended above the planar electrode. The tip of the former can melt after long durations (~10minutes). The dielectric barrier is the blue disk. Here the required applied potential to initiate breakdown was ~9kV. The separation between pin and plate can be varied here (typically from 4mm – 10mm).

The electrodes displayed in figure 2.8 and figure 2.9 show a coaxial cylindrical arrangement. This configuration permits high-applied potential

differences without the electrical discharge transforming into a thermal arc. The dielectric sheaths the cylindrical electrode almost completely. The path length required for the discharge to "arc around" the dielectric sheath is so great (several tens of centimetres) that it surpasses sensible operating voltages (>30kV). Even if it were possible for the discharge to undermine the dielectric sheath by circumventing it, the resistance would increase to such an amount as to ensure that thermal arc transition does not occur (Experience has shown that even without the dielectric barrier, large electrode gaps will control the observed current of the discharge. See figure 2.4 and figure 2.5(n)). The diagrams in figure 2.8 and figure 2.9 represent the photograph of figure 2.10. Variation of electrode overlap area was achieved by retracting the required electrodes. Voltage-current characteristics were obtained for different areas.

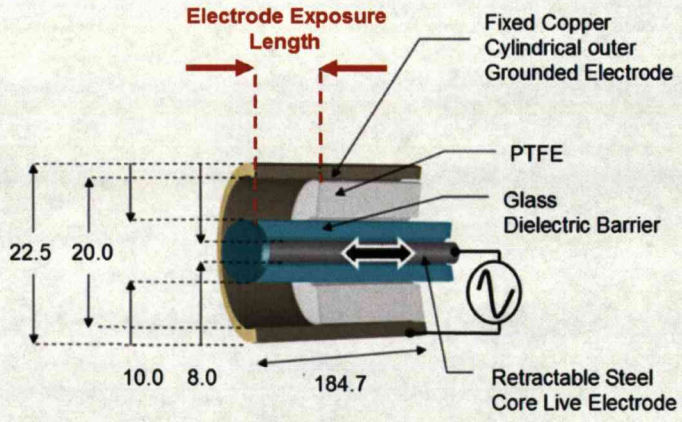

Figure 2.8 illustrates that experiment DBD(B) had a retractable live shaft. Dimensions are in millimetres. The fixed length ground electrode (outer electrode) extends along the full length of the PTFE tube and is attached to the chassis. In this experiment, the live electrode was moved together with its glass dielectric barrier and the grounded electrode fixed. Electrode overlap length is marked on the illustration and represents the length at which the steel core live electrode protrudes from the PTFE tube. The red lines (left and right) mark the end of the live core electrode and the PTFE tube opening (flat surface) respectively.

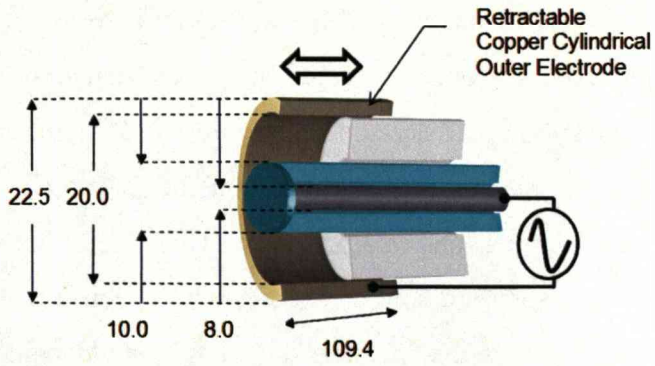

Figure 2.9 shows that experiment DBD(C) had a retractable grounded cover. Dimensions are in millimetres. The glass length is approximately equal in length to the moveable ground electrode. In this experiment, the live electrode was fixed and the grounded electrode moved. Electrode overlap length is the distance from the opening of the outer electrode to the PTFE tube opening.

Figure 2.10 is a photograph of the conditions portrayed in figure 2.9. The experimental setup can also be changed to adopt the configuration depicted in figure 2.8.. These two arrangements were chosen to observe the affect of increasing electrode area on current and voltage. If the length of the live electrode has any effect, it would show from the results of DBD(B) and if length of the grounded has any effect it would show from the results of DBD(C). These experiments will reveal some natures of the discharge and show whether or not the discharge makes use of available electrode area or remains confined to a pre-determined spot or region.

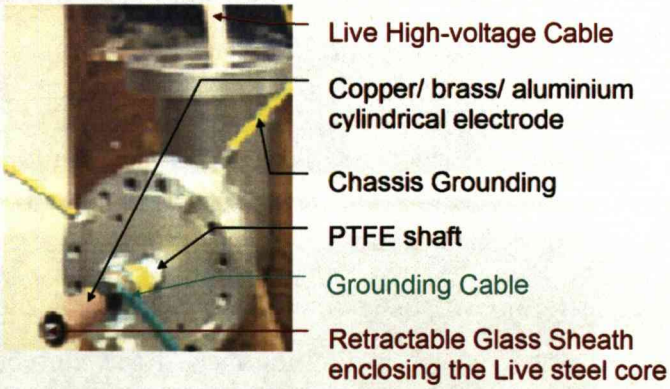

Figure 2.10 Sparkplug of figure. 2.1 attached and exposed externally onto the elbow-shaped rig. Coaxial configuration fitted on the PTFE shaft. This photograph is represented by figure 2.9.

2.3 Experimental Procedure and Observations

The relation between voltage, current and electrode area was investigated for the cylindrical electrode configuration. Detailed experimental work was not done for the other configurations because too many associated effects were observed that created instability in measurement. If current-voltage characteristics are sought for a given dielectric material, these would be undermined as the increase of voltage would compromise, or cause the discharge to circumvent the dielectric (See figure 2.6 and figure 2.7).

The inner core was insulated by a glass layer ~1mm thick. Electrode area was changed by controlling the exposed overlap between the live and grounded electrodes (See electrode overlap length of figure 2.8). For each increment in electrode area, or overlap length, the voltage was increased incrementally and the current measured and recorded. The voltage increments and corresponding current-readings gave a range of data points with which to analyse in later sections. The overlap length was increased by ~10mm on each occasion, a reasonable distance considering the dimensions of the system. The voltages across the potential divider (R_2) parallel to and the current-resistor (R_i) in series with the electrical discharge were measured (See figure 2.2). The two voltage waveforms were captured and their RMS and Peak to Peak values manually recorded with a digital oscilloscope. This was done repeatedly for each voltage increment of the autotransformer. The electrical discharge voltage and current could be calculated by scaling and Ohm's law respectively. The meaning of the RMS values are discussed in the analysis section.

The repetition in readings (multiple screen-captures, each of one and a half cycles) was averaged to find the mean RMS currents and voltages (for a given electrode overlap length) and its standard uncertainty. The oscilloscope also displays RMS voltage values. The nominal resistances were given in figure 2.2 however the actual voltage divider ratio is

$6149.92 \pm (0.53\%)$ and the current measuring resistor value was $455.00\Omega \pm (0.25\%)$. It should be noted that the current was filamentary nature. These appeared as signal spikes superimposed on the waveform displayed on the oscilloscope. The amplitudes of these spikes were unpredictable and so the uncertainty percentages for these voltage signals were much greater than those calculated for the resistance (This also depended upon the oscilloscope resolution). The significant source of uncertainty was due to the current-signal and not due to the resistance of the resistors mentioned.

The experiments were carried out with apparatus illustrated in figure 2.8 and figure 2.9. The first set of experiments had a copper tube completely covering the PTFE shaft and extending 111mm beyond its termination. (See the distance marked "electrode overlap length" in figure 2.8). The moveable live inner steel electrode was initially flush with the PTFE tube face (0.0mm overlap) then extended to 13.0mm, 26.0mm, 30.3mm, 64.0mm and 111.0mm overlaps. At each of these lengths, several voltage increments (more than ten) were made from 0V to 18.5kV. At each increment the voltage across the voltage divider and the voltage across the current-resistor were repeatedly captured (five or six times) and recorded. This data was represented by the graph and legend of figure 2.15. The raw data are to numerous to be tabulated here.

In the case of the experiment illustrated by figure 2.9, the live electrode was kept at a protrusion length of 64.0mm and the moveable grounded electrode moved to 0.0mm, 9.5mm, 20mm, 29.5mm, 40.0mm, 55.0mm and 64.0mm electrode overlap distances (see the bold white arrow of figure 2.9). At each distance, the voltages of the potential divider and current-resistor were measured in much the same way as previously described. This data was graphed with a legend in figure 2.17.

Coaxial cables were used wherever possible to limit the effect of electromagnetic noise from the discharge interfering with the main signal. The use of high-voltages required a very conscious effort to ensure that the separation between live points and points of lower potential was at least ten times the separation inter-electrode separation. Electrical discharge was intended to exist at the electrodes only. This factor in combination with safety issues resulted in thoughtful high-voltage electrical engineering. As the measurement cables left the high-voltage cage to the oscilloscope, the risk of electrocution for the experimenter and passers by became very real. The measurement cables were attached across a resistance much smaller than the total resistance and at the grounded end of the resistor stack (R_2 of figure 2.2 also see he potential divider of figure 2.3). The experimental surface is a table of approximately one metre in height with a metal sheet fitted to it.

Several electrode configurations were tested for their stability under high-voltages and safety (See figure 2.5). Of them all, figure 2.5(o) and figure 2.5(q) were observed to give diffuse, large-volume discharges at the relatively low-frequency of 50Hz. Their configurations were cylindrical and co-axial with the interior of the elbow-shaped rig. The inter-electrode spacing was approximately 50mm. This large separation is quite remarkable for an atmospheric discharge at such low frequencies. The author attributes the diffuse nature of the discharge to the thin polymer sheet used as a dielectric barrier. As already stated, this was not further developed due to its inability to withstand heat. It was however the only dry material observed to generate such a discharge at such low frequencies.

Glass and ceramic were used as dielectric barriers and the pin-planar electrodes were used although this did not prevent thermal arcing. (See figure 2.10) Eventually a co-axial cylindrical electrode configuration was used and a stable long duration discharge was available for testing. The

discharge could run indefinitely to the best of the author's knowledge. Without the threat of condensation occurring as with the wet electrodes and the absence of significant heating on the apparatus after hours of use, this electrode configuration was very reliable.

The electrode overlap area did not change the current (which was sporadic in magnitude to say the least). The increase in voltage did however increase the frequency of appearance of the filament as well as their luminosity. This luminous filamentary discharge was a non-thermal arc or in the abnormal glow regime. Ozone gas was produced and typical currents were in the tens of milliamps and applied voltages ~10kV. This is indicative of oxygen radical formation and recombination to the triatomic ozone molecule as well as the diatomic oxygen molecule.

At a later date aluminium shavings were placed on the electrodes and the dielectric barrier removed. Large currents resulted as thermal arcing ensued at small electrode separations whilst non-thermal arcing was prevalent for larger separations. The aluminium shavings were used to utilise an even smaller radius of curvature than the fixed point electrode and high electric fields. These were used to "seed" and initiate the discharge at relatively lower voltages (<10kV) and were rapidly oxidised by the heating effect of the filaments with short periods of time (~15minutes). A brown gas was seen to emerge from the apparatus and this accompanied the detection of an acrid odour. Figures 2.12 and 2.13 give typical waveforms for the electrical discharge voltage and current measurements. Their features correspond to the DBD(B) and DBD(C) experiments.

Figure 2.11 illustrates the dielectric barrier discharge experiment displayed in figure 2.8 and figure 2.9. The pictures show increasing voltage from (a) to (c) and are viewed along their natural axis. (a) shows the formation of filaments within the glass sheath and from the steel core. This cannot be a reflection of light because there were no luminous filaments between the glass dielectric barrier and the outer grounded electrode. (b) displays a thin filament forming from the glass sheath exterior to the surrounding grounded electrode interior. (c) is the brightening and thickening of that filament. As denoted from he background, observations of DBD were made in a darkened room.

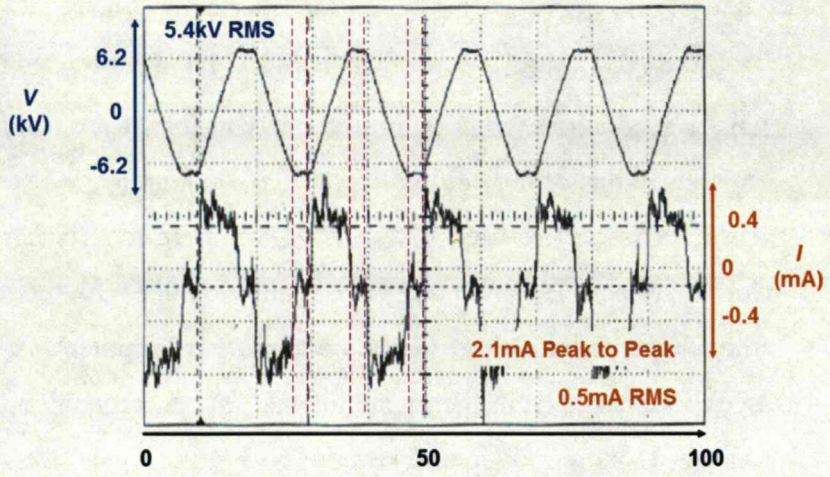

Figure 2.12 is printout of oscilloscope traces. The top and bottom traces represent voltage and current respectively. The numerical readings are calibrated data. Also note the "phase" of the current waveform and how it leads voltage by 90^0.

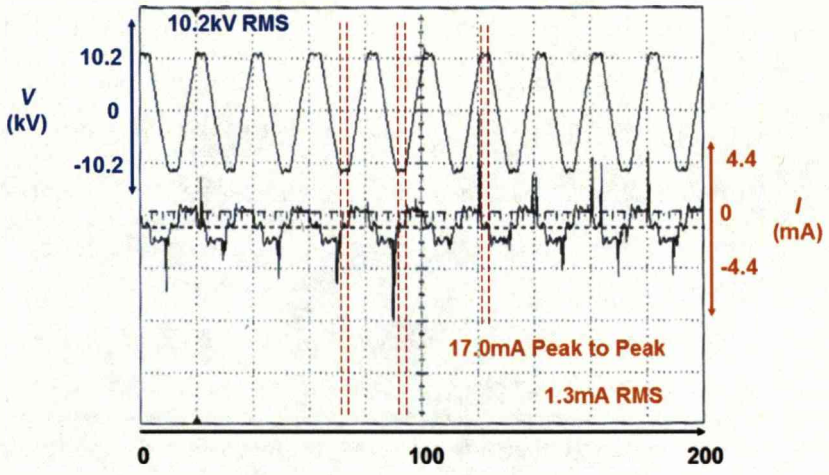

Figure 2.13 is similar in format to figure 2.1.2 but at a lower voltage. Note how the filaments (current-spikes) are of the same polarity as the voltage waveform. The current spikes occur as the voltage-time waveform gradient tends to zero. The filament duration is ~10ns. Sample point spacing is ~ 40μs therefore each filament represents 1 sample point out of the 5000 per channel.

2.4 Results

Figures 2.15-2.23 display the results from DBD (B) and (C). With the exception of the graph of figure 2.20, each dot represents a mean RMS voltage-RMS current data point. Each voltage-current data-point represents the mean values of five RMS voltage and five RMS current data pairs. The voltage across the resistor R_i (of figure 2.2) was divided by the resistance (whose value has been previously quoted in the text). The standard uncertainties on the mean were added in quadrature with experimental uncertainties (negligible). The five RMS current readings (whose mean comprises the current co-ordinate of a data-point) contain the largest significant uncertainty (as opposed to voltage). These were represented by each vertical uncertainty bar for a given data-set.

In the graphs of figures 2.15-2.18, each dot colour represents an electrode overlap length quantified by the legend enclosed by the black broken-lined boxes. To follow one colour of dots from left to right is to observe the voltage-current trend for a single electrode overlap length. For each electrode overlap length there is a linear voltage-current relation at low-

voltages and a scattered voltage-current relation at higher voltages. The electrode overlap length did not greatly influence the voltage-current relation. The discharges were observed to originate from localised regions on the dielectric barrier's outer surfaces and not the entire exposed area. This is probably related to the actual surface condition of that electrode.

The graph of figure 2.19 was plotted because there was very little difference between DBD(B) and DBD(C) experimental results. It features the points of both of these experiments plotted on a common axis. The linear region at lower voltages was used to calculate the displacement current. Since this was expected and linear by observation, it can be used to deduce the luminous filament's contribution to current at a later stage. It also features a highlighted data-point whose voltage-current co-ordinates are featured.

The graph of figure 2.20 is reconstructed from the oscilloscope trace of the system in figure 2.14. The expected displacement current was deduced (simply by scaling due to its linear voltage dependence) by multiplying the RMS current of figure 2.12 to the ratio of RMS voltages in figure 2.13 to that in figure 2.12. By scanning the oscilloscope trace and locating current spike magnitudes and positions in bitmap pixel co-ordinates, the current contribution of the luminous filaments (whose duration[1] is 1ns - 10ns and can only be detected by one oscilloscope sample point each) can be ascertained. (The oscilloscope sensitivity at 5ms per division causes several potential current-spikes to be missed. The alternative was to increase the sensitivity to capture single current-spikes. The latter option captures the waveform over smaller time intervals and more acquisitions will have to be made to reduce statistical uncertainty. The duration of the experiment favoured the course of action taken). The displacement current wave-form can be displayed in detail by the 5000 sample points available to each channel of the oscilloscope. The results of this analysis are concisely

represented in the table of figure 2.23. The filaments although relatively infrequent in comparison to the ever-present displacement current (at non-zero voltages) make a substantial contribution the total measured RMS current.

The RMS current was measured and this is related to the filamentary current in a way described by equations 2.1 where i is current, the subscripts L and D indicate luminous (conductive current) and dark (displacement currents respectively. n is the number of sampling point (5000), $n_{filament}$ is the number of filaments (typically two per wave-cycle and 15 per screen on the oscilloscope as shown in figure 2.13). The subscript x is merely the summation index.

$$i = \int \mathbf{J} \bullet d\mathbf{A}_{filament} + \int \dot{\mathbf{D}} \bullet d\mathbf{A}_{Capactive} = i_L + i_D$$

and

$$i_{RMS} = \sqrt{\frac{i_1^2 + i_2^2 + \ldots + i_n^2}{n}} = \sqrt{\frac{\sum_{x=1,2..n} i_x^2}{n}}$$

$$= \sqrt{\frac{(i_{L1} + i_{D1})^2 + (i_{L2} + i_{D2})^2 + \ldots + (i_{Ln} + i_{Dn})^2}{n}}$$

$$= \sqrt{\frac{\sum_{x=1,2..n} i_{Lx}^2 + 2\sum_{x=1,2..n} i_{Lx} \cdot i_{Dx} + \sum_{x=1,2..n} i_{Dx}^2}{n}}$$

Equation 2.1

Inspection of figure 2.13 reveals the occurrence of filaments on the positive and negative plateau of the displacement current wave-form. This indicates that the displacement current magnitude is approximately equal whenever a filament occurs and that the central term of the square root in equation 2.1 is small in comparison with the first term provided that the peak current of the filamentary discharge is substantially larger than the magnitude of the current plateau. Therefore we can write the following:

$$i_{RMS} \approx \sqrt{i_{LRMS}^2 + i_{DRMS}^2}$$

$$\therefore i_{LRMS} \approx \sqrt{i_{RMS}^2 - i_{DRMS}^2}$$

Equation 2.2

Where i_{DRMS} is calculated from in the fit of the graph of figure 2.19. From figures 2.16 and figure 2.18 it is clear that the filamentary discharge current overtakes the displacement current at voltages above a threshold. This implies that $\sum_{x=1,2..n} i_{Lx}^2 > \sum_{x=1,2..n} i_{Dx}^2$. From figure 2.14 it can be seen that **J** and **D** are in parallel in the circuit. As a result the total current (waveform and spikes) is the sum of the conductive and displacement currents. This allows us to mathematically isolate the filament current by subtracting the total current from the capacitive current. This and its RMS expression were defined in equations 2.1.

Another distinctive feature present in figure 2.12 and figure 2.13 is the formation of a capacitive current plateau when the applied voltage across the electrodes reaches from 5kV to 10kV. The temporal width of the plateau matches the duration over which the applied voltage varies linearly (to a close approximation). This is much clearer on figure 2.13 at higher applied voltage. Filamentary discharge occurs in both polarities. Careful

inspection of the current-voltage waveform reveals that the observed filamentary discharge always occurs at the instant when the current rises steeply from the zero-point to the current plateau. Both the current and voltage waveforms deviate from sinusoidal form.

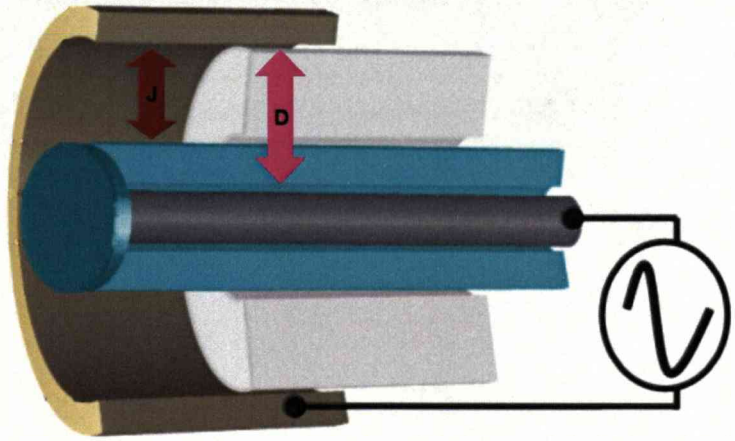

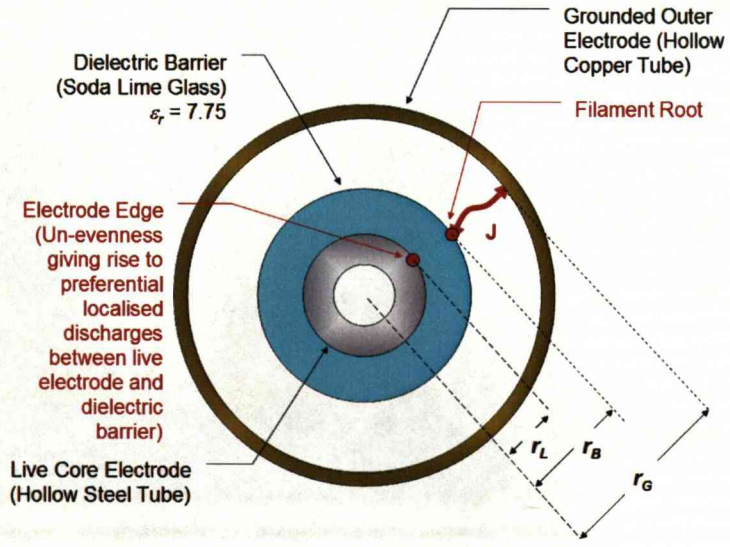

Figure 2.14 (Top) is a generic illustration of the DBD experiments. At low voltages, the capacitive or displacement current dominates and depends upon capacitive reactance (which is constant at constant frequencies for a given geometrical arrangement). The displacement current is the time-derivative of **D** shown above and is manifested in graph of figure 2.20 (coloured coded). The conductive current J is represented by the scattered points on the graph of figure 2.20. It exists between the dielectric surface and the cylindrical outer electrode and appears as luminous filaments (see figure 2.11). (Bottom) This diagram is observed end-on from the illustration above it. Its dimensions may be found from figure 2.8. The white areas here denote

air. The potential difference measured in experiment was between the live steel core electrode and grounded outer copper electrode.

When the voltage amplitude reaches a maximum value, then the applied electric field between the electrodes reaches a maximum value also. This occurs when the time-derivative of voltage approaches or reaches zero. Hence the time derivative of the electric field also becomes zero. The displacement current therefore must be zero and the conductive current appears to dominate at these instants in time (voltage waveform peaks and troughs coincide with current-spike formation. See figure 2.13 and the first line of equations 2.1).

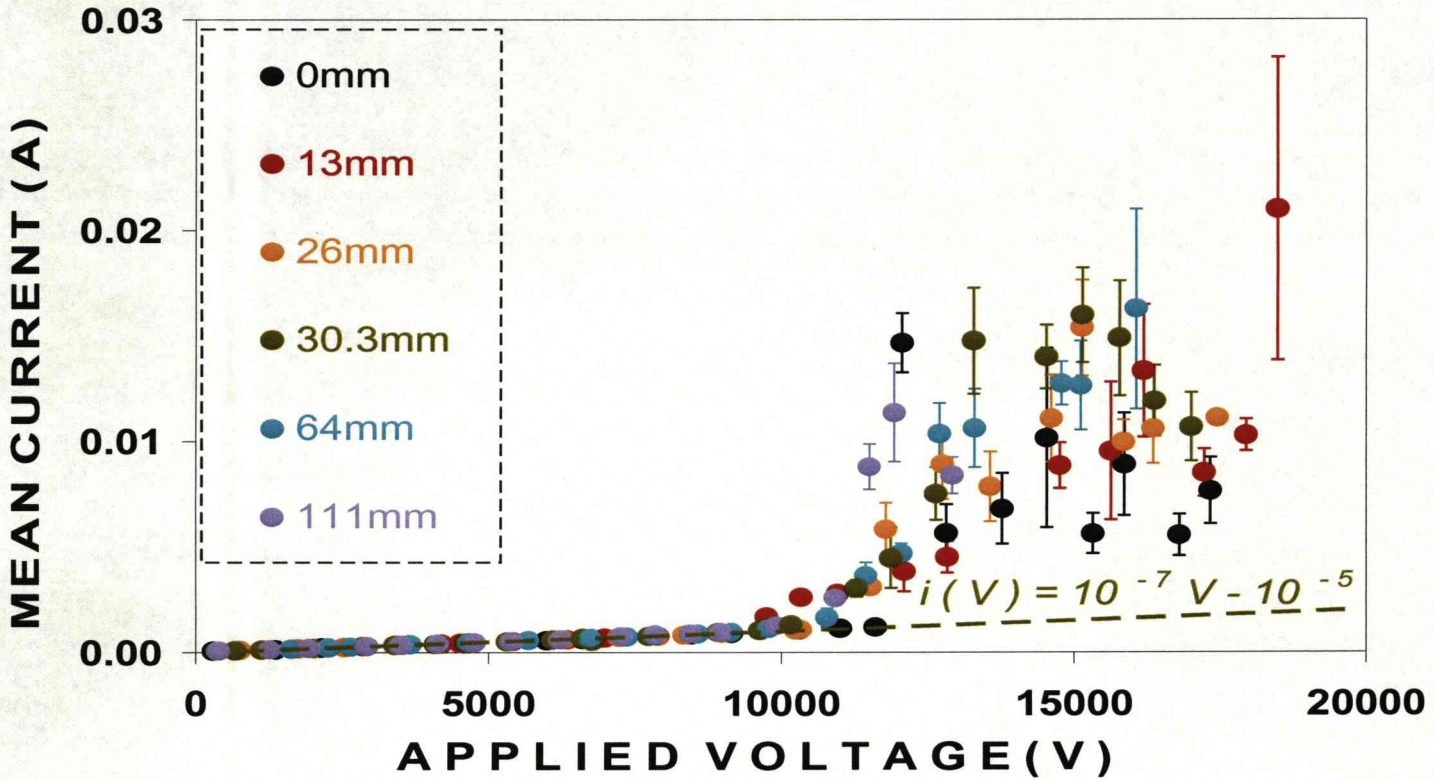

Figure 2.15 represent DBD experiments B results plotted as a graph of voltage versus current for varying electrode lengths. The lengths are displayed in millimetres. These refer to the fixed grounded electrode and moveable live electrode experiments. The points begin to scatter near and above 10kV. This indicates he luminous (filamentary) discharge regime. Prior to this the points appear to lie on a line whose gradient (Conductance) is due to capacitive currents.

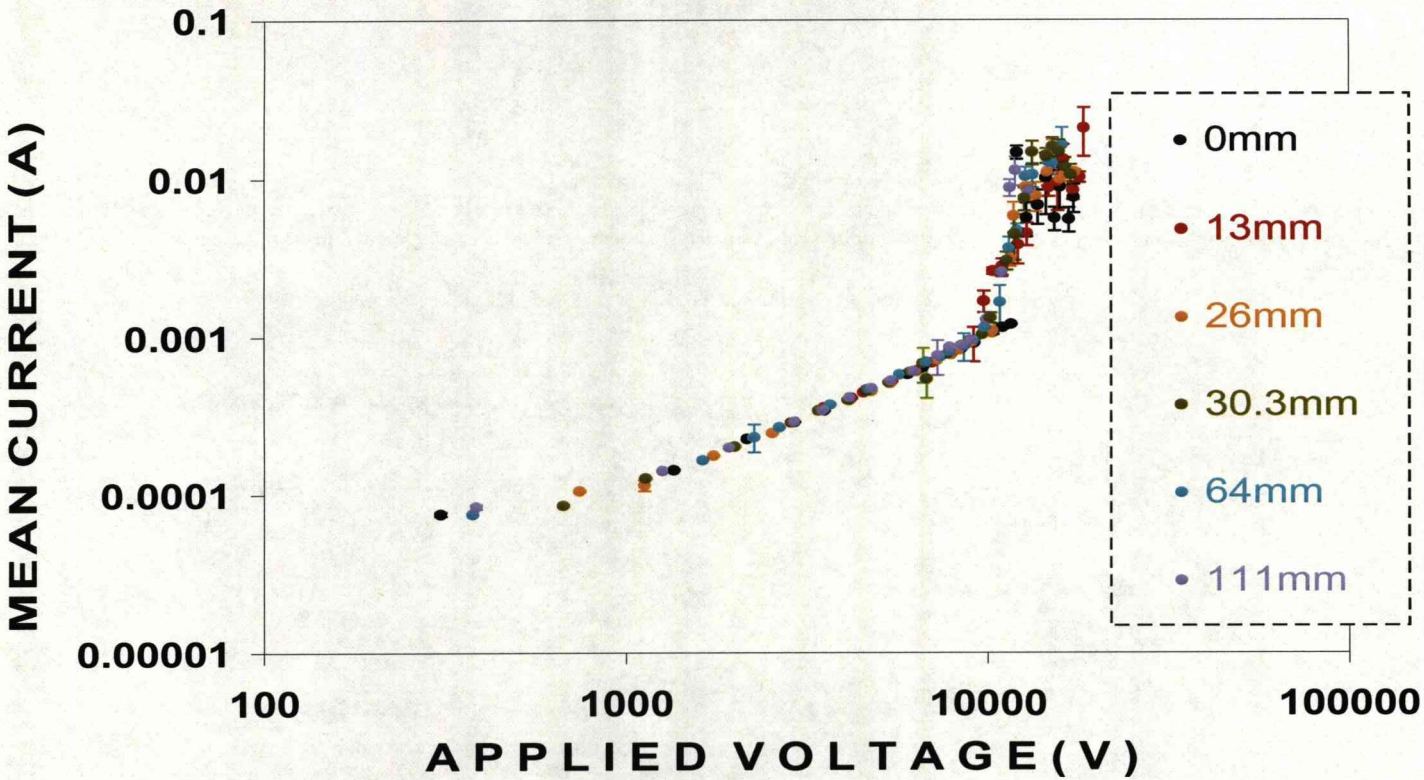

Figure 2.16 represent DBD experiments B results plotted as a graph of logarithmic voltage versus logarithmic current for varying electrode lengths. The lengths are displayed in millimetres. Even on a logarithmic plot, the luminous discharge does not appear to have an observable current-voltage trend. The electrode overlap area seems to have no effect at all on the current-voltage relation as the scatter of dots appear to overlap one another for differing electrode protrusion lengths.

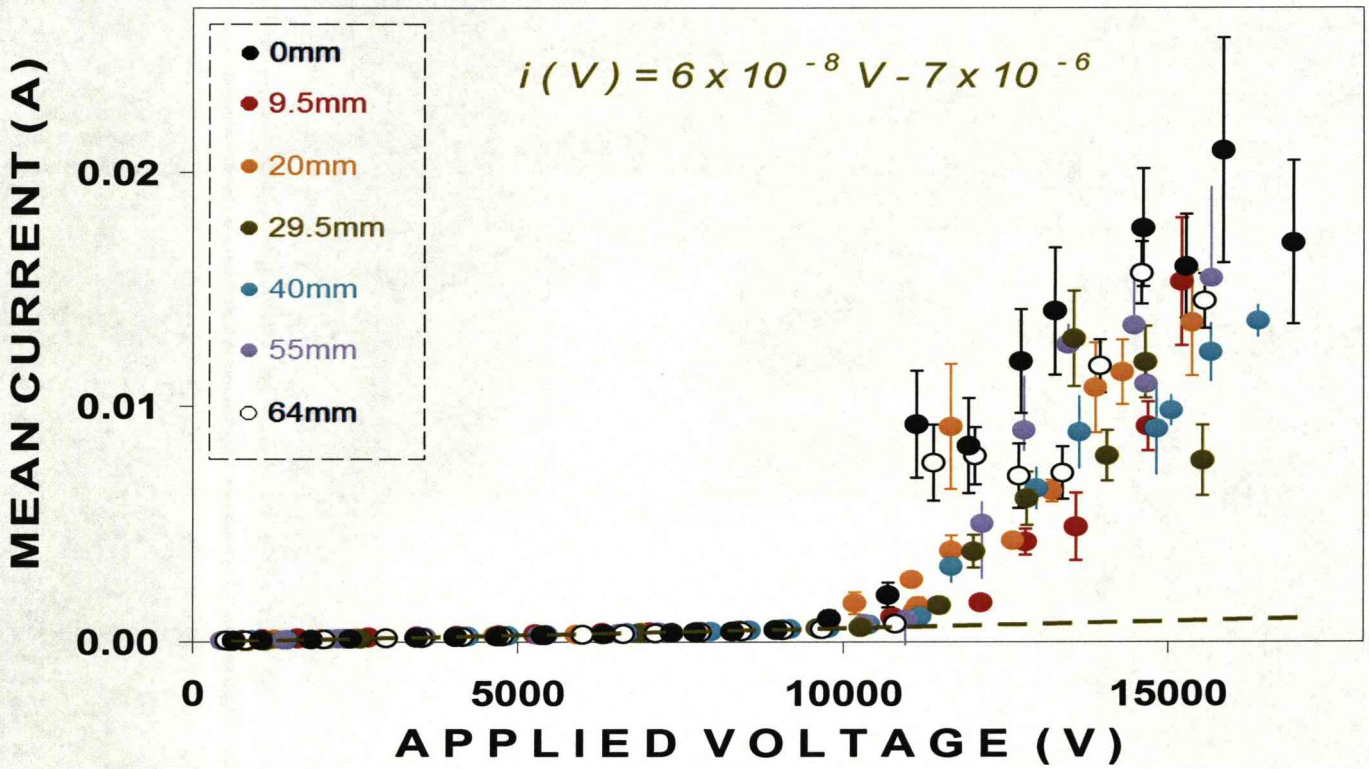

Figure 2.17 represent DBD experiments C results plotted as a graph of voltage versus current for varying electrode lengths. This graph does not vary much from the graph of figure 2.15 for DBD(B).

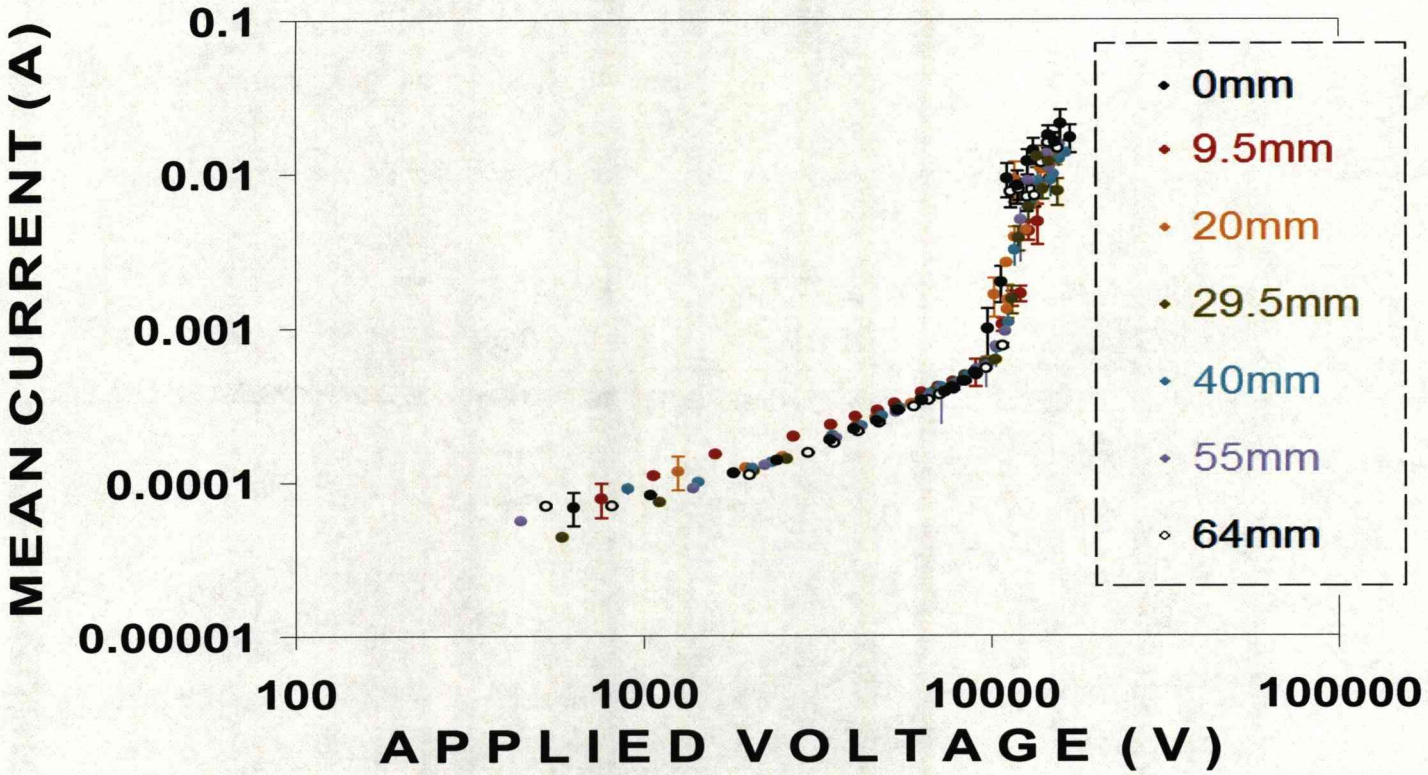

Figure 2.18 represent DBD experiments C results plotted as a graph of logarithmic voltage versus logarithmic current for varying electrode lengths. The plot does not differ greatly from that of DBD(B) of figure 2.16.

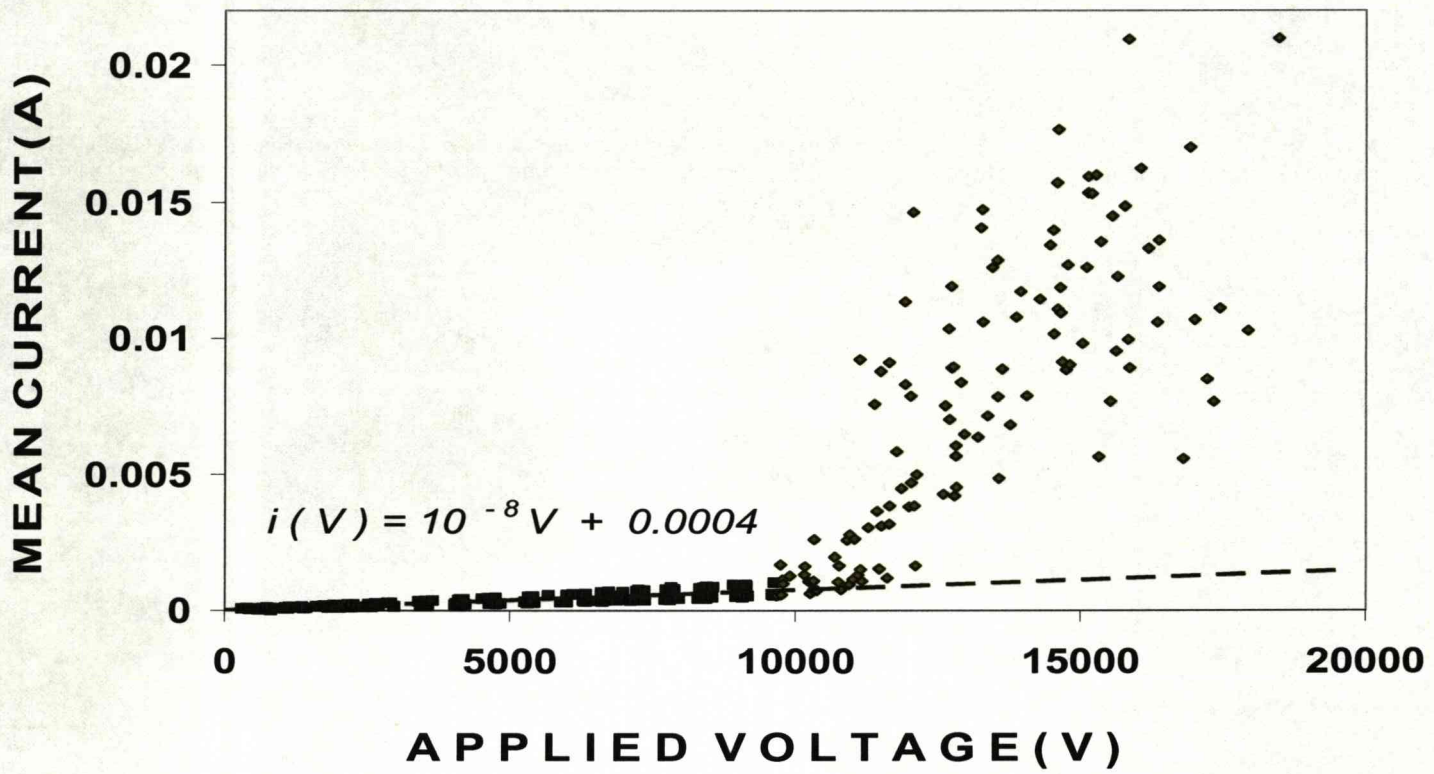

Figure 2.19 represent DBD(B) and DBD(C) experiments plotted on common axes henceforth (The graphs of figure 2.15 and figure 2.17). The dark regimes are dark green and the luminous regimes are lighter green. The dark regime has a fit describing the displacement (dark) current. It is later used to derive the luminous component of the current.

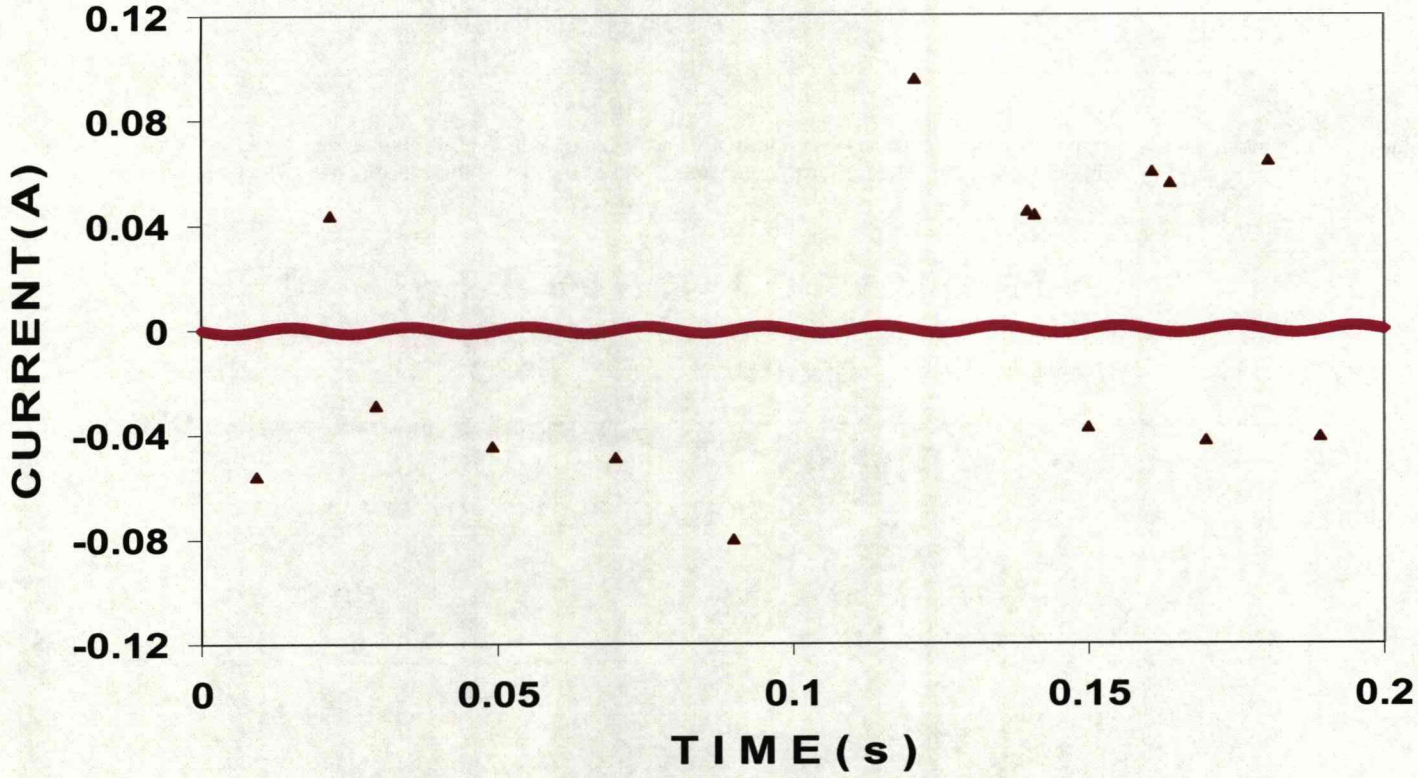

Figure 2.20 is a graphical reconstruction in Excel of the plot of figure 2.13. The complex (repetitive) waveform is represented by a simplified harmonic function (Sinusoidal) of 5000 data-points (pink). The 15 filaments or current spikes are positioned as in figure 2.13 (brown triangles).

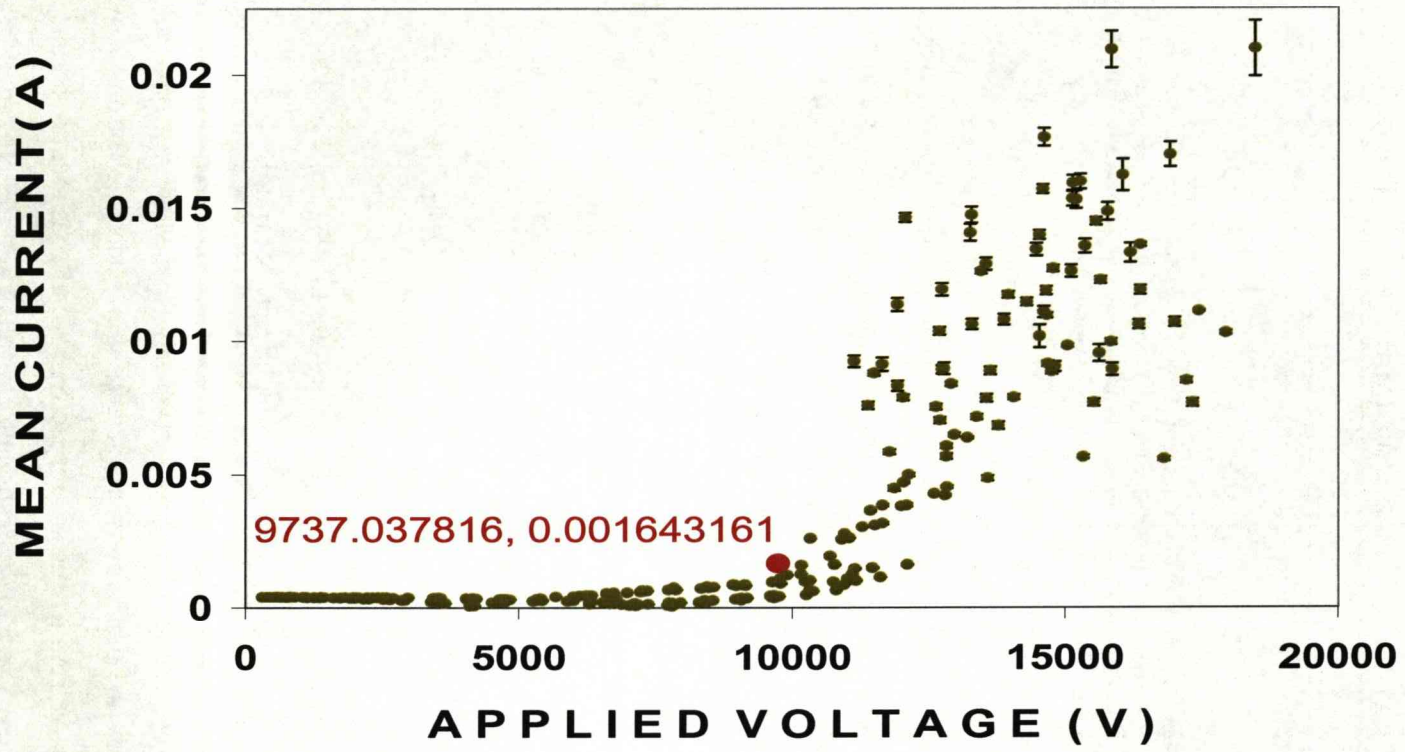

Figure 2.21 is a graph of applied voltage versus mean current for all DBD experiments. The minimum voltage that was observed to initiate breakdown is highlighted as the red dot with its co-ordinates.

RMS Current Values

Total (mA)		Harmonic (mA)		Ratio (%)	
Value	%	Value	%	Value	%
9.4	0.47	0.9	0.14	10.0	0.5

Figure 2.22 is a table of Total RMS current, the RMS current excluding the filaments and the ratio between the two expressed as a percentage. The uncertainties are also expressed as percentages. The filaments, though few in number compared to the number of sample points comprising the waveform (See figure 2.20) dominate the overall current.

2.5 Analysis

As the live dielectric barrier becomes charged by the voltage source, it becomes polarised. An induced surface charge builds up and for non-uniform fields (such as from the edges of the live steel core electrode of figure 2.8 and figure 2.9) regions of elevated charge density can exist on the surrounding dielectric surfaces (glass dielectric barrier in our case). The nature of the dielectric prohibits the dispersal of surface charges and the charge produces an electric field induced by the steel live core electrode. When the induced electric field becomes strong enough, the air around the dielectric breaks down and a narrow discharge channel forms between it and the opposing electrode (typically less than a millimetre in diameter; see figure 2.11 (b). Breakdown near the dielectric is mentioned because it sheaths the electrode with the smallest area and highest local electric field in our case, the grounded copper cylindrical outer electrode).

Figure 2.12 and figure 2.13 show current spikes at negative and positive polarities hence the dielectric barrier can possibly accept electrons as well as emit electrons from its surface respectively (electrons mentioned instead of ions since the lower mass of the latter results in their domination of the electric current). Fast electrons or ions bombarding the dielectric surface will form microscopic pits on it[1] melting, vaporising and ionising the

surface. During the course of the discharge electrons bombard and excite the molecules in air, and light is emitted upon de-excitation (See figure 2.11(c) for light emission).

The current spikes in figure 2.13 have different strengths indicating that there is a level of variation of discharge energy in the filaments. It appears that most of the filamentary discharges at 10.2kV total applied voltage take place with negative polarity, but there are some filaments occurring with positive polarity (as shown at 180ms in figure 2.12). The smoothness in the voltage record irrespective of the current spikes indicates that the discharge current, and hence the discharge power in the filament can be comfortably supplied by the power source without distorting its voltage.

The current waveform of figure 2.12 resembles the saw-tooth waveform (upon close inspection) attributed to capacitive elements in the circuit. At a voltage rating of 5.4kv there is a lack of filamentary discharge. The most obvious capacitive structure is the dielectric barrier itself. For a constant capacitance without any discharge formed, the current and voltage should follow a sinusoidal form. The observed deviation reflects the change of the system characteristics caused by dark or filamentary discharge (although a detailed description is not available at present). The regions bound by vertical parallel line-pairs that around the flattened voltage-peak, current is at zero. In figure 2.12, it can be seen that the voltage waveform can be described by three distinct features. After its negative plateau it increases in a similar fashion to the charging of a capacitor by a DC source. It then has a positive plateau followed by what resembles the voltage across a discharging of a capacitor. The coincidence of voltage peak or trough with zero current is manifested in figure 2.12 despite the absence of large current spikes (luminous filaments). The dark regime (discharge without emitting visible light) conductance represented by the gradient of the trend-line of the voltage-current graphs represent reciprocal impedances (see

figure 2.19) of tens of Mega ohms. This impedance is several orders of magnitudes too low for a purely resistive configuration of series elements (PTFE and soda-glass) for the stated electrode dimensions of figure 2.8. This clearly shows the presence of discharge substantially increased the conductivity because of the generation of free charges in the electrode gap. The capacitive current is indicative here and this indication is supported by the phase shift of 90^0 between voltage and current in figure 2.12.

Although the current is not smooth at low-voltage, as shown in figure 2.12, it still approximately follows a sinusoidal profile. This means that we can, as a first approximation, use a root mean square value of the current to assess the effect of the discharge current. When the voltage increases, as given in figure 2.13, the base capacitive current increases, and in addition, the filamentary discharge current (the spikes) starts to superimpose on the capacitive current.

The overall trend in discharge parameters will now be analysed (figures 2.15-2.18). The first feature of the discharge is that the electrode overlap area has no distinguishable effect on voltage-current characteristics for the coaxial DBD experimented at 50Hz. Looking at the experimental uncertainties given in figure 2.15 for configuration B (structure shown in figure 2.8), there is no clear evidence that the mean discharge current increases with the electrode contact area. However, if the scattered data is looked into the more carefully, there seems to be a trend that shows when the exposed length of electrode increases, the points statistically shift upwards in the positive current axis. For configuration C, this trend becomes less distinguishable, as shown in figure 2.17. Therefore no clear conclusions can be drawn on the influence of the electrode overlap area although a trend appears in the results.

Another particular point that needs to be addressed is the result labelled as 0mm in both figure 2.15 and 2.17. The discharge current in these two cases are different. In figure 2.15 the points are scattered at the bottom of the collection. By contrast those points in configuration C are located on top of the collection of points. Configuration C produces a current spike that is nearly twice that of Configuration B. The linear (dark regime) current of configuration B is almost twice that of configuration C. The previous two observations are related to the larger grounded electrode area of configuration B (See figure 2.8). The increased area results in increased capacitance and reduced capacitive reactance and impedance. This permits larger (dark) capacitive currents to flow. Conversely, the reduced area of configuration C forces the current to manifest itself as luminous filaments as the capacitive current has been suppressed. Hence higher filament currents were intended by this design feature (minimum grounded electrode area on the PTFE shaft) and observed (compare figures 2.8-2.10) experimentally.

Referring to figure 2.8, when the live electrode is at its 0mm position, only its edge area is involved in the discharge and the edge effect in electric field is caused by the live electrode edge. By contrast, in figure 2.9 the live electrode surface is always fully engaged in the discharge and the rim of the outer cylindrical contact edge is supporting the discharge when it is at 0mm position. The difference in the two 0mm configurations results in a lower RMS current for configuration B. Configuration C is therefore more favoured when discharge power is a major factor in a process.

Using a logarithmic scale, the change in discharge current as a function of voltage can clearly be seen in figures 2.16 and 2.18. The discharge was observed to occur at a few isolated locations on the dielectric surface despite the ample area available made by extension of the electrodes (see figure 2.11). The dark regime (capacitive regime, no light emitted) had an

approximately linear voltage-current relation despite the observed distorted current waveform. For configurations B, $I(V) = (10^{-7}V - 10^{-5})$A in the voltage range 1kV - 10kV before the onset of filamentary discharge. The luminous regime produced highly unpredictable currents (spikes on the waveform and scatter on the graphs) and statistically the discharge current is an increasing function of the total applied voltage in the range from 10kV to 18kV. There is a threshold voltage above which discharges switches from dark regime to the luminous filamentary discharge. This threshold is similar in both configurations, which is ~10kV total applied voltage and therefore represents the electrical characteristics of the medium and materials involved. This voltage corresponds to a voltage to electrode separation ratio of roughly 2kVmm^{-1}, as compared with a standard electric field of 3kVmm^{-1} for smooth planar electrodes.

It helps us to observe the effect that electrode extension may have in forestalling the transition from the dark current to the luminous current regimes (namely the DBD(B) 0mm and DBD(C) 9.5mm) experiments (see the region between 10kV to 15kV) figure 2.15 at and figure 2.17 respectively). In the DBD(B) 0mm case the live electrode is flush with the PTFE tube and the filaments (which form from the glass dielectric barrier adjacent to the edges of the steel live core electrode) are obstructed in some part by the PTFE tube. In the DBD(C) 9.5mm case, the ground electrode edge is 9.5mm from the flat PTFE surface. The live electrode edge is 64mm away from the flat PTFE surface! The filament length would be several times longer than the radial gap between electrode and dielectric barrier if the vicinity of the live electrode length is the only possible site for filament formation. An alternative site may exist and the electrical characteristics of the filaments that are formed near it may differ from those formed near the edge (since their geometries also differ). These two different regimes of filamentary discharge results in different filamentary

current (current spikes). The live (cylindrical) steel core electrode preferentially forms filaments near its sharp edge (the circle defining the circular face and the curved surface which was 64mm away from the flat PTFE surface) rather than its smooth, curved areas (assumed to be only ~9.5mm away from the flat PTFE surface. See figure 2.8 and figure 2.9).

Inspection of figure 2.1 shows that a copper shaft runs along the length of the hollow PTFE cylinder. Figure 2.8 shows that a steel tube is fitted onto the copper shaft for extension. The glass dielectric barrier partially covers the steel tube. The grounded outer electrode is insulted from the live steel core electrode by PTFE, glass and air. This configuration is capacitive. Inspection of the graphs of figure 2.15 and figure 2.17 show that two experiments depicted by figure 2.8 and figure 2.9 have different current-voltage relations in the dark regime. The outer electrode of figure 2.8 is longer than the outer electrode of figure 2.9. Similarly, the gradient of the fit in figure 2.15 is steeper than the gradient of the fit in figure 2.17. This is because the gradient is the inverse of the capacitive reactance and the capacitance is inversely proportional to the capacitive reactance. The capacitance is therefore proportional to the gradient and therefore the electrode overlap area.

The 0mm protrusion length of the live-core electrode (DBD experiment (B) of figure is the experiment in which minimum live electrode area is exposed. This means that field contributions to the filament from other surfaces of the live electrode is minimised. The filament has to impinge upon the live core-electrode at one particular site. The case of the DBD(B) 0mm experiment most resembles the pin-electrode of trials (See figure 2.7) in the sense that electric field appears to have its source (or sink) at one position on the live electrode and that position coincides with the region of filament impingement. The similarity of DBD(B) 0mm experiment with the experimental trial of figure 2.7 is inferred. (In the experimental trial

electrode separation was varied from 4mm -10mm; similar in dimensions to DBD(B) discharge gap length of 5mm). In addition to this, the unpredictability of RMS current for all DBD experiments (can only be estimated within an order of magnitude (1mA – 10mA). These conditions allow the following generalisation: Under the present experimental conditions, the dielectric barrier discharge's electrical characteristics (voltage and current) are weakly dependent on electrode geometry. However, geometry is crucial for stability and operational durability (lifetime of electrodes).

It must however be noted that the observation that filamentary discharge in the current configuration seems to be localised on the electrode surface cannot be generalised because localisation may be caused by the asymmetry of the co-axial structure during the assembling process. With a much more symmetric surface arrangement, the filamentary discharge is expected to spread the whole electrode surface in a statistic sense, thus distributing the discharge energy in the whole electrode gap.

Let us assume that within the accuracy of an order of magnitude, the experimental trial of figure 2.7 (at 5mm live-electrode to dielectric barrier separation) has similar electrical characteristics of DBD(B) 0mm (see figure 2.15. The filament that forms after electrical breakdown impinges upon the pin-electrode of figure 2.7 and makes contact with the dielectric barrier. The pin-electrode is made live and the planar electrode beneath the dielectric barrier is grounded. The potential at ground is nominally zero and at the pin electrode the potential is therefore the applied voltage $V_{ap.}$. Since the dielectric barrier surface (facing the pin-electrode) is some distance away (1mm) from the grounded planar-electrode it has a potential at its surface V_b . The copper electrical cable resistance is assumed negligible as are voltage drops across them.

As seen from the filament, the electrical field radiates from a point on the pin-electrode (see figure 2.23). This field is attenuated along the filament by distance according to the inverse square-law and the screening effect due to charge-carriers. By describing the potential along the axis of a pin-electrode as that due to a point-charge and establishing the boundary-conditions described in the previous paragraph, the Debye length of the electrical discharge may be deduced.

The region with the greatest electric field in the pin-electrode configuration is usually near the pin-tip (assuming all other surfaces are smooth). For electrical breakdown to occur the field at the pin-tip must equate or exceed the electrical breakdown-field. By using Gauss's law, the associated surface-charge (enclosed by a Gaussian volume) can be calculated from the filament diameter[1] and the electrical breakdown field. Once breakdown occurs, this charge is dispersed into gaseous electrical discharge towards a region of lower potential-energy (the opposing electrode). The use of Gauss's law and the breakdown allows generalisation of the following result to any high-voltage pin-electrode configuration in a gaseous medium. Although the breakdown field is attenuated and screened through the length of the filament, it remains strong near the tip until the discharge is extinguished. It is the threshold condition but other quantities such as capacitance and applied voltage may be used to derive the magnitude of the effective point-charge. From the graph of figure 2.15, the gradient gives the inverse capacitive reactance. With the applied voltage and frequency known, as well as the typical live electrode area ~$0.01m^3$ the total charge may be deduced. A simple scaling calculation may be used to find the mean charge in the area defined by the typical filament diameter. The value gives a similar result to the Gaussian law calculation (a few Pico-coulombs).

$$\int \mathbf{E} \bullet d\mathbf{A} = \frac{Q_{enc.}}{\varepsilon_0} \therefore Q_{enc.} = \varepsilon_0 \cdot E_{break.} \cdot \pi \cdot r_{fil.}^2$$

$$\Phi(r) = \frac{Q}{4 \cdot \pi \cdot \varepsilon_0} \cdot \frac{\exp\left(-\frac{r}{\lambda_D}\right)}{r} = \frac{E_{break.} \cdot r_{fil.}^2}{4 \cdot} \cdot \frac{\exp\left(-\frac{r}{\lambda_D}\right)}{r}$$

$$\left| \frac{r}{\ln\left|E_{break.} \cdot r_{fil.}^2\right| - \ln\left|4 \cdot r \cdot \Phi(r)\right|} \right| = \lambda_D$$

Equations 2.3

From equations 2.3, Q, $Q_{enc.}$, ε_0, E, $E_{break.}$, $r_{fil.}$, r, Φ and λ_D are the charge, the enclosed charge, the permittivity of free space, Electric field, the electrical breakdown field ($3MVm^{-1}$), the potential and the Debye length respectively. All that remains is to define the potential at the pin-electrode $V_{ap.}$ and the potential at the dielectric barrier V_b.

The potential difference $V_{ap.}$ is simply the applied voltage however V_b. is not so trivial. Although the latter was not directly measured, it can be inferred from the current ranges observed. The continuity of current and conservation of charge dictates that the current density incident on the dielectric (from the electrical discharge) must be equal to the displacement current density across it. This is dealt with in equations 2.4.

$$\mathbf{J} = \dot{\mathbf{D}} = \frac{i}{\pi \cdot r_{fil.}^2} \hat{\mathbf{k}} = \varepsilon \cdot \dot{\mathbf{E}} = \frac{\varepsilon_0 \cdot \varepsilon_r \cdot V_b}{d \cdot \tau_{fil.}} \hat{\mathbf{k}}$$

$$\therefore V_b = \frac{i \cdot d \cdot \tau_{fil.}}{\pi \cdot r_{fil.}^2 \cdot \varepsilon_0 \cdot \varepsilon_r}$$

Equations 2.4

From equations 2.4, **J**, **D**, d and τ_{fil} are the (conductive) current density, the displacement current density, the dielectric thickness (1mm) and the filament lifetime[1] (1ns – 10ns) respectively. The unit vector $\hat{\mathbf{k}}$ is added for completeness. ε_r is the relative permittivity of soda-lime glass (~7.75). Returning to equations 2.3, the radial distances from the pin-electrode (corresponding to the potential at the pin-electrode tip) and grounded electrode (V_{ap} and V_b respectively) are r_{live} and r_{ground} respectively. For the sake of comparison with DBD(B) 0mm; r_{live} will be equal to the pin-electrode's radius of curvature (see figure 1.3 of chapter one. This is comparable to the radius of the filament, r_{fil} which according to literature[1] is approximately one tenth of a millimetre) and r_{ground} will be 5mm (to tally with the separation between the dielectric barrier and the outer-grounded electrode of the DBD(B) and DBD(C) experiments. See figure 2.8 and figure 2.9 respectively).

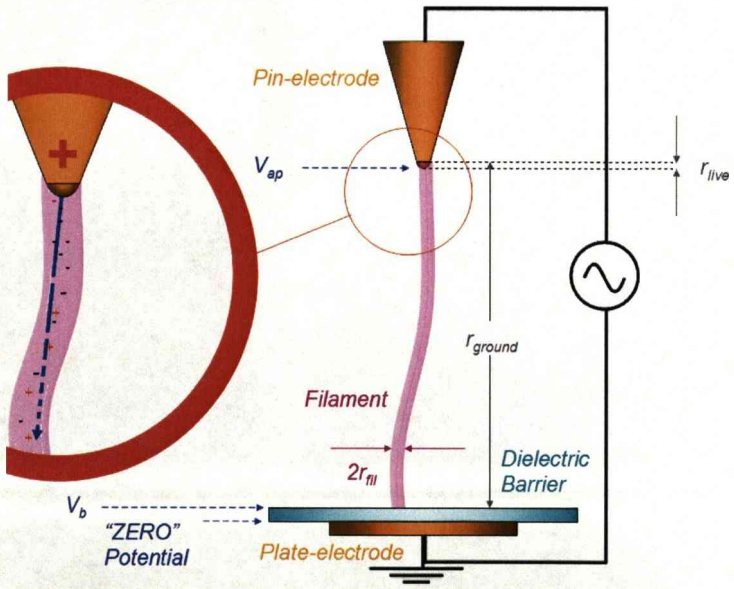

Figure 2.23 is a simplified diagram of a generic DBD pin-plate electrode configuration. The mathematical quantities are illustrated throughout. The physical components are named and colour-coded. The enlarged section denoted by the thick red arc to the left shows how at a given voltage polarity (positive in this case) the electric field (Blue arrow) is attenuated by the presence of mobile charge-carriers. The live-pin-electrode behaves as a point-charge in the presence of the mobile charge-carriers.

Recalling equations 2.3 and equations 2.4, V_{ap} and i may be quoted from the highlighted co-ordinates of figure 2.21. In this case $762V \leq V_b \leq 7622V$. This range arises due to the variation in filament duration. The impedance, voltage drop and displacement current depend upon the temporal duration of the input voltage spike. The Debye length is therefore $20.5\mu m \leq \lambda_D \leq 802.5\mu m$ calculated using the appropriate values to find the minimum and maximum ranges.

Let us assume that the neutral gas temperature and ion temperature are similar (due to the high-particle concentrations under atmospheric pressures) and that the ion temperature is close to ambient[1], then the Debye length will become chiefly dependent upon the ion number density. If we assume quasi-neutrality (due to the small value of the Debye-length in comparison to the electrode gap) and that the majority of ions are singly-ionised then equations 2.5 hold.

$$T_e >> T_i,\ n_e \approx n_i \text{ and } T_i \approx T_{ambient}$$

$$\lambda_D = \frac{1}{e}\sqrt{\frac{\varepsilon_0 k_B}{\left(\frac{n_e}{T_e}+\frac{n_i}{T_i}\right)}} = \frac{1}{e}\sqrt{\frac{\varepsilon_0 k_B}{n_e \cdot \left(\frac{1}{T_e}+\frac{1}{T_i}\right)}} \approx \frac{1}{e}\sqrt{\frac{\varepsilon_0 \cdot k_B \cdot T_i}{n_e}}$$

$$\therefore n_e = \frac{\varepsilon_0 \cdot k_B \cdot T_i}{\lambda_D^2 \cdot e^2}$$

Equation 2.5

Equations 2.5 hold if the charge carriers responsible for screening the point-charge (live pin-electrode) obey the Maxwell-Boltzmann distribution. Since the ions are of similar mass and volume to the neutral gas molecules, their collision cross-section and mean free path will be

similar to those of the neutral molecules also. The ionised gas is highly collisional and momentum transfer between ions accelerated by the electric field is efficient.

Let us assume that an ion is accelerated from rest by the breakdown field ($3MV^{-1}$) and the typical mean free path is 0.1μm. The ions will posses a kinetic energy of ~0.3eV prior to collision. This is an order of magnitude greater than the average kinetic energy of neutral particles at room temperature. The electric field value decreases on the onset of DBD formation due to the presence of mobile charge-carriers and hence the energy an ion gains from the electric field in DBD will be less than 0.3eV. From this kinetic energy, mass of the nitrogen ion and the mean free path, the velocity and the time between collisions was found to be ~10ps. This is three to four orders of magnitude greater than the DBD filament duration. The ions therefore have ample time to make several collisions and establish a Maxwell-Boltzmann kinetic energy distribution amongst themselves if not amongst the ambient neutral gas molecules also.

These ions (in thermal equilibrium with one another and possibly with the ambient neutral gas) surround the pin-electrode tip (because the tip is enveloped in and impinges upon the DBD filament). Coronal (non-luminous) discharges were detected (sound and current spikes on the oscilloscope) on the apparatus when high-voltages were applied. These discharges generate electron-ion pairs (mobile charge-carriers) that populate the region surrounding the pin-electrode. The pin electrode was surrounded by mobile charge-carriers and so the conditions for equations 2.5 are valid and we continue the calculation of the electron number density range.

From equations 2.5, k_B, T_i and n_e are the Boltzmann constant, ambient temperature (~300K) and electron number density respectively. Using

these equations and the range for the Debye lengths found previously the electron number density range is $2.2\times10^{12}\,m^{-3} \le n_e \le 3.4\times10^{15}\,m^{-3}$ whose upper bound agrees with the literature[1].

2.6 Conclusion

The co-axial design of the DBD system produces a stable and durable discharge in a relatively large space. The contact area of the electrode can also be conveniently adjusted, thus permitting possible application for energy production in future. The mean filament electrical current of the DBD(B) and DBD(C) experiments was found to be $7.7\text{mA} \pm 6.2\%$ (RMS). The filament current ranges from 1.6mA to a little over 20mA in our case.

A novel method of calculating electron number density $\left(10^{12}\,\text{m}^{-3} \le n_e \le 10^{15}\,\text{m}^{-3}\right)$ from the Debye length was utilised in this thesis. The small discharge area was approximated to a point charge whose electric field was attenuated by distance and mobile charge carriers in the discharge medium.

Below the threshold value of 9740V, the discharge is silent and the capacitive current prevails. Results show that the DBD was not diffuse or uniform but filamentary at discharge voltages higher than 9740V. This effect is ascribed to the low applied frequency and the edge effects of the steel core electrode, or more generally the surface conditions of the electrode. At higher frequencies, electron and ionic bombardment of the glass surface is expected to be reduced due to the charge-trapping mechanism of the rapid electric field oscillation. The frequency of these oscillations can be selected to allow the lighter and faster particles (electrons) to reach the dielectric surface. Their collision with gas molecules sustains the glow mechanism as these molecules de-excite.

It is found that configuration C, corresponding to a fixed, fully exposed live electrode on the axis of the discharge space, produced, on average, higher discharge current, therefore higher discharge power. This configuration is therefore favoured for application where discharge power is a key factor. To summarise, the capacitance of the electrode configuration must be minimised in order to channel power to the luminous discharge efficiently. The way this was done in the present work was to reduce the outer electrode area.

Based on the results obtained in this chapter, a modification to the electrode design used in DBD(B) and DBD(C) is proposed. If high frequencies are applied to the new design, a uniform, highly robust electrode assembly for DBD generation may be envisaged. It also has the design advantage of the previous electrodes in that its outer electrode area may be adjustable (Use of a telescopic retractable outer electrode).

With minor modifications as illustrated in figure 2.24 and the application of suitable frequencies, the current density and electron number density of the electrical discharge may be controlled geometrically as well as electrically if materials of different properties are used for the dielectric barrier. This may also be of value for material decomposition and other process conditioning.

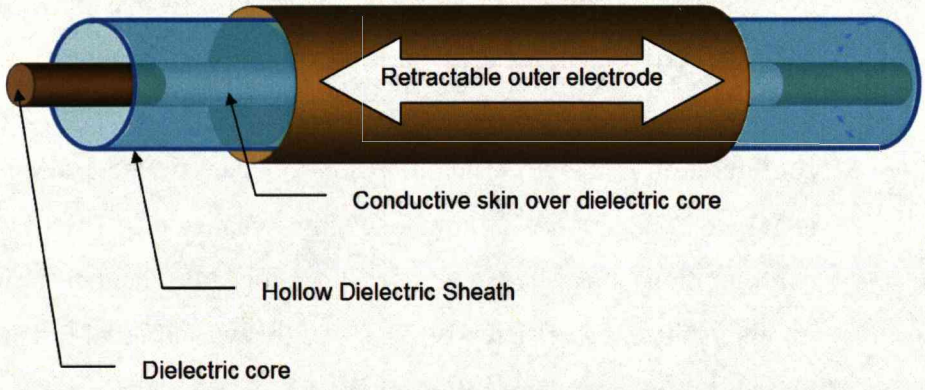

Figure 2.24 is a proposed DBD reactor modified from those used in the present work. (See figure 2.8 and figure 2.9). No edge effects should prevail and support filamentary discharges in this case (since the core electrode is conductive). The retractable outer electrode may also be telescopic.

Chapter 3

GLOW DISCHARGE ELECTROLYSIS (GDE)

3.1 Introduction

The second experimental aim of this thesis is to assess by characterisation the potential of using non-thermal plasmas in achieving energy production. The use of non-thermal plasma could be advantageous over other traditional methods in the following ways. It does not consume excessive amounts of electrical power. It does produce substantially high-energy electrons however and active chemical species/radicals. The latter are needed to activate useful chemical reactions. Whether an energy gain can be realised by chemical reaction depends not only on the plasma environment, but also on the intended chemical reaction. To release energy, the formation enthalpy of the reaction end-products must be lower than the formation enthalpy of the reactants.

To make the potential process commercially exploitable there must be an abundant supply of the reactant from natural resources. These aspects are important but cannot be fully explored in the present work due to the complexity involved. Emphasis is therefore given to the establishment of stable discharges to produce non-thermal plasmas that can be potentially used for the purpose of energy production.

A flame is lit and some type of carbon-based fuel is added to kindle the flame and release energy for conversion (like for fossil-fuelled power stations). Hence GDE plasma is generated in the hope that chemical species that are dissolved in its electrolytic virtual electrode may migrate

up towards the plasma column and react with the atmosphere (not necessarily air). As the reactants are in the gaseous phase (in the plasma column) the total reagent surface area is maximised as is the expected rate of reaction.

Experiments with setups in the previous chapter produce only microscopically thin filamentary plasmas. When generated for some period of time and at high power levels, gases such as ozone and nitrogen dioxide form. For certain applications where these gases need to be avoided, water can be used as an electrode and these gases are no longer detectable (further work may be done to assess the effectiveness of other liquids for this role). The plasma volume appears much larger than the microscopically thin filamentary plasmas.

For any chemical reaction, it is useful to maximise the reagent's surface area to accelerate the reaction-rate. Grinding rocks for example into a water-based paste is better than leaving them whole. Dissolving the minerals into aqueous solution is better still. GDE was used to observe whether or not dissolved compounds would appear in the plasma column above the electrolyte surface.

Rocks like bauxite and sandstone were chosen for their iron, aluminium and silicon content. These three elements are highly abundant and were of great initial interest. Aqueous sodium chloride solution was used for its chlorine and hydrogen content also.

In this chapter, a GDE system has been developed and experiments conducted under specified conditions. The characteristics of the plasma were investigated with the help of residual gas analysis, spectroscopy and high-speed photography.

3.2 Design Considerations and Experimental Trial

The experimental setup used for the present work is similar in many ways to that used by Laroussi et al.[36] where a non-equilibrium diffuse discharge was generated in atmospheric pressure air. An electrode was immersed in liquid water and another suspended above the water surface (but not in contact with the water). When a large potential difference is applied a relatively large volume plasma column was generated under atmospheric conditions

A series of configurations were used to perform tests to see which ones were most stable and suitable for experimentation. As shown in figure 3.1, the electrodes that were immersed in water were grounded. This was done for safety reasons to prevent direct electrical contact between the experimenter and the high voltage power source in case of spillage or water vessel leakage. The suspended dry electrode was therefore made live. Figure 3.1 shows electrode configurations (all have rotational symmetry about the z-axis. The z-axis is the electrode axis, that is to say the imaginary line that runs through both electrodes' centre of mass). The aluminium foil ball of figure 3.1 (e) however was free to float and its position or geometry does not reflect rotational symmetry. Figure 3.1 (f) is the only experiment depicted in figure 3.1 with a steel bolt (submerged electrode). The reason for this is that steel tends to rust and discolour the electrolyte. Figure 3.1 (d) and figure 3.1 (e) illustrate the live electrodes as glass capillaries holding water in the suspended electrode so that both electrodes would be aquatic. These suspended water electrodes did not produce long-lived plasmas. It should be noted that using water as the material for both electrodes was attempted to spare the metallic contacts and ablate the only material desired to participate in the plasma; namely the electrolyte.

Initially at small air gaps (~12mm) the upper plate exhibited an orange incandescent flash (See figure 3.2(a) and figure 3.2(d)). This observation was more pronounced at lower applied frequencies and was not very repeatable at 500W (See oscilloscope traces later in this chapter). Once the applied input power was raised to 1.25kW the effect was not only repeatable, but the plasma appeared white and more luminous also (see table of RMS voltage and RMS current later in the chapter). Water was used in all cases except in figure 3.2(f) where aluminium nitrate crystals or metallic aluminium shavings were heaped up under the live electrode in place of water (The initial height of the heap was ~10mm. Its apex was 10mm-20mm below the point of the suspended spike-electrode). It was observed that aqueous aluminium nitrate produced a similar effect to water at least upon direct inspection. Jade sparks appeared on the surface of the aluminium electrode facing the electrolyte in figure 3.1(a). Purple filaments were observed to bridge the air gap in all cases.

With the gap closed further (~5mm) the aqueous electrolyte from the poly-tetra-fluoro-ethylene (PTFE) beaker rose to bridge the gap in all cases involving an electrolyte (liquid). Even after the circuit was de-energised and grounded, this water bridge still remained. Once the plasma was active for a length of time (~ 1 minute), the water vapour condensed on the inner surface of the Perspex chamber (see figure 3.2). This formed a conductive path and the electric current (between a few tens of milliamps and a hundred milliamps) in that secondary circuit bypassed the plasma after ~5 minutes. The plasma was therefore extinguished in the enclosure. The cells illustrated by figure 3.2 (b) and figure 3.2 (c) extinguished their plasmas faster than the others because the electrolyte was depleted in the capillaries. The design conclusions were that the rig has to be open or the vapour produced has to be immediately removed away from the surfaces adjoining the electrode and electrolyte surfaces in order for the electrolytic plasma to

be sustained (The experiments of figure 3.2 showed this). Also, the capillaries drained and so their cells produced the shortest-lived plasmas.

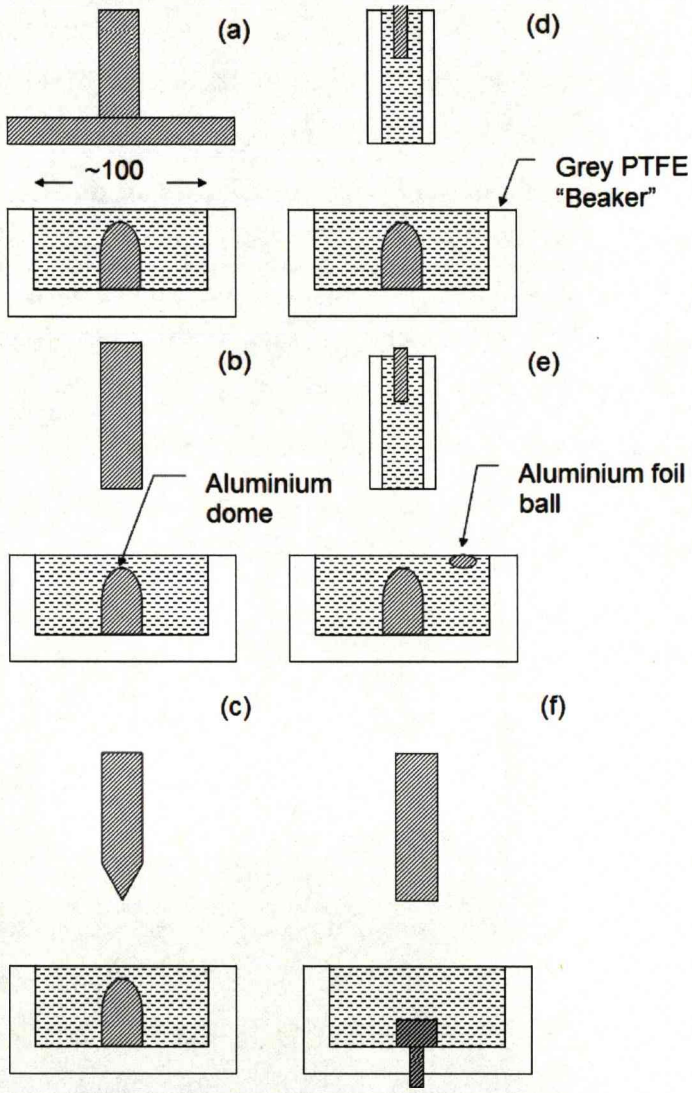

Figure 3.1 illustrates a few experimental arrangements of an open plasma system. The diagonally shaded regions are aluminium and the horizontal broken lined region represents liquid water. Dimensions are in millimetres and configurations (a) to (f) are described in the script. As shown in experiment (a), the container's inner diameter and height were both ~100mm. PTFE beaker capacity was ~800ml. Aluminium dome ~50mm in height and 20mm in diameter. The darkest shaded region in (f) was a steel bolt.

Generally, the suspended electrode must be in the solid state for prolonged discharges to be sustained. The experimental setups of figure 3.1 were the first batch of tests. For reasons explained shortly their designs were

enhanced and long-duration (~15 minute) experiments were run and results obtained. The tests undertaken (represented by figure 3.1 and figure 3.2) used drinking-tap water. In later experiments filtered tap water was used.

For the residual gas analysis of the water plasma, figure 3.1(c) was developed further (as aluminium does not react with water as much as iron does). Aluminium is a reactive metal and quickly forms a oxide layer on its surface that prevents further reactions with its environment.

PTFE has been used for pulsed plasma thrusters (PPT's)[92] in a similar method as it is being ablated in figure 3.3. PPT's utilise a plasma current density vector that is perpendicular to the vector area of the PTFE or Teflon surface. In other words the plasma is in contact with the PTFE/Teflon surface. There is a self-induced magnetic field perpendicular to both the current density vector and the vector parallel to the PTFE/Teflon plane. Ablated PTFE/Teflon will flow outward from the plane. This motion is induced by the Lorentz force and thrust is derived (as well as the expanding vapour). The magnetic field is sizeable due to the short duration and large magnitude of the current-pulse.

Although the situation is similar here in terms of materials used and vector alignment, the electrostatic force draws the plasma column to the electrode in figure 3.3 and the Tufnell column in figure 3.4. The electrode-electrolyte gap has electric fields that initiate the discharge. The plasma cannot therefore exist in a stable state without coming into contact with both electrode and electrolyte. The forces involved in discharge formation and (spatial) plasma stability must be electrostatic. The Lorentz force is a secondary effect as it is dependent upon the current. The latter is dependent upon the applied voltage and the voltage drop across electrodes is indicative of electric fields and the electrostatic force (the initial force that initiates the discharge). Currents are ~1mA and the self-induced magnetic

field is low. The Lorentz and electrostatic forces are working in tandem so the force that is keeping the plasma column away from the electrode tip (the most likely point of connection due to its proximity to the water surface and high electric field) is probably buoyancy.

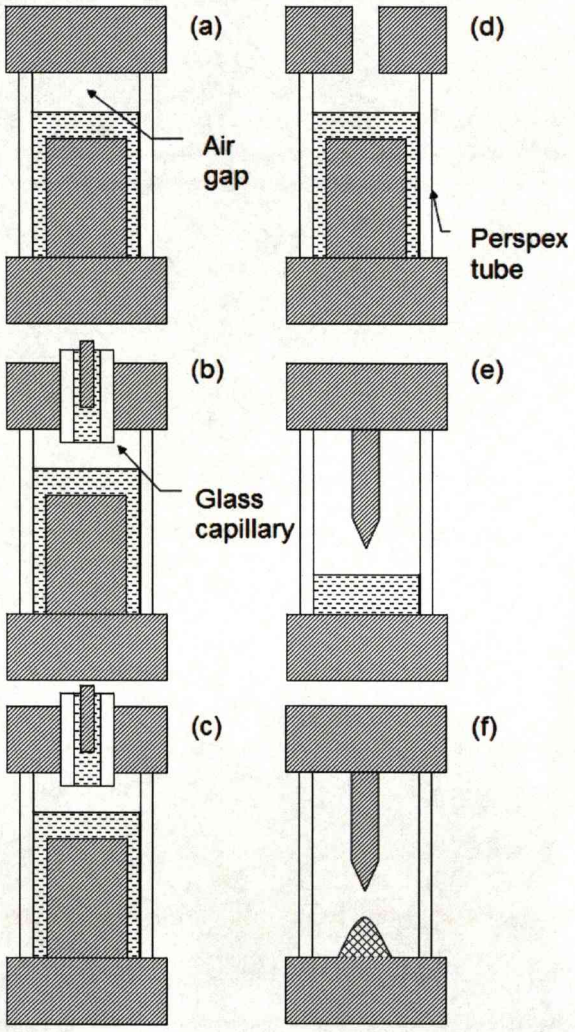

Figure 3.2 illustrates enclosed electrode configurations. Shading conventions from figure 3.1 apply. The heap or mound in figure 3.2 (f) are aluminium shavings and aluminium nitrate crystals. The Perspex tube walls were ~ 5mm thick. Diagrams are rotationally symmetric about their axes of symmetry.

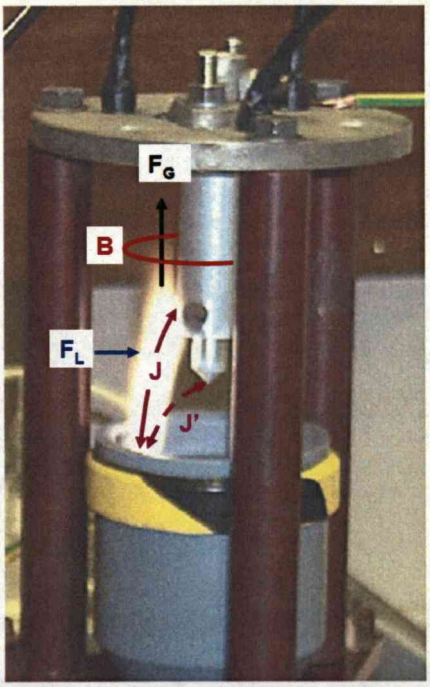

Figure 3.3 shows the PTFE container is participating in the discharge and most likely evolving its constituent chemicals as vapours. $\mathbf{F_G}$ is the buoyancy of the hot gases. $\mathbf{F_L}$ is the Lorentz force (always radial and negative. It should be noted that the entire suspended shaft is conducting and constitutes the electrode-surface). **B** is the magnetic field. **J** is the observed current density vector and **J'** is the expected current density vector from the electrode tip to the inner container wall (top to bottom respectively). The container is the same illustrated in figures 3.1 and it houses the live (submerged electrode) for the RGA experiments. The plasma column impinges upon the electrolyte at the shown position because of unevenness in the laboratory floor-level. Water surface area vector is therefore not parallel with suspended electrode axis. Typical voltages and currents were ~3kV and ~10mA respectively. The discharge is highly luminous and of relatively great length (~100mm) for ~30W dissipated power due to the participation of chemical reactions involving the PTFE (whose surface became sooty and brittle at the point of discharge-contact during the experiment).

Before discussing buoyancy it should be noted that the oxide layer of aluminium would form a resistive barrier over the electrode tip and hence force the discharge to find a more conductive region of the electrode (See figure 3.3). In fact, what was observed during testing was the discharge connecting with the tip and moving upward along the electrode surface in a "brushing" action. This was periodic (~1s) and would extinguish itself as the plasma column became more vertical. Using the PTFE container always resulted in this flame-like effect and the point where the discharge impinged upon the liquid surface was near the Tufnell container's inner

wall. The discharge would connect to the same region of the inner wall due to the water surface's vector area not being parallel to the electrode axis (The floor or working surface was uneven).

Returning to buoyancy, it can be seen clearly from the tail of the black arrow in figure 3.3 that there is part of the discharge that does not respond strongly to the electrode and hence electric fields. This neutral gas was hot and the discharge appeared flame-like. PTFE consists of carbon and hydrogen atoms. It is not difficult to deduce that the electrical discharge in some way initiated chemical reaction. This is a plasma assisted chemical reaction however using PTFE as a fuel is not beneficial economically or experimentally as it is expensive and its vapours will disturb residual gas analysis (RGA) readings. One cannot therefore use it if any reasonable attempt is to be made to investigate the nature of the water plasma as PTFE ablation must undoubtedly release vapours into the atmosphere that contain elements foreign to tap-water.

Water is vaporised and condenses on the Tufnell columns and electrode mount to form a conductive path that bypasses the plasma column to the more distant suspended electrode tip as shown in figure 3.4. The plasma behaves like a switch that connects the container's water to the moist Tufnell column thus igniting it and conducting current over its moistened surfaces.

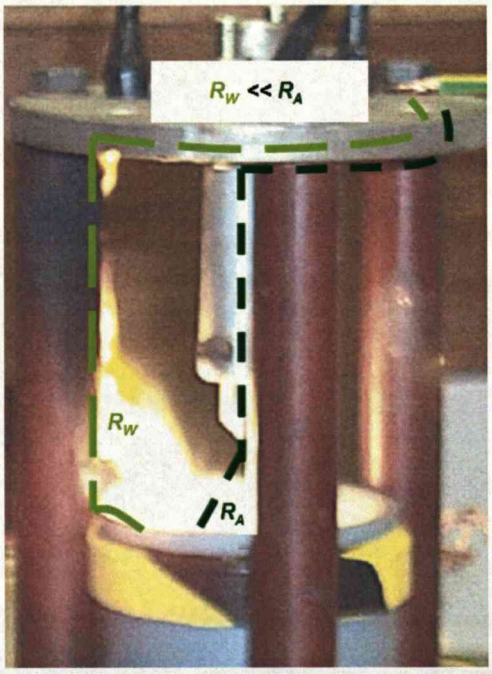

Figure 3.4 shows that the Tufnell columns are also participating in the discharge and most likely evolving its constituent vapours. The dark green dashed lines illustrate the higher resistance path across a larger air gap to ground via the electrode. The light green dashed lines illustrate the lower resistance path to ground via the nearer moist Tufnell pillar. This occurred after 30 minutes of experimentation.

GDE occurs not only between the suspended electrode and the bulk of the electrolytic fluid (see figure 3.5), it occurs between the suspended electrode and wet surface in contact with the opposing electrode (see figure 3.6). When GDE occurs on the electrolyte bulk the discharge energy is transferred to the electrolyte which may vaporise and convect upwards (see figure 3.5). If GDE occurs on a moist surface then there is insufficient electrolyte to absorb the discharge's heat and the remaining heat is transferred to the surface and ablation occurs. Species native to the surface are evolved as vapours and may become ionised and populate the discharge as illustrated by figure 3.6 or remain largely partially un-ionised and convect upwards like the plume of a flame as displayed in figure 3.3 (label $\mathbf{F_g}$).

In the case of figure 3.4, the plasma column heats the moistened surface of the inner wall of the PTFE container either by direct contact or due to its close proximity. This transfer of heat initiates a chemical reaction resulting in gases being produced. In the case of figure 3.3, it was seen that buoyancy forces $\mathbf{F_g}$ are significant. The plume of gas convecting upwards and uninfluenced by the electrode were released from PTFE or are native to water. The gas plume can consist of a mixture or compounds of hydrogen (1312 $kJmole^{-1}$), carbon (1087$kJmole^{-1}$), nitrogen (1402$kJmole^{1}$), oxygen (1314$kJmole^{-1}$) or fluorine (1681$kJmole^{-1}$). Their ionisation energies are quoted in the brackets.

If figure 3.6 is recalled, then it should be noted that the discharge impinges on the moist ceramic vessel. The ceramic was porcelain and contained many elements however silicon (786.5 $kJmole^{-1}$) and aluminium (577.5 $kJmole^{-1}$) are prevalent amongst them. These two are not in their pure form but exist as compounds. The vapours evolved here are strongly affected by the electrode (converging upon its tip) and therefore must be strongly ionised since the gas appears conical (as expected from the electrical field pattern of a point-planar electrode configuration. Note Gauss's law of diverging electric fields). The ionisation energy of aluminium is lower than all of those mentioned in the previous paragraph and this gives a clue as to the nature of GDE.

The glow discharge heats, vaporises and ablates whatever material that it impinges upon or is in close proximity to. The resulting vapours may or may not be strongly ionised due to their relatively low or high ionisation energies (respectively) and the electron temperature of the discharge. Strongly ionised gases will behave like plasma; following the course mapped out by the electric field (see figure 3.6). Fire is a weakly ionised plasma and the water-plasma in figure 3.3 and figure 3.5 behaved in that manner. By inspection of figure 3.5 and figure 3.6 it can be said that water

was weakly ionised (cylindrical plasma column generally centred on the electrode) but the ceramic vessel's evolved vapours were strongly ionised (highly-focused cone impinging upon the electrode-tip; the estimated region of greatest electrical field). This places the energy of bombarding electrons and ions between the ionisation potential of the water molecule and aluminium (suspended electrode material).

Since the PTFE container seemed to be ignited by the plasma column, as did the Tufnell columns for prolonged experimentation, a smaller ceramic container was used to prevent these effects occurring. Ceramics are well known for their resistance to heating. Under the experimental conditions no macroscopic damage to the ceramic container was observed. It would not ignite as easily as a carbon-based polymer.

3.3 Experimental Method and Observations

3.3.1 Residual Gas Analysis (RGA)

The RGA experiments were done to ascertain plasma composition. The container and rig combustion or ablation products should be limited for accurate plasma vapour detection. This was not always achievable in the case of the container because the plasma column would periodically move to the edges of the container releasing ablation vapours. The plasma will not only produce vapours from water but from the container also. The configuration of figure 3.5 was found to be stable both for residual gas analysis and spectroscopy. It will therefore be discussed in further detail.

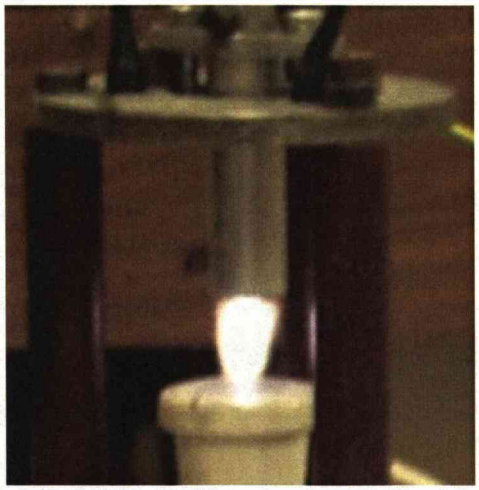

Figure 3.5 shows stable and repetitive discharge that does not involve the Tufnell columns in ablation or even the ceramic container when at full capacity. Note the flame-like appearance of the discharge and its weak response to the point-electrode (obscured here but revealed in figure 3.6). As shown in later oscilloscope plots; the voltage waveform was not sinusoidal, the current was negligible except for spikes at negative voltage polarities hence power spikes occurred and "phase" is ill-defined.

Figure 3.6 shows how as the water level eventually declines (after ~15minutes), the container participates in the discharge as is characterised by the change in plasma colour. Here an incandescent point is revealed at the electrode tip from where the discharge diverges. The plasma regime here is different than that displayed in figure 3.5 as the gas is more strongly ionised. The voltage and current levels were not adjusted from figure 3.5. The water level has dropped to approximately one-third of the ceramic container's height (not shown). See figure 3.7 and figure 3.8 for dimensions. Voltage and current were ~2kV and 9mA respectively. The currents for GDE were expressed as an RMS value. The apparently high luminosity may be explained by the high magnitude of the current-spikes (See analysis of chapter two and compare RMS current values to current-spike magnitudes in the oscilloscope traces illustrated later in this chapter).

A residual gas analyser is similar to a mass spectrometer in concept but quite different in operation. In RGA, the sample is already in the gaseous phase and is drawn into the device by negative vapour pressure applied to the whole system. In RGA the gases are ionised using a filament and drawn into a region of space where an electric quadrapole deflects the ions by certain degrees according to their mass to charge ratio. This ratio of atomic mass unit and electronic charge can be used to identify atomic or molecular ions. It was used to analyse some of the long-lived species produce by the plasma. These are chemically stable and are not transitory like a free radical (ozone and the oxygen radical respectively for example). A free-radical exists for only a fraction of a second and cannot be detected by the RGA reliably.

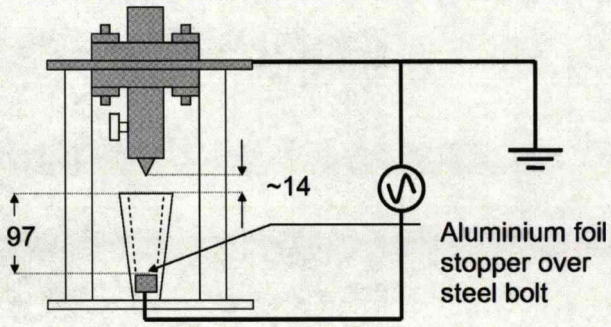

Figure 3.7 is an electrical diagram and the electrodes are featured in grey as opposed to black to illustrate detail. Dimensions are in millimetres.

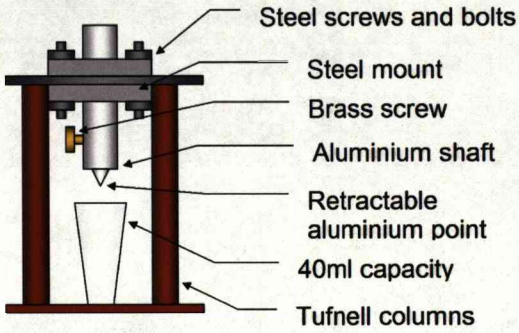

Figure 3.8 illustrates that the vessel of 40ml capacity is ceramic in composition. The whole cell is the "open rig" referred to in the text.

The RGA was configured to automatically make a reading sweep every seven minutes between 1 to 50 atomic mass units per electronic charge. Readings before, during and after plasma ignition were made and recorded. During plasma ignition the plasma column impinged upon the water-surface. The RGA took its reading during this regime. Afterwards the plasma column impinged upon the ceramic container. The RGA took its final reading during this regime or closely after deactivation. Figures 3.7-3.9 illustrate the apparatus. The electrode in the container was made live and the suspended electrode grounded to protect the RGA gas inlet tubes connected as show in figure 3.9. Figure 3.7 shows that the entire mount for the suspended electrode was grounded and in electrical contact with the suspended electrode. This was done to protect the RGA from high-voltages.

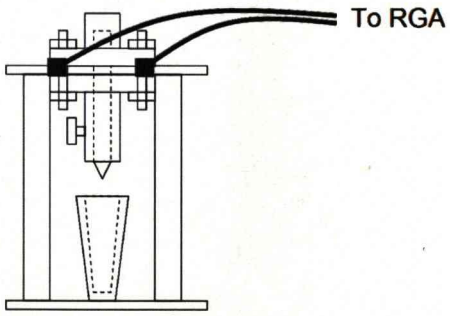

Figure 3.9 illustrates the positioning of the RGA tube inlets on the apparatus. There were three tubes (only two are shown here) and the diagram is rotationally symmetric through the electrode axis.

3.3.2 Glow Discharge Electrolysis Spectroscopy

When large concentrations of a salt was dissolved in water or a solid (like sandstone or bauxite) left to stand in water under the live copper-rod electrode (see figure 3.10), the gases produced were assumed unsafe and as a result the plasma was contained in the elbow-shaped rig. This rig was sealed. The elbow-shaped rig has an internal volume of 2070ml and the copper rod and PTFE shaft (insulating the copper rod in figure 3.10) occupied a volume of 84ml within it. Condensation (and adverse

conduction of current away from the plasma) was not an issue on most occasions due to the internal geometry of the rig. The current usually passed between the liquid and the live electrode without finding some alternate path to bypass it.

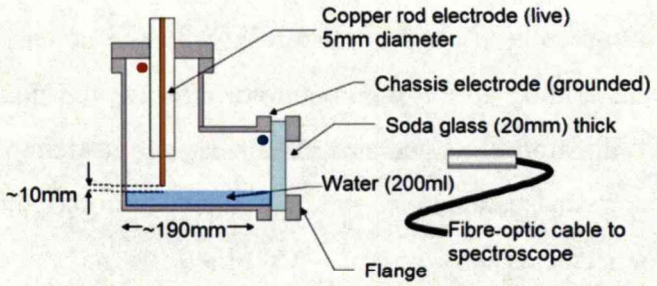

Figure 3.10 is the "Closed rig". This is an elbow-shaped experimental rig (inner volume ~ 2000ml) with fibre-optic cable leading to spectroscope of figure 3.12. In preliminary tests, rock samples were placed beneath the copper rod and stood in the water. The fibre optic cable terminal was placed ~50mm from the soda glass viewing port. The red and blue dots are the positions of the two temperature probes to be discussed later.

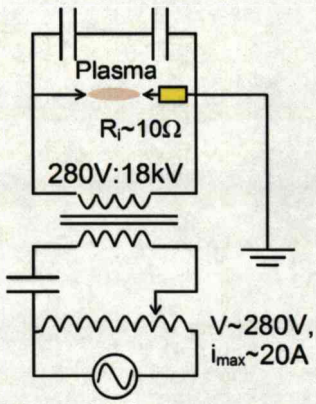

Figure 3.11 is the experimental circuit for plasma spectroscopy. It is similar to previous circuits. Capacitors were used in place of resistors and a transformer with a lower turn ratio used. These measures were taken to maximise plasma current and spectral intensity.

Capacitors were used in place of resistors in parallel to the plasma because at the low frequencies at which the experiment was run, they yielded larger impedances than their resistive counterparts. Passing as much current through the discharge was more crucial than obtaining a high level of accuracy for current and voltage in these particular experiments.

Calorimetry was not the primary aim of GDE experiments. The experiments aim to provide conclusive evidence of the migration of aqueous species from the liquid electrolyte into the plasma column. To achieve this, as much current must be supplied to the plasma as possible. A capacitor was also placed on the primary circuit because during experimentation, the circuit was drawing currents in excess of the fuse rating. These were used for the following experiments unless and until otherwise stated. A transformer with a lower turn ratio was used as it allowed higher plasma currents at only a few kilovolts (opposed to eighty kilovolts previously made available in the DBD experiments of chapter two). The transformer used was an 18kVA TEC (Transformer and Electronics Company) high-voltage transformer. The same Hewlett-Packard oscilloscope was used here as referred to in chapter two.

The closed rig was used in case there may be hazardous substances produced. In addition, spectra were taken during tests where tap water or low salt concentrations were used from the open rig (See figure 3.8). The experimental setup was virtually identical to that shown in figure 3.10. The only exception was that the elbow-shaped rig was replaced by the "open rig" illustrated in figure 3.8. The following data regarding the technical features of the spectroscope are taken from the Engineering and Physical Science Research Council's (EPSRC) engineering instrument pool website.

The spectroscope operates with a diffraction grating. A charged coupled device reads the spectral lines. Certain chemical elements radiate light at well known wavelengths and by analysis, plasma chemical composition can be deduced. The Princeton Instruments system includes 3 cameras, a PG-200 pulse generator, an ST-138 controller (spectroscope-CPU interface in figure 3.12), a 320 PI spectrometer (spectroscope in figure 3.12), an optical fibre and a PC. The spectroscopy kinetics CCD camera with 1024 x 256 (pixel) and Imaging/spectroscopy intensified CCD camera with 512 x

512 chips were used. The CCD detectors are sensitive in the range, 300nm -1000nm

The camera was designed for fast spectroscopy and involved the masking of all the rows of the chip except one, which is exposed to the light for a pre-set time. This can be varied from the microsecond range upward to milliseconds. After this exposure the data in the exposed row is transferred rapidly downward behind the mask. In this way, up to 252 rows of time resolved data can be captured before the chip is full. It is then read out in a much longer time before the camera is ready for the next set of data. In this way, transient spectra may be captured and stored. Software enables the captured spectra to be displayed and read out for further analysis.

The ST-138 Controller has two A/D converters allowing the conversion of analogue signals from the camera to be converted to digital signals sent to the PC, via an RS232 link. 16 bit data acquisition is possible at speeds of up to 430 thousand pixels/second and is fully controlled by the computer provided.

The 320PI Spectrometer obtains light through a slit at the front. The light is collected by collimating mirrors. It then strikes the grating and is dispersed into individual wavelengths which are then re-imaged in the CCD camera, which is coupled to the exit port of the spectrometer. An optical fibre can be connected to the opening slit of the spectrometer to allow more flexible positioning of the system. When the computer has collected the required data, the gathered information can be analysed within the software provided.

Prior to experimentation, the wavelength of the instrument was calibrated with a mercury-argon lamp. Absolute intensity was not calibrated as there was no requirement to measure absolute spectral intensity. A program was

written however by the camera's producer to adjust relative intensities according to the wavelength dependent sensitivity of the CCD chips. This program was used wherever necessary and its output is labelled in the thesis as "corrected" spectra (A calibration-curve is presented in appendix 3).

The experiment proceeded as follows; small capacitances capable of withstanding high-voltages were placed in parallel with the plasma in order to shunt as much current as possible through the latter, thereby making it more luminous.

The optical fibre was placed at a safe minimum distance from the discharge. 40ml of filtered water was used to fill the ceramic vessel in the "open rig" experiments depicted in figure 3.8. Approximately 200ml of filtered water was used in the "closed rig" depicted by figure 3.10.

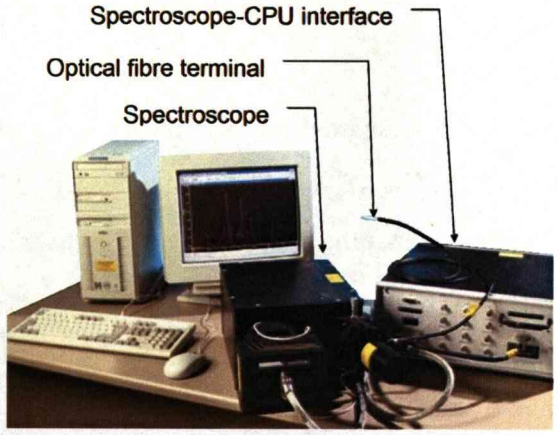

Figure 3.12 shows the apparatus required for spectroscopy. All electrical equipment was hidden behind a metal screen to protect the hardware from interference from the plasma. Only the optical cable was exposed to the plasma.

The voltage was raised from the mains by a Zenith Electrical Company LTD Variac (230V output, 5-7kVA power rating and fused rated at 20amps current). A corresponding transformer output voltage was supplied

to the apparatus (2kV). An extremely low current (~10mA) was measured flowing through the discharge.

Using the program on the CPU connected to the spectrometer, readings of varying exposure durations were taken. Multiple exposures were taken during the period of the voltage wave-cycle (20ms) in order to observe the spectral development of the plasma with time as well as its overall luminosity fluctuation integrated over all wavelengths. The light emitted from the discharge was observed in a darkened room (for long exposures). For short exposures darkening the room proved inconsequential.

These processes were implemented for rock samples, situated in water as well as for dissolved sodium chloride, filtered and unfiltered tap water. Under the high temperatures generated by the plasma and the chemical activation of airborne species, the use of distilled water would be unnecessary (nitric acid formation).

3.3.3 Glow Discharge Electrolysis High Speed Photography

Water plasma possesses many interesting properties. Although it may be spectacular to observe with the human eye, high-speed recordings can give a more detailed insight into the discharge mechanism. Photographs of the open rig inserted into a large transparent vessel were taken (ceramic or PTFE container removed). The purpose of this setup was to see as much as possible of the plasma; from the structure of the water below to the formation of the plasma near the electrode above. The water was grounded on all legs of the rig so that there was no obvious preferential path for the current to take underwater and for the plasma to be affected by the current flow.

Sodium chloride was added to the water to observe the effect of high-voltages on different electrolytes. The container was sealed in this case.

The camera was run at 125 frames per second. A higher frame-rate was available however this provided the clearest view of the electrodes and relative positions. High frame rates result in short exposure durations and darker images. The electrolyte, plasma or electrode cannot be distinguished from these images so they were not included. The camera was situated approximately 1.5m away from the discharge and at 45 degrees (as seen from the photograph of figure 3.13) from the electrode axis (the red line of figure 3.14).

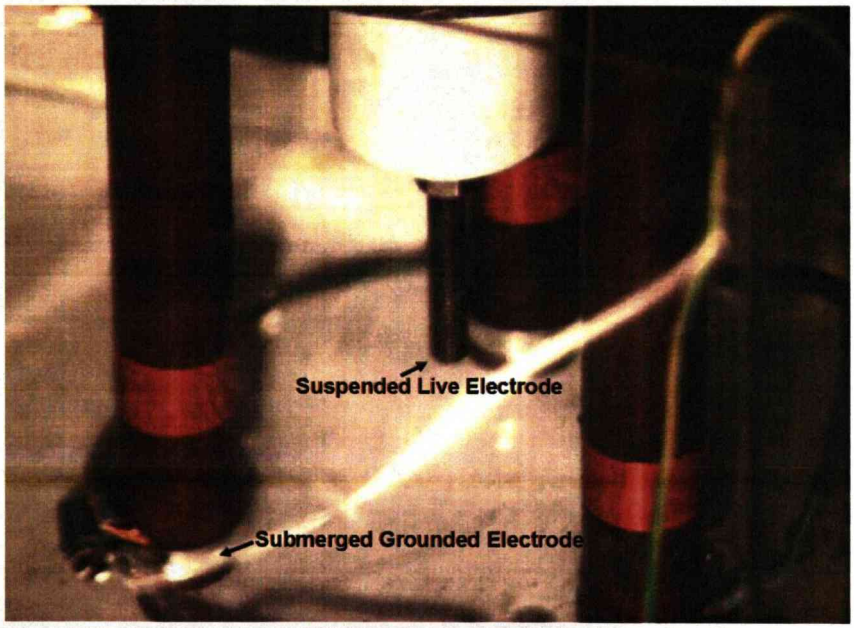

Figure 3.13 is a photograph of the high-speed photography water plasma apparatus; Constructed for enhanced visibility. The suspended electrode is clearly labelled and one of the three submerged grounded electrodes is labelled.

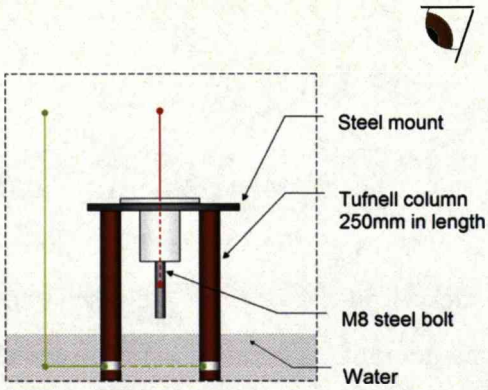

Figure 3.14 is a diagram (profile) of figure 3.13. Note that figure 3.13 is a photograph taken from the high-speed camera itself at a similar angle to that of the experiments. The position of the camera (~1.5m away from the discharge gap and ~45^0 from the electrode axis) is indicated by the "observer's eye" in the top right-hand corner of the diagram.

3.4 Results

With an initial electrode tip to water level separation of 14mm, a ~2kV potential difference was applied to the apparatus photographed in figures 3.5-3.9. The observed current was ~10mA. The relative abundance of gases and vapours with different mass-to-charge ratios was observed and recorded. There was a significant peak at A.M.U:e 49 however there was no strong corroborating evidence to positively identify the species responsible. Further discussion of the find is featured in the discussion section of this chapter. The RGA data are classed as "findings" as no completely convincing "result" was found.

The graph of figure 3.15 displays the mean intensity of plasma spectra with respect to time. The mean intensity was the arithmetic mean of the intensity values between 300nm and 800nm for one shot or spectral capture (see figure 3.17). Although this value also depends on the spectral response of the CCD unit, only its relative change with other mean intensities is of importance. The water plasma spectra were taken once every 4ms and the mean intensity of each spectrum was taken and plotted against time. A spectrum consists of 1024 data-points. Each point consists

of an intensity and wavelength reading. For any given spectral capture, the arithmetic mean of 1024 intensity readings was found. This process was repeated for each spectral capture (shot or exposure). Each exposure was approximately 4ms with the shutter opening and closing times being a few microseconds. Shutter timing therefore had a negligible effect upon recorded spectra. The graph data points are separated by increments of 4ms parallel to the horizontal axis. From this it can be seen that the period of intensity is half that of the applied voltage and the odd maxima are more luminous than the even between 450ms and 800ms (see the graph of figure 3.15 and figure 3.27). The flat line on the left of the plot indicates the pre-ignition stage. After re-ignition the relative intensity varies producing rapid oscillations at a set period. The trend-line (set to the same period as the applied voltage) increases steadily during the 1-second period. The variation in intensity may also indicate a change in the plasma properties such as the size of arc-column and discharge current.

Uncertainty bars were not added to this graph as they were very small and would cause some confusion. Each data-point had a maximum uncertainty of $(\pm 0.0296 \text{ relative intensity units})$. The graph is of observational value and does not present absolute intensity. Relative scales for the non-RGA graphs are always the graphical value divided by a suitable point (which was usually the maximum displacement from the x-axis on non-discontinuous plots). The relative scale was used because absolute intensity is a function of the positioning of apparatus, electrode separation and other parameters. Temporal relations are of interest and so relative intensity sufficed.

Figure 3.16 is a table of photographs of aqueous sodium chloride GDE. Here periodicity (of colour) and spatial resolution are displayed from photographs taken every 4ms. There is an interval of inactivity (where no luminous phenomena is observed) every 20ms (28, 48, 68, 88, 108, 128,

148 and 168) ms (this is the period associated with applied frequency of 50Hz). This indicates that inactivity occurs once every cycle and not each time the current is zero. There is an orange afterglow succeeding every white flash (indicative of the presence of sodium. See frames 4&8, 32&36, 52&56, 72&76, 112&116, 136&140 a well as 152&156 of figure 3.16). Careful inspection reveals that there is a white flash, orange afterglow, white flash and orange afterglow then an interval of inactivity. Symmetry would suggest that there is a white flash, orange afterglow and then an interval of inactivity followed by a white flash, orange afterglow and interval of inactivity. This was not observed. Current occurs when the voltage magnitude is nonzero. The magnitude of a sinusoidal voltage input should have twice the frequency of a sinusoidal voltage input. The discharge mechanism therefore favours one polarity of the voltage cycle over another. This phenomenon of reduced frequency is represented in the oscilloscope traces of figure 3.24 and figure 3.25. The dark frames (interval of inactivity) succeed the extinction of the orange afterglow. The nature of the white plasma, orange afterglow and electrode polarities will be discussed conclusively later in the chapter when further supporting evidence is presented.

Figure 3.17 is an overlay of water plasma spectra from the open and closed experimental rigs (see figure 3.8 and figure 3.10). In this case a single spectrum was taken from each experimental rig (open and closed). The spectra have been left uncorrected (differing sensitivity of the spectroscope to different wavelengths) in order to display raw data only. The open rig spectrum is less smooth with several predominant peaks (To be identified in the next paragraph). These arose due the unavoidability of plasma contact with the ceramic container (causing the excitation, de-excitation and spectral emission from elements that are not native to tap-water in detectable quantities). Another explanation of the formation of spectral

peaks can be the excitation, de-excitation and subsequent spectral emission of elements (atomic radiators) native to tap-water and air. The case that is true in the present work will be deduced shortly. In the open rig, the light produced is free to reach the spectrometer. For the closed rig the spectrum is relatively smooth. The enclosed apparatus allows water vapour to accumulate and this acts to increase the optical thickness of the medium between the plasma and the spectroscope. The fine detail of the atomic spectra may become obscured by absorption. The closed rig also has the benefit of excluding all objects from interacting with the plasma except for the water, the air and the copper electrode (see figure 3.10). The spectra of figure 3.17 were taken directly without much data manipulation except for the removal of the background spectrum which is a simple matter of subtraction applied in all electronic data presentation methods (all reported data underwent the subtraction of background or noise readings). The similarity in relative intensity for closed rig and open-rig spectra comes about due the method of calculation of relative quantities (In this case it is the division of spectral intensities by the maximum spectral intensity for any given spectral profile).

The graph of figure 3.18 shows the spectra (corrected to account for the differing spectral sensitivities at varying wavelengths) in terms of emitted photon energy (as opposed to wavelength) and relative intensity. This was done to illustrate the de-excitation photon energy of the water plasma or bremsstrahlung cut-off energy. It was found to be ~3.8eV. Other factors such as the optical thickness of the plasma may be responsible for the observed cut-off or absorption at certain photon energies however inspection of the graph's open spectra suggests the existence of ionised elements. The reasoning behind the presence and detection of ions will be discussed shortly. The single-digit numbers (1-9) represent the most likely element associated with the peaks they occur at. In order of appearance

they are **Al(1)**, **Si(2)**, **N^+(3)**, **Si(4)**, **Si(5)**, **O^+(6)**, **Cu^+(7)**, **O^+(8)** and **Cu^+(9)**. The jade-coloured numbers are indicative of elements observed exclusively in the open rig (silicon is prevalent in the ceramic container and the electrode was composed of aluminium). The blue numbers represent elements observed exclusively in the closed rig (copper electrode) and the orange numbers represent elements common to both configurations (oxygen in the water and from the atmosphere). The NIST database as well as Griem's book on plasma spectroscopy were used to identify the peaks with the most abundant elements in the experimental setup.

Returning briefly to figure 3.5 and figure 3.6, it can be seen that the more-strongly ionised plasma (RMS Current twice as large as with water-electrode plasma) appears conical in geometry as compared to the weakly ionised plasma which appeared cylindrical. Casting our minds back to the sparkplug featured in chapter 2, figure 2.1 (the copper electrode of the closed rig experiments in the present chapter) it should be noted that the copper shaft was ~5mm in diameter. The electrode "tip" was rounded (due to melting) but the plasma generated between it and the water was a cylinder (much like in figure 3.5) of diameter ~10mm. Ionised copper (as observed in the closed rig) would be located near the electrode. It would most likely be located near the centre of the discharge and along the electrode axis. The axial distance from the live suspended electrode to the water-surface is the shortest length of the discharge gap. Charged particles will most likely be situated near the axis as this is where the electric field is strongest. This means that the luminous volume of neutral gas would surround the ionised species (see the difference in plasma geometry and volume between figure 3.5 and figure 3.6). If the plasma were optically thick (at the wavelengths copper was observed, 440nm-520nm or in terms of photon energy; 2.8eV to 2.4eV) then the copper ions would not be

detected (especially since the light must traverse the several centimetres of water vapour (see figure 3.10) before being detected.

The water plasma was therefore optically thin in the photon energy range depicted by the two red dots on the graph of figure 3.18 (their co-ordinates are marked in red also). The 1.92eV point in the spectra may represent an electronic state for the water molecule and will be discussed in further detail in the analysis section. The humid environment of the closed rig (trapped water vapour in a ~2000ml vessel) did not prematurely attenuate the light (at lower wavelengths) as the two plots of figure 3.17 coincide at zero relative intensity.

The graph of figure 3.19 shows an overlay of the closed rig spectra. The purple plot is corrected and the blue plot is uncorrected. The correction was mentioned earlier and refers to the wavelength related sensitivity of the spectroscope. Two blackbody curves were fitted to the data for spectral peaks corresponding to 3900K and 5000K temperatures. These would apply if the plasma were optically thick however the limited range of the spectroscope prohibits knowledge of the fits over the complete electromagnetic spectrum. Conversely, two red dots were highlighted and their co-ordinates revealed on the smooth tail of the corrected plot. These do not represent the two dots on the graph of figure 3.18. Different sets of dots were used to derive electron temperature from the bremsstrahlung process. This is (as well as recombination) typified by the smoothness (continuum) of the spectral plots.

The graph of figure 3.20 displays $NaCl_{(aq)}$ electrode plasma spectra from behind a soda glass window. Spectral lines were identified by the numbers 1-10. Numbers 1,2,4,5,6,7,8 and 10 are atomic sodium lines. Numbers 3 and 9 are ionised sodium and atomic chlorine respectively. The appearance of strong spectral lines from ~325nm to ~440nm supports the claim that the

water plasma and the closed rig are optically thin at this wavelength range since the relative intensities of the lines are comparable to the sodium D-lines. Spectral lines are emitted at wavelengths less than 400nm and these UV photons can be detected by the spectroscope. This observation also re-enforces the fact that there is maximum de-excitation energy or cut-off wavelength observed in figure 3.17 and figure 3.18 and that it was not an artefact of the spectroscope or due to the UV light being blocked by the soda glass (which could only be the case for the closed rig experiments). The graph of figure 3.21 focuses on the sodium D-lines previously shown in the graph of figure 3.20. The green and orange lines refer to lower and higher applied voltages respectively.

The legend of figure 3.20 indicates the lines observed at lower and higher voltages. These low wavelength (green on the graph) spectral lines did not occur often enough to note the corresponding voltage at their appearance however the approximate operating range was 10kV to 15kV prior to ignition and ~2kV to 3kV for sustaining the discharge post-ignition. Figure 3.21 displays the shifting and broadening of the sodium "D-lines". The multiple curves comprising the graphs of figure 3.20 and figure 3.21 each represent an acquisition of spectra at different exposure durations. Since the intensity and specific form of the spectra varied from one acquisition to another without any clear trend reflecting exposure duration or input voltage, the curves were simply overlaid to illustrate the raw data. Several factors may contribute to this but it was found that the Stark shift and Doppler broadening were not realistic candidates for this phenomenon (the former produced unrealistically low temperatures and the later produced unrealistically high temperatures). The vast quantities of water molecules (highly-polar) amongst the radiating sodium atoms may behave as charge-centres obscuring the effect of ions in the plasma (making pressure-broadening calculations untrustworthy). As a result, a direct measurement

of gas temperature remained elusive and was inferred from the electron temperature deduced from figure 3.18, figure 3.19 and the observed temperature within the closed rig.

The basic observable properties of GDE under atmospheric pressure in the apparatus displayed in figure 3.9 (open rig) were calculated and presented in figure 3.22 and figure 3.23. The RMS voltages (between the live and submerged electrodes) and currents (through the plasma) were calculated automatically by the oscilloscope and displayed in figure 3.22. The physical data obtained in experiment was observed, recorded and summarised. Here, changes in electrolyte's temperature, pH, and volume are displayed as well as the duration of the experiment. Experiments with the closed rig detected temperatures within the rig exceeding 1500K at 200mm above the discharge and near room temperature ~310K at 200mm horizontal displacement (See figure 3.10's red and blue dot respectively). This indicates that there is convective heat flux upwards. The electrolyte became acidic, and partially vaporised. Naturally its temperature increased also (measurements made by a "K-type" thermocouple). Acidification was most likely due to the presence of water, nitrogen and oxygen at high-temperatures.

In light of these observations, it was indicated from the tables of figure 3.22 and figure 3.23 that the maximum possible energy (deduced by the product of RMS voltage, RMS current and experimental duration) supplied by the electrical power source was a few times less than the minimum required energy to arrive at the thermodynamic states indicated by the table of figure 3.23 (under constant atmospheric pressure). It should be noted that there are large current uncertainties as given in figure 3.22 and this effect is better studied with the apparatus of the next chapter due to its calorimetric design. The large uncertainties in current casts doubt upon the statistics and accuracy of the observation made here. The previous

paragraph further supports the argument for the energy imbalance. The last column in the table of figure 3.23 finds the sum of energy required to heat the water that remained in the ceramic container, the amount required to heat the missing liquid to the boiling point and the amount required to change its phase from a liquid to a gas. This is the minimum required energy to obtain the temperature and volume changes reported in the table of figure 3.23. It does not account for the heating of the vaporised water past the boiling point to temperatures exceeding 1500K! Possibilities for this apparent excess heat will be analysed and considered in the following sections.

The oscilloscope records of figures 3.24-3.26 are not taken from the detailed experiment using the RGA, spectroscopic or photographic equipment. They nonetheless are representative of GDE and can be used with the evidence above. They came from the trial tests and in particular refer to the apparatus labelled (a) and (d) of figure 3.2. These trials were done using a signal generator, and audio amplifier connected to the high-voltage transformer previously mention in this chapter. The variac was replaced and voltage was controlled using the former two devices. Frequency and voltage amplitude were varied to observe the behaviour of the water plasma.

The observations were carried out with 1kW and 500W power-supplies. The cells of figure 3.2(a) and figure 3.2(d) were filled with drinking (tap) water and ~10mm and ~5mm air gaps were observed. In the situations where liquid water did not bridge the gap, a purple (noisy) filamentary discharge was observed (similar to the dielectric barrier discharges of chapter two). These were quickly succeeded by a diffuse (quiet) orange flash discharge. For example, with a frequency of 0.24Hz (obtained using a signal generator), the discharge period was ~4 seconds. Less than a second after the filament was seen and heard, the orange diffuse flash was

observed. This occurred when 500W of power was available. In the case where 1kW was available at 50Hz the orange flash and filament was replaced by white, jade or blue steadily glowing plasma (these colours would occur spontaneously for the water-plasma without any applied changes by the experimenter). Figure 3.26 shows that the discharge currents (negative or positive) favour negative voltage polarities. The voltage waveform is distorted from the original sinusoidal input signal. Positive and negative voltage polarities occur in close succession (filamentary and orange flash respectively).

3.5 Analysis

3.5.1 Plasma Luminosity

Water plasma spectral intensity variation with time was measured inside the closed rig using the spectroscope on 4ms exposure for a series of exposures. The typical discharge gap was ~10mm. The enlargement of the graph of figure 3.15 in figure 3.27 shows the mean spectral intensity (across the near UV, visible and near IR wavelengths). The intensity was not absolute but this was not required. The relative variation with time was plotted in figure 3.15 and explained in further detail in figure 3.27 and its accompanying caption. The voltage is the principle driving agent that heats and subsequently illuminates the plasma. The discharge preferentially emits light due to one voltage polarity at certain durations (after these durations the luminosity is indistinguishable between polarities). On the opposite polarity, less light is emitted yet this still exceeds the minimum intensity corresponding to zero driving voltage. Figures 3.24-3.26 support this finding at lower frequencies (orange flash and purple filaments at lower power levels).

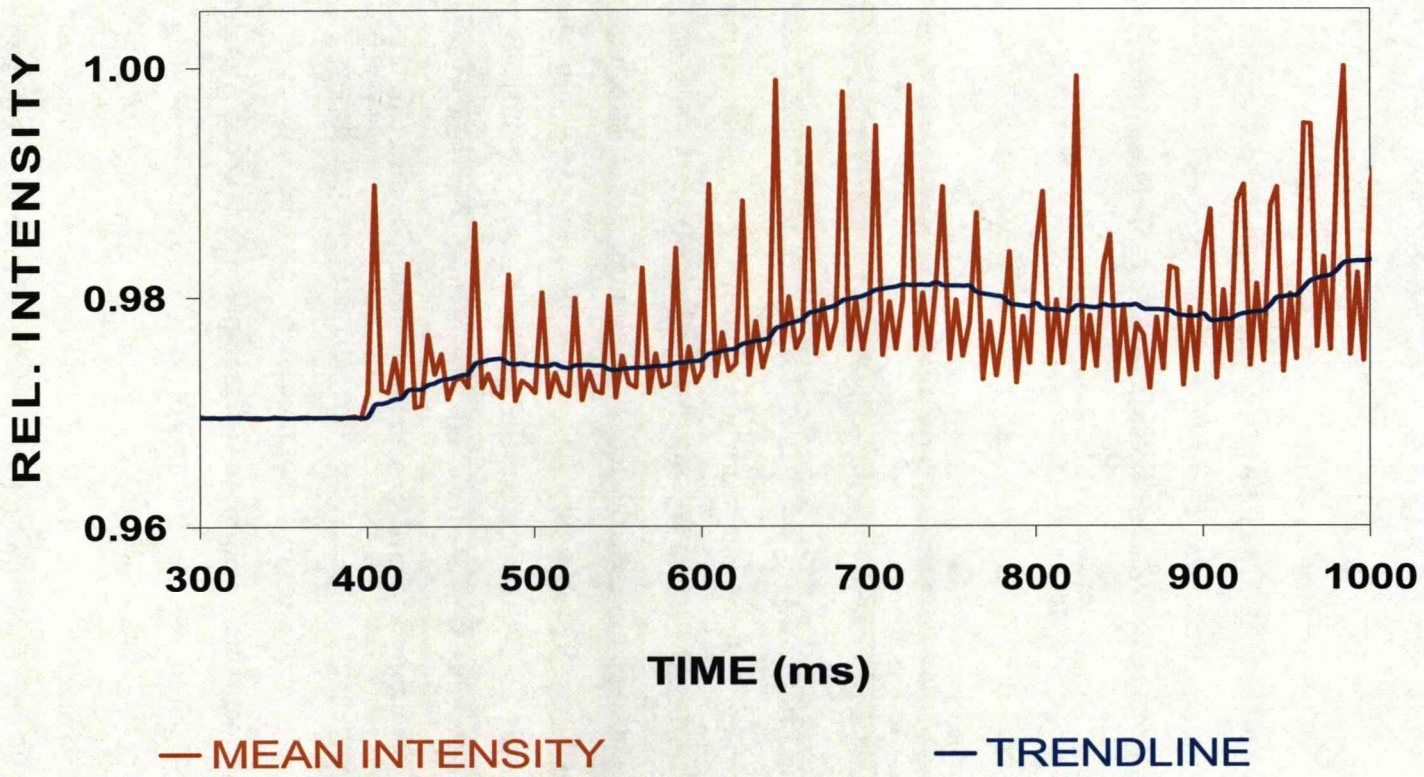

Figure 3.15 shows the variation of mean intensity over visible wavelength range for the water plasma against time. See figure 3.27 for more details. Each data-point is separated by a 4ms time interval. Note the alternating intensity spike magnitudes between 450ms and 800ms. Since these occur at 20ms intervals with a voltage frequency of 50Hz it is clear that intensity favours voltage polarity (at least in this limited duration). Before 450ms and after 800ms the intensity spike magnitudes are less different.

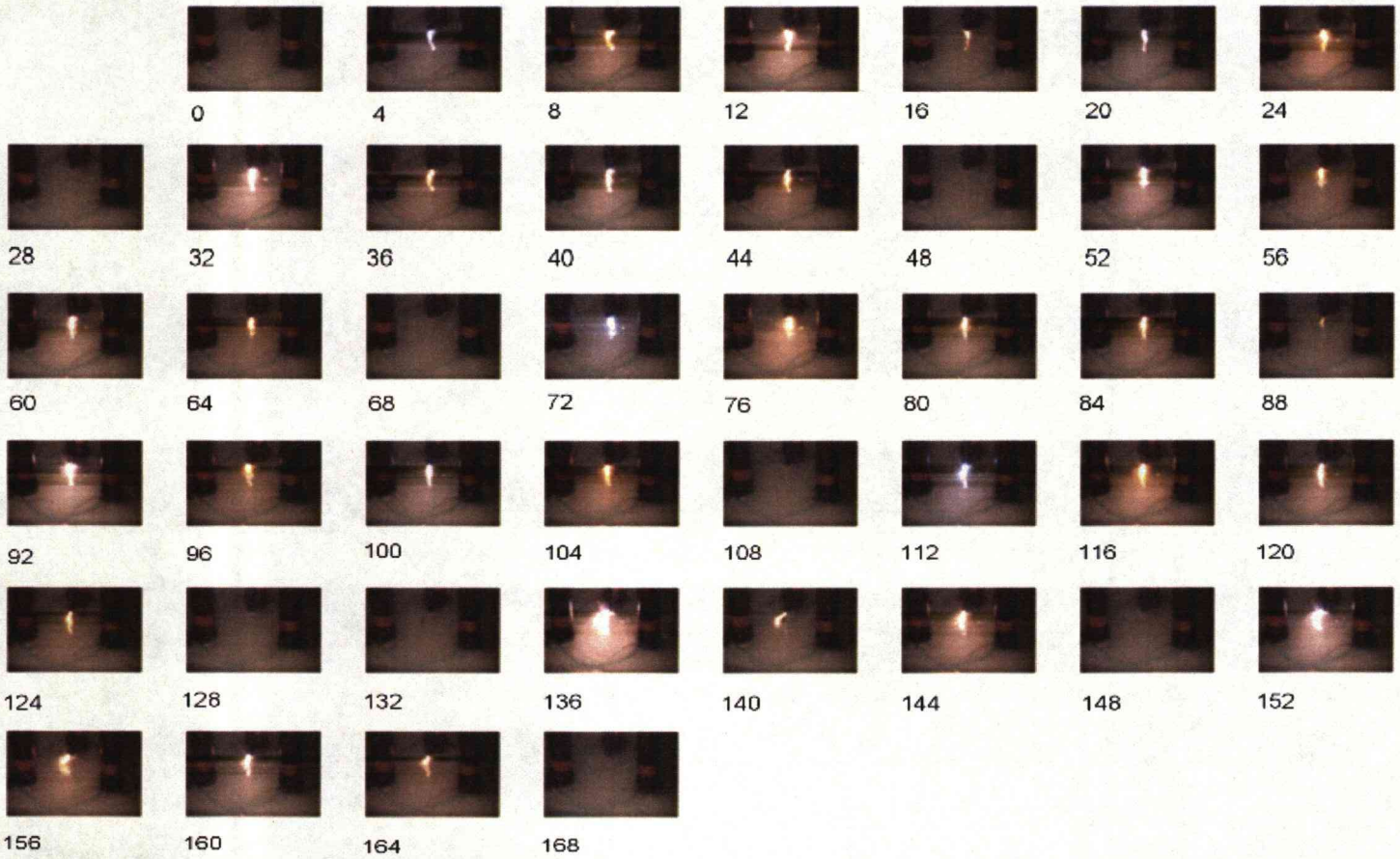

Figure 3.16 are photographs that show the periodicity of the aqueous sodium chloride-electrode plasma. Numbers indicate time elapsed in milliseconds.

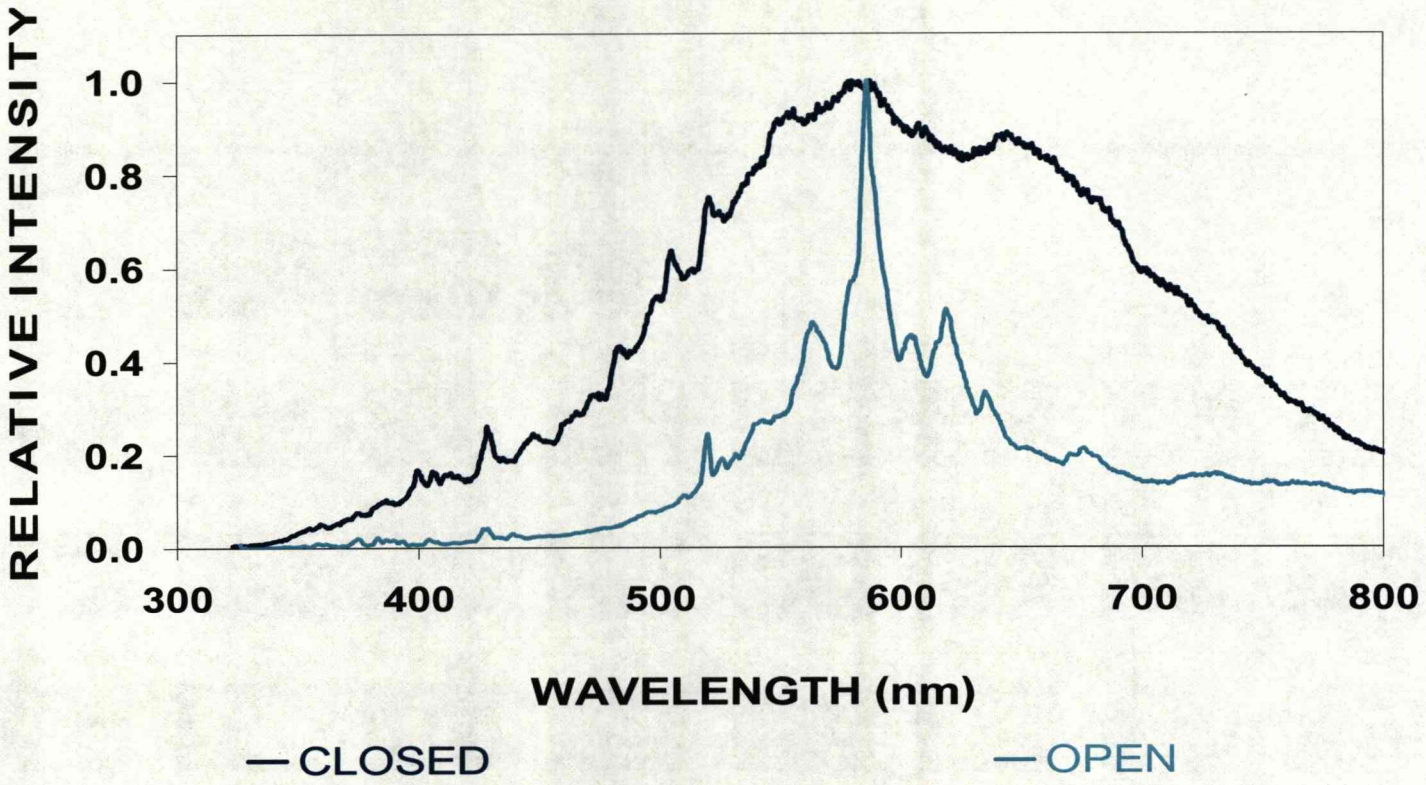

Figure 3.17 is a graph illustrating the water plasma spectral intensity against wavelength for closed and open rig GDE experiments. Typical exposure times are 1 second to 100 milliseconds. These two plots have the same exposure time but were scaled to the same set of axes.

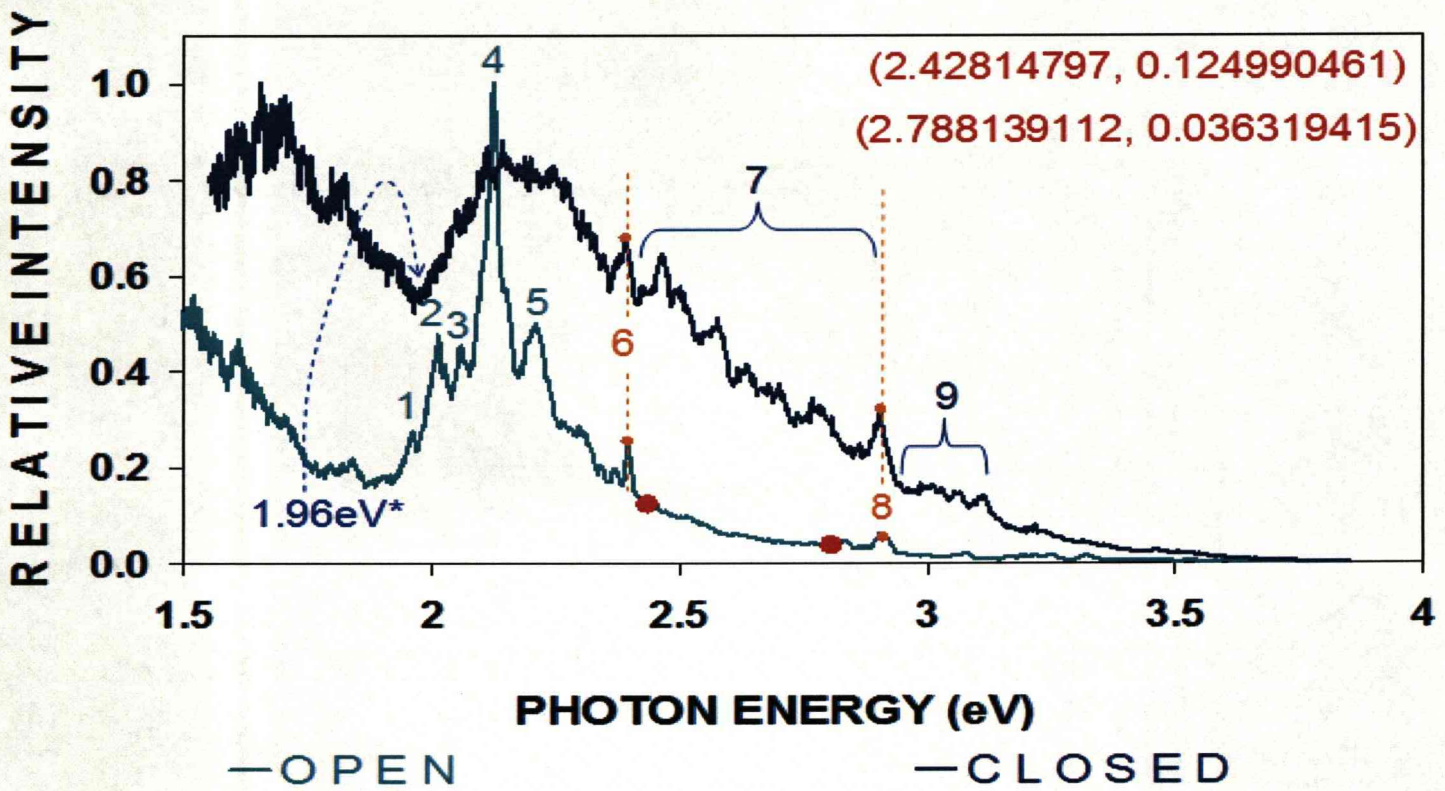

Figure 3.18 is a graph of relative intensity versus plasma's emission photon energies derived from figure 3.17. The open and closed rig spectra have distinct features (jade or blue single-digit numbers) of their own and share some common traits also (orange single-digit numbers and broken lines). The distinctions and similarities in spectra and experimental conditions are taken into account in this section and the analysis in detail. The single-digit numbers indicate atomic spectral lines. The two red points mark the continuum spectrum window whose co-ordinates are given in the red font on the graph.

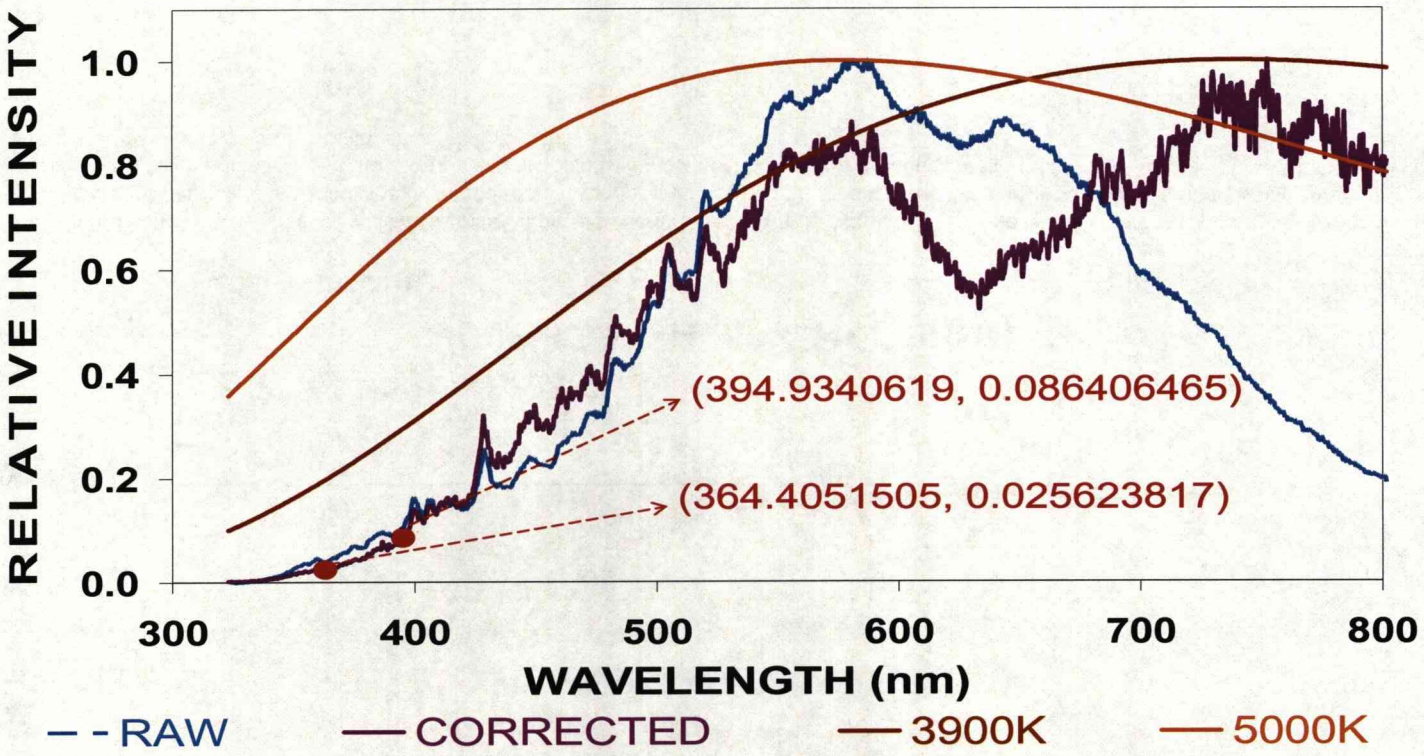

Figure 3.19 shows two plots of the water plasma intensity curves and two black-body fits. Raw data (Raw), corrected intensity sensitivity to wavelength (Corrected) and black body radiation fits at 3900K and 5000K are all scaled to the same set of axes. The continuum region of the closed spectra are bound by the two red dots.

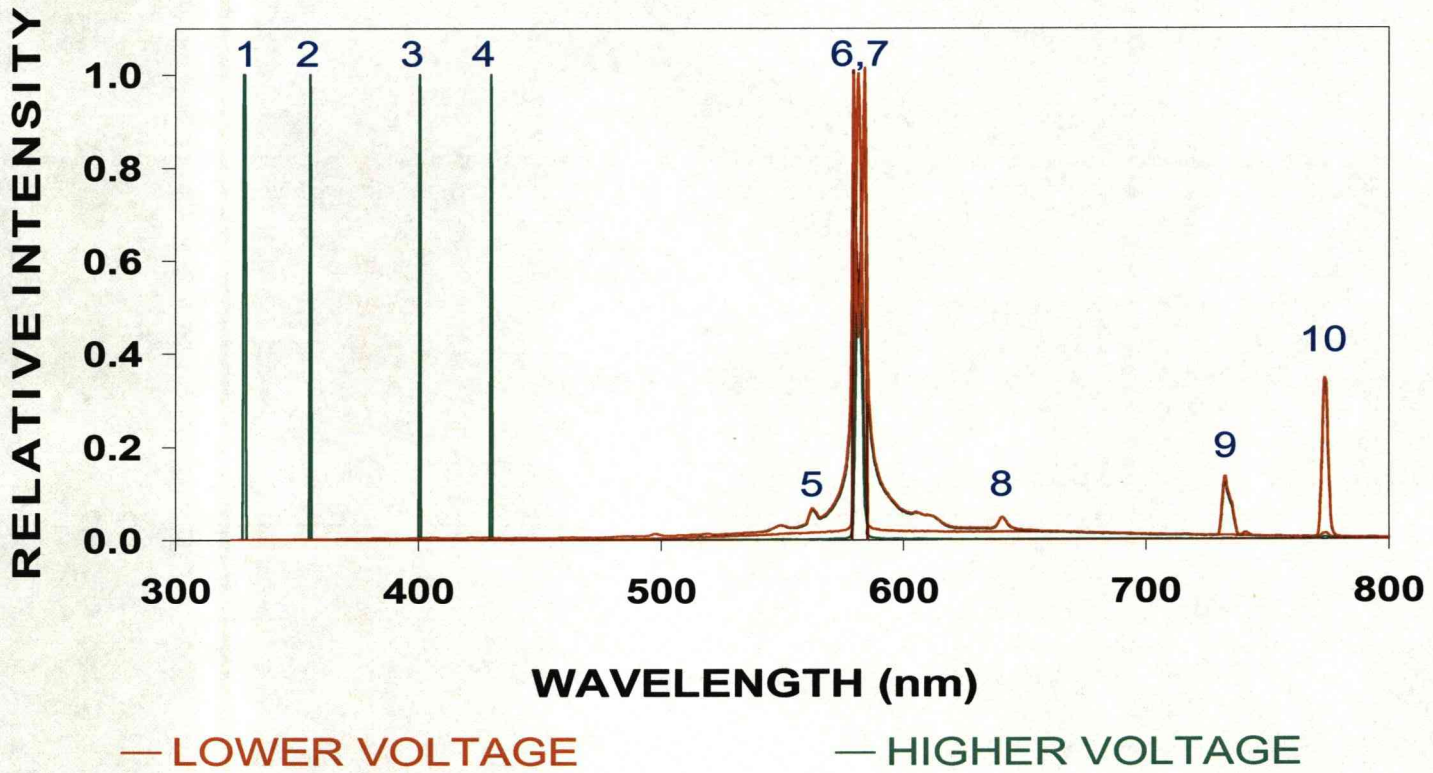

Figure 3.20 is a graph of spectral intensity versus wavelength for the aqueous sodium chloride plasma. 1,2,4,5,6,7,8 and 10 are atomic sodium lines. 3 and 9 are ionised sodium and atomic chlorine respectively. All lines are slightly shifted despite pre-calibration of the spectrometer. The multiple overlaid lines are merely multiple overlaid spectral acquisitions.

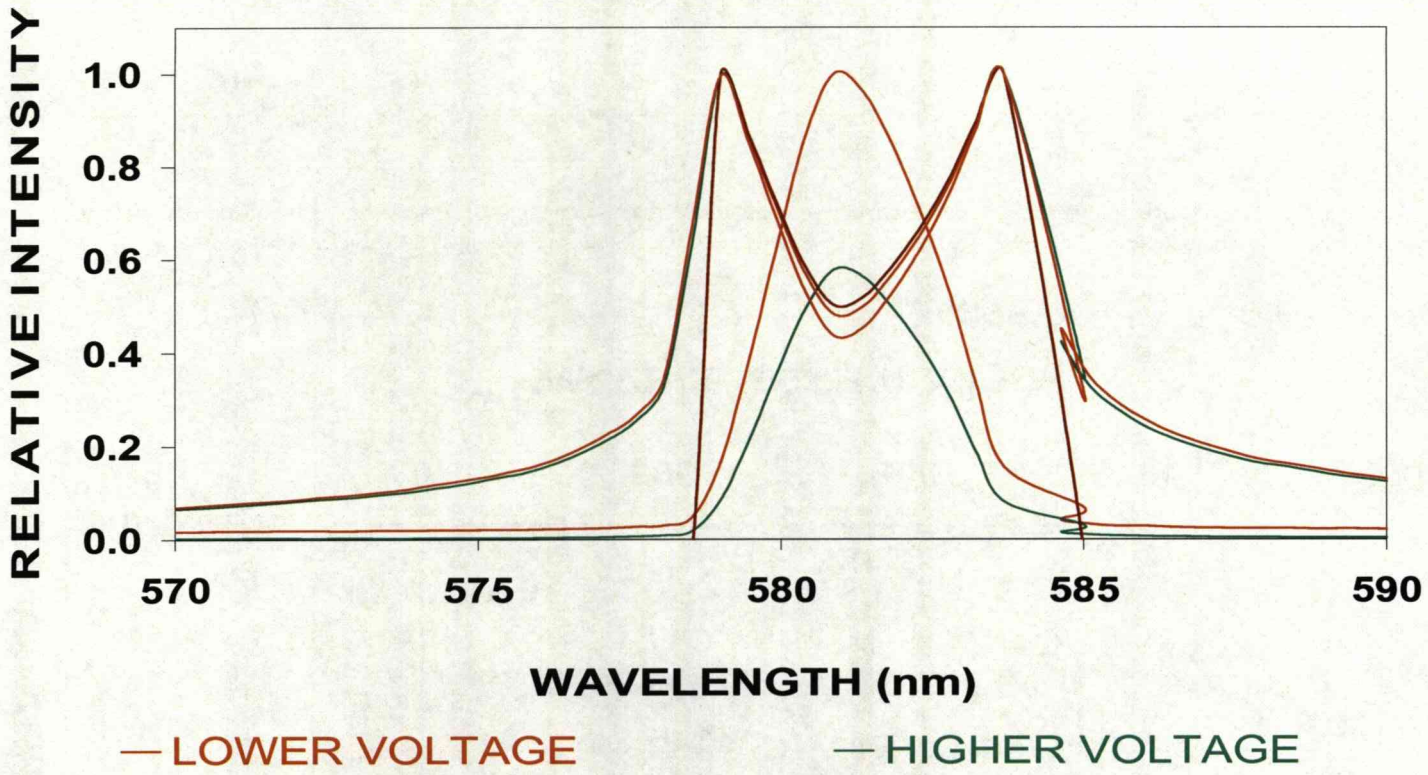

Figure 3.21 shows the broadening and shift of the sodium "D-lines". These produce unphysically high temperatures when considering Doppler broadening and unrealistically low temperatures when considering Stark shifts. Thus the above graph merely illustrates different spectral acquisitions at different times, exposure durations and applied voltages.

RMS GDE Electrical Values

V		*I*		*V - I Product*	
Value	%	Value	%	Value	%
2304	8	0.009	49	19	49

Figure 3.22 is a table of electrical values for the glow discharge. Note the level of uncertainty in red font. *V* here represents plasma potential difference. The *V-I* product is not power but is used as a dimensionally sound comparison and gauge for heating power calculations (see figure 3.23). The product is not accurate calorimetry and is only for characterisation.

GDE Physical Results

ΔT		ΔpH		ΔV (ml)		Δt		$(dU / dt)_{Min}$	
Value	%	Value	%	Value	%	Value	%	Value	%
59.7	0.8	-2.3	0.2	25.5	2.0	900	3.3	73.2	3.8

Figure 3.23 is a table of physical properties of the electrolyte supporting the glow discharge. *T*, *V* and *t* here refer to electrolyte temperature, volume and time respectively. The delta symbol prefixed to these quantities represents overall change (before and after experimentation). The pH symbol has the usual meaning and the change is negative (Acidification). $(dU/dt)_{min}$ is the minimum energy required to heat (product of heat capacity and temperature increase) and vaporise (product of latent heat of vaporisation and mass vaporised) the electrolyte. Note the factor by which it exceeds the maximum available voltage-current product supplied by the electrical power-source.

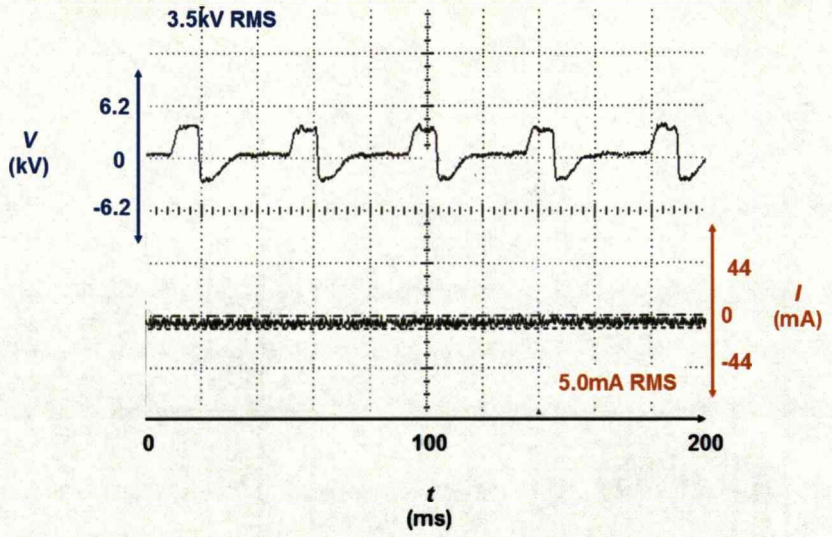

Figure 3.24 are oscilloscope traces of voltage (top) and current (bottom). The numbers on the vertical axes represent the voltage (top) and current (bottom) sensitivities. (i.e. kilovolts per division (top) and milliamps per division (bottom)) The horizontal axis represents time. The RMS voltages and currents are displayed on the plots as 3.5kV and 5.0mA respectively. The applied frequency is 23.81Hz. Note the flat regions at (40, 80, 120 and 160) ms.

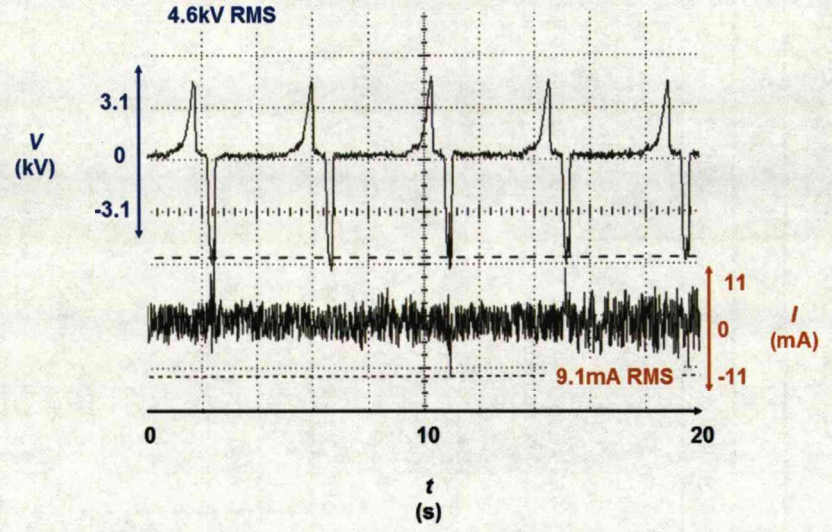

Figure 3.25 oscilloscope traces have the same layout as in figure 3.24. Voltage and current sensitivities have been increased and the applied frequency has been decreased to 0.24Hz. Close inspection reveals that the current-spikes appear only when the voltage polarity is at a minimum. Negative voltages induce discharge currents. Note the current-spikes at 2.2s, 11s and 15s. These are indicative of the filament or luminous discharge (No current-spikes, no luminous discharge). At all other times according to this waveform, the discharge gap would be dark (interval of inactivity).

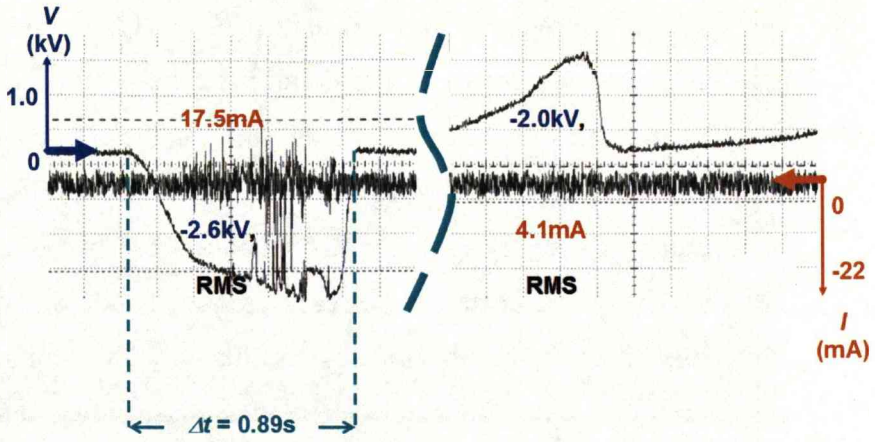

Figure 3.26 shows oscilloscope plots from the same wave-cycle, frequency, voltage and current sensitivities. The frequency is still 0.24Hz however the temporal sensitivity has been increased and the typical discharge duration (negative voltage polarity) has been labelled on the left plot. The discharge occurs and the voltage (negative polarity) increases towards zero as the current decreases away from zero (current spikes). As the gas becomes more conductive during electrical breakdown the charges flow and reduce the electric field strength so the required voltage to sustain the field is reduced (in magnitude). Negative polarity refers to the suspended electrode-water surface potential difference. In this case the suspended electrode has a negative potential with respect to the water surface.

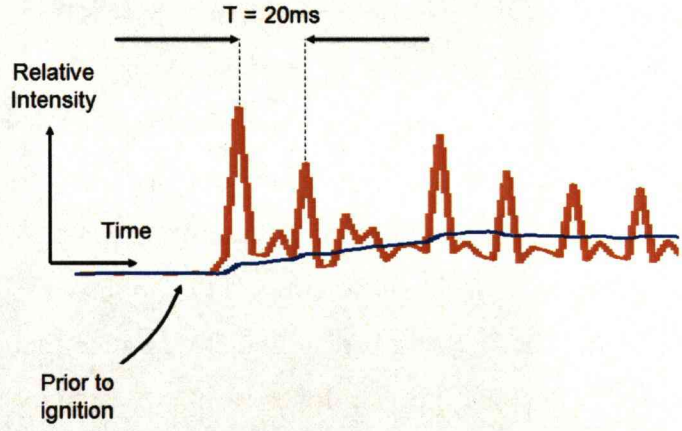

Figure 3.27 shows the orange trace was the mean spectral intensity. The blue trace was the average fit of this value produced in excel. The period of oscillation is labelled. It can be seen that the luminosity and voltage frequencies are the same and that for selected durations of time one voltage polarity produces more light from the discharge than the opposing voltage polarity. See (450-800) ms on the graph of figure 3.15. These durations occur after the initial activation (after 6th spike from the left on the above diagram) and prior to the saturation of the gaseous medium with vaporised water (t > 800ms on figure 3.15).

Different voltage polarities indicate different species of particle bombarding the water surface, producing different characteristics of plasma emission. This is the most probable explanation since discharges

between dry electrodes in steam were not observed to reproduce the water plasma. If we only focus on the column of the plasma, incandescence may be sustained by interactions of ions and electrons with neutral species or ions. The polarity reversal only changes the direction of these interactions in a spatial sense (i.e. collisions from opposite directions). The two voltage polarities in this case produce conditions of symmetry. The only asymmetry that arises is due to the composition and configuration of the opposing electrodes (suspended aluminium and liquid water).

Although from figure 3.15 and figure 3.27 it is impossible to tell which polarity produces more light, figures 3.24-3.26 from low-frequency experimentation suggest that it is the negative polarity (water acting as virtual anode). Therefore it is electronic bombardment of the water-surface that is the more luminous process (as opposed to ionic bombardment). One possible explanation is that upon bombardment, the lighter electron is more likely to excite the internal structure of the water molecule whereas the heavier ion is more likely to transfer momentum and impart translational kinetic energy to water molecules due to their similar masses. It should be stressed that in the closed units, this differing luminosity is only observed in the steady-state (not initiation conditions at $t < 450$ms) and prior to times where the activity of the discharge has populated the gas-gap with vaporised water (thus enhancing the symmetry of environments near the electrode and virtual electrode; From an initially dry gas-gap and wet virtual electrode situation to a humid gas-gap and wet virtual electrode situation. See $t > 800$s on figure 3.15).

3.5.2 Spectral Profile of the Water-Plasma

Spectroscopy revealed some interesting features of the water-plasma that will be discussed here. We refer to the graph of figure 3.18 and discuss

photon energies rather than wavelengths. The physical properties of the open rig and closed rig will be recalled in this paragraph. The spectra observed in the graph of figure 3.18 will be discussed in detail in the following paragraphs. The open rig water-plasma occurred in two regimes. Initially the virtual live electrode was the bulk of the water-electrolyte (predominantly) and towards the end of the experiment it was the moist ceramic surface. The grounded electrode was a suspended aluminium pointed electrode. Even in the water (virtual electrode regime) the discharge would impinge upon the ceramic container's rim at times (See figure 3.5 and figure 3.6). This resulted in the emission of spectral lines from materials native to the ceramic container. The closed rig housed the live (suspended copper pointed electrode) and the grounded container (elbow-shaped steel chassis. See figure 3.10). The spaciousness of its design ensured that the discharge can never be in contact with the steel (inner) walls but was always in contact with water. Unlike the open-rig, the closed rig trapped the water vapour producing a very humid environment around the discharge. Condensation occurred behind the soda-glass viewing port. Any detected light had to escape this environment first.

In ascending emitted photon energy, the open rig curve of figure 3.18 has a relative intensity of ~0.5 at ~1.5eV and then decreases to ~0.2 at ~1.8eV. This is representative of IR transitions reaching a minimum value. These transitions are caused by the change in vibration-rotation states within the water molecule. Because these transitions release visible (energetic photons), molecular (electronic) orbital (MO) transitions are also possible and likely. There are then six main peaks between 1.8eV and 2.4eV (the dominant peak being ~2.1eV). These are not consistent with the apparent trend below 1.8eV and after 2.4eV. A quick comparison to the closed rig plot ensures us that the base trends of these

peaks are representative of the water plasma (as they are common to the open and closed rig spectra. The open and closed rig plasmas occur under different conditions and impinge upon different materials. The common factor in this case is the presence of the water plasma). The peaks were identified as atomic spectra of elements native to the atmosphere, the water and the ceramic container. These spectral lines are produced by the de-excitation of atoms. The elements N, O, Al and Si have several atomic lines close to each other and they account for the width of the spikes. Lastly, beyond 2.4eV the spectrum is smooth and indicates continuum as opposed to line or band radiation (indicative of atomic and molecular emissions). Bremsstrahlung radiation mainly contributes to spectra in this range.

In ascending emitted photon energy, the closed rig curve of figure 3.18 has two peaks; one at 1.75eV and the other at 2.2eV. This may be due to absorption of IR photons (by the moisture inside the closed rig) between those energies. What it does have in common with the open rig spectra is the intensity minima at 1.9eV. This effect is illustrated in figure 3.28.

Figure 3.28 and figure 3.29 show that whatever energy-state the water molecule is excited to, it exhibits bimodal de-excitation with photon energies of 1.8eV and 2.2eV. This indicates that there is a 0.4eV energy difference between two excited states. It assumes that the 1.8eV peak is truly a peak and not just absorption at low adjacent photon energies (as suggested by the absence of a peak for the open rig water plasma spectra at this energy. See figure 3.18). This also assumes the transitions are purely vibration-rotational. If the de-excitations had an electronic component, they would occupy anti-bonding MOs and contribute to dissociation[43] and the radicalisation of the water molecule (~6eV). However the literature[44] indicates that vibration transitions produce

photons in IR to visible range (514nm). Inspection of the graph of figure 3.17 (open spectra) indicates that continuum spectrum dominates below this wavelength (smooth curve) with the exception of low lying atomic spectra below ~430nm.

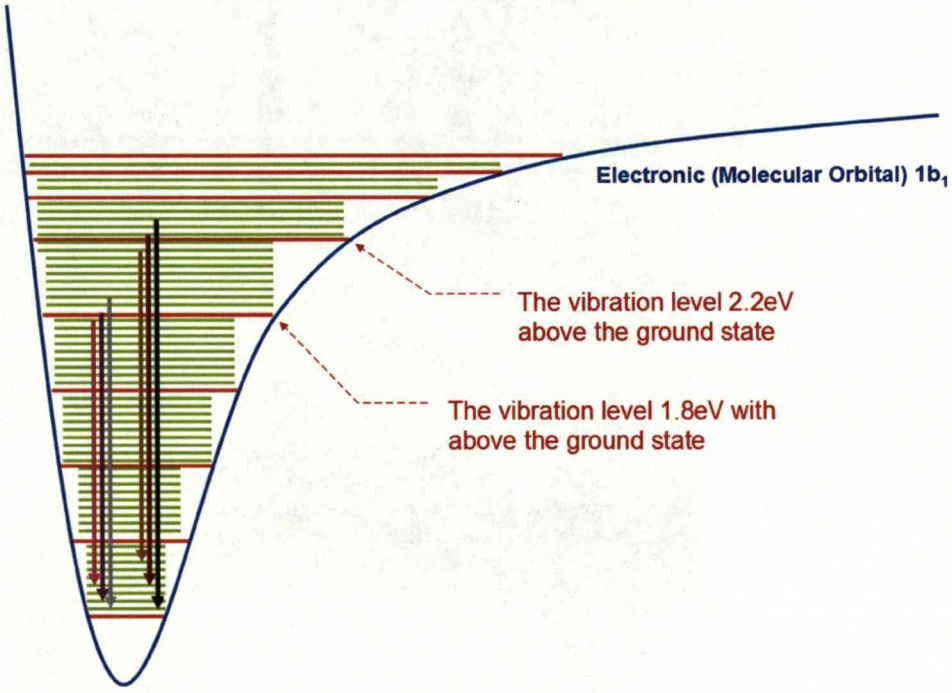

Figure 3.28 shows the blue curve as the highest populated MO in the ground electronic state ($1b_1$). The red and green lines (bands) represent vibration and the closely spaced rotational energy levels respectively. The three arrows on the left represent transitions from an excited vibration state to a lower vibration state. The three arrows on the right represent the transition from a higher excited state to a lower vibration state. The length of the arrows denotes the photon energies. Each vibration transition must originate and terminate at different rotational states with respect to the vibration level below it. This conserves angular momentum from the emission of the photon. The two groups (of three) arrows represent emission lines bunched together to form molecular bands. These correspond to the two peaks observed in the graph of figure 3.18 and illustrated in the diagram on figure 3.29.

A useful result that can be derived from the spectral profile of water in the region of the continuum spectrum is the electron temperature. This can be achieved by assuming the optical thinness of the water plasma (see earlier) and observation of smoothness in the spectral profile of water from figure 3.18 and figure 3.19 (denoted by the region between the two red dots)

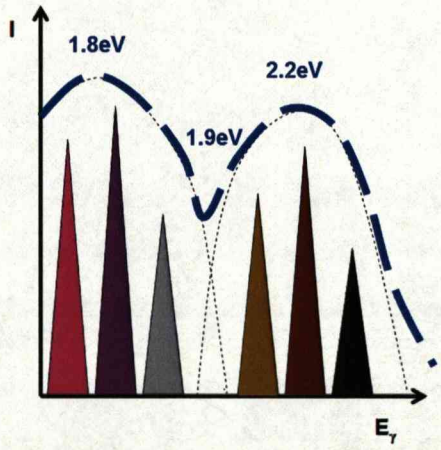

Figure 3.29 shows a representation of the double-peak of figure 3.18 for the closed rig water plasma spectra. The two peaks slightly overlap and are derived from the range of possible transitions from an excited vibration state to a lower vibration state and the transition from a higher excited vibration state to a lower vibration state. This range of possible transitions occurs (denoted by three spikes in the present figure) because of the multitude of vibration and rotation states (See the arrows of figure 3.28). As a result, bands of transition lines (three triangles in the present diagram) occur instead single transition lines (compare figure 3.17 to figure 3.20). Since two bands appear to have overlapped (indicated by the double peak of figure 3.18) then two main vibration transitions occur at optical wavelengths. The arrows in figure 3.28 correspond to the spike or "spectral lines" in the present diagram and are colour coded. The longer the arrow, the further along (to the right) it appears on the photon energy axis (horizontal). The peak photon energies are displayed (1.8eV and 2.2eV) along with the local minima (1.9eV).

$$T_e = \left| \frac{\epsilon_1 - \epsilon_2}{k_B \cdot \ln\left|\frac{I_2}{I_1}\right|} \right| = \left| \frac{h \cdot c}{k_B \cdot \ln\left|\frac{I_2}{I_1}\right|} \cdot \left(\frac{1}{\lambda_1} - \frac{1}{\lambda_2} \right) \right|$$

Equations 3.1

Equations 3.1 were taken from chapter six of the book edited by Keen on plasma physics (see bibliography). The arguments made to justify the use of this equation were made in the previous paragraphs. T_e, k_B, I, ϵ and λ are the electron temperature, Boltzmann constant, intensity, energy and wavelength respectively. The energies, wavelengths and intensities have

subscripts that refer to the co-ordinates of the two dots in the graphs of figure 3.18 and figure 3.19. The electron temperature was found to be 3,413.9K for the open rig water plasma and 1,737.8K for the closed rig water plasma. The temperature measured by the thermocouple placed ~200mm above the water plasma in the closed rig was found to reach temperatures exceeding 1,500K within a few minutes of experimentation (before the thermocouple failed). The gas temperature is often comparable to the ion temperature in plasmas under atmospheric pressure. Neither of these two temperatures exceeds the electron temperatures in the type of arrangements described in this thesis. The electron temperature gives an upper bound for the ion temperature and the failing thermocouple gives a lower bound. $T_{gas} \approx T_e \therefore T_i \approx T_e$. The water molecule is efficient at absorbing electron kinetic energy without being ionised.

3.6 Discussion

3.6.1 Residual Gas Analysis

The following section reports the RGA findings of the gas and independent Inductively Coupled Plasma (ICP) results for the electrolyte. These were not reported in the main body of the thesis for Glow Discharge Electrolysis (GDE) because there was no supporting evidence to positively identify the chemical species of A.M.U:e 49. By careful deduction it is most likely to be TiH formed by Ti from the ceramic container and H from the RGA (see chapter three).

The 44-50 AMU:e (atomic mass units per electronic charge) range was selected as it gave the most significant variation between pre-ignition, water electrode and ceramic electrode curves. The pre-ignition electrode

curve and the water electrode curve do not vary much however the ceramic electrode curve clearly distinguishes itself from the former two curves at AMU:e 49. There is much variation in the pre-ignition trend, the water trend, and the ceramic trend however the uncertainty bars only become separated at AMU:e 49. This means that with statistical consideration, a species of AMU:e 49 was observed to be produced when the wet ceramic surface was the virtual electrode. The abundance (47.2%) relative to argon in the atmosphere (whose relative abundance is 0.96%) was recorded and shown in the graph of figure 3.30.

In this experiment, GDE occurred with filtered tap water electrolyte and the RGA was set to measure and record the gases and vapours produced over three seven-minute intervals. The first occurred before the plasma circuit was activated, the intermediate whilst water was the virtual ground electrode (see figure 3.5) and the final whilst the moist ceramic was the virtual ground electrode (see figure 3.6). The electric current in the later condition doubled but this was not measured to a high degree of accuracy given the short experimental duration (rapid evaporation rates). The legend illustrates the pre-ignition, water and ceramic electrode plasma atmospheres respectively.

Finally, the species corresponding to AMU:e 49 was observed when the moist ceramic vessel was the virtual electrode. The most likely candidate was TiH (Titanium monohydride whose relative molecular mass is 49. The RGA's cracking table was consulted in addition to the periodic table). Private communications and a spectral analysis of the electrolyte by the University of Liverpool's Chemistry Department revealed the existence of light transition metals in the sample. These metals can be released when an acid attacks the ceramic container. GDE in the open rig caused a reduction of pH in the electrolyte (See the table of figure 3.23). The acidic electrolyte

attacks the ceramic vessel to release the titanium which later combines with hydrogen (abundant in the RGA or in the aqueous environment).

Whatever the chemical identity of AMU:e 49, it is more massive than the $O_{2(g)}$, $N_{2(g)}$ or even $H_20_{(g)}$ in the plasma column yet it was detected in the RGA. This suggests that GDE can release species native to the container (virtual electrode) into the gaseous phase.

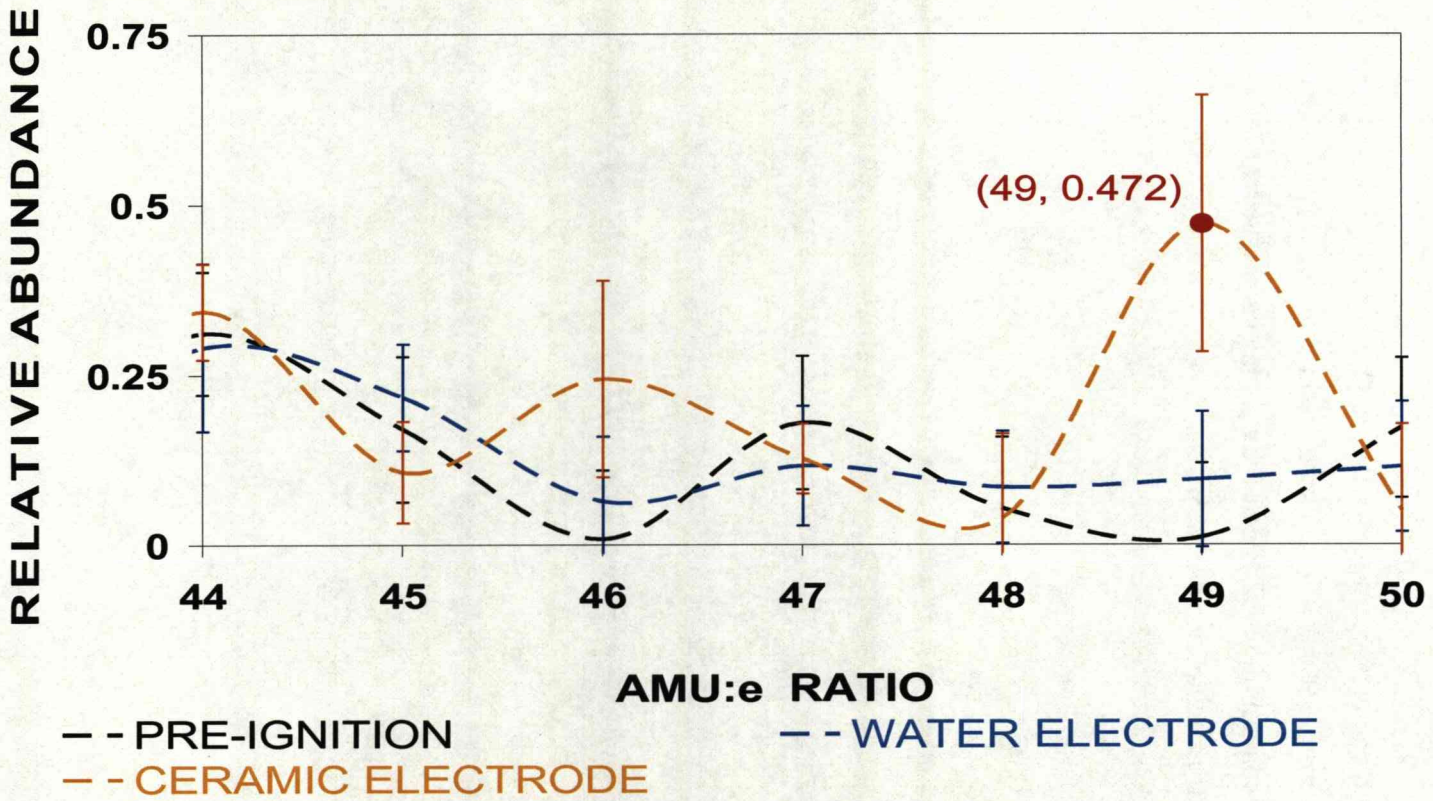

Figure 3.30 is a graph of mass-charge ratios focused upon for pre, water and ceramic plasma conditions. The peak at AMU:e 49 is most likely to be titanium monohydride from the elements available and supported by the discovery of light transition metals found by independent chemical analysis of the post-experimental electrolyte sample. The relative abundance scale was deduced by dividing the partial pressures of the species by the partial pressure of Argon. Argon is used as a standard due to its chemical inertness. There are no visible changes in mass spectra for 1<AMU<44. To include this null-data would be to obscure the important data show here.

It is also possible that direct heating of the moist ceramic surface also contributed to the production of the unknown specie in the atmosphere. The molar concentration of Ar in the atmosphere under s.t.p (standard temperature and pressure) is 22.4mol. per litre. The relevance of using Argon is its chemical inertness. It abundance should therefore be unaffected by changes in applied conditions. It serves as a standard by which to compare the abundance of other chemical species in the atmosphere. Calculating the molar concentration of hydrated ions from the pH (by raising the base 10 to a power equal to the negative pH) in the electrolyte gives a value six orders of magnitude lower than this (2.0×10^{-5} mol. per litre). This eliminates the possibility of the chemical release of the unknown specie from ceramic without another mechanism being involved (heating or energetic particle bombardment).

If the electrolytic acid is monoprotic, and it reacts with the unknown specie in the ceramic, then this gives an upper limit to the unknown specie concentration in the RGA (Note this is the aqueous solution concentration and not the particulate concentration in the vapour-phase). Referring to the tables of figure 3.22 and figure 3.23 for current and experimental duration respectively it can be shown that the number of electrons transferred to the electrolyte surface from plasma is ~280 times the hydrated hydrogen ion population in the liquid. The product of electron-flux and duration may be compared to the product of aqueous hydrogen ions concentration and volume. They are dimensionally equivalent and the method is analogous to Faraday's law for electrolysis (calculated by the pH and initial volume of the 40ml ceramic container. See the table of figure 3.23).

One considers that the electron current dominates and that the ion current at most is equal to the square root of the ratio of electron and ion masses.

The factor of ~280 can be explained if the ions identities are N_2^+ and NO_2^+ (factors of 227 and 291 respectively). Experimental trials of apparatus shown in figure 3.2(e) and figure 3.2(f) were observed to produce a brown noxious gas (NO_x) in the absence of water over long time periods. One of the reasons of using water in the experiments was to absorb and dissolve these gases. The graph of figure 3.30 illustrates a peak forming at AMU:e 46. This corresponds to NO_2 formation when the moist ceramic container is the virtual electrode. Its uncertainty bar overlaps the curves for when water is a virtual electrode and pre-ignition conditions so it was not reported as a clear result.

Perhaps the pH of the moisture on the ceramic is lower (more acidic) than for the bulk of the electrolyte (due to its lower volume and higher current/ion flux). This may increase the hydrated hydrogen ion concentration by several orders of magnitude and facilitate the chemical release of the unknown specie from the ceramic. The overlap of the uncertainty bars (in figure 3.15) and difficulty in measuring the pH of the thin film of hot moisture over the ceramic surface after the experiment (due to evaporation) requires that the argument is concluded here. In closing, bombardment of nitrogenic species[56] (in the discharge gap) on the electrolyte surface is the most likely cause for the reduction of the electrolyte's pH. In earlier experiments, NO_2 was detected in the absence of the water-electrolyte by smell and visual observation of the formation of a brown gas (see figure 3.2(f)). It is therefore logical to assume that in the presence of water, this gas is dissolved and acidifies the water in a similar process to acid-rain formation.

The analysis in this section shows that non-thermal plasma between the suspended electrode and the electrolyte interacted with the electrolyte and substantially reduced its pH, which in turn assisted elements contained in

the solid walls to be released into the plasma environment. This opens the possibility of using non-thermal plasma for process-conditioning involving liquids and solids as chemical reactants. Such an application can be used in the extraction of energy from biomass.

3.6.2 Water Plasma Spatial Resolution

The spectroscope detected sodium species in the discharge region but that does not conclusively prove that they existed in the plasma column. It is possible that they are merely excited on the liquid surface by ionic and electronic bombardment. High speed photography can give the spatial and temporal resolution to observe the discharge structure and not just the colour of light that it produces. The photographs of figure 3.31 illustrate that sodium species exist throughout the length of the discharge and migrate through the plasma column. They also show that the white luminous discharge attributed to the water plasma is succeeded by the orange afterglow of the sodium species.

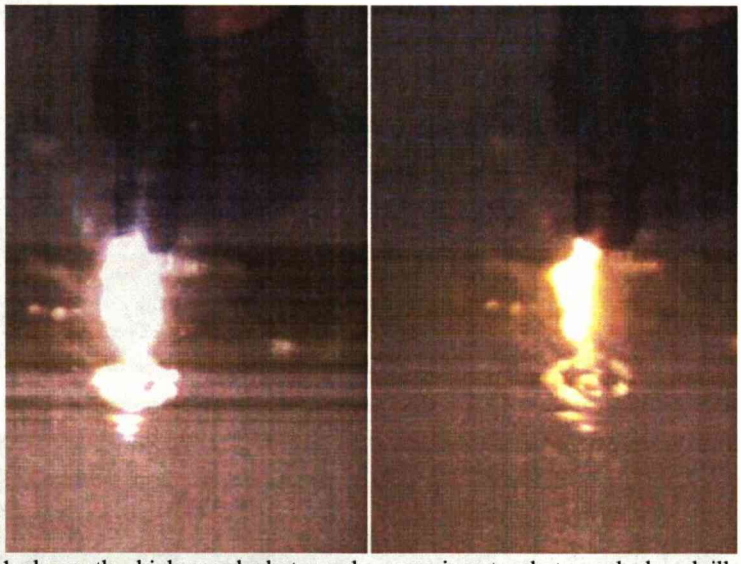

Figure 3.31 shows the high-speed photography experiments photographed and illustrated in figure 3.13 and figure 3.14. The photograph on the left precedes the one on the right by 4ms. The M8 steel bolt (suspended electrode was live). The water has been disturbed by the impact of the discharge indicating relatively high momentum transfer. The discharge gap was ~20mm in length. Applied voltages exceeded 3kV and currents were ~ 10mA. The two luminous spots to the left of each discharge are to be ignored as container imperfections.

Figure 3.31 displays sputtering of the photograph on the left. This phenomenon was not common. The epicentre of the previous impact is not in contact with the discharge in the photograph on the right. This supports the afterglow hypothesis since gas seems to be convecting upwards after being heated by the discharge. The temporal pattern illustrated in figure 3.16 shows that with the exception of the frame taken at 88ms, every 20ms there is a frame of inactivity (28ms, 48ms, 68ms,108ms, 128ms, 148ms and 168ms) where there are no discharges observed. The 0ms frame was taken prior to energising the circuit. The 88ms frame is further proof that for every white incandescent discharge (de-excitation at many wavelengths) there is an orange sodium afterglow (de-excitation of the sodium lines). The 20ms luminosity period is driven by the 50Hz voltage source.

The experiments photographed in figure 3.5 and figure 3.6 will be brought back to our attention. The tables of figure 3.22 and figure 3.23 show that the minimum energy to heat the electrolyte (in the container) and heat and vaporise the remaining amount (populating the plasma) was greater than the maximum available electrical energy delivered by the power supply. Before continuing with this argument the author cautions the reader to note the level of uncertainty in the current value of figure 3.22. On the other hand the author reminds the reader that the water vaporised from the container was not just boiled but superheated to temperatures exceeding 1500K. This reminder justifies the author mentioning this phenomenon and not to simply observe it as faulty readings.

3.6.3 Electro-kinesis

It was observed that in the presence of a non-uniform electric field, steam (transparent) became mist (translucent). Metallic objects were drawn to the electrode and the surface of water bulged at the closest point to the electrode. The polar water molecules are affected by electric fields. A

uniform field will apply an equal and opposite force upon the different poles of the molecule and exert a torque (rotating the molecule) due to the separation of its charge density centres. A field, whose non-uniformity can be observed, at distances of comparable length to a dipole will exert a torque and a translational force on the dipole allowing it to be attracted to the non-uniform field source. A charged particle can be such a source and cause water molecules to congregate around it. This effect occurs in the hydration of a dissolved ion and occurs with coronal discharges in steam.

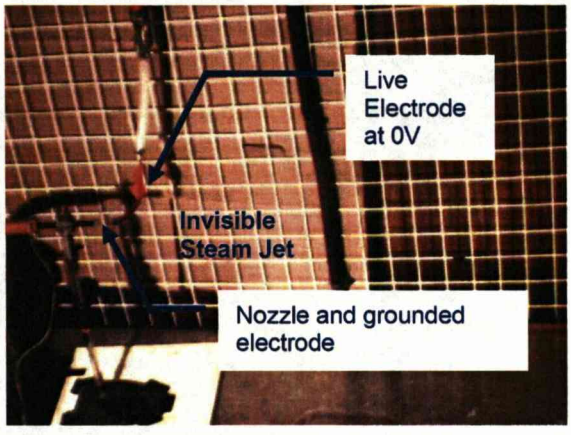

Figure 3.32 shows apparatus with boiler on but applied voltage off. Steam is streaming from the nozzle on the left and moving towards the right. It is invisible yet present.

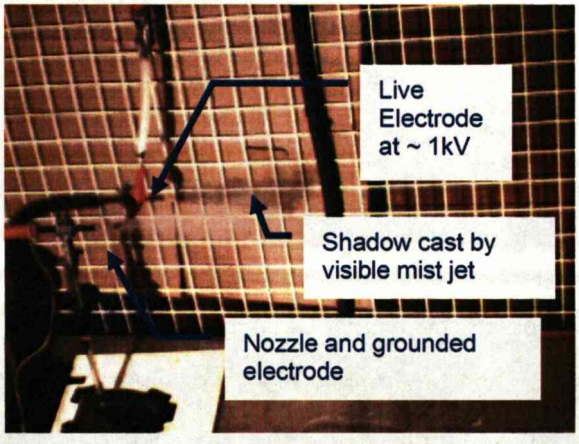

Figure 3.33 shows apparatus with boiler on and applied voltage on. The steam has been condensed to mist by the application of high voltages (~1kV). No significant current is being drawn off as there is no visible electrical discharge (10μA). Work is being done to condense the steam to water but little electrical power is being used.

The photographs of figure 3.32 and figure 3.33 illustrate the electro-kinetic effect on steam. Mass flow rate, and steam velocity were not noticeably altered by these effects under atmospheric conditions.

In the GDE experiments, aluminium foil fragments (not shown) and molten steel droplets (see figure 3.34) were attracted to the suspended steel electrode. The steel colloids formed filaments that bridged the discharge gap from the water surface to the electrode (~20mm apart). This effect was observed at ~3kV with currents ~10mA.

Figure 3.34 shows the sodium afterglow following the initial glare (a few milliseconds prior to it). Note the concentric ripples on the water as well as the dark filament. The ripples were observed in other suspended electrode experiments without a luminous discharge. This effect could be due to an ion wind or coronal discharges imparting momentum to the water surface. The bulging effect of water under an electrode observed in other experiments (low-frequency ~0.23Hz) is also a possible explanation for this ripple at higher frequencies (50Hz)

Returning to the results of the tables of figure 3.22 and figure 3.23, it is possible that the effectively low vaporisation enthalpy arises from the presence of highly non-uniform electric fields generated by charged particles in the proximity of the water surface. When these particles bombard the surface they sputter clusters (not droplets) of water (held

together by the non-uniform fields of rebounding charged particles or other charged particles in the vicinity).

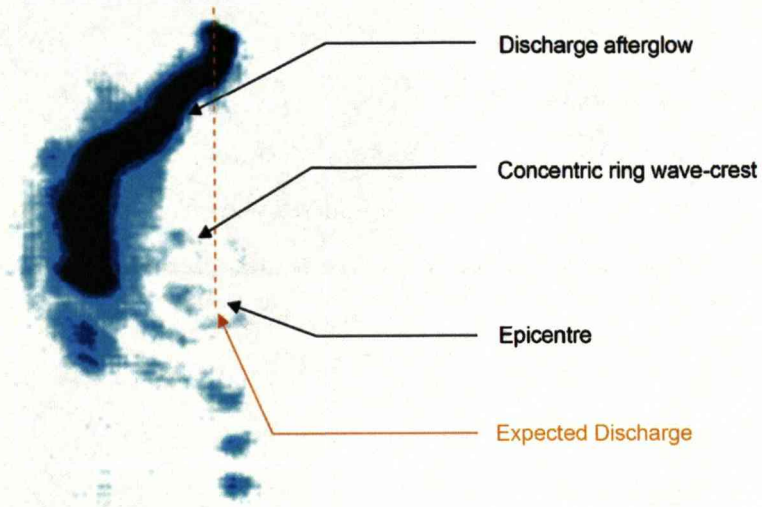

Figure 3.35 is a magnified high-contrast negative image of the afterglow and ripples observed in figure 3.31. Note that the discharge impact has not caused them on this occasion.

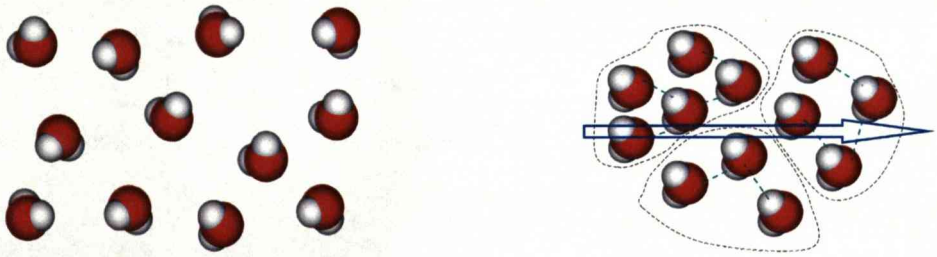

Figure 3.36 illustrates random orientations of water molecules in (invisible) steam (left). On the right, the application of an electric field rotates the molecules. The blue arrow denotes the field. It is drawn generically to represent rotation and attraction. Once in close proximity (like molecules in a cluster) their mutual hydrogen bonding forces augment the clustering effect.

The traditional value for enthalpy of vaporisation is not valid in this case because the clusters are not vaporised, merely fragmented away from the liquid bulk. Instead of many molecules leaving the water surface individually as steam, they cluster together and leave as mist. Less intermolecular bonds are broken. The mean cluster population *N,* is the same factor by which the expected "vaporisation enthalpy" is reduced.

The high-gas temperatures make long-term survival of these clusters unlikely and present a problem when attempts are made to account for the missing electrical energy when balanced against the observed heat.

3.7 Conclusion

Sodium species were introduced into the plasma column (up through to a height of 30mm from the liquid surface) from pre-mixed sodium chloride solution. This is a positive result as the migration of dissolved species into the gas phase was an intended goal of GDE. With the correct choice of electrolyte, atmosphere above the electrolyte surface and contact surface (for the electrolyte) it may be possible for exothermic chemical reactions to occur. Process conditioning is certainly an option; the formation of acid from water and atmospheric nitrogen by electricity was realised.

The work in this chapter forms a platform on which further experimental studies can be performed to advance the use of non-thermal plasma for process conditioning. The acidification of a liquid in contact with metal-containing substances can release hydrogen to be consumed as a fuel in other applications.

Chapter 4

CONTACT GLOW DISCHARGE ELECTROLYSIS (CGDE)

4.1 Introduction, purpose and aim

Non-thermal electrical discharges can be generated in gaseous environments as was discussed in chapters two and three or generated in liquid environments. In this chapter, the basic characteristics of contact glow discharge electrolysis will be investigated. This type of discharge is featured with relatively lower discharge voltages and small size (of the discharge region) however it could be very useful in processes where a micro-discharge is needed to condition a process. Because of the relatively small discharge size, quantification of the discharge and electrical parameters can be more easily carried out in comparison with the type of discharges dealt with in chapters two and three. In this chapter we will first discuss the design of the electrical discharge system followed by typical experimental measurement/results. We will then attempt to explain how the system works and give estimates on the electrical discharge's parameters.

4.2 Experimental Setup and Procedure

4.2.1 Novel Electrode Design for Calorimetry

A novel and relatively self contained electrode configuration and calorimetric capsule was devised. The setup is shown in figure 4.1. A cable contact and silicon electrode were both encased in epoxy resin and housed in a copper reducer which acted as the grounded electrode. This design is

novel in that it permits the use of an end-cap (heat exchanger) to trap the electrolysed and vaporised gases long enough for them to transfer heat to the electrolyte. There are two gas vents near the receptacle that allow the gases to escape and electrolyte to enter, facilitating electrolysis (only one is shown in figure 4.1 but both are shown in figure 4.8). With the end-cap in place, the electrolyte's internal energy gain to electrical energy input ratio can be accurately measured (This ratio was used to calibrate the apparatus and find the specific heat capacity of the electrolyte). Without the end-cap in place, the internal energy of the gas is not efficiently transferred to the electrolyte. It escapes from the liquid without increasing the internal energy of the electrolyte and this will not allow a measurement of the energy possessed by the gas.

The novelty and operation of the electrode configuration in figure 4.1 is explained below. The red wave-arrows represent heat transfer from the discharge region to the liquid. The solid black lines represent the reducer/grounded-electrode. The silicon electrode is represented by the solid black polygon. It shares a common axis of symmetry with the reducer. The translucent grey region (enclosed by thin dotted lines) is the heat exchanger/end-cap. It was removable. There were two vents to encourage the flow of liquid into the unit and the escape of gas out of the unit (only one is shown in figure 4.1 for clarity). Assuming that the brown line (as seen in figure 4.1) within the reducer also shares this axis of symmetry; then the reducer, end cap and electrode recess are rotationally symmetric (The brace is a hollow cylinder with two circular apertures on its curved surface. The nylon rod is inserted through them).

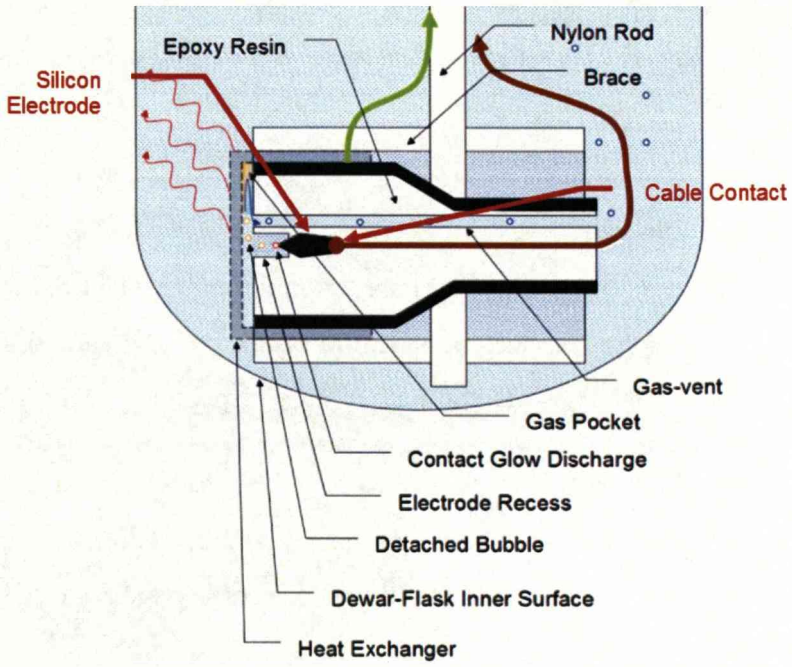

Figure 4.1 illustrates a novel design of the electrodes devised for electro-calorimetry calibration. The entire unit is a capsule with adjoining nylon rod. Green and brown arrows represent ground and live cables respectively. Bubble colours represent temperature. (Red to blue, hot to cold). The brown cable contact (live) is attached to the silicon electrode and they are both encased in epoxy resin. Only one gas-vent is shown here for clarity. The black solid lines at the bounds of the epoxy resin region represent the copper grounded electrode (The live silicon electrode, live cable and gas vents are contained within the copper grounded electrode). This apparatus was used for calibration. The calibration for a given electrolytic solution was implemented by comparing its input electrical energy to its output thermal energy increase. The electrolytic solutions used in detailed experiment in this chapter were found to have the specific heat capacity of liquid water (within the bounds of uncertainty).

The purpose of the capsule (unit submerged in the Dewar-flask that does not include the nylon rod) was to calibrate the input electrical work with the electrolyte's internal energy increase. This was done with the heat exchanger cap in place so a detailed energy balance measurement could be carried out. If any chemical reactions took place in the discharge region, then the energy gain/loss via the chemical reaction will manifest itself in the energy balance measurement. In the case where there are no chemical reactions taking place in the discharge region the following equation then holds:

$$\int_{t_i}^{t_f} V(t)\cdot i(t)dt = c_l \cdot m_l \int_{T_i}^{T_f} dT + c_g \cdot \int_{t_i}^{t_f} \dot{m}_g \cdot T_g dt$$

Equation 4.1

Where t_i, t_f, $V(t)$, $i(t)$ and t are the initial time, final time, voltage across the two electrodes, current and time respectively. c, m and T are the specific heat capacity, mass and temperature respectively. The subscript l refers to the liquid and the subscript g refers to the gas. $\dot{m}_g$ and T_g specifically are the gas mass flow rate and gas temperature upon leaving the liquid. The specific heat capacities are the values corresponding to constant pressure.

Masses were measured using a top-pan balance with an accuracy of $\pm 0.5\mu g$ The Dewar flask mass was measured and recorded. Filtered water was used as the liquid and its mass also measured and recorded. Mass measurements were accurate and repeat readings were taken. When sodium chloride or any other substance was added to the liquid their masses were also measured.

The liquid temperature was measured with an electronic thermocouple ("Digitron" model T200KC/T202KC type K Thermocouple, -200^{0}C to 1350^{0}C). The exposed metallic parts of the thermocouple were covered with a thin layer of silicon vacuum grease to prevent corrosion in water and a thin envelope of copper made from adhesive copper tape was used to further protect the thermocouple head. These protective layers slow down the temporal response of the thermocouple. In our experiment however, the time scale involved is in the range of 30 minutes. The change in the thermocouple temporal response does therefore not affect the measurement results. This thermal probe was wound around the nylon rod but not allowed to make contact with the grounded electrode. Preliminary results

have shown that the performance of the thermocouple is not diminished by the electrodes. Care was taken to prevent droplets of electrolyte reaching the dry parts of the flask's inner walls. The electrolyte was kept as one unified mass of liquid for accurate temperature measurements.

The initial temperature was measured repeatedly for half an hour (after electrode insertion into the electrolyte) to allow the apparatus and the electrolyte to reach thermal equilibrium. Thermalisation was achieved by using the nylon rod to stir the heated electrolyte. The final temperature was recorded without removing the cork lid. Over an hour later (following discharge cessation), the cork lid was removed and the electrolyte stirred thoroughly yet quickly (30 second duration) and the cork lid replaced. The temperature was taken (and found to be a few tens of Kelvins greater than the initial temperature generally speaking) as well as the time it was recorded. Again, readings were repeated. The temperature change after stirring was typically ~0.5K.

Instantaneous voltage and current readings were taken on a Tectronix 2221A, 100MHz Digital storage oscilloscope and recorded via General Purpose Interface Bus (GPIB) and Wavestar. The electrical waveforms across the voltage and current resistors were recorded five times (at zero applied voltage across the apparatus) to quantify digital noise. The circuit was then energised and timed and as many data acquisitions as were possible were made to record the maximum number of waveforms. The applied RMS voltage from the Variac (see chapter three for make and model) was kept constant throughout each experiment and this was above the discharge threshold value (typically 80V RMS however the threshold voltage varies greatly depending upon electrolyte concentration and electrode surface oxidation) for CGDE to occur.

Timing measurement accuracy was increased by running the experiments for as long as possible. These long durations act to negate the uncertainty in transient conditions occurring for the first and last few seconds of energising and de-energising. The time was recorded upon de-energising. The time interval was the only non-repeatable measurement parameter. Each experiment lasted for half an hour to an hour.

The gas bubble detached (from the electrode) will exchange heat with the surrounding electrolyte however its heat flux due to the random motion and collisions of its neutral particles with the electrolyte-discharge interface will be negligible compared to the directed heat flux of a bubble attached to an electrode (discharge). This is because thermal conduction is being supported by the current density incident upon the electrolyte-discharge interface.

Consistency was guaranteed by repeating the whole experiment several times and at varying RMS voltages. Different calorimetric capsules of the same design were used to calibrate for each electrolyte mixture. Several electrodes (of the type displayed in figure 4.1 and figure 4.2) were used to complete the batch of tests for different electrolytes. The results were highly repeatable and will be discussed later. The results from the apparatus of figure 4.1 showed that the specific heat capacity of the electrolytes discussed in detail in this chapter was the same (within the bounds of uncertainty) as water. Therefore these results were not shown and the electrolytic specific heat capacity was assumed to be the same as that for water.

The apparatus of figure 4.2 was also used for its ability to release bubbles rapidly. The protruding silicon electrode left the bubbles exposed and free to emerge out of the liquid unimpeded. This reduced conduction between the bubble and the electrolyte ensuring that most heat transfer would occur

whilst the bubble is still attached to the electrode. It is designed with opposing criteria to the apparatus of figure 4.1. The electrode was submerged deeply to prevent heating of the electrolyte near the surface, evaporation and rapid heat loss from the electrolyte (although heat loss in the gas was allowed). By placing the live electrode near the base, the warm liquid would rise by convection, mixing and stirring itself to permit the bulk of the fluid to reach thermal equilibrium naturally.

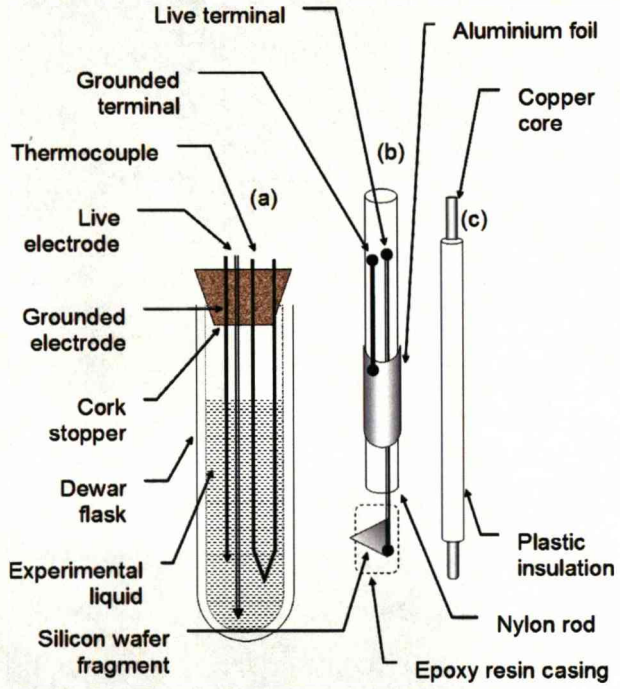

Figure 4.2 (a) illustrates the apparatus of CGDE. The Dewar flask is ~200mm tall and ~10mm in inner diameter. Such small dimensions are not suitable for high-voltages as coronal discharges would stream from the cables into the electrolyte. Electrode assembly (b) and copper cables (c) have radii of ~5mm and 2mm respectively. The experiments described in this chapter were implemented using this apparatus. The apparatus of figure 4.1 was used to confirm the accuracy of the calorimetric experimental method taken by comparing calculated electrical power to internal energy change of the electrolyte. It was used for calibration only.

4.2.2 Practical Considerations

When a coaxial lead was inserted into brine with its core and braids attached to live and neutral terminals respectively, bright yellow luminous discharges were observed on the live core and neutral inserted

braids. It was discovered that the lights were not formed primarily by chemical reaction but rather by the electrical discharge.

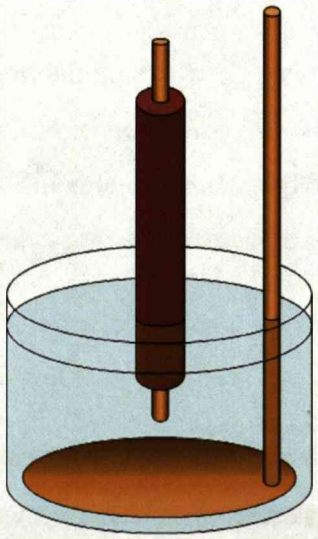

Figure 4.3 illustrates a shallowly submerged insulated copper live electrode (brown) with neutral-grounded counter-electrode. Note the possible ease of escape of heat as gas bubbles may convect towards the surface without radiating or conducting significantly to the electrolyte bulk (This apparatus was used in experimental trials only).

One design step was made by partially insulating the working electrode. For experimental purposes one electrode was modified to sustain the discharge and the other for normal electrolysis. Copper was selected as the discharge electrode material and standard insulated wire was deeply submerged to allow escaping gases to thermalise before reaching the surface. Figure 4.3 illustrates this initial design step. Literature review in chapter one shows that some form of partial insulation of the working electrode was used by other researchers[54]. This prevents the electrolysed gases forming an envelope that was in contact with the atmosphere above the electrolyte surface. The heat produced by CGDE could easily be lost by convection and join the atmosphere above the electrolyte surface rather than being conducted and radiated to the electrolyte. For

calorimetric purposes we need as much energy to be transferred from gas bubbles to electrolyte before they escape from the liquid.

The short lifetime of the discharge under high power (~hundreds of Watts) and atmospheric pressure was of concern. Copper had the disadvantage of not being able to withstand high power inputs due to its high conductivity (It allowed high currents and the metal also reacts chemically with the electrolyte and electrolysed gases). The rapid degradation (wear) of metals is not suitable for running prolonged and accurate atmospheric tests. A more durable electrode material was found by using silicon. This element is one of the most abundant substances in the earth's crust and therefore economically suitable. It was used as an electrode in the hope that it would resist rapid erosion. The resistance of the silicon electrode limited current and prolonged the duration of discharge activity thus sustaining CGDE for long periods of time. It was often difficult to initiate the discharge so its surface was scratched beforehand to remove its oxide coating. The aluminium-foil counter electrode (grounded) was wrapped around the insulation of the live electrode cable.

Silicon fragments were encased in epoxy resin to prevent electrolyte contact with the copper cable core attached to it to supply current. If the desired electrode area is large, regular electrolysis will occur. To target the discharge near silicon one must ensure that the silicon electrode is the only live conductive material in contact with the electrolyte (in the case of AC); hence the epoxy resin casing was used. Epoxy resin is stable at temperatures up to 130^0C yet the discharge managed to bore a recess into it after several minutes by heat and ablation despite the fact that it was also rock-hard. The shattering of the silicon electrode and the breached epoxy resin are illustrated in figure 4.4.

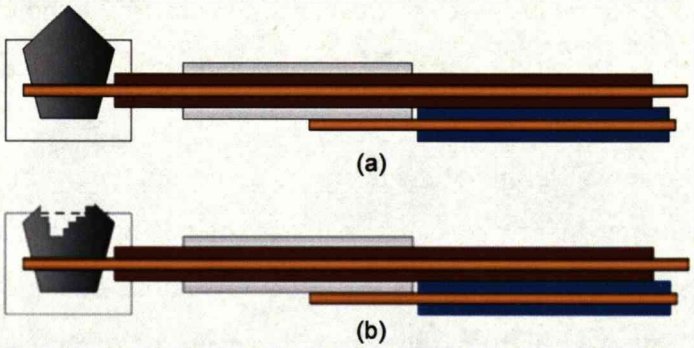

Figure 4.4 (a) illustrates the cross-section of the encased silicon (grey pentagon) electrode in the encasing epoxy resin (White rectangle). The live insulation (Brown) is also encased in the epoxy to prevent copper-electrolyte contact. The neutral cable (Blue and orange) is in contact with the aluminium counter-electrode (Grey bars). The orange bars are the copper cores. (b) The silicon electrode is shattered and consequently the epoxy resin has been breached. The electrodes have been rotated by 90^0 for aesthetics. These electrodes were used for detailed experiments and are featured in figure 4.2.

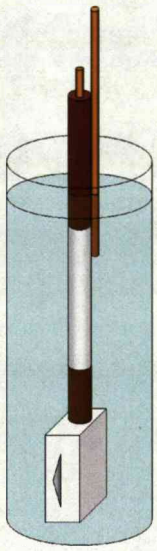

Figure 4.5 illustrates the apparatus of figure 4.4 immersed in the electrolyte. The neutral insulation was omitted as it is superfluous. This is a perspective view.

4.3 Observation of Common Physical Phenomena

The apparatus of figures 4.1-4.3 were tested for suitability. Figure 4.4 and figure 4.5 are detailed images of the apparatus illustrated in figure 4.2. The detailed experiments were done with this apparatus and reported here. The operation of figure 4.1 was photographed and displayed in this thesis.

Because it was constructed from a component of standard dimensions (copper reducer 15mm-10mm) it was photographed in order to gauge the discharge's dimensions).

The mains can supply readily available and sufficiently high-voltage to initiate and maintain CGDE. The discharge was underwater, and in this environment accurate calorimetry is achievable in order to quantify the energy processes that are taking place in a discharge of minute volume.

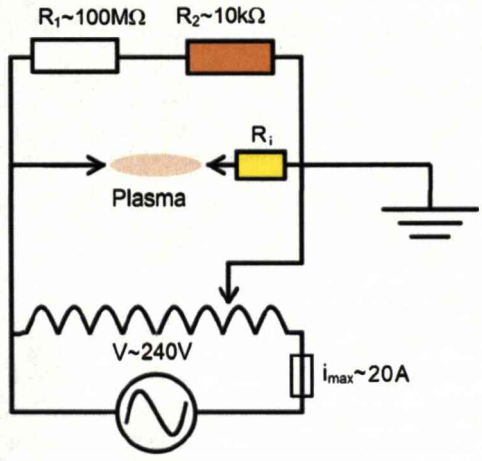

Figure 4.6 Note the absence of the high-voltage transformer. What this illustration does not show are the relatively small dimensions of the electrical components due to the low operating voltages. The electrical discharge is underwater as are the electrodes.

Figure 4.6 shows that the high-voltage transformer was not required here. The experiment was carried out by using two different sized electrodes. The grounded electrode was large and made of aluminium. Bubbles (from electrolysis) cannot completely cover the surface of the large electrode so the glow discharge will not occur there. The smaller normally sharp-tipped electrode was made of silicon.

Each silicon electrode could only be used once as the heating and shockwaves[90] fragment the brittle semi-metal and destroys the epoxy resin. The appearance of current spikes on the oscilloscope, luminous flashes

(intermittent after the first ten minutes of the experiment), audible rumbling and sporadic bubble emission are the related phenomena that typify the contact glow discharge. One can usually tell if copper was exposed to the solution by discolouration of the electrolyte (from clear to blue). If copper was exposed then the effective working electrode composition has radically changed during the experiment and the whole procedure was aborted.

The working (small) electrode was submerged near the base of the flask and enough electrolytic liquid to absorb the heat from the rising bubbles was added to the flask. The majority of the heat remained in the flask although the escape of gases was inevitable and necessary to prevent the cork stopper being forced off the flask. Since specific heat capacity at constant pressure was used for calorimtery, the electrolysed gases were allowed to escape to prevent a build-up of pressure which would invalidate calculation and damage the glass vessel. The cork stopper held the electrodes and thermocouple in position for the duration of the experiment.

The change in mass before and after experiment was not measurable within reasonable levels of accuracy. A top-pan balance was used and fluctuations in air-pressure and apparatus positioning were a significant factor in the uncertainty estimates (despite the use of a flask-holder for positioning on the top-pan balance). The expected gas yield and mass loss from the apparatus by electrolysis under the experimental conditions (~100mA current flowed for ~30 minutes) are of the order of the uncertainty estimate of the top-pan balance. Under experimental conditions and with the well reported non-faradic evolution of gases from CGDE[54], it would be ill-advised to estimate energy loss from the electrolyte by escaping gases here. This estimation is best made in the analysis section. The uncertainty in heat capacity accuracy became an issue for high ammonia concentrations. The results for the ammonia-

containing electrolyte are not reported here however some observations made with this substance will be noted. The heating of the electrolyte caused the release of ammonia into the atmosphere. Sodium chloride did not present a problem as its aqueous solution's heat capacity variation is well documented with concentration.

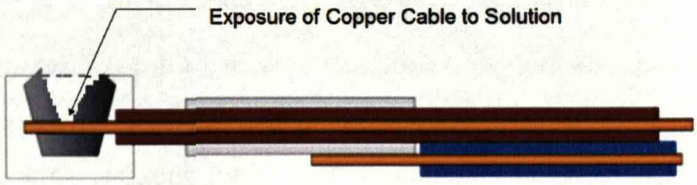

Figure 4.7 shows the electrode assembly after the production of nitrogen trichloride. The extensive damage done to it exposes the copper cable by shattering the epoxy resin.

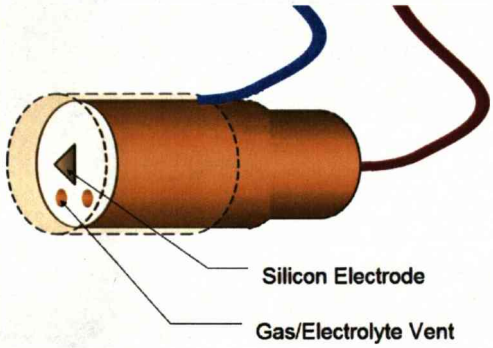

Figure 4.8 is a perspective view of a CGDE capsule for advanced heat exchange. The triangle, two circles below it and the area enclosed by the broken-line represent the silicon electrode, ventilation shafts and heat exchanging end-cap respectively. This apparatus was used for calibration with the end-cap on. It was useful for observational work also.

When sodium chloride and ammonia were added to water in 3:1 molar concentrations, the intended explosive reaction occurred when nitrogen trichloride was formed. These submerged explosions removed the cork stopper (shown in figure 4.2(a)) and caused damage to the electrode as shown in the illustration of figure 4.7). In this case, the epoxy resin insulation is shattered exposing the copper cable. This occurs within a few seconds (as compared to the several minutes of electrode-wear with

other electrolytic solutions to produce the effect of figure 4.4(b)). The electrode-wear in the nitrogen trichloride case is more substantial and occurs in shorter durations. The exposure of copper to the solution in the electrolysis process turns the electrolyte blue. This was not observed when nitrogen trichloride was not formed.

All photographs of CGDE were taken of the capsule depicted in figure 4.8. This capsule is the same as in figure 4.1 (excluding the brace and nylon rod). The dimensions of the electrical discharge were measured by CGDE in dilute aqueous magnesium sulphate solution. Sodium chloride was not used because the light produced in aqueous magnesium sulphate solution provided greater contrast than the light produced in aqueous sodium chloride. A photograph was taken of the discharge in a flat faced container (To minimise optical aberrations) in an electrode casing of standard dimensions (15mm copper reducer). An apparent standardised length (the reducer's diameter) was measured (in pixels) as well as the diameter of the discharge in full contrast and minimum observable brightness (This explains the requirement of a high-contrast image and the use of magnesium sulphate over sodium chloride). This diameter was also measured in pixels and a simple scaling calculation performed to asses the discharge's diameter. There was concern only with the luminous region. This is not the same as the detached bubble dimensions as several small bubbles coalesced after detachment to form fewer, larger bubbles. Luminous region radius was estimated: $r_D = 1.88 \times 10^{-4} m \pm (4.4\%)$

The contact glow discharge is quite a luminous object. Luminosity increases with applied voltage and concentration. Luminosity was not measured in the calorimetric experiments. Concentrations were ~0.1M and applied power ~10W. It was aimed to capture a moment when the discharge intensity was faint in order to observe the electrode as well as

the discharge. Photographs were taken by the method depicted in figure 4.9. The electrolyte in this case was magnesium sulphate (see figure 4.10). The photograph of CGDE in aqueous sodium chloride solution was taken in figure 4.11. The capsule configuration differed in this case as the silicon electrode was placed at the 10mm diameter end of the copper reducer. The epoxy resin was not flush with the copper reducer opening. The silicon electrode did not protrude from the reducer opening but was further back in a niche (hidden in this photograph by glare). An estimate on discharge dimensions was made (See figure 4.13 for photographs of three such attempts). These had their colours inverted in order to conserve ink during the printing of this thesis. The discharge regions appear darker and this still serves the purpose of observing CGDE dimensions.

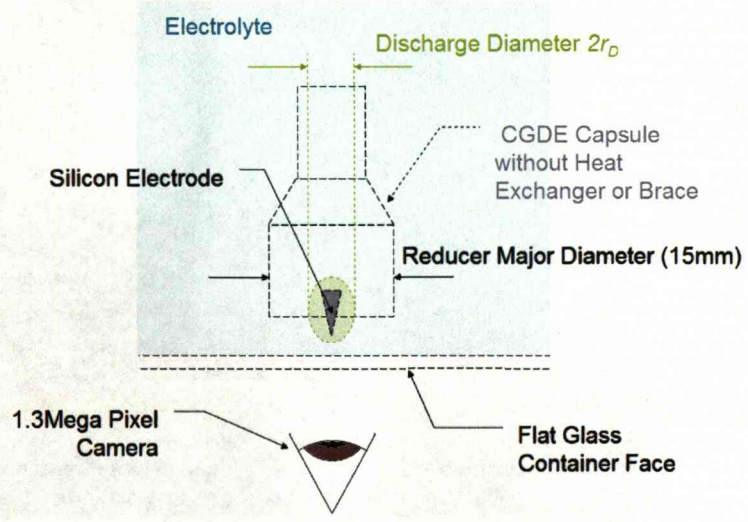

Figure 4.9 is a diagram of CGDE still photography. The eye represents observation and position of the camera (~100mm away from the flat glass container's face). The discharge and reducer's major diameter (15mm) were measured in pixels and calculated in metres using a simple scaling relation.

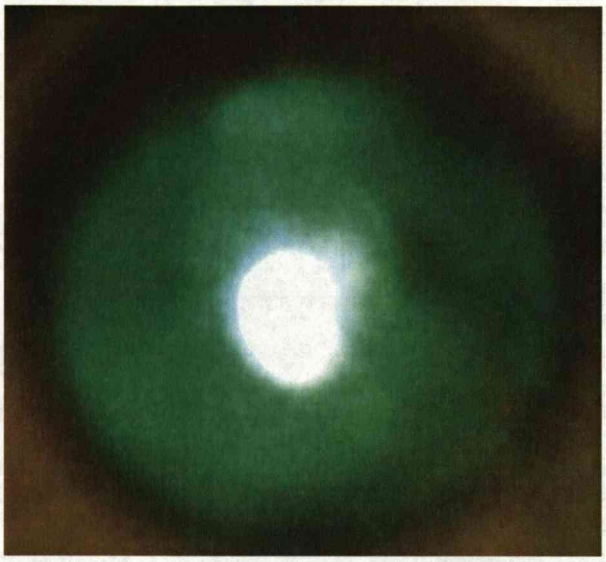

Figure 4.10 is a photograph taken of CGDE in magnesium sulphate solution and standardised length copper reducer of 15mm diameter with a 1.3 mega-pixel camera. The applied voltage was 240V under the conditions described in figure 4.9. Note how the glare makes the discharge appear ~4mm in diameter although it is an order of magnitude smaller.

Figure 4.11 is CDGE in sodium chloride and ammonia solution (The blue electrolyte colour is due to the copper counter-electrode). The applied voltage here was ~80V. The aperture (illuminated) was ~10mm in diameter and the sodium chloride concentration in this case was ~1M. It is the only photograph where the electrode was inset in the 10mm end of the 15mm-10mm copper reducer.

Using the direct photographic method, the discharge diameter, D_d was found to be ~0.36mm if D_d is assumed to be the true diameter. Figure 4.12 and figure 4.13 all show size of the photographic glare but the last photograph of figure 4.13 illustrates a possible candidate for the true discharge diameter (as best as can be seen).

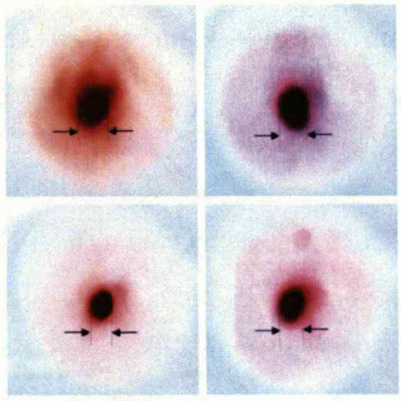

Figure 4.12 is a group of four inverted colour photographs in magnesium sulphate solution (early in the experiment). The applied voltage in this case was 240V in the experimental setup represented by the diagram of figure 4.9. The diameters of the luminous (glare) regions were ~ 4mm.

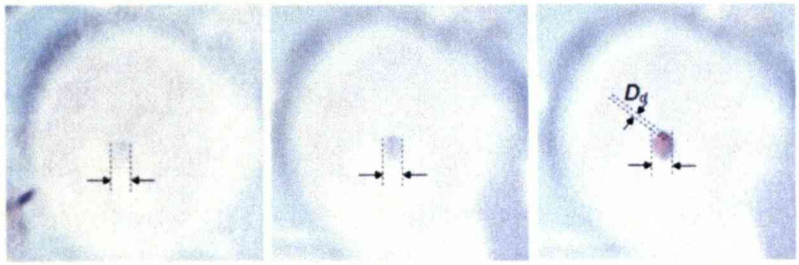

Figure 4.13 is a group of three inverted colour photographs of CGDE in durations of low-intensity (Late in the experiment) under the same conditions as in figure 4.12. The first and second photograph from the left are barely recognisable but were added to convey the true nature of the discharge's luminosity. The exposed area of the silicon wafer was ~0.28mm x 5mm. The discharge diameter D_d is a function of the conducting area (oxide layer removed). The distances unlabelled in the photographs correspond to glare.

4.4 Results

4.4.1 Raw Data and its Manipulation

Electrical discharge voltage and current were calculated using voltage dividers and ohms law respectively (See figure 4.6). The resistors R_1, R_2 and R_i are illustrated in figure 4.6 and their values stated in figure 4.14 for the record. The resistances were measured accurately using an LCR Databridge. Repeat readings were made and systematic uncertainties were

considered. The voltage signals across resistors R_2 and R_i in figure 4.6 were displayed on a two-channelled Tektronix 2221A digital storage oscilloscope (100MHz sampling rate). Two channels were used simultaneously.

This oscilloscope was connected to a CPU via GPIB as mentioned earlier. The oscilloscope was set to "chop". This function prevents discontinuities in the waveform by matching the approximate sweep-rate range to the duration of desired observation (~50ms). The waveforms were acquired and stored on the CPU using the "Wavestar" software program. This is important as the raw data from the oscilloscope was later transferred to a spreadsheet in Excel. The first calculation made was to establish a background noise signal on the oscilloscope when the applied voltage was zero.

The maximum value of the digital noise signal was found and an exclusive logic function applied to the spreadsheet to negate all values whose absolute value was less than that of the noise. This logic correction produced zeros where there were once minute values and so infinities resulted when division operations occurred between data points and these were excluded. The mathematical function of subtraction of background noise from desired signal resulted in uncertainties. These arose due to conscious judgement in selecting a threshold (below which, data was ignored). This required finding the mean and subtracting so the additive law for combining uncertainties was invoked.

Background corrected voltage inputs were used to derive discharge voltage and current. In this way the raw data was manipulated to yield voltage and current waveforms against a common time-base. To conclude this subsection, the shear volume of data from the two typical CGDE experiments (lower and higher voltage) related here must be stressed.

Approximately eighty-two voltage-time waveforms were taken per experiment on each oscilloscope channel.

Resistance

R_1 (MΩ)		R_2(kΩ)		R_i(Ω)	
Value	%	Value	%	Value	%
10.01	0.1	11.11	0.1	5.371	0.1

Figure 4.14 table of CGDE resistor values with their percentage uncertainties. See figure 4.6.

There are 82 voltage-time and 82 current-time waveforms per experiment. Each voltage waveform consists of 4096 individual voltage-time data-point pairs and each current waveform consists of 4096 current-time pairs. With these datasets, the analysis of the contact glow discharge's electrical characteristics will be undertaken.

4.4.2 Voltage, Current, Impedance and Power Graphs

The experimental conditions behind the results are to be explained here. Raw data for five noise signals were plotted along with two experimentally derived data signals on the graph of figure 4.15. This raw data has its plots labelled as "noise", "voltage (1)" and voltage (2)" respectively. The minimum signal to noise ratio was 5.27. These were only a sample of the raw data. Excluding the noise, there were eighty-two experimentally derived data signals. Operations were done to produce figures 4.16 - 4.21. These represented CGDE at a higher voltage (See figure 4.22); namely ~279V. Detailed analysis of the higher voltage CGDE experiments were carried out due to the relative smoothness of data achieved at higher voltages. Increasing voltage has the effect of increasing the frequency of the discharge's appearance. This was true of DBD in chapter two and it is

true of CGDE here. The statistical advantages gained by observing higher-voltage CGDE outweigh the disadvantages of excluding lower voltage CGDE graphs. This is because although higher and lower CGDE conditions were similar, the experiments were done for different electrodes.

Electrode geometry changes during experiment due to the shattering effect on silicon by underwater explosions (see figure 4.4). As a result, differing geometrically related electrical characteristics will occur for any two electrodes. It would be confusing to the reader to note these differences and cause distraction from the main arguments. Besides this, no geometric-electrical correlations can be formed for each electrode as the point of conduction changes during experiment.

Although only higher-voltage graphical data will be represented here, tabulated data for lower-voltage experiments will be displayed for comparison with the higher-voltage case. The statistical superiority of the higher-voltage case required that it was treated in the analysis section (to the exclusion of the lower-voltage case).

The graphs of figures 4.16 - 4.21 are of voltage, current, impedance and power versus time for the higher voltage CGDE experiments. Figure 4.17 and figure 4.18 are voltage-time and current-time plots respectively (Their deduction was described in the previous section). Each of these graphs comprises of several plots taken over two and a half periods. Several plots were displayed on the common axes and colour-coded from lighter to darker hues representing the many waveforms obtained early and late in the experiment respectively. They show an evolution of the waveform with time. Several waveforms were taken and this approach was used to illustrate to the reader that which was experienced during experimentation.

A single voltage and corresponding current waveform were taken and plotted on the same axes in the graph of figure 4.16. Note the lack of smoothness in the current waveform when the voltage magnitude tends from a maximum to zero. This is indicative of the discharge regime within the bubbles formed during electrolysis and joule heating. Figure 4.17 reveals that the voltage was quite unaffected by the discharge regime unlike GDE in chapter three (where voltage waveforms deviated from sinusoidal). The current-time graph of figure 4.18 shows how the current-time waveforms change in amplitude with time. Again, the discharges or current-spikes occur when the voltage magnitude tends to zero from a maximum value. Large current spikes (such as the spike observed after 30ms) coincided with audible (crackling and rumbling) sounds observed during experimentation. This suggests that smaller spikes are also electrical discharges and the smoother sections of the waveform are not indicative of CGDE. In experimental trials (transparent container) these sounds were accompanied by flashes of light (not always visible from the silvered Dewar flask. It was sometimes possible to observe these discharges from a sealed flask due to the reflection and refraction of light through the glass envelope of the flask. These details are mentioned to emphasise the intensity of light from the submerged discharge).

The impedance plots of figure 4.19 were drawn from the data of the voltage-time and current-time spreadsheets. Voltage-time and current-time waveforms were drawn from common time durations (50ms) as the inputs V_1 and V_2 were taken simultaneously by the oscilloscope. The voltage-time and current-time waveforms are really a series of voltage values and current values that are captured at a series of instants in time for the duration of the snapshot (4096 instants in 50 milliseconds duration). It is therefore possible to find the voltage and current at any given instant in time and deduce the instantaneous impedance by dividing the voltage by

the current at that instant. This was done for each voltage-time and current-time waveform pair to produce an impedance waveform. This process was repeated for all voltage-time and current-time waveform pairs and a series of impedance waveforms were plotted on common axes. Again the lighter and darker hues represent earlier and later times respectively.

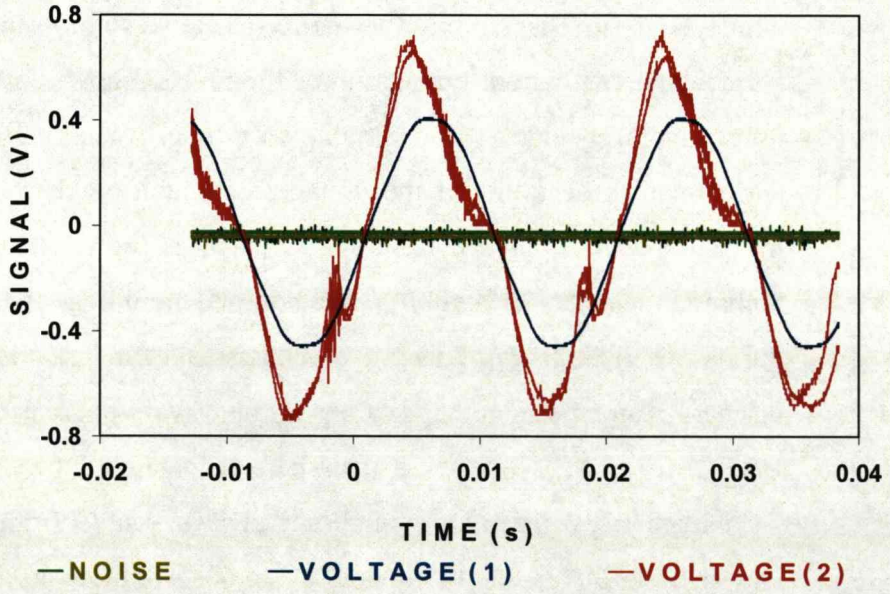

Figure 4.15 is a collection of graphs of directly plotted raw data. There was no data manipulation here. Digital noise from both oscilloscope channels were plotted (five plots overlaid and in green). Voltage signals from both oscilloscope channels were plotted when 279V RMS was applied to the experimental cell. The noise to signal ratio was 5.27.

The impedance-time plot reveals the quasi-linear (constant) impedance of the derived waveform from 5ms-10ms, 15ms-20ms, 25ms-30ms and so on (corresponding to the electrolysis regime). At 2ms-4ms, 12ms-14ms, 22ms-24ms (and so on) the impedance waveform consists of spikes (whose amplitudes follow a somewhat linear trend of non-zero gradient. These correspond to the filament impedance and it varied with time or rather; applied voltage). Some impedance values were negative suggesting capacitive or inductive properties of the circuit. The geometry of the bubble surrounding the electrode would be somewhat capacitive. The coils

comprising the auto-transformer are the obvious candidates for the inductance.

The power plots of figure 4.20 were achieved in a similar manner to that of the impedance plots described in the paragraph preceding the last. The only difference here is that the operation between the instantaneous voltage and instantaneous current was multiplication and not division. Lighter and darker hues represented earlier and later times respectively. The power-time plots reveal the varying power magnitudes at opposing voltage polarities. Since the voltage waveforms were equal in area above and below the zero-voltage level (voltage origin in figure 4.17) then the current must not be equal in area above and below the current origin (see figure 4.18). The current and hence the power favour positive voltage polarities (i.e. the live silicon electrode is at a positive potential with respect to ground and the electrolyte). The large power spike occurring after 30ms was due to the large current spike occurring at the same time (see figure 4.18).

Mean instantaneous values were taken from each electrical quantity to plot a single waveform per electrical quantity (voltage, current, impedance or power) instead of several per common axis as before. The overview plots of figure 4.21 were quite different from the four that preceded it. In these plots, the mean values of instantaneous voltages in a certain phase of the wave were taken for all voltage waveforms acquired in an experiment and plotted against time. This was done for all phases throughout the 50ms duration (or two and a half wave-cycles). This process is then repeated at different times (phases) across the voltage-time plots to give one mean voltage plot against time.

This entire operation was carried out for the current-time; impedance-time and power-time plots to produce one plot each of voltage, current,

impedance and power against a common time-base (or phase to be more precise). These values have different quantities and units and so they were normalised and plotted to a common abscissa axes. Each quantity (voltage, current, impedance and power) had its mean instantaneous values divided by the value of maximum displacement from the ordinate axes. In other words; the mean instantaneous value was divided by that of the greatest magnitude. The choice in this manner of representation is as follows; analytically, for example each current waveform can be examined individually for basic features however when representing general results, it is also required to observe the whole or average to assess the range of variation in the electrical quantities.

The impedance waveform has two sections per voltage cycle. The discontinuity is due to omitted infinities previously mentioned (occurring from the division of voltage by zero-current). The two-sectioned impedance waveform is repeated at every voltage-cycle. Each section will be described in turn.

Looking at figure 4.21 for one period of the impedance waveform from 14ms the impedance rises from zero (corresponding to zero applied voltage) and plateaus. It is essentially constant from 15ms to 17ms (constant impedance indicative of ohmic behaviour. This is suggests the normal electrolysis process is taking place). After this time its gradient is linear and positive from 17ms to 21ms (during this time, the live electrode is enveloped by electrolysed and vaporised gases. Its effective area is reduced and its impedance rises). This is seen more clearly in figure 4.19. From 21ms to 23ms the current-spikes dominate and the impedance gradient seems to increase yet again (there is complete coverage of the live electrode by gases. Conduction occurs by electrical breakdown of those gases. This is indicated by the luminous discharge). This section of curve resembles the point of inflection of a polynomial of odd-number order.

From ~25ms the impedance falls slightly and then plateaus between 26ms and 30ms (this is the electrolytic ohmic conduction regime). After 30ms it rises (as though tending to positive infinity. Observation of figure 4.19 at this time reveals current-spikes. The luminous discharge (current-spike) regime occurs when the voltage magnitude tends to zero (as previously mentioned and for both sections of the impedance waveform). This section of the curve however resembles the minima of some polynomial function.

4.4.3 Tabulated Results

Figure 4.22 is a table of RMS voltage, RMS current and average power for each experimental condition (lower or higher voltage CGDE). The RMS values were calculated by squaring all relevant instantaneous (voltage or current) values and finding the arithmetic mean of these squared values. The square-root of the arithmetic mean was then found. The time co-ordinate was not important here. All of the voltage-time and current-time data points were just treated as a series of voltage and current values respectively. For each experimental condition the voltage or current values of approximately 82 waveforms (each with 4096 data points) were used to find the RMS voltage or RMS current respectively. The use of RMS value is sensible here since the voltage and current waveforms are roughly following a sinusoidal profile. The process of finding the square-root of the mean-square of the data points involved using the index, additive and quadrature uncertainty combination laws.

Average power was found by taking the arithmetic mean of the power data points in the power-time plots (again time was not considered and the power-time data points were just assumed to be a series of power data points). This is equivalent to calculating the energy per unit time. Since the current was not truly sinusoidal, the RMS value of current multiplied by voltage RMS values does not produce the average power. Therefore RMS values are for indication only. The uncertainty in average power was found

by calculating the standard uncertainty on the mean. The average impedance and its uncertainty were calculated in the same way as the average power and uncertainty values were calculated for power. It should be noted that for tabulated electrical quantities, the calculated uncertainties were added in quadrature with the instrumental uncertainty in the reading. The latter turned out to be negligible but is mentioned in appendix 2.

It can be seen from the table of figure 4.22 that the current remains quite similar for higher and lower voltage CGDE. Although this provides no conclusive results (since the electrodes were slightly different and must have fragmented differently), the electrodes were constructed of the same materials and are similar enough to observe the limitation of current to ~70mA. It is possible that bombardment of the electrolyte by charged particles and radiation induced evaporation (although the effect of the latter may be only small) produces sufficient steam to populate the discharge and inhibit current by increasing resistivity (see the elevated impedance at higher-voltage magnitude despite the presence of electrical discharges in figure 4.19 and figure 4.21). A negative feedback mechanism seems to be in operation here. Despite this, higher voltage result in higher electrical power as expected.

Figure 4.23 is a table of absolute temperature, mass, duration and electrolytic heating power (internal energy increase rate). Repeat readings for temperature and mass were made for both lower and higher voltage CGDE. These readings were taken within seconds of each other. Their mean values are featured on the table as well as their associated uncertainty. The duration of the experiments was the only reading that could not be repeated per experiment. It should be noted that for tabulated non-electrical quantities, the calculated uncertainties were also added in quadrature with the instrumental reading uncertainty. For temperature (accurate to within $\pm 0.05K$) and duration (accurate to within $\pm 0.5s$) these

were not negligible (See appendix 2). The electrolytic heating power (which is also the thermal power received by the electrolyte) was calculated by using the first term on the right-hand side of equation 4.1 and subsequently the first three columns of the table of figure 4.23 with a specific heat capacity of $4186.8 JKg^{-1}K^{-1}$. The experiment at lower voltages was implemented over a longer time period. The higher-voltage experiment was responsible for higher observed electrolytic heating power as expected. The graph of figure 4.24 compliments the table of figure 4.23. The curves prior deactivation (steep positive gradient) and post deactivation (shallow negative gradient) represent steady heating and controlled cooling respectively (the difference in magnitude of the gradients is indication of the heat retention of the apparatus and the accuracy of the experiment).

Figure 4.25 is a table comparing the ratios of electrolytic heating power to electrical input power for the lower voltage CGDE, higher voltage CGDE and the typical glow discharge electrolysis (GDE) experiments. The average power for the GDE experiments were not calculated with the mathematical rigour of the CGDE experiments. "Average power" in the GDE case was merely the product of RMS voltage and RMS current to give a nominal power value. CGDE transfers heat more efficiently to the electrolyte than GDE since the former occurs underwater.

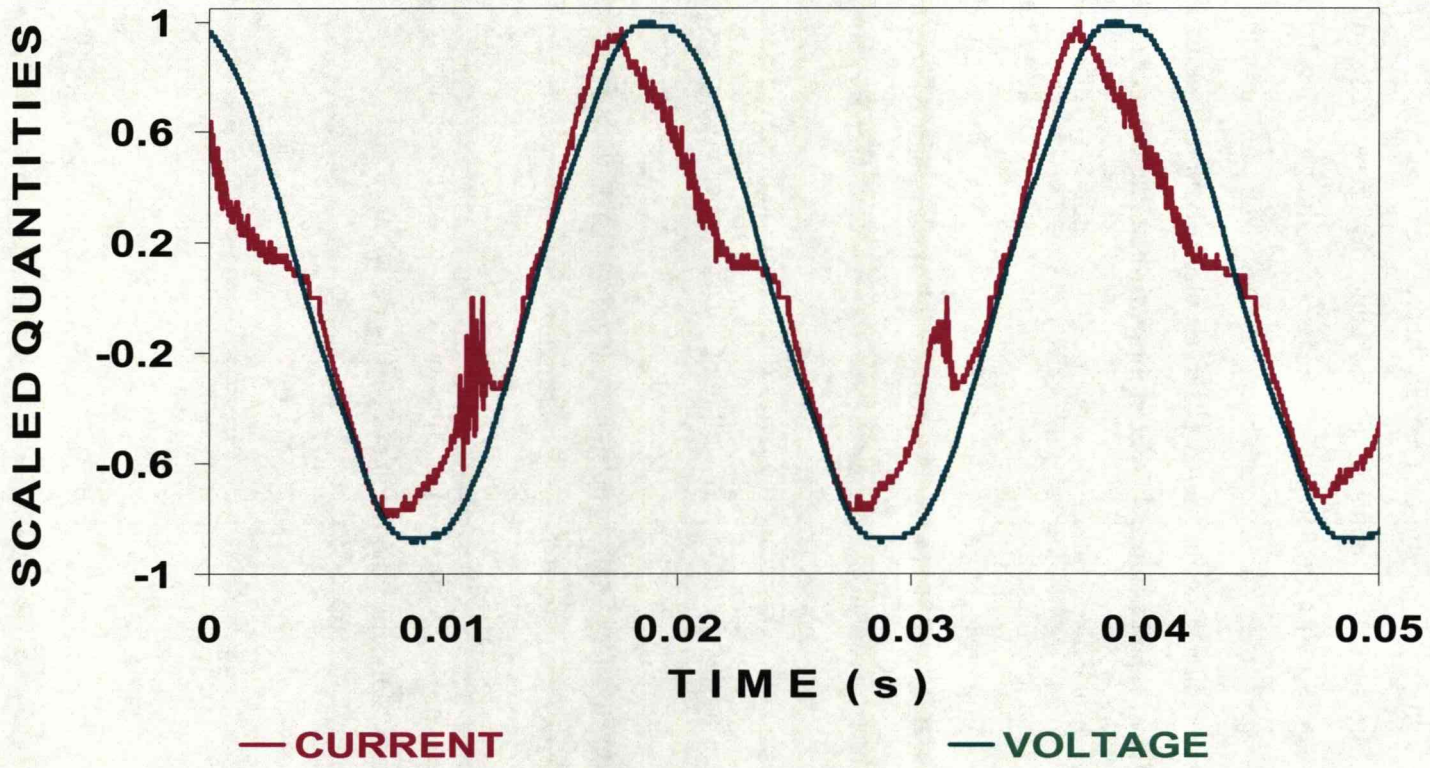

Figure 4.16 is a single current and voltage plot versus time and scaled on the same axes. The voltage amplitude was ~400V and current amplitude ~100mA. As with all graphs from this point forward and including figure 4.15 it represents the higher voltage CGDE experiment.

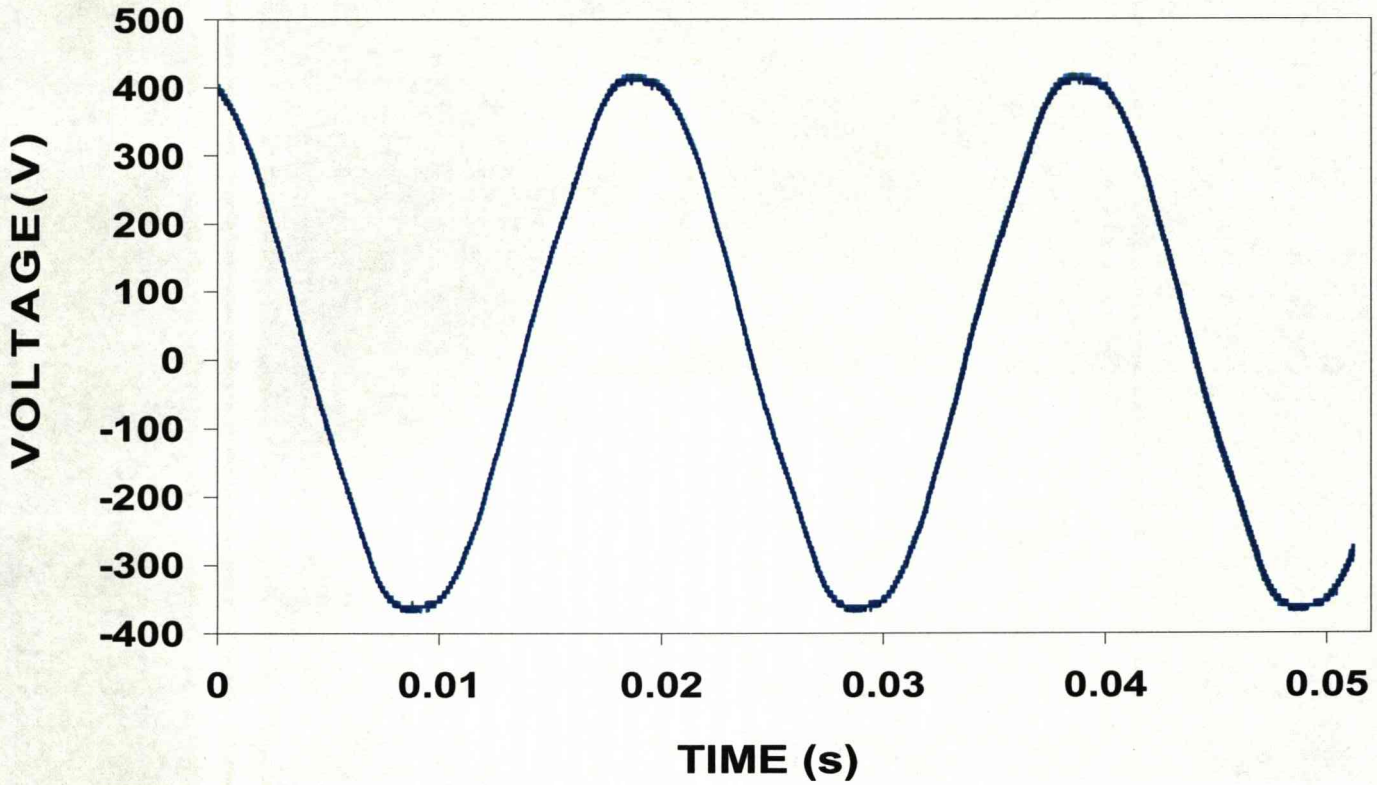

Figure 4.17 is a graph of multiple overlaid plots of voltage versus time for higher-voltage CGDE. This waveform is smooth and indicates that there are no dramatic changes in discharge impedance.

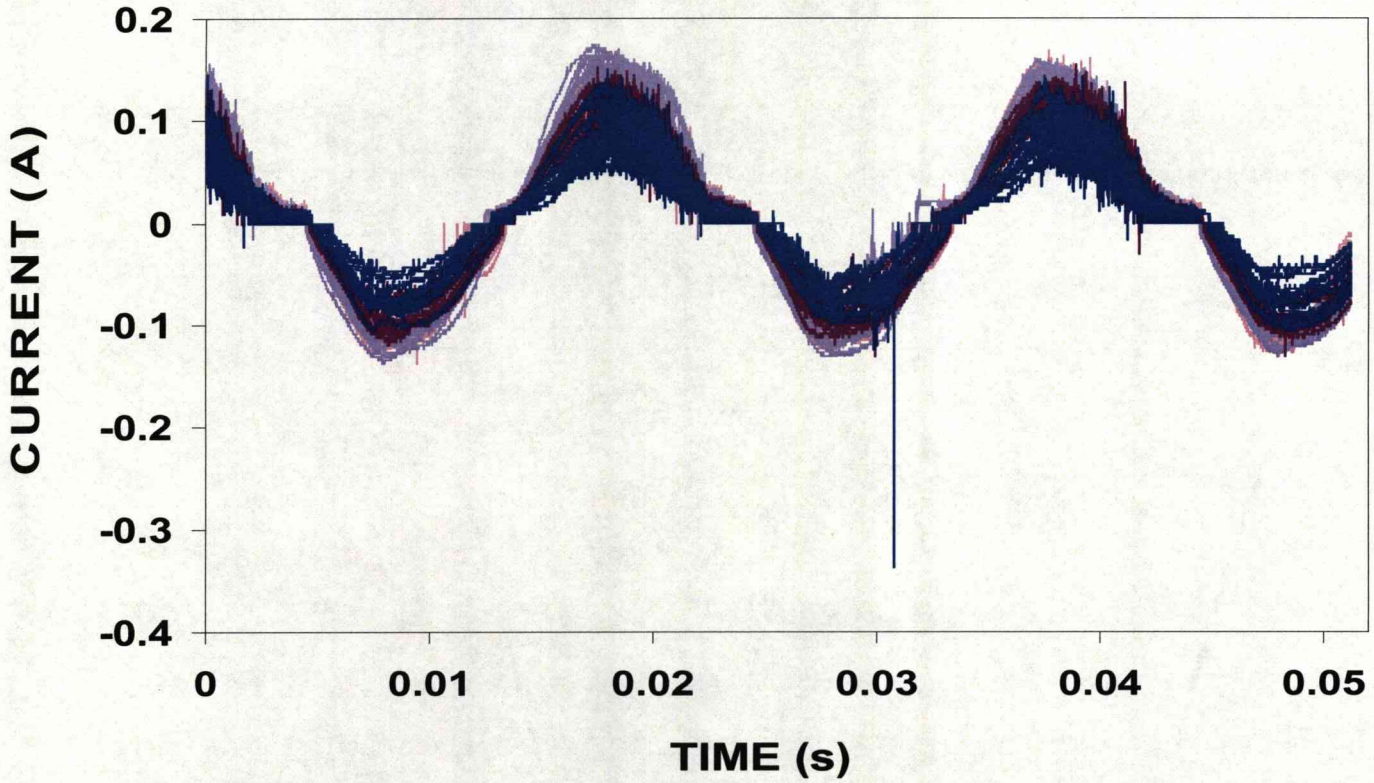

Figure 4.18 is a graph of multiple overlaid plots of current versus time for higher-voltage CGDE. The discharges (current spikes) occur most frequently as the voltage tends to zero. Note the large filament after 0.03 seconds.

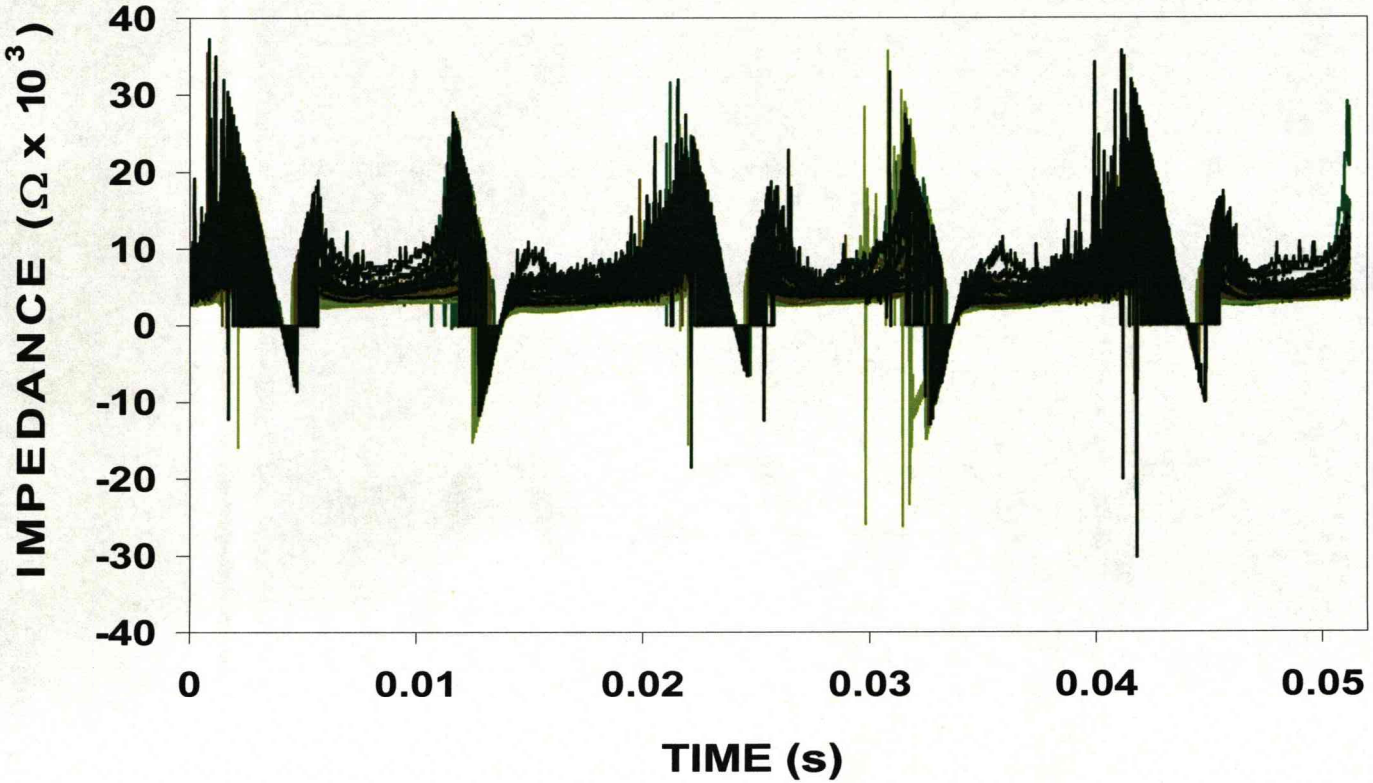

Figure 4.19 is a graph of multiple overlaid plots of impedance versus time for higher-voltage CGDE. The regions of negative impedance represent discharges opposing the applied voltage. Impedance changes with time due to the contact glow discharge formation within a dielectric gas bubble. Prior to this, impedance was due to the electrolyte and electrode only.

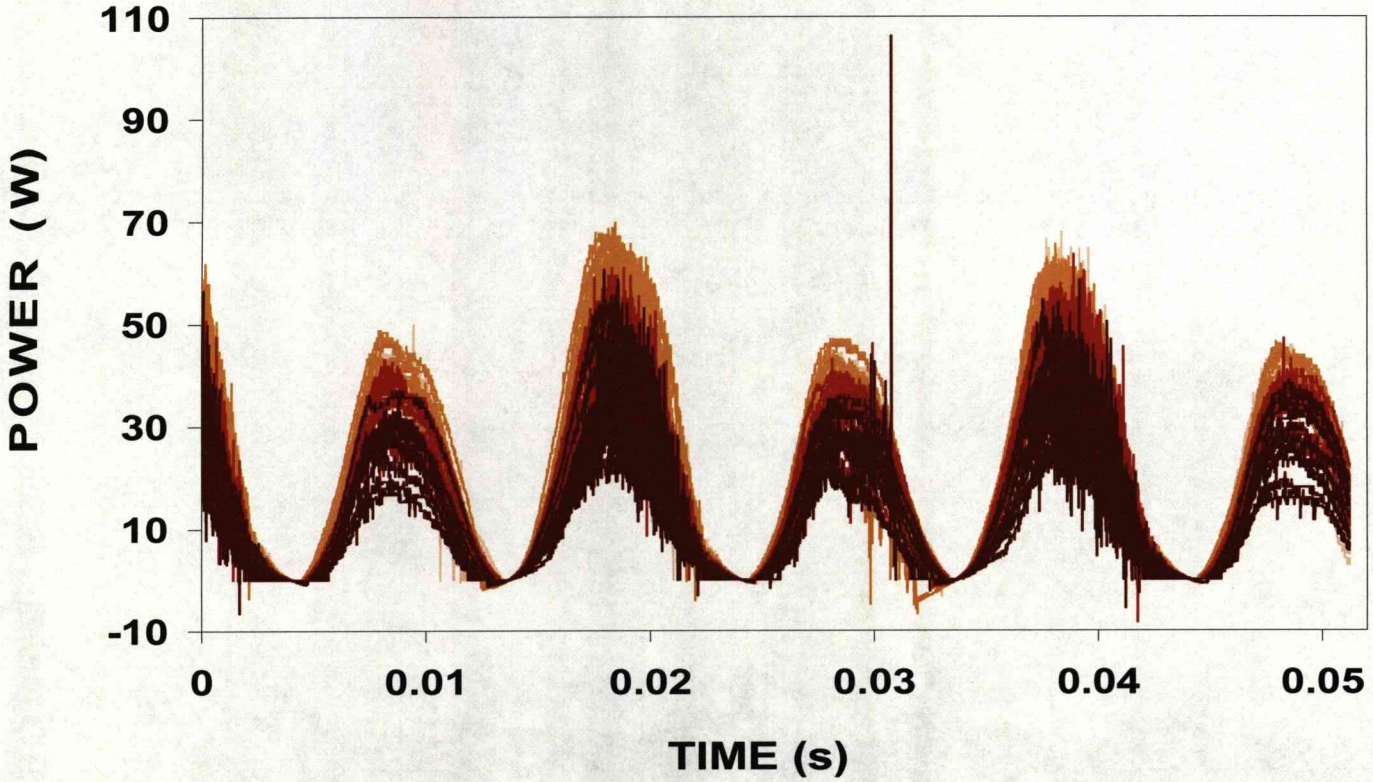

Figure 4.20 is a graph of multiple overlaid plots of power versus time for higher-voltage CGDE. The power favours the positive polarity. The current spikes favour positive polarity and tend towards the negative.

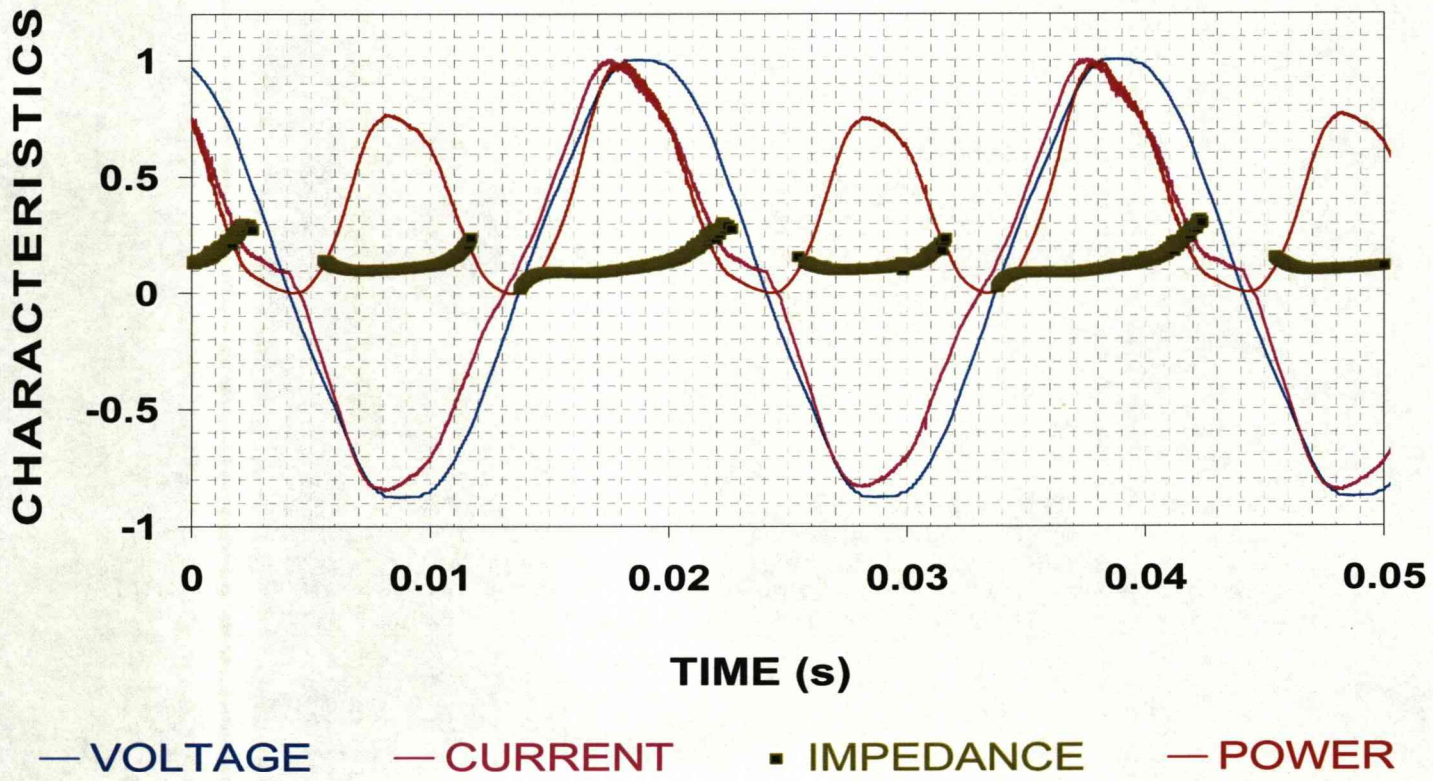

Figure 4.21 is a graph of four plots of mean voltage, mean current, mean impedance and mean power versus time for higher-voltage CGDE. Here the asymmetry of the current is stark yet it appears in phase with voltage.

CGDE Electrical

V_{RMS}		I_{RMS}		$P_{Average}$	
Value	%	Value	%	Value	%
173.719	0.03	0.0781	0.2	13.143	0.2
278.979	0.01	0.0710	0.4	18.625	0.4

Figure 4.22 is a table of RMS values of voltage V in volts and current I in amps respectively. Average electrical power P is in Watts. The percentage columns represent uncertainty bounds. Note that the value of current remains largely unchanged for these two different electrodes, solutions and applied voltages. With increasing voltage and power, the electrolyte interface is bombarded with more energetic particles and releases more steam. The increase in electrical discharge (neutral particle) population increases resistance thus limiting the current at a given voltage (Unless otherwise stated, all units are S.I).

CGDE Hydro-Thermal

ΔT		m		Δt		dU_E/dt	
Value	%	Value	%	Value	%	Value	%
29.8	0.5	0.426	0.0002	4496	0.02	11.8	0.5
20.5	0.4	0.486	0.0002	2920	0.02	14.3	0.4

Figure 4.23 is a table of lower voltage (top row) and higher voltage (bottom row) CGDE experimental data. Electrolyte temperature difference ΔT in Kelvins, electrolyte mass m in kilograms, time elapsed Δt in seconds and average thermal power (electrolyte heat energy absorption rate) dU_E/dt in Watts. The latter quantity was the observed internal energy change rate. It is the sum of the heat transferred from the discharge and the joule-heating effect of the current passing through the electrolyte. Note the high accuracy of the mass measurements. The first three columns compute the value of the fourth column with the specific heat capacity of water at $4186.8 Jkg^{-1}K^{-1}$. The use of this value of specific heat capacity was justified by calibration tests performed with the novel apparatus featured in figure 4.1.

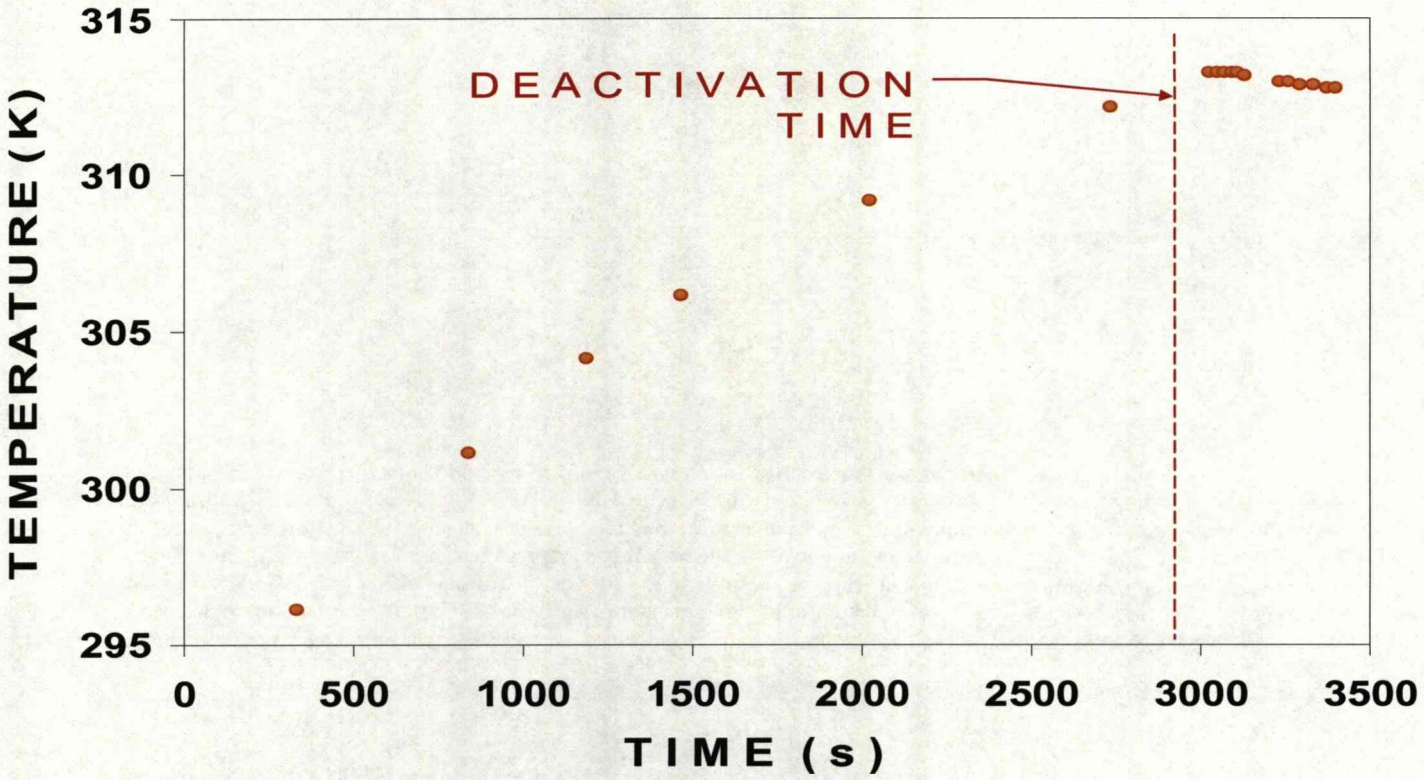

Figure 4.24 is a graph of electrolyte temperature at the thermocouple over time elapsed from energising the circuit. The electrolyte was stirred after deactivation time and temperature recorded frequently as shown by data-point spacing.

Comparative

Experimental Type	$U_E : W$ Ratio	
	Value	%
Lower CGDE	0.899	0.5
Higher CGDE	0.769	0.5
GD	0.212	49.5

Figure 4.25 is a table showing the ratio between observed internal energy increase in the electrolyte and electrical input power. $V.I.\Delta t$ (Voltage-current-duration product) was tabulated for the GDE experiment. Lower and higher (CGDE) as well as GDE experiments are tabulated in descending order.

4.5 Analysis

CGDE occurs at sufficiently high voltages. The current rises and the amount of gas produced by electrolysis and joule-heating is sufficient to cover the smaller live silicon electrode. This gas is dielectric and initially inhibits conductive current flow. When the voltage is raised further, an electric field near the silicon live-electrode becomes strong enough to breakdown the dielectric gas. Electrons are liberated from the electrode and a discharge is then formed. This is best observed on the impedance versus time graphs (see figure 4.26-4.29). The voltage can be raised manually to initiate this process in the DC case but in the present work the AC applied voltage caused the voltage magnitude to be raised from zero on a periodic basis. The CGDE phenomena are assumed in the present work to be of hemispherical geometry. The silicon-electrode is the live electrode submerged in the electrolyte. An electric current passes through the electrolyte, ionised gas-sheath and silicon-electrode.

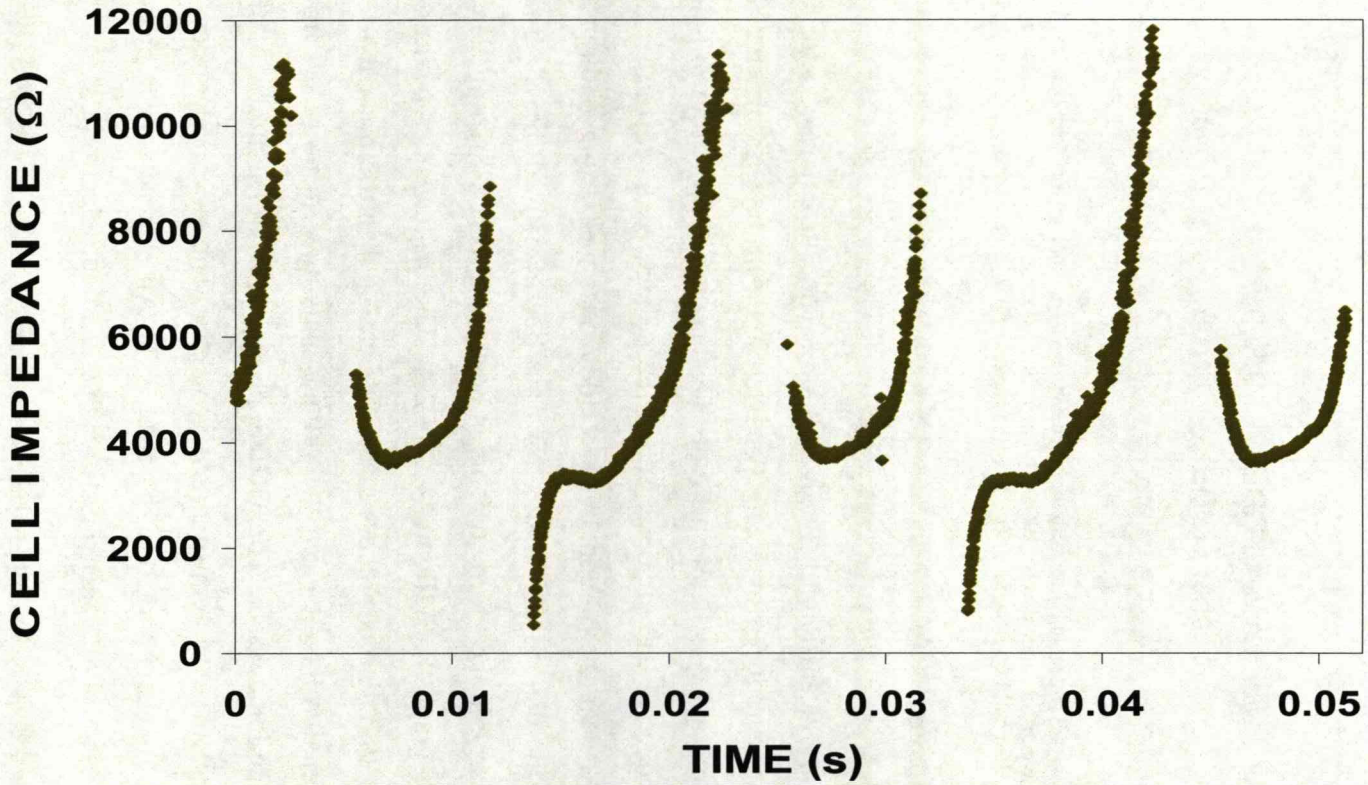

Figure 4.26 is a graph of mean impedance versus time and is plotted with units shown (see figure 4.21). The minimum resistance value is the sum of electrolytic and silicon electrode resistances in series (~800Ω).

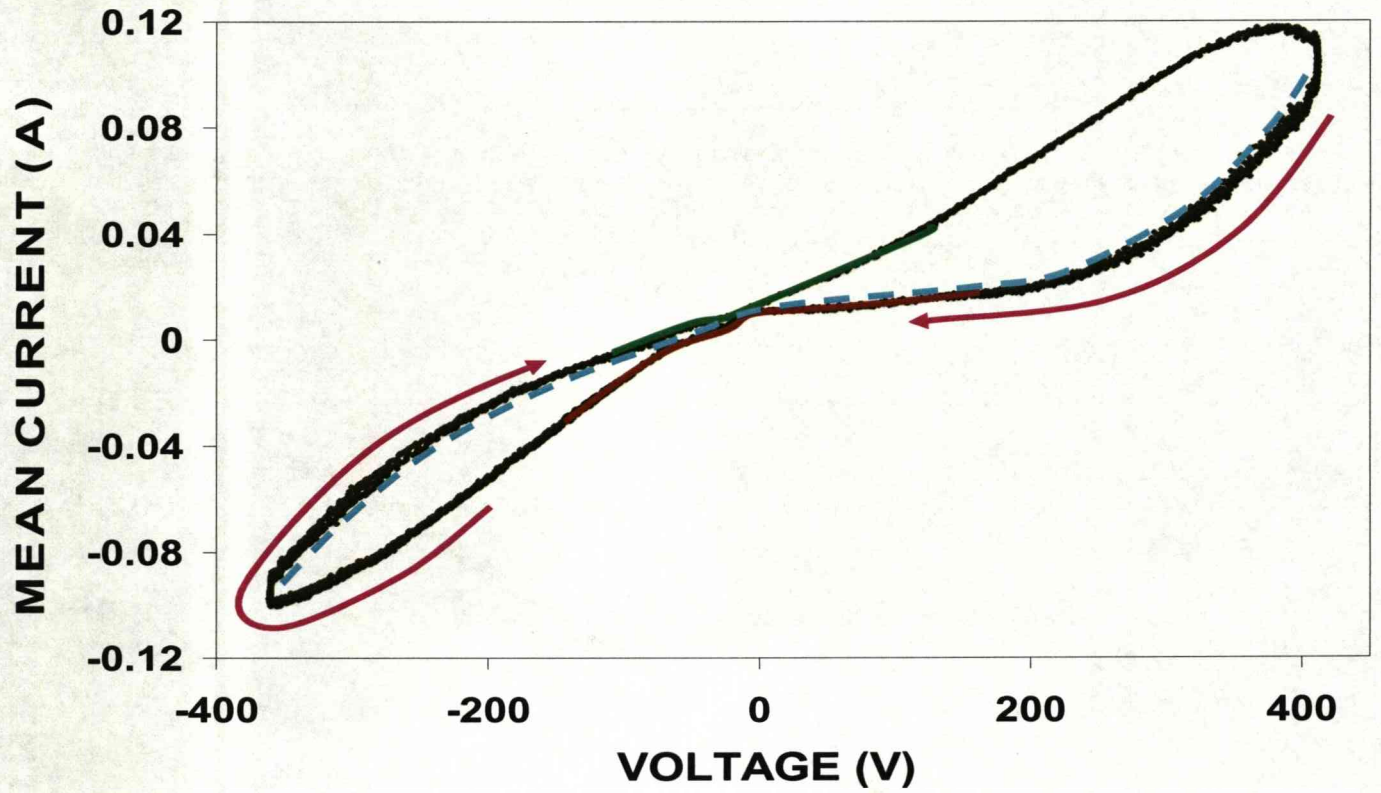

Figure 4.27 is a scatter graph of voltage versus current for two and a half cycles of the voltage waveform. Purple arrows indicate time ordering. Green and brown lines show there is no cross-over of the *V-I* loop. The blue broken line is the filament trend and it occurs where the dark green data-points are most scattered.

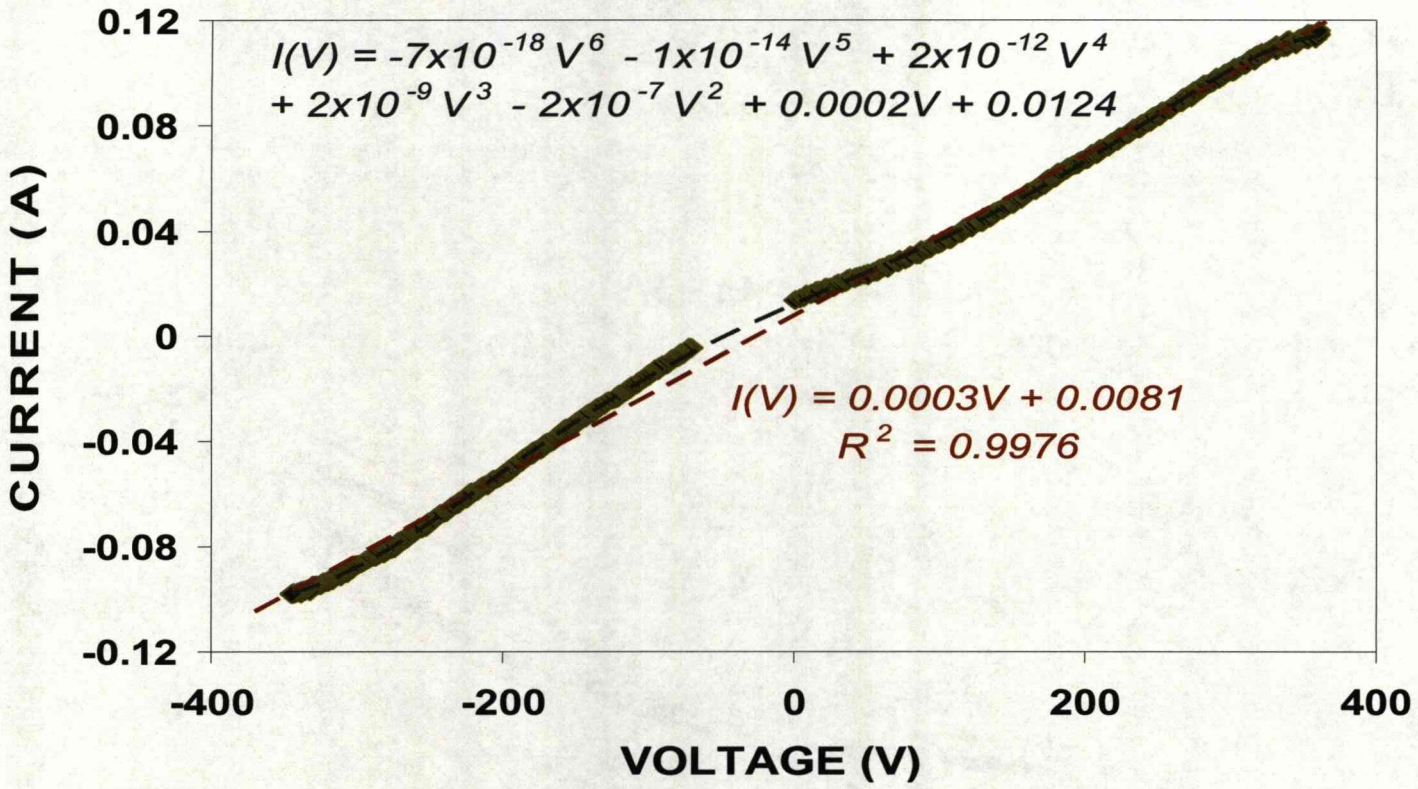

Figure 4.28 displays the linear section of the voltage-current waveform. The voltage and current have a linear dependence whose inverse gradient is electrolytic impedance. These sections obey Ohm's law to close approximation, yet their range over high voltages excludes the possibility of purely electrolytic resistance.

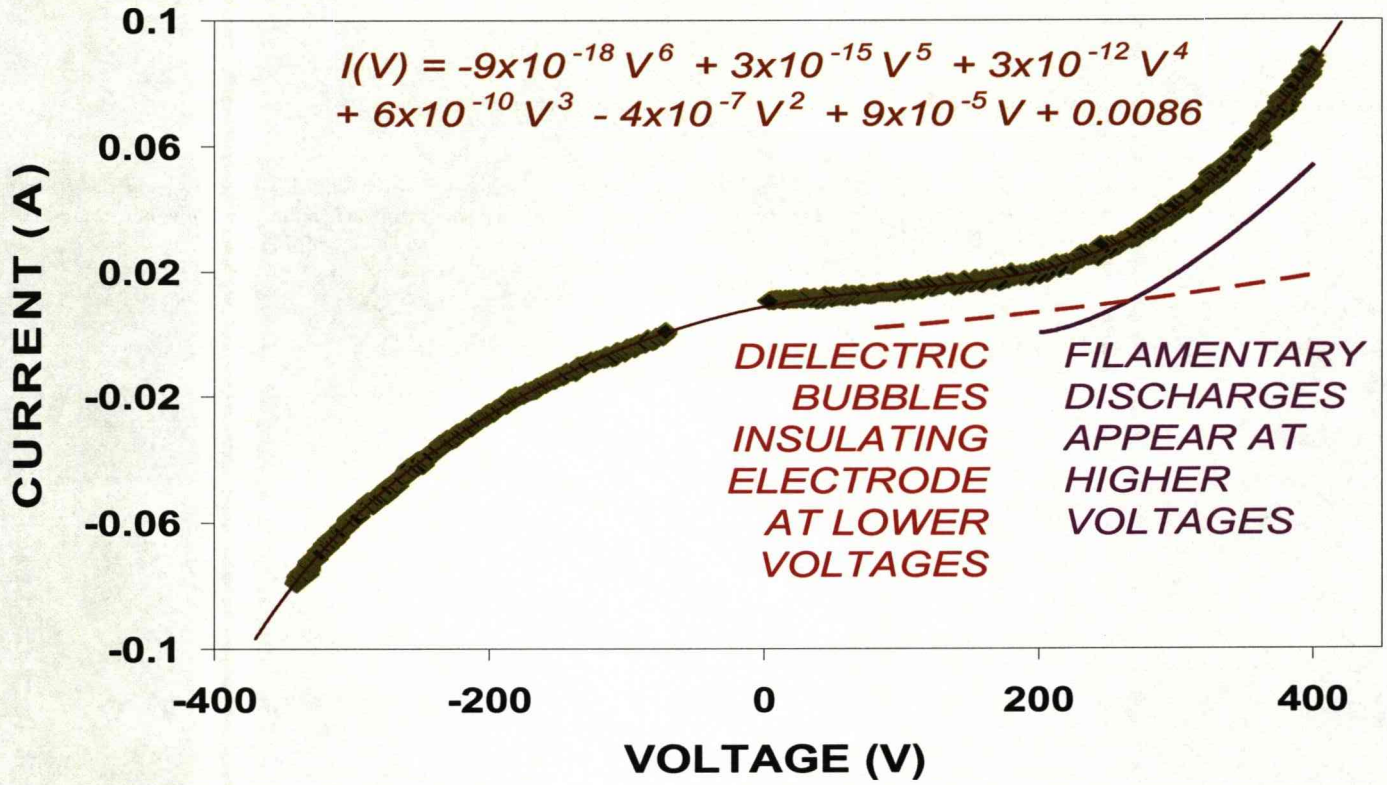

Figure 4.29 shows that the voltage-current trend can be non-linear. Current undergoes two regimes: The purple is highly conductive and indicates electrical discharges and gaseous breakdown (higher-voltages); the red is more resistive (dielectric bubble formation).

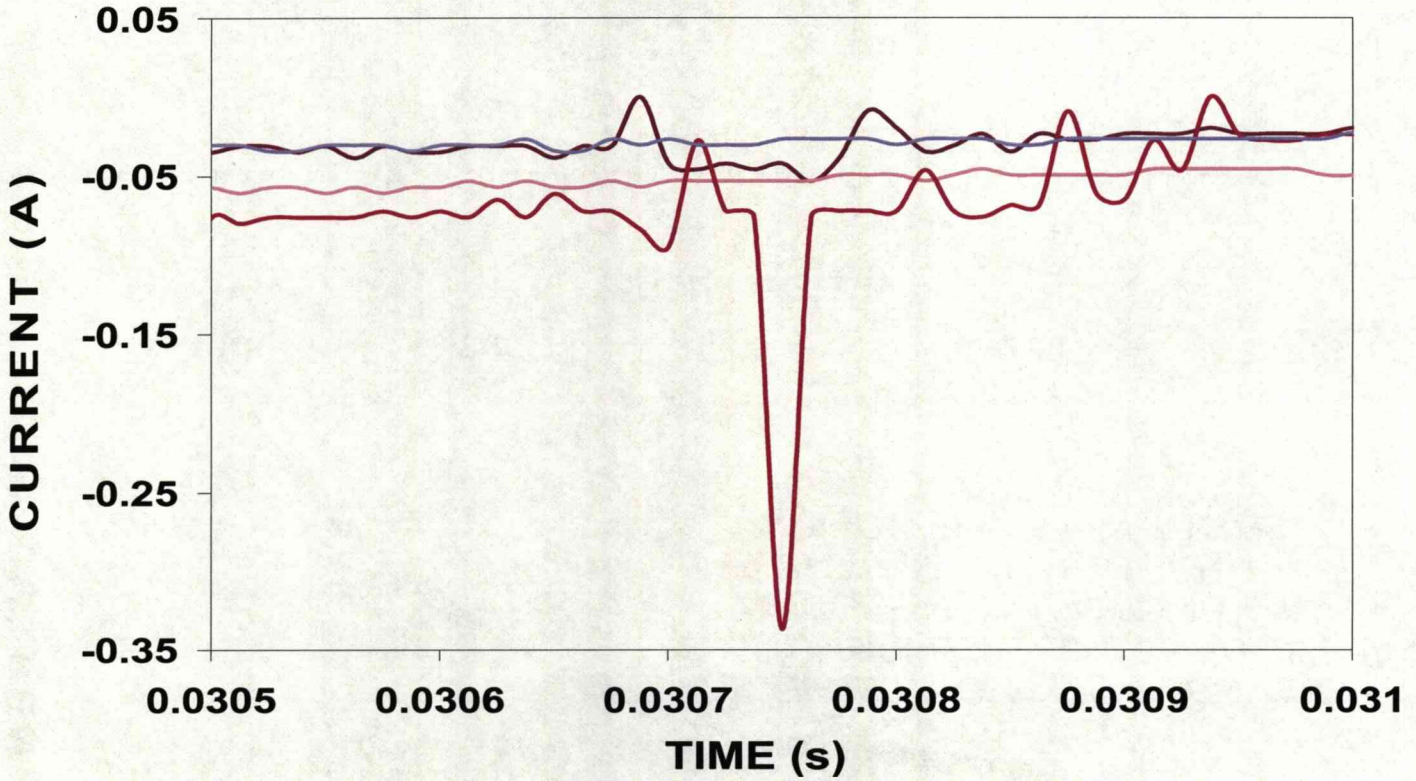

Figure 4.30 is a closer examination of four current-time plots. The filamentary nature of the discharge is highlighted here. Mean filament duration was found to be ~0.2ms; much longer than those reported for DBD in chapter two. Note that the current spike amplitude is comparable with the RMS current (see large current-spike of figure 4.18).

It will be assumed that the electrolyte and silicon electrode are one system and that they reach thermal equilibrium in the timeframe of the experiment (~30 minutes).The table of figure 4.23 shows the internal energy gained (in total) by the electrolyte (and the electrode) U_E. This is the sum of the heat absorbed from the discharge Q_D, and the joule heating effect of the current flowing through the electrolyte and electrode (self heating).

$$\dot{U}_E = \left|\dot{Q}_D\right| + \left|i_f \cdot V_E\right| \approx \left|\dot{Q}_D\right| + i_f^2 \cdot R_E$$

Equations 4.2

The approximation of equations 4.2 reflects the fact that some voltage (~1eV) is used to electrolyse the electrolyte. Since AC is applied and electrolysis occurs over a small, live and hot electrode, the recombination of oxygen and hydrogen gases (both produced by the live electrode) is inevitable. Also, the applied RMS voltages are far greater than chemical potentials required for electrolysis. The upshot of these considerations is to assume that the electrolyte is a purely resistive element.

From equations 4.2, i_f is the factored current (See next paragraph for definition) and V_E is the voltage drop across the electrode and electrolyte. R_E is the resistance of the electrolyte and electrode in series prior to dielectric insulation and discharge formation. It is therefore the minimum impedance measured (see figure 4.26). It was found by taking the mean of the minimum values displayed in figure 4.26. Therefore, the combined electrolyte and electrode series resistance $R_E = 847.6\Omega \pm 3.3\%$. This value was assumed constant (see figure 4.28) and any deviation from this linearity (see figure 4.27) meant that bubbles were being formed (see the red curve in figure 4.29) and that the filamentary discharges have been initiated (see the purple curve in figure 4.29).

The factored current i_f has been introduced to account for the discrepancy between the calculated average power, RMS voltage and RMS current product. The factored current is more useful than the RMS current here as it links potential difference to energy conversion rates. The factored current can be calculated by taking the ratio between calculated power and RMS voltage.

$$\frac{\overline{P}}{V_{RMS}} = i_f$$

Equations 4.3

Electrical Work Rate & Factored Current

V_{RMS}		$P_{Average}$		$I_{Power\ Factored}$	
Value	%	Value	%	Value	%
173.719	0.03	13.143	0.2	0.0757	0.2
278.979	0.01	18.625	0.4	0.0668	0.4

Figure 4.31 is a table of RMS voltage, average electrical power (electrical work rate is used in this argument) and factored current.

The factored current has been ascertained. We may now compute the heat transferred to the electrolyte and electrode from the discharge by rearranging equation 4.2 and using the value of the minimum resistance that was previously mentioned.

Joule Heating & Heat Absorption

dU_E/dt		P_E (Joule Heating)		dQ_D/dt	
Value	%	Value	%	Value	%
14.3	0.4	3.8	3.3	10.5	3.3

Figure 4.32 is a table whose columns' values (from left to right) are total observed electrolytic and electrode internal energy change rate (from figure 4.23) as well as deduced joule heating power of the electrolyte and electrode. The final column is the heat transfer rate from the discharge.

The voltage applied via the power supply is equal to the sum of the discharge, electrolytic and electrode voltage drops. Since the resistance of the electrolyte and electrode is known, the discharge voltage drop may be calculated using the factored current.

$$V = V_E + V_D \quad \therefore \quad V_D = V - V_E = V - i_f \cdot R_E$$

Equations 4.4

V and V_D are the total applied voltage across the supply and discharge voltage drops respectively. In un-magnetised plasma, the conductivity between any two points in the plasma is usually very high and the voltage-current relationship can be linear (Ohms law). However the accumulation of charges within a few Debye lengths of the electrodes can change the linearity of the voltage-current relation. As electrons are drawn to the anode, they form a cloud over the anode surface (between the anode and the cathode). This cloud arises due to the balancing of thermal and electrostatic energies of the electrons. In other words, the kinetic energies acquired by the electron from the electric field and their subsequent velocity randomised by collisions with other particles and each-other causes the electrons to accumulate near the anode surface instead of being

admitted directly into the bulk of the anode. The electron cloud repels other incoming electrons (from the cathode) whose kinetic energies are insufficient to penetrate the cloud (space-charge limitation). The electrons with sufficient energy (from the cathode) to penetrate the cloud contribute to the current. Electrons within the cloud whose momentum-vector are directed towards the anode fall towards the anode (in the absence of further obstructing collisions. See Keen's book titled "Plasma Physics").

Let us assume that the discharge is space-charge limited (see the purple curve of figure 4.29 whose voltage co-ordinate was computed by inputting the factored current and discharge radius into the Child-Langmuir law) then we can calculate the theoretical space-charge voltage drop.

$$|\mathbf{J}| \approx \frac{i_f}{{r_D}^2} \approx \frac{4 \cdot \varepsilon}{9} \cdot \left(\frac{2 \cdot e}{m_e} \right)^{1/2} \cdot \frac{V_{SC}^{3/2}}{r_D^2} \quad \therefore V_{SC} \approx \left[\frac{9 \cdot i_f}{4 \cdot \varepsilon} \cdot \left(\frac{m_e}{2 \cdot e} \right)^{1/2} \right]^{2/3}$$

Equations 4.5

Equations 4.5 were presented in this form by Keen. $\mathbf{J}$, m_e and V_{SC} are current density, electron mass and voltage across the discharge gap assuming it were evacuated and the electrode was space-charge limited. It was decided for comparative purposes to use the discharge parameters found experimentally and compare them with the vacuum case (same current, voltage and dimensions but with a vacuum between the electrodes instead of the electrolysed gases). CGDE is a glow discharge and when a low-pressure glow discharge has its electrode separation reduced, its structure (dark space, positive column etc.) does not scale down with the decreased separation, but rather the features of the discharge are lost. The near-electrode region (space-charges) remains until the electrode separation is virtually reduced to zero. CGDE is a small volume discharge.

Although it produces light (unlike the dark region near the anode of a DC low-pressure glow discharge) this may be due to the bombardment of electrons and ions on the virtual electrolytic electrode. There may not be a luminous gaseous electrical discharge column where electrons and ions exist in equal concentrations in any given portion of the contact glow discharge (gas envelope surrounding the electrode). Therefore quasi-neutrality may not apply. If the space-charge region is found to be comparable in size with the discharge radius, then we cannot treat the contact glow discharge (under the conditions described in this thesis) as a quasi-neutral electrical discharge or plasma.

Discharge and Space-Charge Voltages

V_D		V_{SCe}		Ratio (%)	
Value	%	Value	%	Value	%
222.4	0.8	935.6	0.4	23.8	0.9

Figure 4.33 is a table showing the discharge voltage drop, the estimated electronic space-charge sheath voltage (at low-pressures, but similar current and dimensions) and the ratio between the two values expressed as a percentage. The subscript *e* represents the instantaneous near-anode region.

Although the voltage drop value is ~24% of that expected from a vacuum or low pressure, it shows that since CGDE is a discharge of minute dimensions, its space-charge region is significant. If the approximation in equations 4.5 were replaced by an exact geometric factor based on spherical geometry, the ratio between observed and space-charge voltage drops would be ~80%. The geometrical factors were excluded because CGDE geometry was not observed in enough detail. Since current density is a function of r_D and due to the generic ellipsoid geometry of the

discharge, the square of the discharge "length" is approximately equal to its area.

It is doubtful if CGDE can be called plasma. Its behaviour is dominated by space-charges (as seen in figure 4.29). Its dimension can be calculated by rearranging equations 4.5 for the vacuum space-charge limited discharge gap, d_{sc}

$$|\mathbf{J}| = \frac{i_f}{\pi \cdot r_D{}^2} = \frac{4 \cdot \varepsilon}{9} \cdot \left(\frac{2 \cdot e}{m_e}\right)^{1/2} \cdot \frac{V_{SC}^{3/2}}{d_{SC}^2} \quad \therefore d_{SC} = \frac{2 \cdot r_D}{3} \cdot \left(\frac{\pi \cdot \varepsilon}{9 \cdot i_f}\right)^{1/2} \cdot \left(\frac{2 \cdot e}{m_e}\right)^{1/4} \cdot V_{SC}^{3/4}$$

Equations 4.6

ε is the permittivity (assumed to be equal to that of free space since the dielectric constant of steam under atmospheric pressure is close to unity).

Discharge Radius & Sheath Thickness

r_D (μm)		d_{SCe} (μm)		Ratio (%)	
Value	%	Value	%	Value	%
183.8	4.4	131.5	4.4	71.5	6.2

Figure 4.34 is a table of measured discharge radius, computed vacuum electronic space-charge thickness and the ratio between them expressed as a percentage (values from left to right).

The table of figure 4.34 was computed from measurement and theory. No approximations were made in regards to its validity as in equations 4.5. It is shown in the table that the space-charge thickness (given the same voltages and currents measured experimentally) for electrons in a vacuum tube is comparable to the observable discharge length. Quasi-neutrality therefore does not apply.

Heat is being transferred from the discharge to the electrolyte and electrode via conduction and charged particle bombardment. Heat transfer also occurs when the discharge bubble detaches from the electrode and floats towards the surface of the liquid. The former scenario is directed and driven by electric fields. The latter scenario occurs by random collisions of neutral particles within the bubble incident on the electrolyte-bubble interface. Heat transfer is greatest when the bubble is attached to the electrode and the detached bubble's heat transfer is negligible in comparison.

Heat loss via evaporation occurs from joule-heating of the electrolyte and electrode. The slightly elevated temperature of the liquid due to this effect causes heat loss from the liquid surface. Since the liquid temperatures at the instant of deactivation are similar to pre and post deactivation temperatures one can see from the graph of figure 4.24 that electrolytic and electrode ohmic heat loss are negligible compared to heat gained from the discharge (also see figure 4.32).

If all of the kinetic energy of the charged particles bombarding the electrolyte and electrode is absorbed (especially in the case of the electrolyte) then the rate at which the electrolyte and electrode acquire heat from the discharge Q_D is equivalent to the rate at which the charged particles bombard and transfer energy to the electrolyte and electrode. Heat lost from the discharge is primarily due to charged particle bombardment since the neutral species are unaffected by potential differences (energetic neutrals obtain their energy from collision with a charged particle or charge exchange). The energy lost per charge by the charged particle's collision upon the electrode or electrolyte surface may be ascertained by dividing the electrolyte's and electrode's absorbed heating power by the factored electric current. The current is electron-dominated so we will speak of electron energy transfer instead of charged particle transfer.

$$\frac{d \in_k}{dq} = \frac{1}{e} \cdot \frac{d \in_k}{dt} \cdot \frac{dt}{dN_e} \equiv \frac{\dot{Q}_D}{i_f} = V_Q$$

Equation 4.7

Where V_Q and N_e are the kinetic energy lost per charge in the near electrolyte or electrode region (whereupon it transfers its gained kinetic energy to the electrolyte or the electrode) and the number of electrons crossing the discharge-electrolyte/electrode boundary respectively. q is charge and e is electronic charge.

The electrons at the energies suggested here tend to collide elastically with the water molecule[41-46] in most cases. Momentum transfer does occur as well as ionisation and excitation however very few electrons backscatter upon collision. The continuation of forward motion ensures electrons enter the bulk of the medium whose surface they collide with. Also, electrons with high kinetic energy have low interaction cross-sections allowing them to penetrate a medium before slowing down, increasing their interaction cross-section and eventually thermalising with thier new environment. This is true for surfaces of zero or positive potential however at high current densities, electron clouds may form near the electrode or electrolyte region and reflect other incoming electrons. That is why it is crucial to our analysis to consider the space-charge limited case.

$$|\mathbf{J}| = n_e \cdot \mathrm{e} \cdot \nu_\mathrm{e} \quad \therefore n_e = \frac{i_f}{\pi \cdot r_D^2 \cdot e} \cdot \left(\frac{m_e}{2 \cdot e \cdot V_Q} \right)^{1/2}$$

Equation 4.8

Where n_e and v_e are electron number density at the electrolyte or electrode surface and electron "drift" velocity respectively.

Current and Electron Number Densities

J (kAm^{-2})		v_e (kms^{-1})		n_e	
Value	%	Value	%	Value	%
314.4	4.4	7451.6	1.7	5.3×10^{17}	4.7

Figure 4.35 is a table of current density, electron ballistic velocity and electron number density at the electrolyte interface assuming hemispherical geometry of the discharge. The first and last columns are to be doubled for the electrode interface assuming planar geometry.

The table of figure 4.35 displays the electron number density. It is the highest estimate made in this thesis and is indicative of the relatively high currents of CGDE in comparison to DBD and GDE. The ratio in the table of figure 4.33 was entered into the spreadsheet as an uncertainty bound when calculating n_e. The subsequent electron deposition energy into the electrolyte or electrode (from the velocity measurement) was found to be; $\in_{ke} = 157.6eV \pm 3.4\%$

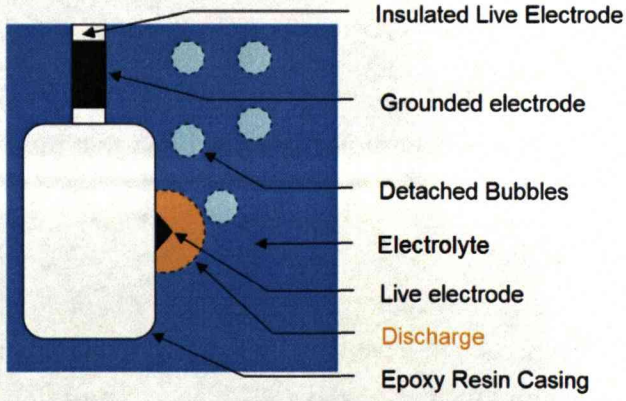

Figure 4.36 is an illustration of CGDE: The solid black areas denote electrodes. The orange area is the discharge and the pale blue circles are bubbles.

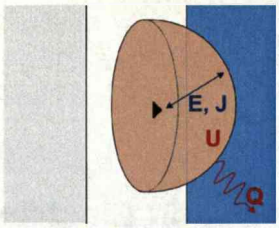

Figure 4.37 is a perspective view of CGDE. The colours closely match those of figure 4.36. The blue region is the electrolyte, the grey shows perspective only on the (cuboid-shaped epoxy-resin casing). Discharge diameter ~0.1mm. **E, J**, U and Q are electric field, current density, internal energy and heat-loss. The heat lost from the discharge to the electrolyte is responsible for part of the latter's internal energy increase. The joule heating effect of the electrolytic current also increases the electrolyte's internal energy. Here the subscript D usually connected to Q is omitted since the discharge was the main feature of the illustration.

4.6 Conclusion

The illustrations of figure 4.36 and figure 4.37 show the CGDE process. The joule-heating process was not illustrated (for simplicity). This joule-heating effect was calculated and accounted for in the beginning of the analysis section so that the discharge parameters could be examined in detail. U in the illustration of figure 4.37 was responsible for heating, electrolysis and vaporisation of the uncollected gases. It was the unknown factor in the equation and without direct gas analysis all detailed estimates involving U are speculative. Most of the energy was in Q and this was measured and analysed in detail.

The electrical and energetic aspect of novel contact glow discharge electrolysis was investigated in this chapter. Results show that the discharge produces a uniform luminous circular region which can serve as a light source in open liquid. It was found that the electric current remains at a more or less constant value despite a substantial change in the total applied voltage.

The discharge in the small region surrounding the live electrode substantially affects the total conductance of the system in statistic manner. The fact that the current remains largely un-altered under different voltages implies that the system self-regulates the current by releasing different

amounts of gas under different applied voltages. With a silicon pointed electrode in aqueous sodium chloride electrolyte a typical power of 18W is dissipated in the system with an applied voltage of 279V (RMS) and equivalent current of 67mA. The discharge region has a typical dimension of 0.5mm which puts it into the category of "micro-electrical discharge" at atmospheric pressure.

With the low currents of CGDE, electrolysed gas population of the discharge volume is far less dense than the electrolytic liquid. Therefore the electrons are more likely to collide with the electrolyte and excite its molecules. It is reasonable then to assume that most of the light from CGDE originates from electrolyte de-excitation (following electronic bombardment) or bremsstrahlung rather than gas-phase collision and de-excitation. Super-heated and vaporised electrolyte (bombarding electrons heating and vaporising molecules originally in the liquid-phase) is also likely to de-excite and produce light. It is argued that this light is more intense than collision of high-energy electrons with already-vaporised molecules (The luminosity observed in the GDE water plasma could not be recreated by passing steam between two dry electrodes. Direct impact of the electrons with water in the liquid-phase is responsible for the apparent brightness of the discharge. See chapter three).

Despite its categorisation as plasma, strong electric fields (indicative of the steep voltage drop across the small discharge region) support the observation of a non-luminous discharge in the gaseous region. The term "contact glow discharge electrolysis" is perhaps better suited than "plasma electrolysis" as reported in some sources. The electron number density and electron deposition energy incident upon the discharge-electrolyte/electrode interface was found to be $n_e = 5.3 \times 10^{17} m^{-3} \pm 4.7\%$ and $\in_{ke} = 157.6eV \pm 3.4\%$ respectively. Its low-

current and high electron energy could superheat thin layers of an electrolyte to high temperatures. The low vaporisation rate would make it a promising candidate for high-specific impulse propulsion for spacecraft microthrusters.[90,101.]

Chapter 5

APPLICATIONS AND FUTURE WORK

5.1 Overall Summary of the Work

The characteristics of three types of electrical discharge have been experimentally studied for potential applications in process conditioning. Non-thermal refers to an electrical discharge state where electron temperature is or may potentially be much higher than that of the heavy particles. Since potential engineering processes involve gas or liquid environments, the electrical discharge environments that have been studied in the present work includes electrodes in gas (DBD in Chapter 2), electrodes in liquid (CGDE in Chapter 4) and electrodes in a gas as well as in a liquid (GDE in Chapter 3). The power supply to the electrical discharge system uses power frequency which is an advantage for industrial applications.

For the purpose of process conditioning, a natural requirement is that the electrical discharge as a means of controlling process environment should not consume large amount of electrical energy otherwise it would not be economically viable. To this end the electrical discharge was generated with a barrier in the supply current to limit power dissipation. The other requirement would be that chemically active species are present abundantly in the electrical discharge environment. For the activation of any reactions or micro processes the charged particles, especially the electrons, must possess a certain level of energy. This requires the existence of relatively strong electric fields somewhere in the non-thermal electrical discharge region. In the present work this was realised by the application of high

voltages across the electrode gap or the use of specific electrode configurations.

The operation of an electrical discharge system with relatively large discharge space is of paramount importance for process conditioning. A novel DBD based discharge system has been developed in chapter two for the generation of filamentary discharges (volume-discharges) with adjustable dimensions. This configuration produces a stable, durable discharge environment. In addition to this, the contact area of the discharge electrodes can be easily adjusted. The typical contact gap is 10mm and the coaxial electrode length can be varied between 0mm and 110mm. It was found that there exists an applied transition voltage of 10kV above which the discharge switches from silent discharge to noisy filamentary regime. This threshold value is independent of the electrode contact area. The typical current in the electrical discharge is 9mA and a rough estimate shows that the electron density in the filamentary electrical discharge is in the order of $(10^{12} - 10^{15})m^{-3}$ which is comparable with figures given in other publications.[1] The wide range in electron density given here arises from the assessment of the discharge in the breakdown to steady-state regimes.

Glow discharge electrolysis occurs when an electrode is suspended above the surface of a liquid, as described in chapter three. This type of electrical discharge exists in large volumes with specific features. The design of the electrical discharge system has considered the possible problem of the current bypassing the discharge via supporting rods in a vaporised environment. Liquids, such as water or aqueous sodium chloride solution, were used as current control media between the two electrodes. The generated electrical discharge is stable and highly luminous. Spectroscopic investigation has shown that the electrical discharge environment is dominated by species originating from the liquid (and sometime the

container depending upon the configuration. The suspended electrode releases chemical species native to itself as it is an inevitable participant in the discharge). Detailed electrical characteristics have been given. There are important observations from the present work that could facilitate future important applications. It has been observed that on moist environments, fierce exothermal reactions on solid surfaces (PTFE) could be initiated by non-thermal electrical discharge under high voltage. This could have a positive implication towards future application for energy production in processes that cannot be initiated using conventional methods of activation such as ordinary heating. The migration of species in the liquid towards the electrical discharge is an interesting feature that requires further investigation. It opens the possibility that chemical species that are required in the discharge process can be transported from the liquid in a controlled manner. This type of electrical discharge could find potential use in sterilisation involving species produced from liquid media or inject desired species into a gaseous medium in a heated and chemically active state that may initiate exothermic reactions for energy production (high reported temperatures of GDE and CGDE, the production of ozone from DBD and the change in pH of electrolyte in GDE). There was evidence to suggest that the formation of acid (on moist surfaces on the ceramic container) from the nitrogen in air assisted in the release of metals native to the ceramic. Metallic reactions with acid release hydrogen (an environmentally friendly fuel).

Contact Glow Discharge Electrolysis (CGDE) represents another type of electrical discharge in liquid environment. Its rather small discharge region puts it into the micro-electrical discharge category. In the present work an electrical discharge system with silicon is used as the active electrode around whose tip the electrical discharge forms. Unlike the electrical discharges investigated in the previous two cases, sustaining CGDE only

requires a voltage level in the range of a few hundred volts because of its small size. With a small active electrode area, this type of discharge results in a bright discharge region whose diameter is in the order of a fraction of millimetre. Its stable operation implies that this type of discharge can be considered for use as an open light source in liquid with luminosity similar to a powerful LED. Applied voltage does not significantly affect the electrical discharge conductance (the current remains largely unchanged). This leads to the conclusion that CDGE is self-regulated in energy dissipation in the electrolyte. The excessive energy dissipated in the discharge system is used to produce the gas in the electrolysis/vaporisation process and further heat it. The typical current in this discharge configuration is 0.071A. The present studies have provided an overall characterisation of diverse experimental configurations in different environments for the generation of the aforementioned types of electrical discharges. Their electrical behaviour as well as their optical behaviour was experimentally observed. This forms a platform upon which further detailed investigation can be made and potential applications employed.

5.2 General Discussion

Due to the complexity of experiments with high-voltage electric discharges, there have been various difficulties that prevent the present investigation going into any further detail. However, as the results show there are many interesting issues that require further experiments and analysis. One immediate direction for further investigation is the chemical properties of the three types of electrical discharges generated. Before any attempts are made to engage these electrical discharges in process conditioning, there needs to be diagnosis of the electrical discharge composition, the chemically active species or radicals generated and the electron temperature and number density. In the case that other gases or liquids are introduced into the discharge system, then the interaction

between the incoming species and the electrical discharge need to be studied for the purpose of control of the discharge process.

The energy balance analysis for the CGDE case is not complete since the mass and composition of the gas generated in the discharge process was not measured. It would be important to see what the gas composition is when a mixture of materials is used for the liquid electrolyte. By measuring these two important parameters the conclusion that the electrical discharge is self-regulated for its energy dissipation in the electrolyte can then be directly checked.

5.3 Detailed Summary, Results and Observations

5.3.1 Dielectric Barrier Discharge (DBD)

The dielectric barrier discharge is the electrical discharge generated between two electrodes (at least one of which is isolated from the other by a dielectric barrier and a gas filled gap). When high AC voltages are applied to the electrodes, surface charges accumulate on the dielectric until the local electric fields exceed the breakdown voltage of the medium.

At the frequencies applied in the present work, this discharge appeared as a thin filament that was acoustically noisy and produced ozone from the oxygen in the atmosphere (Unlike the diffuse large-volume discharges generated by Roth et al[1]. which consisted of thousands of these filaments in parallel) and were of small volume ($\sim 10^{-8} m^{-3}$). The typical applied voltages were ~10kV and current of ~10mA. The current of a single filament seemed to be unaffected by the voltage or the available electrode area.

From observation, analysis and computational work[5] it was concluded that the dielectric nature of the barrier constricted the dispersal of charges over

its surface. As a result, high-current densities were estimated at ~40kAm^{-2}. Conditions at the onset of the luminous discharge were examined and the similarity in voltage-ranges and current-ranges for pin-planar and cylindrical coaxial electrodes was noted. The electric field (at breakdown from the pin-electrode) attenuates along the length of the discharge by Debye screening (ion temperature close to ambient[1,5]). By relating discharge potential drop to the electrostatic potential of a screened point charge, a novel method was used to calculate the Debye length and hence electron number densities. The result agreed with the literature and was estimated in the range of ~10^{12}m^{-3} to ~10^{15}m^{-3}.

5.3.2 Glow Discharge Electrolysis (GDE)

Glow discharge electrolysis occurs when an electrode is suspended above the surface of a liquid. The opposing electrode is submerged beneath the liquid surface and upon application of high-voltage, electrical breakdown occurs in the gas near the suspended (usually pin-shaped) electrode. Electrons drift towards the liquid surface and then bombard it (with energies depending upon the voltage-drop approximately one mean free path away from the liquid surface). This ionises the molecules of the fluid and sends the ions upward towards the instantaneous cathode contributing to the current. This is a form of high-voltage electrolysis for which gases comprised of different chemical species are released at the electrolyte surface. Dissociation and vaporisation of the electrolyte take precedence over the normal electrolysis processes due to the higher energy fluxes involved.

In the present work, GDE was used to introduce dissolved species into the electrical discharge column. Sodium chloride was dissolved in water so that it would enter the electrical discharge phase. This experiment was successful as spectroscopy confirmed the presence of sodium species in the discharge. Sodium species were located along the entire length of the

discharge column. This was verified by high-speed photography. In addition to this, the electrolyte (water only) was observed to become acidic during the experiment. The acid attacked the interior of the ceramic container and released metals contained in the ceramic into the electrolyte and subsequently into the atmosphere. The abundance of an unknown specie of AMU:e 49 (suggested to possibly be titanium monohydride) was found to be ~50% of argon's (by mass) in the local atmosphere.

The glow discharge was a weakly ionised electrical discharge characterised by its low current magnitude (~10mA) whilst water was the virtual electrode. It was a more strongly ionised electrical discharge (~20mA) when moist ceramic was the electrode. This occurred without increasing voltage or decreasing the discharge gap length. This phenomenon was due to the high ionisation potential of water (~13eV) as compared to that of aluminium (~6eV) titanium (~7eV) or silicon (~8eV) present in the ceramic (see figure 3.5 and figure 3.6 of chapter 3). This gives us an indication as to the characteristic energies of the bombarding electrons. GDE produced gas temperatures exceeding 1500K and were between 3900K and 5000K according to black (or grey) body spectral fits. The water plasma was optically thin however so its electron temperature had to be determined from bremsstrahlung radiation. It was found to be ~3400K. This temperature places an upper limit on the ion and gas temperatures making both ion and electron temperatures comparable. Despite the low currents observed, the water plasma in this case was in thermal equilibrium (equilibrium plasma, much like a flame; weakly ionised). The water plasma is of relatively large volume (~$10^{-6}m^3$), has a large diameter (~10^{-2}m) and has large surface and cross-sectional areas.

5.3.3 Contact Glow Discharge Electrolysis (CGDE)

Contact glow discharge electrolysis occurs when an electrode of small area is inserted into an electrolyte with its counter electrode (electrode area may

be larger in this case). At high enough voltages the current rises and electrolysed and vaporised gases (due to electrolysis and joule-heating) envelop the smaller electrode completely and restrict the flow of current. When the voltage is further raised the gas envelope breaks down, an electrical discharge sustains the current between the two electrodes and through the electrolyte. The discharge is luminous and high current densities rapidly heat and erode the working (live) electrode.

In the present work, silicon electrodes were experimented with instead of the metallic wire electrodes referred to in the literature[54,57,58]. Silicon is much cheaper than the platinum and tungsten wire usually used and survives longer under atmospheric pressures. The work in this thesis reports experimental durations lasting up to an hour at 279V RMS and 0.071A RMS. Metallic electrodes of 10mm length and 1mm diameter would last for less than ten minutes under the same applied voltage.

The CGDE experiments possessed the highest (controlled) current magnitudes of all the three types of electrical discharge featured in this thesis (and also the lowest voltages). The current ~0.1A indicates that CGDE has currents magnitudes similar to the abnormal glow discharge or non-thermal arc regimes. Current densities ~1MAm^{-2} were observed and the typical discharge area was ~10^{-8}m^{-2}. The current magnitude did not increase much with voltage however the filaments appeared more frequently as the voltage increased.

Statistical analysis of several current spikes (filaments) and waveforms suggest that CGDE obeyed the Child-Langmuir law when its current-voltage relation was scaled up by the relevant geometric factors. The small electrode area and small volume resulted in short discharge gaps that were only a few hundred times greater than the electron mean free path in air under atmospheric pressure.

The consequence of the findings reported in the previous paragraph permits an insight into CGDE electric fields and electron number density. The vacuum-case space-charge thickness for electrons (computed from experimentally derived current, voltage and discharge radius measurements) was comparable to the discharge gap. This brings into doubt the existence of a quasi-neutral plasma column for CGDE. Like a DC glow discharge at low pressures, reduction of the electrode spacing does not scale down the discharge structure[1] but removes the various luminous and dark regions. When the discharge gap is reduced further the luminous electrical discharge column (plasma) reduces in length and so the light produced from CGDE is not mostly produced in the discharge gas but generated by charged particle collisions with the more-dense transparent electrolytic virtual electrode (liquid). Thus the phrase "contact glow discharge electrolysis" is more accurate than the commonly used "plasma electrolysis" as CGDE may not always produce a quasi-neutral plasma.

Electron speeds are subsequently high and the drift speed approaches the ballistic speed acquired by the electron transferring potential energy from the electric field between the electrode and electrolyte into kinetic energy. The electron number density $n_e = 5.3 \times 10^{17} m^{-3} \pm 4.7\%$ near the electrode region (instantaneous anode). The discharge voltage drop $V_D = 222.2V \pm 0.4\%$ (voltage drop between the electrode and electrolyte). Heat transfer to the electrolyte and electrode at a rate of $\dot{Q}_D = 10.5W \pm 3.3\%$.

5.3.4 Overall Findings, Commonality and Distinctions

DBD is an electrical discharge several millimetres in length and less than 1mm^2 in cross-sectional area. For the input power supplied to it (~10W) it showed no evidence of significantly increasing gas temperature. It is logical to assume that the energy is mostly possessed by the electrons (as

these are mobile and conduct the current ~10mA). The filaments it produces are luminous along its length (~5mm). The applied voltage was ~10kV. The ratio between this voltage and distance is $2MVm^{-1}$. The electrical field necessary to cause breakdown in air is $3MVm^{-1}$. The presence of low electric fields despite high applied voltages is indicative of the availability of mobile charge carriers. It is safe to regard this region as plasma (since the filament length exceeds typical laboratory Debye lengths), although the low gas temperatures[1,5] suggests that this type of plasma is non-equilibrium.

GDE produces an electrical discharge with lengths of several millimetres and its highly luminous discharge columns have cross-sectional areas ~$1cm^2$. Its low current (~10mA) and voltage (~1kV) afford it powers ~10W. The power is more or less equally shared between the electrons and ions. This conclusion is arrived at because GDE power levels are similar to DBD power levels however the gas temperature in the former vastly exceeds the gas temperature of the latter. Also, the electron temperature deduced by bremsstrahlung (~3400K. see "Plasma Physics by B.E. Keen) was an upper boundary set for the ion temperature. The gas temperature (comparable to the ion temperature, see chapter 3) exceeded 1500K.

A possible reason for the highly efficient absorption of electron kinetic energy upon collision with the water molecule can be attributed to the water molecules' hetero-nuclear nature. The existence of a permanent dipole for the water molecule arises due to differences in electronegativity between oxygen and hydrogen atoms. The permanent molecular dipole allows energy transfer due to the angular momentum of the water molecule (de-excitation rotation emission spectra following collision-excitation).

With similar dimensions and voltages to DBD, the ratio between voltage and discharge length is $0.1MVm^{-1}$- $1MVm^{-1}$. This effective or averaged

field is lower than the electric breakdown field of air and suggests the presence of screening mobile charged carriers throughout its length. The highly luminous discharge (despite its low current) can be categorised as equilibrium plasma. This statement can be made because the typical laboratory Debye length is far smaller than GDE dimensions. This permits quasi-neutrality. The issue of weakly ionised plasma being in thermodynamic equilibrium can be addressed by highlighting the flame-like behaviour of the highly luminous discharge. Fire tends to be in thermal equilibrium and is weakly ionised.

CGDE is an electrical discharge whose length is less than a millimetre (~0.1mm). Its volume ~0.001mm^3 means that the typical laboratory Debye length is comparable to the dimensions of the discharge. Its current ~100mA is larger than those observed for DBD and GDE whereas its voltage ~100V is much lower. The ratio between voltage and discharge length is ~1MVm^{-1} which is comparable to the electrical breakdown field of air. This suggests that there are few screening charge-carriers in the volume or that the inter-electrode spacing is small (like the high-field near-electrode region in a low-pressure glow discharge). Since a relatively substantial electric current was observed, the latter explanation seems more plausible. The similarity between the averaged electric field and the electrical breakdown field suggests that the field is uniform and of large magnitude throughout the length of the discharge (this is not the case for typical plasmas). From the present work, under atmospheric pressure CGDE is therefore unlikely to be plasma.

Current-voltage trends indicate that the discharge follows the Child-Langmuir law (see figure 4.29 of chapter four) when the appropriate dimensions are inputted into the relevant equation. This claim may seem contradictory since the CGDE bubble has the same particle number density as air under standard temperature and pressure (assuming faraday's law,

the current and volume already given and the discharge duration ~100μs) yet the resemblance of the CGDE current-voltage curves to the three-halves power law is uncanny and deserves explanation. Even with the minute dimensions of the CGDE bubble (~0.1mm), the mean free path in the gas is (~0.1μm). This value however can vary for the electron depending upon its kinetic energy. Electrical breakdown occurs in air when a high electric field accelerates free electrons. Since these free electrons (secondary) are generated from background radiation (from radioactive sources or cosmic ray particles) they posses high kinetic energies. They therefore have a low collision cross-section[41-43] and long mean free path. This effect is amplified by the acceleration caused by the electric field producing runaway electrons. Although the cross section for elastic collisions with water decreases ~10eV (electron kinetic energy), the incident electron is generally deflected[42,45] to shallow angles. This enables the electron to maintain most of its previous momentum and accumulate kinetic energy between collisions from the electric field (thus supporting the runaway effect). Some of the electrons therefore move as though they were in a vacuum despite the fact that the gas is quite heavily populated.

The features common to the various discharges are as follows;

1. DBD and GDE are plasmas. They are likely to posses regions of quasi-neutrality. If the typical laboratory Debye length is ~0.1mm then it is possible that there is a region within the plasma column in which electron and ion number densities are almost equal (Typical column lengths ~10mm).

2. GDE and CGDE utilise one liquid electrode. They are both highly luminous and their currents favour negative voltage polarities. The similarity in virtual electrode composition (liquid water) and the negative feedback mechanism that seems to restrict CGDE currents

at ~0.071A may suggest highly efficient kinetic energy transfer from electrons to water molecules. This was observed for GDE and was responsible for the high gas temperature. The high gas temperatures of CGDE was not directly observed in detailed experiment but indicated in the construction of a rudimentary CGDE thruster (See later sections).

3. DBD and CGDE were discharges that impinge upon small areas (on the respective electrodes). The absence of gas heating despite the supplied power suggests that DBD produced electrons with high kinetic energy. The high electric fields, relatively high-currents (always electron dominated) and heating power transferred to the electrolyte (presumably and most likely from electron bombardment) suggest that the electrons produced in CGDE were also (initially) of high kinetic energy.

Distinctions between the three electrical discharges are highlighted here;

1. DBD is non-thermal plasma: This is suggested by its low observed and reported gas temperatures. By inference, the ion temperature was also assumed relatively low in comparison to the electron temperature. The filament length exceeded typical laboratory Debye lengths.

2. GDE is weakly ionised thermal plasma: This is deduced by observing the lower limit of gas temperature and calculating the electron temperature. These were found to be comparable within less than an order of magnitude. The low observed current can be attributed with low ionisation cross-section of water at the given electron temperatures and the ability of water to absorb electron kinetic energy (from drift momentum or random motions). Its

discharge column length also exceeded typical laboratory Debye lengths.

3. CGDE is not likely to be typified as plasma under the conditions reported in this thesis: Its small dimensions are comparable to typical laboratory Debye lengths. The ratio between its discharge voltage drop and its length were comparable to the electric breakdown field of air suggesting that the screening effect by mobile charge carriers was negligible. The existence of such a high electric field in a virtual DC case (voltage cycle period = 0.02s; discharge duration ~ 100μs) is indicative of a significant degree of charge separation. Quasi-neutrality therefore does not apply. CGDE is best described as an electrical discharge in the near electrode (silicon, live) region impinging upon water (grounded virtual electrode).

5.4 Future Work

5.4.1 Furthering Present work

The following section briefly outlines the projected courses of investigation following the present work described in this thesis had more time been available. Other aspects of the DBD, GDE and CGDE observed during experimentation have been relevantly collated and will be mentioned and described here.

It was noticed that the application of high non-uniform electric fields condensed steam into mist without observable luminous discharges occurring. This phenomenon was observed using a boiler and an isolated high-voltage wire-electrode. In the GDE experiments, water was observed to vaporise at lower electrical energies than the latent heat of vaporisation.

One possibility[85-88] is the formation of water cluster around ions formed by coronal discharges in air. Such clusters allow small volumes to leave the bulk fluid collectively instead of completely dissociating into separate water molecules. Less intermolecular bonds are broken in the former case than in the latter and the observed energy to achieve the former would be lower than the enthalpy of vaporisation. Detailed analysis of the gas temperatures and masses would quantitatively determine the role of the electric field in the vaporisation of water.

A novel co-axial electrode design was used for DBD experiments in this thesis that allowed the electrodes to be extended or retracted thus varying their effective area. An advancement of that design was also proposed. With adequate time for development and research, a high-frequency, high-voltage source may be applied to observe discharge (spatial) uniformity in the electrode gap. Discharge regime (normal glow discharge or abnormal glow discharge) may be controllable by adjusting the effective area of the electrode in addition to voltage amplitude manipulation.

5.4.2 Possible Novel Applications of Findings

The three experimental findings and observations that have been earmarked in this thesis for their possible benefit are spacecraft propulsion, and underwater lighting. The properties of the experimental observations and findings will be shortly discussed and their application and role suggested. Lastly in each case their advantage over existing systems shall be mentioned.

The first application utilises the condensation of steam to minute water droplets (mist) and has been observed in experiment at atmospheric pressures and near high-voltage wires. It is reported to be caused by the formation of coronal discharges and these are inevitable when applying high-voltages to objects with small radii of curvature. Condensation heat

transfer[87,88] may be used on spacecraft for the re-condensation of steam into water vapour for the purpose of thermo-stasis of spacecraft systems. Without a cold reservoir, a spacecraft can trap heat and its only natural means of heat dissipation is via radiation into the vacuum of space.

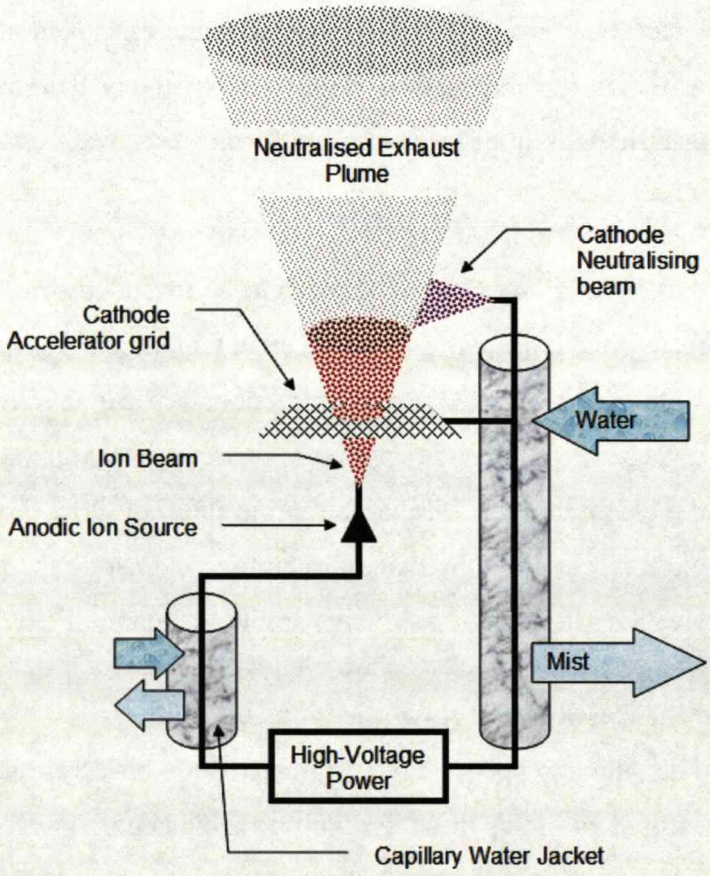

Figure 5.1 is a typical electric propulsion unit with novel electro-kinetic heat exchanging system. Steam (produced by possible heating of cables or other systems) is allowed to condense near high-voltage conduits and circulate. Further condensation allows the water to re-enter the heat exchange cycle.

Complex heat-exchange equipment and pumps add mass, expense and maintenance considerations to already complex space missions. Many spacecraft utilise electric propulsion where the generation of high-voltages is necessary. If water vapour is passed over high-voltage conduits it will condense rapidly, cooling the warm conduits at little energy expense to the

spacecraft's onboard power source (safety measures must be taken to insulate the high-voltage conduits and isolate water near regions of differing electrical potential).

Despite the uncertainty in observing excess heats from chemical reaction in CGDE, a second application was realised when a rudimentary nozzle was constructed similar to that illustrated in figure 5.2. A shaft was fashioned into the epoxy resin from a calorimetric capsule (featured in chapter four) and jets of orange-coloured incandescent steam were observed and thrusts ~0.3N were recorded using the top pan balance for indicatory measurement. The concept of deriving thrust from CGDE is feasible. The illustrations of figure 5.2 display a generic rocket-engine whose chemical fuel injection system is replaced by a CGDE coaxial electrode. Only the tip of the silicon core electrode is made conductive by removal of its oxide layer.

The electrolyte trickles through the capillary which also doubles as an outer counter electrode. CGDE occurs and the electrolyte is boiled and vaporised. The temperature of the steam is determined by the mass flow-rate of the electrolyte and the applied voltage (note that liquid water can be vaporised and heated above boiling by electron impact[41-43]). The steam expands supersonically out of the nozzle to produce thrust. The rough estimates for thrust and specific impulse are competitive with present electro-thermal propulsion devices[90-101]. The thermodynamic properties of CGDE measured accurately in chapter four may be used model CGDE thrusters using the ideal rocket equation.

5.5 Closing Comments on Novel Findings

This thesis reports three electrical discharge systems that were experimented with in detail. Novel findings or methods were developed for each experiment and these will be outlined in the following paragraphs.

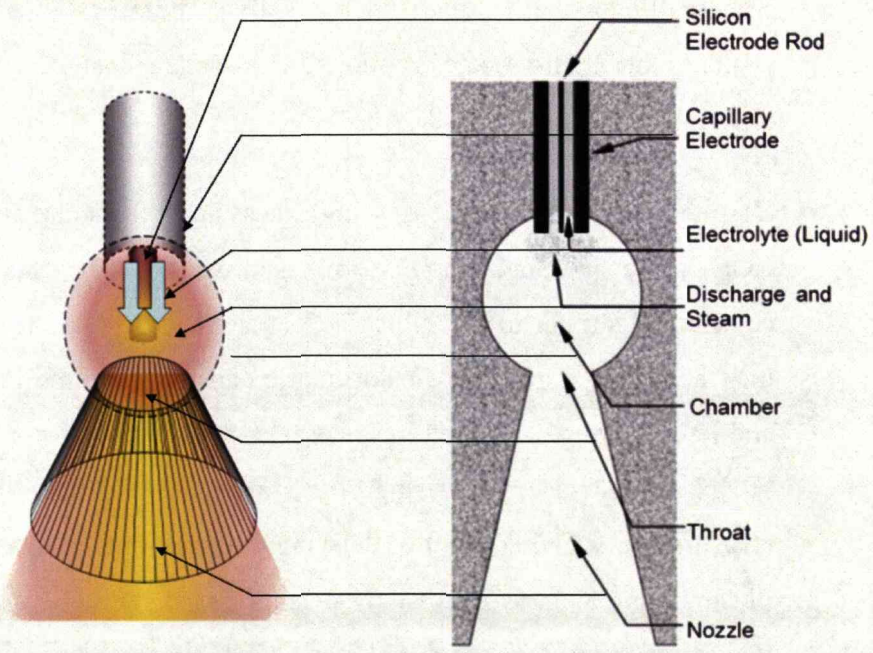

Figure 5.2. (Left)The blue arrows represent the electrolytic flow (dribble) rate whilst the yellow-red region denotes gaseous expansion due to heat transfer from the discharge. The discharge here is spherical and centred upon the conducting tip of the silicon electrode that is furthermost in the chamber. (Right) A cross-section of CGDT. Grey area is ceramic housing.

A novel electrode configuration was designed and tested for the DBD experiments. Its cylindrical geometry and electrode coverage with the dielectric barrier were extremely robust and could withstand high voltages (~20kV) despite its dimensions (~10mm radius). Its electrode area could be varied from 0 to 174.4cm^2. By assuming the root of a thin filament on a pin-shaped electrode to be equivalent to a point-charge, a novel approach derived from the Debye length and potential drop across the discharge was devised to determine the electron number density in atmospheric pressure non-thermal plasma.

Sodium chloride solution was prepared in order for sodium species to migrate from the electrolyte towards the electrode via the electrical discharge column. Spectroscopic observation and high speed photography revealed that sodium species were excited in plasma and that they

populated the entire length of the plasma column. This is an ideal mechanism for encouraging gas-phase reactions for sterilisation or possible exothermic reactions (in a specially chosen gaseous atmosphere) with further research. It was also observed that NO_x were not detected when water was used as a virtual electrode. Instead the water became acidic and this (possibly augmented by joule heating) released elements native to the water-container. A specie of AMU:e 49 (possibly, but not confirmed to be TiH) was found to be 50% of Ar abundance in the local atmosphere (by mass). Metals may be liberated directly from suitable minerals (in the presence of specially chosen gaseous atmospheres) by the action of GDE. Metals and acids react to produce hydrogen (although this is generally not the case for nitrogen atmospheres); an environmentally friendly fuel.

The contact glow discharge was probed extensively to assess its physical nature and discharge mechanisms for the first time. It was found here that its electron number density was $\sim 10^{17} m^{-3}$ and that it is unlikely to be quasi-neutral in general since its calculated space-charge thickness near the electrolyte or electrode is comparable to the discharge's physical dimensions. Calling the contact glow discharge "plasma" may not always be accurate and certainly was not under the conditions reported in this thesis. Since the existence of a plasma column and hence a gaseous luminous region is brought under question, the discharge's luminosity most likely originates primarily from charged particle bombardment upon the dense electrolytic (transparent) virtual electrode. De-excitation and bremsstrahlung radiation from the electrolyte liquid is more likely from electrolyte than from the less dense gas that occupies the discharge.

REFERENCES

[1] Roth, R.J., Rahel, J., Dail, X. and Sherman, D.M. "The physics and phenomenology of One Atmosphere Uniform Glow Discharge Plasma (OAUGDP™) reactors for surface treatment applications". J. Phys. D: Appl. Phys. 38. (2005)

[2] Roth J.R., Sherman D.M. and Wilkinson S.P. "Electrohydrodynamic Flow Control with a Glow Discharge Surface Plasma". AIAA Journal, Vol. 38, No. 7, pp 1166-1172. (2000)

[3] Roth, J. R., Nourgostar S. and Bonds T.A. "The One Atmosphere Uniform Glow Discharge Plasma (OAUGDP®) - A Platform EHD Technology for the 21st Century". IEEE Transactions on Plasma Science, Vol 35, No 2, pp 233-250. (2007)

[4] Chen Z. "P-Spice Simulation of One Atmosphere Uniform Glow Discharge Plasma (OAUGDP™) Reactor Systems". IEEE Transactions on Plasma Science, Vol 31, No 4, (2003)

[5] Gibalov V.I. and Pietsch G.J. "The Development of Dielectric Barrier Discharges in Gas Gaps and on Surfaces". IOP, J. Phys. D: Appl. Phys. 33 pp 2618-2636. (2000)

[6] Kogelschatz U., Eliasson B. and Egli W. "Dielectric barrier discharges-principle and applications". J. Physique IV C4, pp 47-66. (1997)

[7] Chen Z. "Impedance Matching for One Atmosphere Uniform Glow Discharge Plasma (OAUGDP™) Reactors". IEEE Transactions on Plasma Science, Vol 30, No 5. (2002)

[8] Muller S. and Zahn R.J. "On various kinds of dielectric barrier discharges" Contrib. Plasma Phys. 36, pp 697-709. (1996)

[9] Drimal J., Gibalov V. and Samoilovich V. "Silent discharge in air, nitrogen and argon". Czech. J. Phys. B 37, pp 641-644. (1987)

[10] Nogueira J.C., Iga I. and Chaguri, J.E. "Total Cross Section Measurements Of Electrons Scattered By Nitrogen And Carbon Dioxide In The Energy Range 500-3000eV". Revista Brasileira De.Flsica Vol. 15, Number 3. (1985)

[11] Tabata T., Shirai T., Sataka M. and Kubo H. "Analytic Cross Sections For Electron Impact Collisions With Nitrogen Molecules". Atomic Data And Nuclear Data Tables 92, pp 375-406. (2006)

[12] Bertein E.H., "Charges on insulators generated by breakdown of gases". J. Phys. D: Appl. Phys. 6, pp 1910-1916. (1973)

[13] Smith P. P., Buchanan R. A., Kamath S.G. and Roth J.R. "Enhanced Pitting Corrosion Resistance of 304L Stainless Steel by Plasma Ion Implantation". J. Vac. Sci. and Technol. B, Vol. 12, No. 2, pp 940-944. (1994)

[14] Gibalov V.I. and Pietsch G. "Energy release in a microdischarge channel". Russ. J. Phys. Chem. 68, pp 1023-1028. (1994)

[15]Yurgelenas Y.V. and Wagner H.E. "A computational model of a barrier discharge in air at atmospheric pressure: the role of residual surface charges in microdischarge formation". IOP J. Phys. D: Appl. Phys. 39 pp 4031-4043 (2006)

[16] Eliasson B., Hirth M. and Kogelschatz U. "Ozone synthesis from oxygen in dielectric barrier discharges". J. Phys. D: Appl. Phys. 20, pp 1421-1437. (1987)

[17] Braun D., Kuchler U. and Pietsch G.J. "Microdischarges in air-fed ozonizers". J. Phys. D: Appl. Phys. 24, pp 564-572. (1991)

[18] Gibalov V.I. "Synthesis of ozone in a barrier discharge" Russ. J. Phys. Chem. 68, pp 1029-1033. (1994)

[19] Xu S., Xu J., Peng X., and Zhang J. "Deposition of Thin Titania Films by Dielectric Barrier Discharge at Atmospheric Pressure". Plasma Science & Technology, Vol.8, No.3. (2006)

[20] Schmidt-Szalowski K., Ranek-Boroch Z., Sentek J., Rymuza Z., Kusznierewicz Z. and Misiak M. "Thin Films Deposition from Hexamethyldisiloxane and Hexamethyldisilazane under Dielectric-Barrier Discharge (DBD) Conditions". Journal Plasmas and Polymers Issue Volume 5, Numbers 3-4, pp 173-190. (2000)

[21] Roth J.R., Rahel J., Dai X. and Sherman D.M. "The physics and phenomenology of One Atmosphere Uniform Glow Discharge Plasma (OAUGDP) reactors for surface treatment applications". J. Phys. D: Appl. Phys. Volume 38 No. 4, pp 555-567. (2005)

[22] Tsai P.P., Roth J.R and Chen W. "Strength, Surface Energy, and Ageing of Meltblown and Electrospun Nylon and Polyurethane (PU) Fabrics Treated by a One Atmosphere Uniform Glow Discharge Plasma (OAUGDP)", Textile Res. J. Vol. 75, No. 12, pp 819-825 (2005).

[23]Tsai P.P., Roth J.R and Chen W "Investigation of the fiber, bulk, and surface properties of meltblown and electrospun polymeric fabrics", International Nonwovens Journal, Vol. 13, No. 3, pp 17-23. (2004)

[24] Tsai P., Wadsworth L. and Roth J. R. "Surface Modification of Fabrics Using a One-Atmosphere Glow Discharge Plasma to Improve Fabric Wettability", Textile Research Journal, No 67(5), pp 359-369 (1997)

[25] Kayes M.M., Critzer Faith J., Kelly-Wintenberg K., Roth J.R., Montie T.C. and Golden D.A. "Inactivation of Foodborne Pathogens Using a One Atmosphere Uniform Glow Discharge Plasma". Foodborne Pathogens and Disease, Vol. 4, No. 1, pp 50-59. (2007)

[26]. Roth J.R., Chen Z., Sherman D.M., Karakaya F., Tsai P. Kelly-Wintenberg K. and Montie T.C. "Increasing the Surface Energy and Sterilization of Nonwoven Fabrics by Exposure to a One Atmosphere Uniform Glow Discharge Plasma (OAUGDP)". International Nonwovens Journal, Vol.10 No.3 pp 34-47. (2001)

[27]. Roth J. R., Sherman D. M., Gadri R.B., Karakaya F., Chen Z., Montie T.C., Kelly-Wintenberg K. and Tsai P. "A Remote Exposure Reactor (RER) for Plasma Processing and Sterilization by Plasma Active Species at One Atmosphere". IEEE Trans. Plasma Sci., Vol. 28, No. 1, pp 56-63. (2000)

[28] Kelly-Wintenberg K., Sherman D.M., Tsai P., Ben Gadri R., Karakaya F. Chen Z., Roth J. R. and Montie T.C. "Air Filter Sterilization Using a One Atmosphere Uniform Glow Discharge Plasma (the Volfilter)". IEEE Trans. Plasma Sci., Vol. 28, No. 1, pp 64-71. (2000)

[29] Kelly-Wintenberg K., Hodge A., Montie T. C., Deleanu L., Sherman D. M., Roth J. R., Tsai P. and Wadsworth L.C. "Use of a One Atmosphere Uniform Glow Discharge Plasma (OAUGDP) to Kill a Broad Spectrum of Microorganisms". J. Vac. Sci. Technol. Vol. 17, pp 1539-1544. (1999).

[30] Kelly-Wintenberg K., Montie T.C., Brickman T.C., Roth J.R., Carr A.K., Sorge K., Wadsworth L.C., and Tsai P. "Room Temperature Sterilization of Surfaces and Fabrics with a One Atmosphere Uniform Glow Discharge Plasma". Journal of Industrial Microbiology & Biotechnology Vol. 2, pp 69-74. (1998)

[31] Tanino M., Wang X., Takashima K., Katsura S. and Mizuno A. "Sterilization using dielectric barrier discharge at atmospheric pressure". International Journal of Plasma Environmental Science & Technology Vol.1, No.1, pp 102-107. (2007)

[32] Yanzhou S., Yuchang Q., Ailing N and Xudong W. "Experimental Research on Inactivation of Bacteria by Using Dielectric Barrier Discharge" Plasma Science, IEEE Transactions on Volume 35, Issue 5, pp 1496-1500. (2007)

[33] Choi J.H., Han I., Baik H.K., Lee M.H., Han D.W., Park J.C., Lee I.S., Song K.M. and Lim Y.S., "Analysis of sterilization effect by pulsed dielectric barrier discharge". Journal of Electrostatics 64, pp 17-22. (2006)

[34] Lelièvre J., Dubreuil N. and Brisset J.L. "Corona Discharges in Humid Air". J. Phys. III France 5, pp 447-457. (1995)

[35] Akiyama H., Sato M. and Davis R.H. "Streamer Discharges in Liquids and Their Applications". IEEE Transactions on Dielectrics and Electrical Insulation 7, pp 646-653. (2000)

[36] Laroussi M., Lu X. and Malott C.M. "A non-equilibrium diffuse discharge in atmospheric pressure air" Plasma Sources Sci. Technol. 12, pp 53-56 (2003)

[37] Hough K.O. and Denaro A.R. "A current regulator for glow discharge electrolysis" J. Sci. Instrum. Vol. 43. (1966)

[38] Ning C.G, Hajgató B., Huang Y.R., Zhang S.F., Liu K., Luo Z.H., Knippenberg S., Deng J.K. and Deleuze M.S., "High resolution electron momentum spectroscopy of the valence orbitals of water". Chem. Phys. (2007)

[39] Lemus R. "Vibrational excitations in H_2O in the framework of a local model". Journal of Molecular Spectroscopy 225, pp 73-92. (2004)

[40] Mota R., Parafita R., Giuliani A., Hubin-Franskin M.J., Lourenc J.M.C., Garcia G., Hoffmann S.V., Mason N.J., Ribeiro P.A., Raposo M. and Lima P. "Electronic state spectroscopy by synchrotron radiation", Vieira a,g, Chemical Physics Letters 416 Water VUV, pp 152-159. (2005)

[41] Gorfinkiel J.D., Morgan L.A. and Tennyson J., "Electron impact dissociative excitation of water within the adiabatic nuclei approximation". IOP. J. Phys B. 35 543. (2002)

[42] Itikawaa Y. and Mason N. "Cross Sections for Electron Collisions with Water Molecules". AIP J. Phys. Chem. Vol. 34, Number 1. (2005)

[43] Thorn P.A., Brunger M.J., Kato H., Hoshino H. and Tanaka, H. "Cross sections for the electron impact excitation of the a3B1: b3A1 and B1A1 dissociative electronic states of water". IOP J. Phys. B: At. Mol. Opt. Phys. 40, pp 697-708. (2007)

[44] Yakovenko A.A., Yashin V.A., Kovalev A.E. and Fesenko E.E. "Structure of the Vibrational Absorption Spectra of Water in the Visible Region". Institute of Cell Biophysics, Russian Academy of Sciences. (2002).

[45] Champion C., Hanssen J. and Hervieux, P.A. "Electron impact ionization of water molecule". AIP J. Chem. Phys. Vol. 117, Number 1. (2002)

[46] Faure A., Gorfinkiel G.D. and Tennyson J., "Low-energy electron collisions with water: elastic and rotationally inelastic scattering." IOP J.Phys. B: At. Mol. Opt. Phys. 37 (2004)

[47] Clements J.S., Sato M. and Davis R.H. "Preliminary Investigation of Pre-breakdown Phenomena and Chemical Reactions Using a Pulsed High-Voltage Discharge in Water". IEEE Transactions on Industry Applications IA-23, pp 224-235. (1987)

[48] Piskarev I.M., Rylova A.E. and Sevast'yanov A.I. "Formation of Ozone and Hydrogen Peroxide during an Electrical Discharge in the Solution-Gas System". Russian Journal of Electrochemistry 32, pp 827-829. (1996)

[49] Lukes P., Appleton A.T. and Locke B.R. "Hydrogen Peroxide and Ozone Formation in Hybrid Gas-Liquid Electrical Discharge Reactors". IEEE Transactions on Industry Applications 40(1), pp 60-67. (2004)

[50] Su Z.Z., Ito K., Takashima K., Katsura S., Onda K. and Mizuno A. "OH Radical Generation by Atmospheric Pressure Pulsed Discharge Plasma and its Quantitative Analysis by Monitoring CO Oxidation". IOP Journal of Physics D, Applied Physics 35, pp 3192-3198. (2002)

[51] Wittig C. and Underwood J. "Two-photon photodissociation of H_2O via the B state". Chemical Physics Letters 386, pp 190-195. (2004)

[52] Aristova N. A., Piskarev I.M., Ivanovskii A.V., Selemir V.D., Spirov G.M. and Shlepkin S.I. "Initiation of chemical reactions with an electric discharge in a solid dielectric-gas-liquid system". Russian Journal of Physical Chemistry 78(7), pp 1144-1148. (2004)

[53] Ivannikov A.A., Lelevkin V. M., Tokarev A.V. and Yudanov V.A. "Atmospheric-Pressure Glow Discharge Treatment of Water". High Energy Chemistry 37(2), pp 115-118. (2003)

[54] Sengupta S.K., Singh R. and Srivastava A.K. "A Study on Non-Faradaic Yields of Anodic Contact Glow Discharge Electrolysis using Cerous Ion as the OH Scavenger: An Estimate of the Primary Yield of OH Radicals". Indian Journal of Chemistry Section A - Inorganic Bio-Inorganic Physical Theoretical & Analytical Chemistry 37, pp 558-560. (1998)

[55] Tezuka M. and Iwasaki M. "Liquid-Phase Reactions Induced by Gaseous Plasma. Decomposition of Benzoic Acids in Aqueous Solution". Plasma & Ions, pp 23-26. (1999)

[56] Malik M.A., Ghaffar A. and Malik S.A. "Water Purification by Electrical Discharges". Plasma Sources Science and Technology 10, pp 82-91 (2001)

[57] Harada K. and Suzuki S. "Formation of Amino Acids from Elemental Carbon by Contact Glow Discharge Electrolysis". Nature 266, pp 275-276. (1977)

[58] Munegumi T., Shimoyama A. and Harada K. "Abiotic Asparagine Formation from Simple Amino Acids by Contact Glow Discharge Electrolysis." Chemistry Letters no.5, 393-394. (1997)

[59] Miller S.L. "Production of Some Organic Compounds under Possible Primitive Earth Conditions". Journal of the American Chemical Society 77, pp 2351-2361. (1955)

[60] Cunnane V.J., Scannell R.A. and Schiffrin D.J. "H_2 + O_2 Recombination in Non-Isothermal, Non-Adiabatic Electrochemical Calorimetry of Water Electrolysis in an Undivided Cell". Journal of Electroanalytical Chemistry 269, pp 163-174. (1989)

[61] Miles M.H. "Calorimetric studies of Pd:D_2O□LiOD electrolysis cells". Journal of Electroanalytical Chemistry 482 pp 56-65 (2000)

[62] Pohl H.A. "Some effects of nonuniform fields on dielectrics". J. Appl. Phys, 29(8), pp 1182-1188. (1958)

[63] Pohl H.A. "Dielectrophoresis the behavior of neutral matter in nonuniform electric fields". The Quarterly Review of Biology, Vol. 55, No. 1, pp 68-69. (1980)

[64] Pohl H.A. "The Motion and Precipitation of Suspensoids in Divergent Electric Fields". J. Appl. Phys. 22(7), pp 869-871 (1951)

[65] Giddings J.C. "Field-flow fractionation of macromolecules". J Chromatogr. 470(2), pp 327-335. (1989)

[66] Giddings J.C. "Field-flow fractionation: analysis of macromolecular, colloidal, and particulate materials". Science. 260(5113), pp 1456-1465. (1993)

[67] Huang Y, Wang X.B., Becker F.F. and Gascoyne P.R. "Introducing dielectrophoresis as a new force field for field-flow fractionation". Biophys J, 73(2), pp 1118-1129. (1997)

[68] Liu M.K., Williams P.S., Myers M.N. and Giddings J.C. "Hydrodynamic relaxation in flow field-flow fractionation using both split and frit inlets". Anal. Chem. 63(19), pp 2115-2122. (1991)

[69] Hagedorn R., Fuhr.G., Müller T. and Gimsa J. "Traveling-wave dielectrophoresis of microparticles". Electrophoresis. 13(1-2), pp 49-54. (1992)

[70] Gross W. "Dielectrophoretic reconfiguration of nanowire interconnects". Nanotechnology 17, pp 4986-4990. (2007)

[71] Fuhr G., Arnold W.M., Hagedorn R., Müller T., Benecke W., Wagner B. and Zimmermann U. "Levitation, holding, and rotation of cells within traps made by high-frequency fields". Biochim Biophys Acta. 1108(2), pp 215-223. (1992)

[72] Gascoyne P.R.C. Huang Y., Pethig R., Vykoukal J. and Becker F.F. "Dielectrophoretic separation of mammalian cells studied by computerized image analysis". Meas. Sci.Technol. 3, pp 439-445. (1992)

[73] Andreux, J.P., Merino A., Renard M., Forestier F., Cardot P. "Separation of red blood cells by field flow fractionation". Exp Hematol. 21(2) pp 326-330. (1993)

[74] Becker F.F., Wang X.B., Huang Y., Pethig R., Vykoukal J. and Gascoyne P.R. "Separation of human breast cancer cells from blood by differential dielectric affinity". PNAS USA. 31, 92(3) pp 860-864. (1995)

[75] Berg H.C. and Turner L. "Selection of motile nonchemotactic mutants of Escherichia coli by field-flow fractionation". PNAS USA, 88(18) pp 8145-8148. (1991)

[76] Burt J.P., Pethig R., Gascoyne P.R., Becker F.F. "Dielectrophoretic characterisation of friend murine erythroleukaemic cells as a measure of induced differentiation". Biochim Biophys Acta, 1034(1): pp 93-101. (1990)

[77] Caldwell K.D. Cheng Z.Q. Hradecky P. Giddings J.C. "Separation of human and animal cells by steric field-flow fractionation". Cell Biophys (4), pp 233-251. (1984)

[78] Parsons R., Yue V., Tong X., Cardot P., Bernard A., Andreux J.P. and Caldwell K. "Comparative study of human red blood cell analysis with

three different field-flow fractionation systems". J Chromatogr. B Biomed Appl. 686(2), pp 177-187. (1996)

[79] Hsu S.H., Wang B.T., Huang M.H., Wong W.J. and Cross J.H. Growth of Japanese encephalitis virus in Culex tritaeniorhynchus cell cultures. Am. J Trop Med Hyg. (5), pp 881-888. (1975)

[80] Schwan H.P and "Linear and nonlinear electrode polarization and biological materials". Ann Biomed Eng, 20(3), pp 269-288. (1992)

[81] Talary M.S., Mills K.I., Hoy T., Burnett A.K., Pethig R., "Dielectrophoretic separation and enrichment of CD34 & cell subpopulation from bone marrow and peripheral blood stem cells". Med. Biol. Eng. Comput. 3(2), pp 235-237. (1995)

[82] Tong X., Ash J.F. and Caldwell K.D. "Rapid swelling of a CHO-K1 aspartate/glutamate transport mutant in hypo-osmotic medium", J Membr Biol. 156(2), pp 131-139. (1997)

[83] Tong X. and Caldwell K.D. "Separation and characterization of red blood cells with different membrane deformability using steric field-flow fractionation". J Chromatogr. B Biomed. Appl. 674(1), pp 39-47. (1995)

[84] Zhou X.F., Mark G.H., Pethig R. and Eastwood I.M. "Differentiation of viable and non-viable bacterial biofilms using electrorotation." Biochim Biophys Acta. 17, 1245(1), pp 85-93. (1995)

[85] Maier H. "Electrorotation of colloidal particles and cells depends on surface charge". Biophys J. 73(3), pp 1617-1626. (1997)

[86] Aldmov A.V., Vatazhin A.B., Likhter V.A. and Sorokin A.A. "Air-Steam Mixture Flow With Condensation On Ions And Electrokinetic Processes". Fluid Dynamic, Vol. 31, No. 1, (1996)

[87] Oh K.J., Gao G.T, and. Zenga X.C., K. J. "The effect of a uniform electric field on homogeneous vapor–liquid nucleation in a dipolar fluid." I. Stockmayer fluid.

[88] Chu, R., Takano, K. and Nishio, S, "Study on Enhancement of Condensation Heat Transfer Using an Electric Field Heat Transfer" Journal Of Chemical Physics Volume 110, Number 5 1 February 1999. Asian Research, Received 24 August 1998; accepted 27 October 1998, 29 (4), (2000)

[89] Chu R.C., Nishio S. and Tanasawa I. "Enhancement of Condensation Heat Transfer on a Finned Tube Using an Electric Field". Asian Research, 29(4), Journal of Enhanced Heat Transfer Volume 8, Number 4. (2001)

[90] Tajmar M. and de Matos C.J. "Water-arc Explosions as a Concept for Advanced Propulsion Thrusters". AIAA-2000-3762. (2000)

[91] Sovey J.S., Hardy T.L. and Englehart M. "A bibliography of electrothermal thruster technology". NTRS (1986)

[92] Cassady R.J., Hoskins W.A., Campbell M. and Rayburn C.A. "Micro pulsed plasma thruster (PPT) for the 'Dawgstar' spacecraft". IEEE Aerospace Conference Proceedings, Volume 4, Issue, pp 7-14 vol.4, (2000)

[93] Ketsdever A.D., Wadsworth C.D., Vargo S. and Muntz E.P. "The free molecule micro-resistojet - An interesting alternative to nozzle expansion". AIAA/ASME/SAE/ASEE Joint Propulsion Conference and Exhibit, 34th Volume 4, Issue, pp 7-14 vol.4. (2000)

[94]Auweter-Kurtz, M., Glocker, B., Gölz, T., Kurtz, H., Messerschmid, E., Riehle, M., Zube, D.: "Arcjet Thruster Development 1083", Journal of Propulsion and Power, Vol.12, No.6, pp.1077. (1996)

[95]Messerschmid, E., Zube, D., Meinzer, K., Kurtz, H: "Arcjet Development for Amateur Radio Satellite", J. of Spacecraft and Rockets, Vol. 33, No. 1, (1996)

[96]Johnson L. K., Rivera A., Lundquist M., Sanks T. M., Sutton A., and Bromaghim D. R. "Frequency-Domain Electromagnetic Characteristics of a 26-Kilowatt Ammonia Arcjet" Journal of Spacecraft and Rockets 0022-4650 vol.33 no.1 pp137-143. (1996)

[97]Crofton M.W., Moore T.A., Boyd I.D and Masuda I., Gotoh Y. "Near-Field Measurement and Modeling Results for Flight-Type Arcjet NH Molecule" Journal of Spacecraft and Rockets 0022-4650, vol.38 no.1 pp79-86. (2001)

[98] Suzuki T., Sakai T and Yamada T. "Calculation of Thermal Response of Ablator Under Arcjet Flow Condition" Journal of Thermophysics and Heat Transfer 0887-8722 vol.21 no.2 pp257-266. (2007)

[99] Morren W.E., Whalen M.V and Sovey J.S. "Performance and endurance tests of a laboratory model multipropellant resistojet" Journal of Propulsion and Power 0748-4658 vol.6 no.1 pp18-27. (1990)

[100] Manzella D.H., Penko P.F., De Witt K. J and Keith T.G. JR."Effect of ambient pressure on the performance of a resistojet" Journal of Propulsion and Power, 0748-4658 vol.5 no.4 pp452-456. (1989)

[101] Enos G. R., Pugmire T. K and Shaw R. "Applied resistojet technology" Journal of Spacecraft and Rockets 0022-4650 vol.8 no.1 pp63-68. (1971)

BIBLIOGRAPHY

Sahni M. "Analysis of Chemical Reactions in Pulsed Streamer Discharges: An Experimental Study". PhD. Thesis, The Florida State University College of Engineering (2006).

Halliday D., Resnick R. and Walker J. "Fundamentals of Physics Extended: Fifth Edition" John Wiley & Sons, Inc. (1997).

Eisberg R. and Resnick R. "Quantum Physics of Atoms, Molecules, Nuclei, and Particles: Second Edition" John Wiley & Sons. (1985).

Griem H.R. "Plasma Spectroscopy" McGraw-Hill, Inc. (1964)

Keen B.E. "Plasma Physics: Lectures from the Culham Plasma Physics Summer Schools, held at the UKAEA Culham Laboratory, Abingdon" IOP & AIP (1974).

Finn C.B.P. "Thermal Physics: Second Edition" Stanley Thornes (Publishers) Ltd (1998)

LIST OF RELEVANT PUBLICATIONS

Quaw M., "Contact Glow Discharge Electrothermal Propulsion" Pending approval AIAA J. Propulusion and Power (2008).

Quaw M., "Field Emission Propulsion and the Solar Wind" Pending approval AIAA J. Propulusion and Power (2008).

Quaw M., "On Ion Beams and their Applicability for Power Generation" Pending approval IOP Nucl. Fusion (2008).

Appendix I

POWER AND SAFETY CONSIDERATIONS

Mains power was tapped directly from a fuse box with an emergency switch. One phase of 240V voltage (1.25kW source) was connected to an interlocking mechanism and an emergency shutdown switch. This interlock mechanism was configured with a high-voltage painted metallic safety cage (a cubicle approximately 2m x 2m x 2m). This cage was grounded to experimental earth which was distinct from the electrical power suppliers' ground (Manweb). The purpose of the interlock was to prevent the high-voltage circuit being energised whilst the cage gate was opened. The 240V, 1.25kW one-phase power conduit was attached to the isolating transformer (5A rating) and then branched into two cables: One to supply the high-voltage transformer via the variable auto transformer (variac) the other to the measurement equipment. It should be noted that all experimental grounding points including those of the measuring equipment were common and if the cage was opened during the experiment, the measuring equipment as well as the experimental apparatus would automatically be de-activated.

The variac is a variable autotransformer whose input potential difference was 240V and output could vary from a leakage potential difference (~0V) to 280V in our particular configuration. The secondary circuit has relatively low current flowing through it and as a result, standard half or quarter watt metal film resistors were connected in series to produce large resistances. As these resistors were connected in series, it was not difficult to connect the terminals of coaxial cable across a certain number of these resistors to configure a potential divider. Once the coaxial cable was fixed

to an oscilloscope, potential differences can be measured that are a safe fraction of the actual potential across the total resistance. The total resistance is in parallel with the plasma so the plasma potential difference may be inferred also.

The plasma circuits were energised in the manner previously described and illustrated throughout the thesis. To conclude, the power source was capable of supplying an open-circuit potential difference of 80kV although a physical stopper was placed on the variac to limit this to 35kV and 1.25kW of power was available from the mains. The fuse on the primary circuit (5A in the DBD case and 20A in the GDE and CGDE cases) determines the maximum permitted RMS current on the secondary circuit. See figure 2.2 and figure 2.3 of chapter 2. Figure A1.1 and figure A1.2 give indication of the safe voltages detected by the oscilloscope due voltage division in the apparatus.

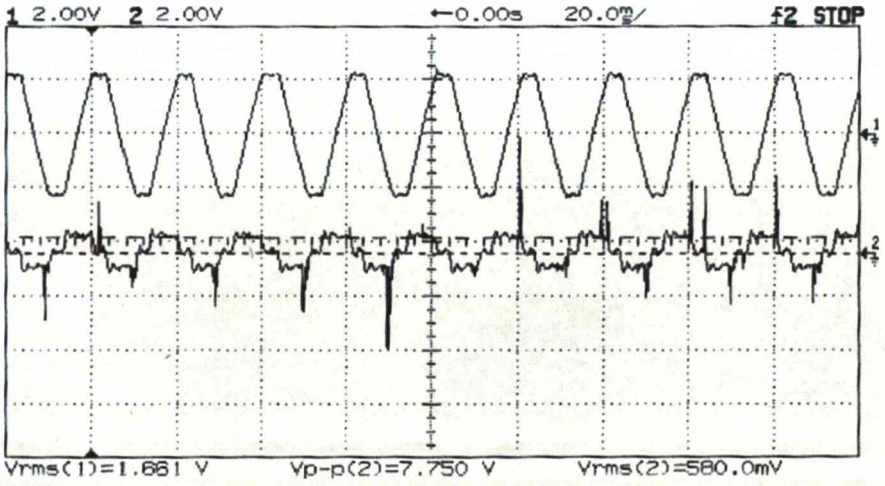

Figure A1.1 Oscilloscope trace. Trace one and two represents voltage and current respectively. The readings are raw data and were presented as such to give the reader some indication of experimental conditions. This waveform corresponds to the DBD experiments and are featured in calibrated units in chapter 2.

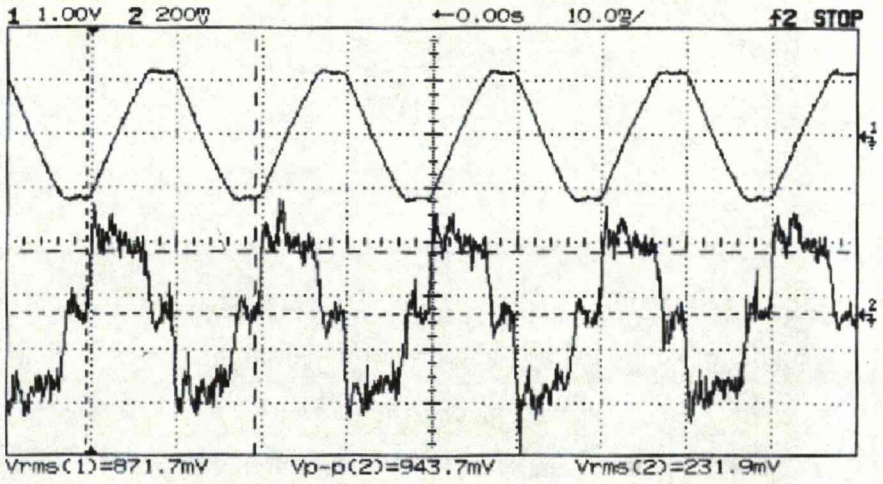

Figure A1.2 Same format as with figure A1.1. The common time-base and the current trace sensitivities have been amplified.

Appendix II

UNCERTAINTY ANALYSIS

The transformation of raw data into calibrated data has been discussed in the relevant chapters. The treatment of uncertainties quoted in the results and analysis sections in the various chapters of this thesis will be dealt with here. References will be made citing relevant examples in the thesis to the calculations in this section. Generic forms of the rules used to deal with uncertainties can be found in standard experimental physics textbooks. They are repeated here in an abbreviated version with the quantities displayed as they appeared in thesis. An example of the relevant rules is given and can be carried forward or repeated for different quantities.

$$I_p = \frac{V_2}{R_i}$$

Equation A2.1

$$V_p = \left(\frac{R_1 + R_2}{R_2}\right)V_1 - V_2 = \left(\frac{R_\Sigma}{R_2}\right)V_1 - V_2$$

Equation A2.2

Where I_p, V_1, V_2, R_i, R_1 and R_2 are the plasma or electrical discharge current, first oscilloscope voltage input (across R_2), second oscilloscope voltage input (across R_i), current-resistor value, larger voltage divider resistance and smaller current divider resistance respectively.

$$R_{\Sigma} = R_1 + R_2$$

$$\therefore \Delta R_{\Sigma} = \sqrt{(\Delta R_1)^2 + (\Delta R_2)^2}$$

Equations A2.3

The uncertainties in R_1 and R_2 were systematic and were $\pm 0.05\text{M}\Omega$ and $\pm 0.005\text{k}\Omega$ respectively.

$$P = \left(V^{+1}\right) \cdot \left(i^{+1}\right)$$

$$Z = \left(V^{+1}\right) \cdot \left(i^{-1}\right)$$

$$\therefore \frac{\Delta P}{P} = \frac{\Delta Z}{Z} \sqrt{\left(\frac{\Delta V}{V}\right)^2 + \left(\frac{\Delta i}{i}\right)^2}$$

Equations A2.4

Where P and Z are instantaneous power and instantaneous impedance respectively. Since $\Delta V = \pm 0.005\text{mV}$ is vanishingly small, it was often neglected. In the case were g was a function f of a variable x, the uncertainty in g may be derived as follows;

$$g = f(x)$$

$$\therefore \frac{dg}{dx} = f(x)'$$

$$\Rightarrow dg = f(x)' dx \therefore \Delta g = f(x)' \Delta x$$

Equations A2.5

Equation A2.3 and equation A2.5 are put into effect when the root mean square was derived for voltage and current from a dataset. This process was done on spreadsheets, involved thousands of points and directly impacts upon the conclusions found in this thesis. Let us first square the voltage V and define this as X.

$$X = V^2$$

$$\therefore \frac{dX}{dV} = 2V$$

$$\Rightarrow \Delta X = 2V\Delta V$$

Equations A2.6

Let us find the sum of the uncertainties in X and define this as Y.

$$Y = X_1 + X_2 + \ldots + X_n \therefore \Delta Y = \sqrt{(\Delta X_1)^2 + (\Delta X_2)^2 + \ldots + (\Delta X_n)^2}$$

$$= \sqrt{(2V_1\Delta V)^2 + (2V_2\Delta V)^2 + \ldots + (2V_n\Delta V)^2}$$

$$= 2\Delta V\sqrt{(V_1)^2 + (V_2)^2 + \ldots + (V_n)^2} = 2\Delta V\sqrt{\sum_{x=1}^{x=n}(V_x)^2}$$

Equations A2.7

$$V_{RMS} = \left(\frac{Y}{n}\right)^{1/2} \therefore \frac{dV_{RMS}}{dY} = \frac{1}{2}\left(\frac{1}{Y \cdot n}\right)^{1/2} \Rightarrow \Delta V_{RMS} = \frac{1}{2}\left(\frac{1}{Y \cdot n}\right)^{1/2} \Delta Y$$

Equations A2.8

Where n is the number of voltage datasets.

Appendix III

SPECTROSCOPIC CALIBRATION CURVE

The spectroscope has different sensitivities (or spectral response) at given wavelengths of light incident on the CCD detector. Although a calibration of absolute spectral intensity (in units of Watts per metre-squared) was not done (unnecessary) the true relative intensity of emitted light at different wavelengths was crucial for analysis. Despite the slight variation in experimental setup, a calibration algorithm was provided by the spectroscope's suppliers for use with spectra taken in the current work. To convey to the reader the spectral response of the CCD detector for light of different wavelengths of the same relative intensity (across all wavelengths), the calibration curve of figure A3.2 was produced. It should be noted that a CCD whose spectral response is independent of the wavelength of the incident light would produce a calibration line of zero gradient.

The graph of figure A3.1 was generated by dividing the relative intensity of the uncorrected spectra by the corrected spectra. The order of division is arbitrary but illustrates the relationship between the two spectra. The spectra involved were taken from the GDE water-plasma in the "closed rig" experiments.

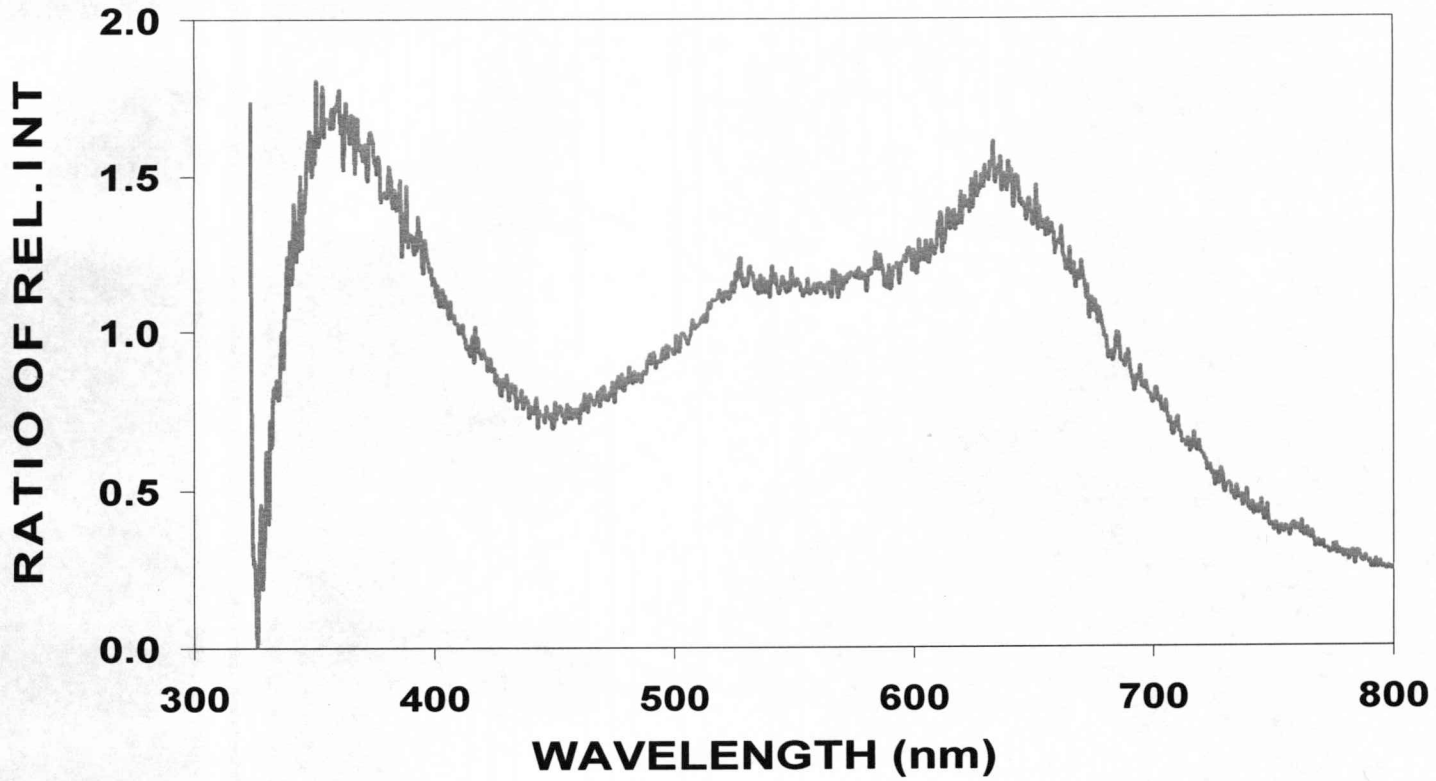

Figure A3.1 Calibration curve of the CCD detector in the (wavelength) range of operation. Its sensitivity peaks at ~360nm and ~630nm. Between ~550m and ~600nm the sensitivity is approximately independent of the wavelength of incident light. Sensitivity tails off beyond ~630nm. Sensitivity rises steeply from 326nm. Spectra were not taken below this wavelength, so the steep line of negative gradient for wavelengths lower than 326nm should be ignored (it was only added to illustrate the full-range).